MULTI-OBJECTIVE DESIGN, OPTIMIZATION, AND CONDITION MONITORING OF HIGH-PERFORMANCE ELECTRIC MACHINES FOR ELECTRIC PROPULSION

A Dissertation
Presented to
The Academic Faculty

By

Shen Zhang

In Partial Fulfillment
of the Requirements for the Degree
Doctor of Philosophy in the
School of Electrical and Computer Engineering

Georgia Institute of Technology

August 2019

MULTI-OBJECTIVE DESIGN, OPTIMIZATION, AND CONDITION MONITORING OF HIGH-PERFORMANCE ELECTRIC MACHINES FOR ELECTRIC PROPULSION

Approved by:

Dr. Thomas G. Habetler, Advisor
School of Electrical and Computer Engineering
Georgia Institute of Technology

Dr. Lukas Graber
School of Electrical and Computer Engineering
Georgia Institute of Technology

Dr. Daniel Molzahn
School of Electrical and Computer Engineering
Georgia Institute of Technology

Dr. Yan Wang
The George W. Woodruff School of Mechanical Engineering
Georgia Institute of Technology

Dr. Lijun He
Global Research Center
General Electric

Date Approved: May 10, 2019

Dedicated to my parents,
Dr. Guoqiang Zhang & Mrs. Junran Hou
for their love and support.

ACKNOWLEDGEMENTS

First and foremost, I would like to thank my advisor, Professor Thomas G. Habetler, offering me tremendous support and guidance and making all this work possible. I can always find inspiration and encouragement from his great personality and enthusiasm, and working with him is a very rewarding experience. His trust in my abilities allows me to freely explore research ideas that eventually result in interesting and fulfilling work. I am deeply grateful to his trust and guidance.

I am also greatly indebted to Professor Ronald G. Harley. Professor Harley is like a co-advisor to me, and I am honored to work with him and benefit greatly from his profound knowledge on electric machine design and his serious attitude towards research. Professor Harley will be deeply missed each and every day.

I am also very thankful to Professor Lukas Graber, Professor Daniel Molzahn, Professor Yan Wang and Dr. Lijun He for being my dissertation committee members and for their time in evaluating my thesis and providing valuable feedback.

I would like to thank Professor Jose A. Restrépo of the Universidad Simón Bolívar and the Universidad Técnica del Norte. I had the pleasure of constructing an inverter with a new sensor board with his tutelage. The hands-on experience I obtained through this process is invaluable. Professor Restrépo is always happy to answer my questions. I have also learned from him a great deal on control of power electronics.

Among numerous staff members I should mention here, I wish to especially thank Louis Boulanger and James Steinberg for helping me with numerous experimental setups.

It is very fortunate for me to have the opportunity to work with so many exceptional fellow students at Georgia Tech. Among them, I wish to especially thank Dr. Sufei Li, Dr. Yi Deng, Yi Du, Xiangyu Han, Zheng An, Liran Zheng, Dr. Yijun Bao, Dr. Nan Liu, Dr. Jie Dang, Dr. Hao Chen, Dr. Chen Jiang, Dr. Qichen Yang, Dr. Liyao Wu, Dr. Bai Cui, Dr. Liangyi Sun, Dr. Rui Fan, Professor Yu Liu, Dr. Cheng Gong, Morteza Rezaee, Omer

Lateef, Hang Shao, Jingfan Sun, Genyi Luo, Abdulaziz Qwbaiban, Xufan Song, Chunmeng Xu, Jia Wei, Boqi Xie, Chiyang Zhong, Yuan Kong, for the helpful discussions and pleasant collaborations. I would also like to thank Dr. Bin Lu, Dr. Long Wu, Dr. Pinjia Zhang, Dr. Siwei Cheng, Professor Liang Du, and Professor Zhaoyu Wang for their friendship and support. I would also like to express my gratitude to my managers at Tesla, Chenny Wang and Dr. Kai Tan, and my hosts and managners at Mitsubishi Electric Research Laboratory, Dr. Bingnan Wang, Dr. Chungwei Lin, Dr. Dehong Liu, Dr. Yebin Wang, Dr. Koon Hoo Teo, and Dr. Jinyun Zhang, who made my summers fruitful and enjoyable.

There are numerous names of faculty, family and friends that I should mention here, who have helped me during my five year at Georgia Tech. I want to express my gratitude to all of the people I know.

Lastly, I would like to dedicate this thesis to my parents. It is their love and support throughout my life that illuminates my entire world. I wish them good health and happy living.

TABLE OF CONTENTS

Acknowledgments iv

List of Tables xii

List of Figures xiii

1 Introduction and Objectives of the Research 1

1.1 Background and Problem Statement 1

1.2 Dissertation Outline 4

2 Previous Work on the Design and Optimization of Switched Reluctance Machines 6

2.1 Overview 6

2.2 Previous Work on the Modeling of Switched Reluctance Machines 7

2.2.1 Previous Work on Analytical Methods 7

2.2.2 Previous Work on Numeric Methods 8

2.3 Multi-Objective Optimization Algorithms Applied to Electric Machines . . 8

2.3.1 Deterministic Algorithms 9

2.3.2 Stochastic Algorithms 9

2.4 Previous work on Multi-Objective Design Optimization of SRMs 10

2.5 Previous Work on Switched Reluctance Machines for Automotive Applications 13

2.6 Chapter Summary 21

3 Previous Work on Fault Modes and Demagnetization Assessment on Permanent Magnet Synchronous Machines 22

3.1 PM Machine Fault Characteristics 23

3.1.1 Drive Inverter Initiated Faults 23

3.1.2 Electric Machine Initiated Faults 23

3.2 Previous work on Demagnetization Analysis of IPMSMs 23

3.2.1 Demagnetization Characteristics 23

3.2.2 Previous work on Demagnetization Analysis 26

3.2.3 Previous work on Experimental Demagnetization Test 28

3.3 Chapter Summary 28

4 Multi-Objective Design and Optimization of Switched Reluctance Machines 29

4.1 Overview 29

4.2 Challenges with the Traditional Design Method of SRMs 30

4.3 Proposed Analytical Design Method of SRMs 32

4.3.1 Specifying Prime Design Variables and Designing the SRM Geometry 32

4.3.2 Determining SRM Inductance at Arbitrary Rotor Positions 34

4.3.3 SRM Performance Calculation 37

4.3.4 Validation of the Analytical Design Model with Finite Element Analysis 40

4.3.5 Flowchart of the Proposed Switched Reluctance Machine Design Method 45

4.4 Multi-Objective Optimization with a Weighted-Sum Scalar Cost Function . 48

4.4.1 Weighed-Sum and Vector Objective Function based PSO 48

4.4.2 Design Constraints 48

4.4.3 Particle Swarm Optimization 49

4.4.4 Optimization Results with Weighted-Sum Objective Functions . . . 51

4.4.5 Post Design Verification with FEA 53

4.4.6 Improvement on Optimization Speed 54

4.5 Chapter Summary 55

5 Integrated Current Profile Optimization of Switched Reluctance Machines and Performance Evaluation of Different Optimization Algorithms 57

5.1 Overview 57

5.2 Integrated Current Profile Optimization 58

5.3 Analytical Model of SRMs Considering Both the Saturation and Commutation Effects 60

5.3.1 Single-Phase Inductance Profile Adjustment with Various Saturation Conditions 61

5.3.2 Multi-Phase Inductance Profile Adjustment with Various Commutation Conditions 62

5.4 Integrating Current Profile Optimization into the Multi-Objective Design Process 63

5.5 Multi-Objective Optimization with a Vector Cost Function 64

5.5.1 Vector Cost Function and Pareto Fronts 64

5.5.2 Multi-Objective Differential Evolution (MODE) Algorithm 65

5.6 Integrated Optimization Results with Vector-Based Objective Functions . . 68

5.7 Performance Evaluations and Comparisons of Multi-Objective Optimization Algorithms for the Analytical Design of Switched Reluctance Machines . . 71

5.7.1 Metrics for Evaluation the Pareto Front 73

5.7.2 Evaluation Results 74

5.8 An Efficient Multi-Objective Bayesian Algorithm for SRM Optimization . . 77

5.8.1 Expected-Improvement based Multi-Objective Bayesian Optimization Algorithm 79

5.8.2 Multi-Objective Extension of Bayesian Optimization Algorithm . . 84

5.9 Optimization Results and Comparison 85

5.10 Chapter Summary 88

6 Visualization and Data Mining of Multi-Operating Point Optimization of Switched Reluctance Machines 90

6.1 Overview 90

6.2 Visualization Challenges in Electric Machine Optimization 91

6.3 Visualization and Data Mining of Switched Reluctance Machine Optimization with Self-Organizing Maps 92

6.3.1 Establishing the Self-Organizing Map Framework 92

6.3.2 Visualizing Multi-Objective SRM Design Candidates with SOMs . 98

6.4 Electric Machine Optimization with Multiple Operating Points 103

6.4.1 Challenges with Visualizing Electric Machine Optimizations 103

6.4.2 Formulation of Electric Machine Optimization with Multiple Operating Points 104

6.5 Visualization of Multi-Objective Switched Reluctance Machine Optimization for Various Operating Conditions with t-SNE 106

6.5.1 Establishing the t-SNE Framework Visualizing Electric Machine Candidates 106

6.5.2 The t-SNE Algorithm 109

6.5.3 Visualizing Multi-Objective SRM Design Candidates with t-SNE . . 109

6.5.4 Case Study 1: Visualization SRM Designs Candidates Optimized for a Single Operating Point 110

6.5.5 Case Study 2: Visualization SRM Designs Candidates Optimized for Multiple Operating Points 111

6.5.6 Chapter Summary 112

7 Rotor Thermal Monitoring of Interior Permanent Magnet Machines via High Frequency Signal Injection 114

7.1 Overview 114

7.2 Principle of Rotor Magnet Temperature Estimation via High-Frequency Resistance Induced by the Eddy Currents 115

7.3 High-Frequency Resistance Extraction in DTC-Controlled IPMSMs 118

7.3.1 Generating the Appropriate High-Frequency Rotating Flux for Signal Injection 118

7.3.2 Generating the Appropriate High-Frequency Torque for Signal Injection 122

7.3.3 Illustration of the Proposed High-Frequency Torque Injection Technique 123

7.4 Real-Time Signal Processing Techniques 125

7.5 Experimental Results 127

7.5.1 Experiment Setup 127

7.5.2 High Frequency Voltage, Current and Flux Linkage Waveforms . . 128

7.5.3 Temperature Estimation at Steady State with HF Signal Injection . . 131

7.6 Conclusion 131

8 Demagnetization Assessment of Permanent Magnet Synchronous Machines with Stator Inter-turn Faults 132

8.1 Overview . . . 132

8.1.1 Analytical Calculation of Electromagnetic Quantities . . . 132

8.2 Stator Inter-Turn Fault Modeling and Demagnetization Characteristics of Rare-Earth Permanent Magnets . . . 134

8.2.1 IPM Stator Inter-Turn Fault Modeling . . . 134

8.2.2 Demagnetization Characteristics of Permanent Magnets . . . 135

8.3 Transient Analysis Results of Demagnetization with A Stator Inter-Turn Fault 137

8.3.1 Input and Circulating Current Response . . . 138

8.3.2 Progression of Irreversible Demagnetization . . . 139

8.3.3 Impact of the Inter-turn Fault Severity Factor and Equivalent Fault Resistance . . . 143

8.4 Experimental Results Assessing Demagnetization Conditions under Inter-Turn Short-Circuit Faults . . . 146

8.5 Chapter Summary . . . 146

9 Conclusions, Contributions, and Recommended Future Work . . . 148

9.1 Conclusions . . . 148

9.2 Contributions . . . 151

9.3 Recommended Future Work . . . 157

References . . . 179

Vita . . . 180

LIST OF TABLES

2.1 Comparison of different multi-objective design methods of switched reluctance machines. 11

2.2 Comparison of different SRMs designed for EV/HEV powertrains. 15

2.3 Comparison of different motor technologies designed for EV/HEV powertrains. 18

4.1 Geometric Parameters of the Benchmark 50,000 rpm 4/2 SRM. 41

4.2 Percentage of Errors of the Inductance Obtained From Analytical Equations and FEA at Different Rotor Positions of the Benchmark 4/2 SRM. 42

4.3 Geometric Parameters of the Benchmark 2,000 rpm 12/8 SRM. 43

4.4 Percentage of Errors of the Inductance Obtained From Analytical Equations and FEA at Different Rotor Positions of the Benchmark 12/8 SRM. 43

4.5 List of constraints for switched reluctance machine design. 49

4.6 Optimal 2.5A-excited, 50,000 rpm 4/2 SRM designs found by PSO. 52

4.7 Optimal 2.5A-excited, 10,000 rpm 6/4 SRM designs found by PSO. 53

4.8 Comparison of average torque and efficiency performance obtained from FEA and the proposed analytical design method. 55

5.1 List of Popular Quality Metrics Accessing the Performance of MOOA Algorithms. 74

7.1 Parameters of the IPM Machine. 127

LIST OF FIGURES

1.1 Types of motor candidates for EVs or HEVs [4]. 2

1.2 Lamination structure of IPM machines and SRMs [4]. 2

1.3 A feature comparison among alternative alternative traction machine types for passenger EVs [7]. 3

2.1 Illustration of the SRM magnetic circuit flux tube method [28]. 7

2.2 An SRM hybrid-electric powertrain assembly [77]. 13

2.3 Prototype electric vehicle with the prototype SRM and (b) the drive circuit for the prototype SRM on the EV [96]. 16

2.4 (a) (a) Prototype in-wheel SRM and (b) applying the SRM to an electric city commuter [102]. 20

3.1 Demagnetization curves of Grade 40 NdFeB up to 180 °C (note the pronounced ”knee" in the B/H curve at temperatures above 90 °C) [111]. . . . 24

3.2 Illustration of real-time demagnetization process of permanent magnets. . . 25

3.3 Magnet demagnetization ratio values after two short-circuit faults [125] . . 27

4.1 Flowchart of the “flux tube" method for calculating the SRM inductance. . . 31

4.2 An SRM geometry demonstrating all the 13 geometric design variables. . . 32

4.3 Flowchart of the analytical derivation of switched reluctance machines. . . . 35

4.4 Comparison of benchmark 4/2 SRM inductance profiles obtained through analytical equations and FEA. 41

4.5 Comparison of benchmark 4/2 SRM torque profiles obtained through analytical equations and FEA. 42

4.6 Comparison of benchmark 12/8 SRM inductance profiles obtained through analytical equations and FEA. 44

4.7 Comparison of benchmark 12/8 SRM torque profiles obtained through analytical equations and FEA. 44

4.8 Plot of flux densities calculated by FEA of 12/8 SRM at (a) aligned position and (b) unaligned position. 45

4.9 Comparison of benchmark 12/8 SRM stator tooth flux density profiles obtained through analytical equations and FEA. 45

4.10 A flowchart of the proposed SRM multi-objective analytical design method. 46

4.11 A flowchart of the proposed SRM multi-objective analytical design method displaying all of the analytical equations. 47

4.12 PSO particle behavior and process to convergence. 51

4.13 Comparison of torque profiles of the optimized designs and the benchmark 4/2 SRM. 53

4.14 Comparison of torque profiles of the optimized designs and the benchmark 6/4 SRM. 54

4.15 Validation of torque profile of the optimized Design B with FEA. 54

5.1 Optimization process in an entire search space. 60

5.2 Single-phase inductance profile comparison of an 6/4 SRM obtained through the analytical model and FEA for various saturation conditions. 60

5.3 Simulation results for the network. 62

5.4 The proposed two-stage SRM multi-objective design flowchart with integrated current profile optimization. 63

5.5 The evolution of the optimization process and the Pareto front of the SRM multi-objective design. 68

5.6 Comparison of the Pareto fronts with 200, 1,000 and 5,000 machine design candidates for (a) torque density vs. efficiency; (b) torque density vs. torque ripple and (c) torque ripple vs. efficiency 70

5.7 The evolution of the optimization process and the Pareto front of the SRM multi-objective design. 75

5.8 Comparison of the quality indicators for the NSGA-II, DE, and PSO optimal search with 5000, 1000 and 200 design candidates. (a) Contribution factor. (b) Generational distance. (c) Maximum Pareto front error. (d) Normalized hyperarea. (e) Spacing 76

5.9 (a) Three simulated sample paths of GPs with different mean and covariance functions (red dotted–quadratic trend with a Matérn $5/2$ kernel, green solid–constant trend with an exponential kernel, blue dotted–constant trend with a periodic Gaussian kernel) and (b) illustration of the principle of GP models predicting the objective function values and the prediction intervals (in blue) showing probable improvement partitioned by the data points. 82

5.10 Comparison of Pareto fronts: torque density vs. efficiency after (a) 200 evaluations; (b) 1,000 evaluations; (c) 2,500 evaluations; torque ripple. . . . 86

5.11 Comparison of Pareto fronts: torque ripple vs. efficiency after (a) 200 evaluations; (b) 1,000 evaluations and (c) 2,500 evaluations. 87

5.12 Cumulative set of SRM design candidates. 88

6.1 SOM representations in (a) output space, (b) input space and (c) after training. 94

6.2 The “surf" and “normcolor" functions to visualize input data features with an SOM. 95

6.3 Parallel coordinate of the SRM design candidates. 98

6.4 Scatter plots and histograms of the four features of the SRM design candidates. 98

6.5 Visualization of SRM design candidate data clustering and distribution: (a) labeling on an SOM and (b) U-matrix and clustering. 99

6.6 Visualization of SRM design candidate components and variables. 101

6.7 Visualization of SRM design candidate (a) hit histogram, (b) PCA projection and (c) data clustering. 101

6.8 (a) Illustration of the New European Drive Cycle (NEDC) for an electric vehicle (red line) and its torque-speed curve; and (b) motor energy distribution and clustering over the NEDC with torque and rotating speed [196]. 105

6.9 (a) Illustration of projecting the data points from the high-dimensional space to the low-dimensional map; and (b) example of a nonlinear manifold in which the Euclidean distance fails to reflect the actual pairwise similarities between points. 106

6.10 Visualization of the 460 SRM design candidates optimized for a single operating point with 5 objectives: (a) visualization by PCA; (b) visualization by Isomap; and (c) visualization by t-SNE. 111

6.11 Visualization of the 460 SRM design candidates optimized for 3 operating points with 13 objectives: (a) visualization by PCA; (b) visualization by Isomap; and (c) visualization by t-SNE. 112

7.1 Simple illustration of an IPMSM with “V-shaped" magnets. 115

7.2 (a) The distribution of eddy current on a permanent magnet; (b) stator flux density waveform (possible position associated with the eddy current direction) and (c) stator flux density and current density profile of a permanent magnet due to a non-predominant skin effect. 116

7.3 High frequency equivalent circuit of an IPMSM at steady state with an “equivalent slip". 117

7.4 Block diagram of the proposed high-frequency torque injection method on a conventional DTC scheme. 124

7.5 Signal process techniques for extracting high-frequency current and voltage. 125

7.6 (a) Experimental setup for the proposed rotor thermal monitoring method and (b) displaying the measured rotor temperature with an Arduino board . . 127

7.7 2-D flux linkage diagram (a) before high-frequency rotating flux injection and (b) after high-frequency rotating flux injection. 128

7.8 High-frequency voltage, current, phasor angle, resistance, and speed signals with high-frequency rotating flux injection at (a) 600 rpm; (b) 900 rpm and (c) 1,200 rpm. 129

7.9 High-frequency voltage, current, phasor angle, resistance, and speed signals with high-frequency torque injection at (a) 600 rpm; (b) 900 rpm and (c) 1,200 rpm. 130

7.10 Rotor temperature estimation performance with high-frequency rotating flux injection. 130

7.11 Rotor temperature estimation performance with high-frequency torque injection. 131

8.1 (a) Prius 2004 IPM motor stator and rotor and (b) motor cross section view [28]. 133

8.2 (a) Six typical points M to S selected on a permanent magnet for demagnetization analysis; (b) cross-section of 1-turn short-circuited; (c) cross-section of 3-turn short-circuited; (d) cross-section of 6-turn short-circuited and (e) cross-section of 9-turn short-circuited 135

8.3 Illustration of real-time demagnetization process of permanent magnets. . . 136

8.4 Prius 2004 IPM motor efficiency map [81] 138

8.5 Current Response to the 9-turn (12.5% severity factor) inter-turn short-circuit fault (a) three-phase current and (b) circulating current. 139

8.6 (a) Flux intensity (H) vector distribution diagram and (b) magnetic flux density waveforms for the six points identified inside the magnet following the introduction of an 9-turn (12.5% severity factor) inter-turn fault shown in Figure 2(e). 140

8.7 B-H curve with an 9-turn (12.5% severity factor) inter-turn fault of (a) point N before the application of inter-turn fault; (b) point N after the application of inter-turn fault; (c) point P before the application of inter-turn fault and (d) point P after the application of inter-turn fault. 141

8.8 Contour plots of the irreversible demagnetization progress with an 9-turn (12.5% severity factor) inter-turn fault. 143

8.9 Illustration of the inter-turn fault short-circuit current with respect to the fault severity μ and contact resistance R_f. 143

8.10 Percentage of the irreversible demagnetization area over the entire magnet surface area for different fault severity μ and contact resistance R_f. 144

8.11 The minimum flux density of the six points M–S specified on the magnet with respect to the number of shorted turns (fault severity μ) and contact resistance R_f: (a) $R_f = 0.05R_{short}$ and (b) $R_f = 0.1R_{short}$. 144

8.12 Experimental setup for introducing the inter-turn fault to the IPM machine. . 146

SUMMARY

The objective of the proposed research is to develop methods for the multi-objective design, optimization, and condition monitoring of electric machines, so as to generate the optimal designs and improve machine robustness for electric propulsion.

To a large extent, the performance and efficiency of electric propulsion systems such as electric vehicles (EV) and electric aircrafts are determined by high-performance electric machines. Among five popular machine types considered for electric propulsion, the switched reluctance machine (SRM) and the interior permanent magnet (IPM) machine have their distinct advantages in many feature categories. However, there are also some major issues compromising the performance and robustness of these machine types.

For switched reluctance machines, the most prominent issue is the intrinsic large torque ripple and acoustic noise caused by their double-salient structure. A comprehensive literature survey also suggests that the conventional and heuristic SRM design process is not able to exploit the trade-offs between design factors from the multi-objective point of view.

For IPM machines, however, the most challenging problem is the limited tolerance to various faults and high temperatures that can lead to irreversible demagnetization. These magnets can stay magnetized indefinitely for benign conditions, while prolonged exposure to a negative d-axis current or high temperatures can demagnetize the magnets of the motors to the point of irreversible demagnetization, which causes low output torque and reduced lifespan of electric propulsion systems. The current art of thermal and demagnetization monitoring of IPM machines is still underdeveloped compared to the maturing condition monitoring techniques for induction machines.

The proposed research first started with developing a fast and generalized multi-objective design and optimization method for SRMs. By introducing an analytical design model which is applicable to SRMs with any feasible stator and rotor slot combinations, a novel method for multi-objective optimization was proposed, and the number of prime variables

to be optimized was reduced to only 5, compared to some 17 design parameters in the tradition SRM design model. To further reduce the unfavorable torque ripple of SRMs, an active current profiling technique was integrated into the multi-objective analytical design and optimization process of SRMs. Stochastic optimization algorithms with penalty functions were applied to find the optimal designs targeted to user defined objective functions. The multi-objective optimal designs with regard to the multiple performance indices were efficiently found, and the accuracy was validated by FEA. The proposed method can generate the optimized SRM designs subject to different design requirements and accelerate the entire optimization process.

The design and optimization of electric machines for propulsion systems are typically performed at multiple operating points, with each point considering four or more design objectives. The decision-making process can thus be challenging for machine designers to select the optimal design candidate in such a high-dimensional space. Therefore, advanced machine learning techniques, including the Self-Organizing Map and the t-Stochastic Neighbor Embedding were implemented on the benchmark study of switched reluctance machines. The visualization results generated by the two algorithms were able to visualize the data clusters and component values in a more intuitive and effective manner when compared to the conventional parallel coordinate and the scatter plot of Pareto front.

To mitigate the risk of irreversible demagnetization under high temperatures, two nonintrusive thermal monitoring schemes using high-frequency signal injection were developed for direct-torque-controlled (DTC) IPM machines. The proposed temperature estimation method was based on analyzing the electrical high frequency resistance of the permanent magnet, which was a byproduct of the excessive eddy current loss induced by the applied alternating high-frequency magnetic field. The high-frequency resistance can reveal the PM temperature since these two quantities are directly proportional, which can also be applied to interpret the magnetization state with prior knowledge of the PM temperature. Detailed derivations of the DTC-controlled IPM machine equations were presented in response to

the injected high-frequency signal, and real-time signal processing techniques were also developed for extracting the high-frequency components of the stator voltage and current. The effectiveness of this proposed PM temperature monitoring scheme was verified with experimental results.

The stator inter-turn fault is considered to be one of the most common yet serious machine-initiated faults for IPM machines. Therefore, the transient demagnetization phenomenon during this type of fault was investigated to assess the risk of irreversible demagnetization under an excessive demagnetization field originated from this fault. The finite element simulation study was performed while the motor was operating on a point along its maximum capability curve. Different contact resistance and different fault severity indicated by the different number of turns were simulated, and results indicated there were certain locations on the permanent magnet that were more vulnerable to demagnetization, and the irreversible demagnetization could occur within one electric cycle for the worst-case condition.

CHAPTER 1
INTRODUCTION AND OBJECTIVES OF THE RESEARCH

1.1 Background and Problem Statement

The electric vehicles (EV) market is a growing industry due to increasing concerns for the depletion of fossil fuels, and global warming. Of all the oil consumed in the U.S., 70 percent is used for transportation. Furthermore, passenger vehicles use 70 percent of transportation oil. By 2050, it is projected there may be as many as 1.5 billion electric vehicles on the road, compared to 750 million in 2010 [1].

This type of demand represents both a challenge and an opportunity to capitalize on new EV technologies. Companies such as Tesla have emerged to compete with automotive giants like Toyota, BMW, Nissan, and General Motors (GM) starting from 2003 [2]. Also, in more recent history, tech titans Apple and Google have also displayed interest in EVs, particularly with self-driving capability [3].

For a significant portion of the history of EVs, auto companies choose to use induction machines as traction motors, which companies like Tesla still use in their current models. In the 1960s, the General Motors Research Laboratory developed a new magnetic material neodymium-iron-boron (NdFeB). This development revolutionized the EV motor industry, and provided higher potential for premium efficiency, low losses and high torque density [4]. This redirected the companies to investigate the use of permanent magnets (PM) motors as opposed to induction motors. One of the big advantages of employing PM motors is the high torque density that minimizes the size of both the auxiliary generator and the traction motor, given the space restrictions in a compact engine bay.

However, rare-earth (RE) permanent magnets used in PM motors have volatile costs together with an uncertain long term availability [5]. Additionally, it is well known that

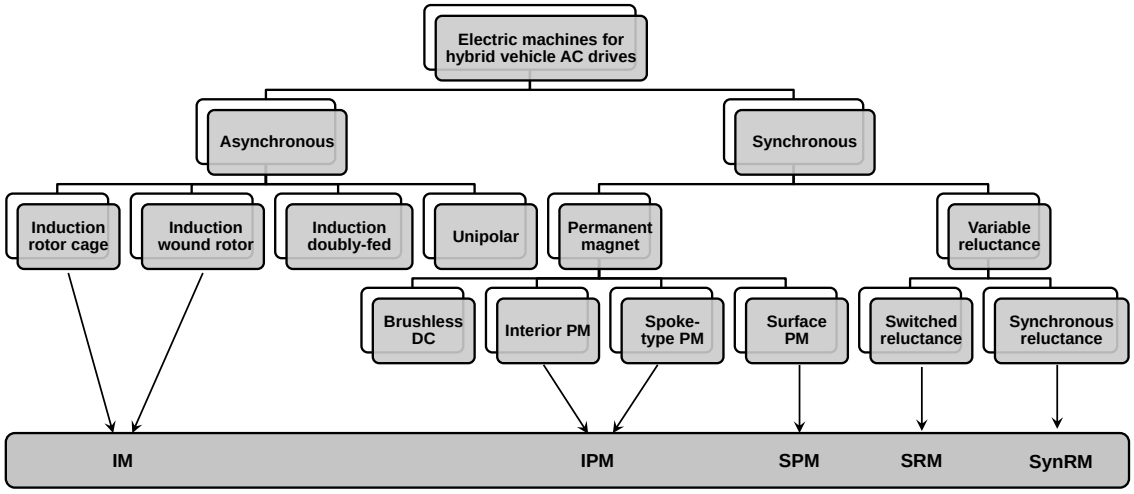

Figure 1.1: Types of motor candidates for EVs or HEVs [4].

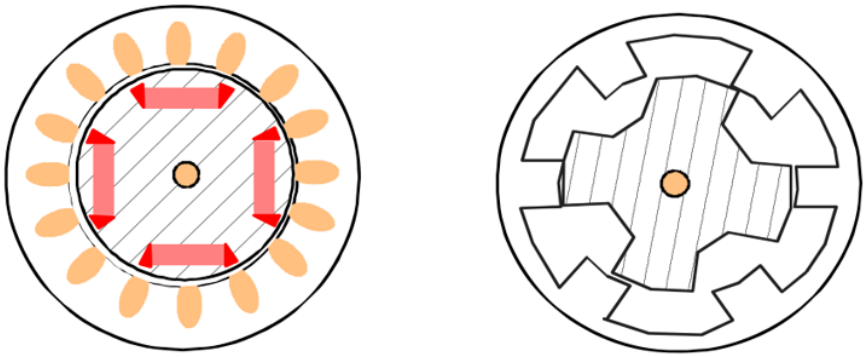

Figure 1.2: Lamination structure of IPM machines and SRMs [4].

the presence of magnets that cannot be turned off in the event of a fault has been an issue that hinders adoption of PM machines in safety-critical applications. Another issue with permanent magnets is that while they remain magnetized indefinitely at room temperature, prolonged high temperatures can cause irreversible demagnetization [6],which reduces output torque and lifespan. Therefore, machines without permanent magnets such as induction machines (IM), switched reluctance machines (SRM), and synchronous reluctance machines (SynRM), are of great interest for light traction applications.

An illustration of the types of motors that could be considered for EVs or HEVs is shown in Figure 1.1. The typical lamination structures of IPM machines and SRMs are illustrated in Figure 1.2 [4].

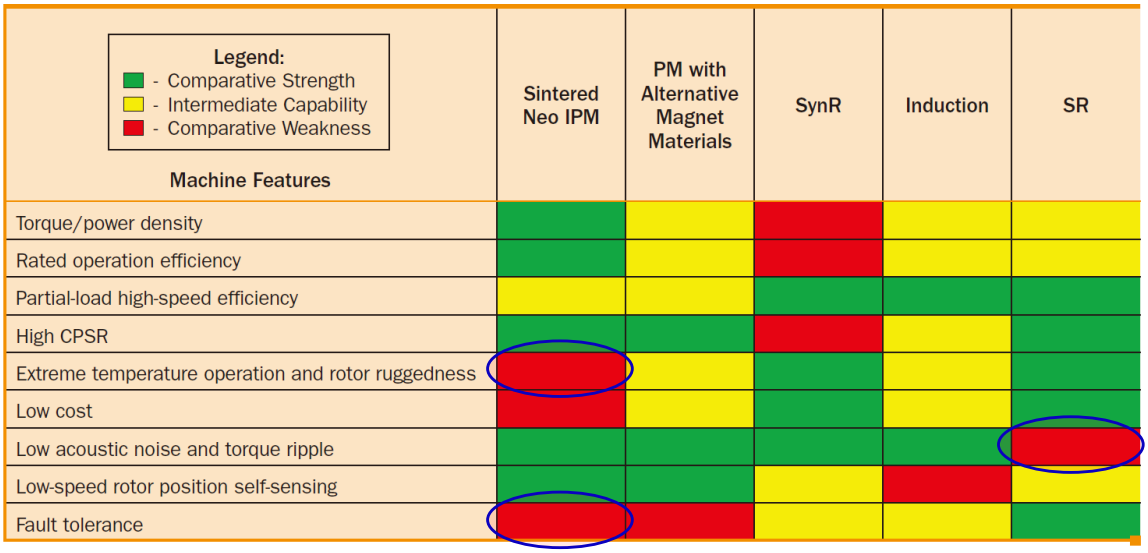

Figure 1.3: A feature comparison among alternative alternative traction machine types for passenger EVs [7].

Although induction machines are relatively inexpensive and had been widely applied to EVs before the introduction of IPM machines, the design and control of induction machines are relatively mature technologies. A synchronous reluctance machine operates on the reluctance torque by creating saliencies with air barriers placed in the rotor lamination. However, the reduction of saliency due to rotor saturation and the poor mechanical strength of the punched laminations limit their widespread application in EVs. Switched reluctance machines, on the other hand, are durable with very low manufacturing cost. Synchronous reluctance motor efficiency, however, is slightly lower than that of IPM motors at rated conditions, but a flatter efficiency vs. speed profile can result in a higher overall efficiency over a typical drive cycle. If properly designed and optimized, the torque density of SRMs can also be superior to induction machines [4].

In spite of their distinct advantages, the application of SRMs presents many technical challenges which must be overcome. The two major challenges are the inherent torque ripple and the fact that both switch reluctance and permanent magnet motors are still designed and optimized based on rules of thumb, heuristic processes and/or computationally-extensive finite element analysis (FEA).

A summary on the feature comparison among alternative traction machine types for passenger EVs is shown in Figure 1.3. As can be observed, there are 9 features compared among five machine types, and both the SRM and the IPM machine have 5 of those features ranked as comparative strengths highlighted in green boxes, while other machine types only have four green boxes or fewer, clearly indicating the inherent high-performance of the SRM and the IPM machine.

Despite their distinct advantages, there are also a few renowned drawbacks of these machine types that need to be carefully addressed if they were to be selected as the motor for electric propulsion. This thesis will thus present research methodologies and results on three main shortcomings: (1) the performance compromise of IPM machines at extreme temperatures; (2) the limited fault tolerant capability of IPM machines; and (3) the intrinsic large acoustic noise and torque ripple of switched reluctance machines.

1.2 Dissertation Outline

The proposed research focuses on the following aspects:

- Chapter 2 will present a comprehensive literature survey of multi-objective design optimization of switched reluctance machines, with an emphasis on electric vehicle traction applications. A literature review for the demagnetization assessment for different fault modes will be presented in Chapter 3.

- Chapter 4 will propose an analytical multi-objective design and optimization framework for switched reluctance machines based on particle swarm optimization (PSO).

- Chapter 5 will first presents an integrated active current profile optimization for multi- objective design and optimization of switched reluctance machines, then the performance and robustness of three mainstream stochastic optimization algorithms are compared. Then, novel Bayesian optimization based SRM design method is proposed.

- Chapter 6 will illustrate multi-objective optimization results for SRMs through the use of self-organizing maps at a single operating point, and applies the applies the t-Distributed Stochastic Neighbor Embedding (t-SNE) algorithm for multiple operating points.
- Chapter 7 will introduce two thermal monitoring scheme for the rotor permanent magnets temperature estimation of IPM machines: 1) a high-frequency flux injection-based scheme; and 2) a high-frequency torque injection-based scheme.
- Chapter 8 will assess the transient demagnetization behavior of IPM machines for the stator inter-turn short-circuit fault with respect to different fault severity and operating conditions.

CHAPTER 2
PREVIOUS WORK ON THE DESIGN AND OPTIMIZATION OF SWITCHED RELUCTANCE MACHINES

Switched reluctance machines are attractive candidates for a use in a variety of applications over a wide range of speeds thanks to their simple, low cost, robust structure. In emerging ultra-high speed applications such as micro-machining, dental spindles, compressors, turbochargers and flywheels [8–10], are expected to rival permanent magnet synchronous motors and pneumatic machines in the marketplace. On the other hand, the automotive sector primarily requires lower speed range applications [11–19]. Although permanent magnet machines still dominate the automotive industry, the relatively inexpensive structure, manufacturing processes, and electrical and thermal robustness of SRMs have all spurred great interest in utilizing SRMs in traction applications. In fact, there has been an SRM reported in the literature that has a comparative performance compared to machines used in the Nissan Leaf [20] and the Toyota Prius [21–23].

2.1 Overview

There have been many modeling, design and optimization methods that have been developed for switched reluctance machines, and most of them can be classified into two categories: 1) analytical-based methods, which includes magnetic equivalent circuits [24–29] and the direct use of Maxwell's equations [30–32]; and 2) and 2) numerical-based methods [33–35]. Analytic methods provide fast computational speed, but with compromise in accuracy, while numerical methods based on FEA rely on an analysis tool rather than design tools, and are very computationally intensive [36]. Therefore, analytical-base design results offer more flexibility (i.e., they have an ultra-fast computational speed and an easily accessible multi-physics interface) to optimize electric machine designs. The research

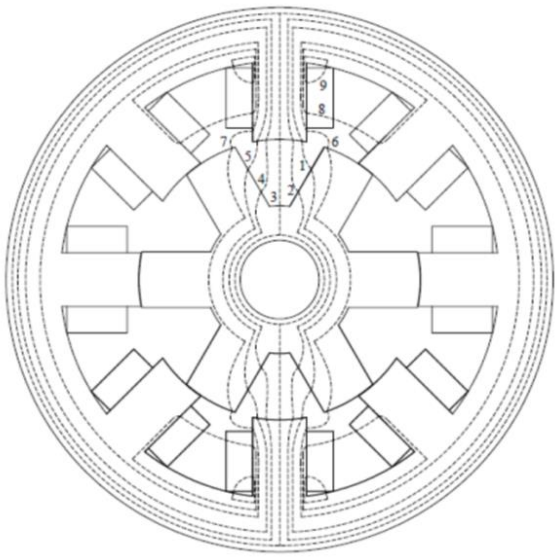

Figure 2.1: Illustration of the SRM magnetic circuit flux tube method [28].

presented here will thus focus on developing analytical-based SRM design and optimization schemes.

2.2 Previous Work on the Modeling of Switched Reluctance Machines

2.2.1 Previous Work on Analytical Methods

In spite of the distinct advantage of the ultra-fast computational speed, accurate modeling and design of SRMs is nontrivial because of their nonlinear characteristics (inductance, flux density, and torque). For example, Figure 2.1 illustrates the modeling of SRMs using magnetic equivalent circuits with seven flux tubes [28, 29] with various shapes. With these models, instantaneous SRM characteristics can be calculated. The downside is the very tedious calculations required to perform such flux path selections at each rotor position. In addition, this method cannot be easily implemented on SRMs with an arbitrary combination of stator and rotor poles, such as 4/2, 6/4 and 12/8, since the flux-linkage distribution changes, and the assumptions for some specific flux paths will not always hold.

Another analytical method is based on Maxwell's equations [30, 31] to first determine the SRM inductance profile, which is more deterministic, as only the boundary conditions

are approximated. However, its accuracy at the unaligned position is affected by simplifying the shape of the stator sectors and the rotor slots to rectangles, resulting in large errors in the analytical estimation due to this misrepresentation of the stator's geometry. Furthermore, no systematic multi-objective design and optimization methods have been developed to date based on these analytical methods. An accurate and efficient analytical design model is therefore needed.

2.2.2 Previous Work on Numeric Methods

Finite element analysis-based computer-aided-design (CAD) software has been widely applied, as it generally offers comprehensive and trustworthy results [33–35]. CAD software packages, such as RMxprt by Ansys and SPEED, are able to carry out machine design calculations and provide a certain level of optimization. However, presently available commercial design software are analysis tools, not design tools. Although FEA results can help identify possible directions and lead to an improved design, a significant computational effort is needed over a large search domain in order to better estimate the Pareto front for an optimized design. Therefore, the most effective machine design method is to efficiently find an initial optimized design through the analytical design model first, and it can be later applied to FEA for verification, or further fine-tuning purposes, if necessary.

2.3 Multi-Objective Optimization Algorithms Applied to Electric Machines

Moreover, previous research efforts on SRM optimization have mostly been done to address only one of the following performance indices (PI): torque ripple [37–41], torque density [42–44], efficiency and acoustic noise. However, the problem with single-objective optimization is the potential reduction in other important performance indices, as trade-offs to the initiated improvements on one single performance index. Therefore, the implementation of the multi-objective optimization algorithms with weighted-sum or vector-based objective functions is necessary in order to accommodate the needs of designing and

optimizing SRMs with different application requirements.

2.3.1 Deterministic Algorithms

There is a large variety of deterministic methods applied in electric machine design optimization problems, such as the sequential quadratic programming (SQP) [45, 46], the Tabu search [47, 48], and the sequential unconstrained minimization technique (SUMT), which is one of the most popular ones [49]. Specifically, SUMT converts a constrained optimization problem into an unconstrained one through the use of a penalty function, and it must then apply sequential nonlinear programming for use in optimization. In principle, SUMT is able to find the optimum in just a few iterations, but it requires a gradient calculation [50].Other deterministic methods include the error-based optimization search [51], the Hooke-Jeeves method [52], the interval branch and bound method [53], the interior reflective Newton method [54], and so on.

2.3.2 Stochastic Algorithms

Stochastic methods tend to require a more stringent evaluation of design candidates, but they are gradient free and, in principle, are not easily trapped by local minima. The most popular stochastic multi-objective optimization algorithms for electric machine design are the genetic algorithms (GA), particle swarm optimizations (PSO) and through differential evolution. Genetic algorithms are based on the mechanism of natural selection and genetics [55] and have been widely applied in electric machine design optimization [56, 57]. The design variables are first transformed into binary, and then coded together as "chromosomes" that are prone to various mutations and crossovers. Particle swarm optimization emulates the behavior of a swarm of bees trying to locate areas with the highest density of flowers. The optimal search is attained by a combination of individual and collective knowledge. Particle swarm optimization is robust with respect to the values of its running coefficients, and hence, by simply following a few guidelines [58], the tuning of the running coefficients

can be usually neglected [50]. This makes it the most robust algorithm, with it being especially robust against small disturbances. Differential evolution also involves multiple generations, each comprising a population of candidate designs. Improvements are facilitated by perturbing the current generation with the scaled differences of randomly selected and distinct population members. The algorithm also includes processes of initialization, mutation, crossover, and selection. Differential evolution has only recently been applied in machine design optimization, but is quickly gaining popularity [59–61].

2.4 Previous work on Multi-Objective Design Optimization of SRMs

The majority of the previous research efforts on SRM design and optimization has mostly been done to address only one performance index. However, the problem with this single-objective optimization is the potential unfavorable decline of other important performance indices, as *trade-offs* to initiated improvements on one single objective. Therefore, the implementation of multi-objective optimization on SRMs [62–72] is necessary to accommodate the needs for different applications.

While the enumeration method (direct search) [64, 65] and the response surface method [62] have both been applied to solve SRM multi-objective design and optimization problems, the majority of the literature employ certain stochastic algorithms to perform the optimal design search by evaluating a large number of design candidates based on several randomly generated independent prime design variables. These variables typically involve some crucial SRM geometric parameters, including the air gap diameter, the stack length, the stator/rotor pole heights and the pole arc angles, as well as other non-geometric quantities, such as the current density and the number of turns. Then, the complete SRM geometry is designed, and various performance indices are then evaluated by either FEA simulations [64–70], through surrogate models such as Kriging [71], through analytical models based on the magnetic equivalent circuit [72], or with Maxwell's equations in this thesis. After all of the performance indices are assessed in a scalar or vector objective function, the

Table 2.1: Comparison of different multi-objective design methods of switched reluctance machines.

References	Modeling method	Optimization method	Average torque	Torque density	Efficiency	Torque ripple	Acoustic noise	Current profile	Cost function dimension	Speed/ Accuracy
Xue [64]	FEA	Enumeration	Yes	Yes	Partial	No	No	No	Scalar	Slow/high
Omekanda [65]	FEA	Enumeration	Yes	No	Yes	Yes	No	Yes	N/A	Slow/high
Choi [62]	FEA	RS	Yes	No	No	Yes	No	No	N/A	Slow/high
Cheng [66]	FEA	N/A	Yes	Yes	Partial	Yes	No	No	Scalar	Slow/high
Jiang [67]	FEA	GA	Yes	No	No	Yes	No	No	Vector	Slow/high
Smaka [68]	FEA	GA	Yes	Yes	No	Yes	No	No	Scalar	Slow/high
Öksüztepe [70]	FEA	DE	Yes	Yes	Yes	No	No	No	Vector	Slow/high
Ma [69]	FEA	PSO	Yes	Yes	Yes	Yes	No	No	Scalar	Slow/high
Ren [71]	Surrogate model	PSO	Yes	No	No	Yes	No	No	Vector	Fast/low
Ilea [72]	MEC	PSO	Yes	No	Yes	No	No	No	Scalar	Fast/average
Mirzaeian [63]	Fuzzy system	GA	No	No	Yes	Yes	No	No	Scalar	Fast/low
Pisch [73]	FEA	GA	Yes	No	Yes	No	No	Yes	Vector	Fast/average
Ma [74]	FEA	DE	No	No	No	Yes	Yes	Yes	Scalar	Slow/high
This work	Maxwell's equations	PSO	Yes	Yes	Yes	Yes	No	Yes	Vector	Fast/average

next-generation prime design variables are generated by the multi-objective optimization algorithms of genetic algorithms [63, 67, 68], particle swarm optimization (PSO) [69, 71, 72], and differential evolution (DE) [70]. The entire process is repeated for a certain number of iterations. It is reported in [62–72] that a significant improvement can be made on one or two targeted performance indices, with a minimal impact on others.

Aside from the geometry design aspect, multi-objective optimizations have also been performed on the control aspect of SRMs. Multiple Fourier Series coefficients approximating the current profile are optimized through differential evolution to simultaneously reduce the torque ripple and the acoustic noise [74]. In addition, the PI controller gains, the steady-state phase current and its turn-on and turn-off angles can also be adjusted as prime design variables with PSO, as reported in [75, 76].

The aforementioned SRM multi-objective design and optimization approaches are summarized and compared in Table 2.1, in terms of the specific modeling/optimization methods, the various performance indices that are to be optimized, the integration of the current profile or other control-related issues, and the dimensions of the objective functions and the computational speed [62–72]. The comparison demonstrates that the integration of the acoustic noise and current profile into the multi-objective design and optimization processes are still largely unexplored in the existing literature, and there is always a demand for fast and highly-accurate machine performance evaluation approaches.

In regards to the emerging trend of the multi-objective design and optimization of SRMs, coupling the multi-physics and the control aspects with the electromagnetic component is becoming increasing popular. This will largely increase the number of design variables at the very first stage of SRM design and optimization. Therefore, the development of computationally efficient FEA methods, parallel computing or pure analytical design models will be vital for maintaining a reasonable optimization efficiency.

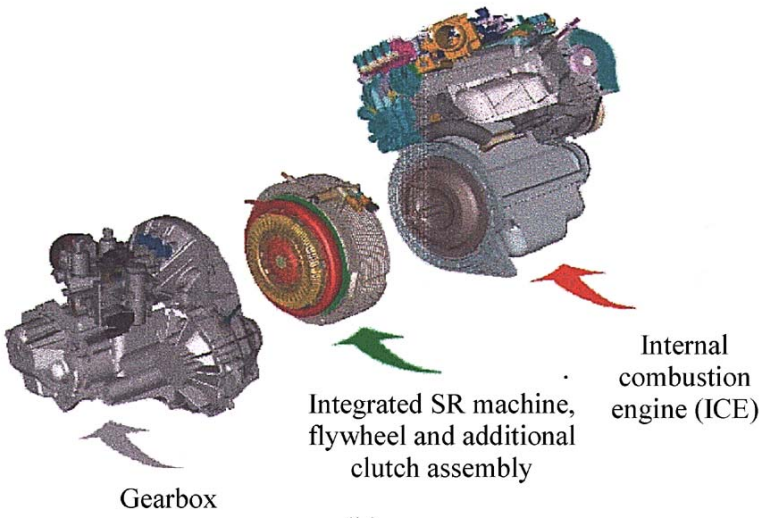

Figure 2.2: An SRM hybrid-electric powertrain assembly [77].

2.5 Previous Work on Switched Reluctance Machines for Automotive Applications

SRMs have the advantage of not possessing PMs in the rotors, and are only constructed with low-loss silicon steel and stator windings, which will inevitably drive the manufacturing cost down and will help maintain an excellent level of mechanical and thermal robustness [11–19], which makes it ideal for HEV applications where the electric motor is coupled with an internal combustion engine, and it needs to endure a high-temperature environment, as illustrated in a classical SRM hybrid-electric powertrain assembly shown in Figure 2.2. However, the radial vibration, acoustic noise, asymmetric bridge converter, and intrinsic large torque ripple have all prevented the widespread adoptions of SRMs on EV/HEV powertrains to date.

During recent years, it is however the interior permanent magnet synchronous machine (IPMSM) with NdFeB magnets that has dominated the field of EV/HEV propulsion systems, because of their high torque density and high efficiency [7, 78–80], and typical examples include the well-known 60 kW Toyota Prius 2010 IPM motor [81], the 80 kW Nissan Leaf IPM motor [82] and the 110 kW GM Chevrolet Volt IPM motor [83].

Despite the fact that Tesla uses induction machines in its Model S sedan and Model X

SUV, it has transitioned to an IPM motor in the latest Model 3 for mass-production [84], as it has proven itself to be the optimal for its range and performance target, mainly due to the efficiency benefit offered by the pre-excitation from permanent magnets. However, the volatile cost of rare-earth permanent magnets, the potential threat of irreversible demagnetization and the fact of that these magnets cannot be “turned-off" in an event of fault [95] have all triggered strong global interests to develop rare earth element-free motors for use in future EV/HEVs, and the SRM is certainly of the highest priority. A comprehensive list of SRMs designed for an EV prototype for use in academia is shown in Table 2.2, and the critical EV motor performance indices are thoroughly presented. However, to the authors' best knowledge, there are no SRM drives currently installed or targeted for installations on commercial EV/HEVs to this date.

The majority of research works are performed by universities in the United States, Japan and the United Kindom, as well as some major companies with relevant businesses; Figure 2.3 demonstrates a test EV with a prototype SRM and drive circuits developed by the Tokyo Institute of Technology [96]. References in Table 2.2 have been ordered by their peak power output, as electric machines designed for EV/HEV propulsions are usually running under dynamic conditions and there are seldom rated conditions or steady-states as compared to other applications. The peak power, a level that the motor is only able to sustain for a few dozen seconds at most, is the motor's physical limit, and is often regarded as an important indicator when evaluating motor performance. The current density for these SRMs typically ranges between 10 to 20 A/mm^2, and thus direct cooling is needed in order to cool the stator end-turns with liquid coolant or water. With proper motor control strategies, all motors can generate their maximum torque when at a standstill, which determines how fast the vehicle can accelerate from zero-speed. A higher maximum speed at the motor's peak torque, also known as the knee point, is also preferred, indicating the vehicle is still able to accelerate at a rate close to the maximum acceleration even if it is already running at a moderate speed.

A general belief regarding SRMs is that their torque density and efficiency are lower

Table 2.2: Comparison of different SRMs designed for EV/HEV powertrains.

References	Affiliation	Peak power	Peak torque	Maximum speed	Maximum speed at peak torque	Maximum power-to-weight ratio	Efficiency over 85% region	Machine topology	Cooling method
[77]	University Manchester	26 kW	120 Nm	4,500 rpm	1,200 rpm	N/A	N/A	24/16	Liquid/Coolant
[85]	Fukuoka Inst of Tech	30 kW	594 Nm	2,200 rpm	482 rpm	N/A	N/A	6/4	Liquid/Water
[86]	Meiji University	40 kW	100 Nm	6,400 rpm	3,000 rpm	N/A	N/A	12/8	N/A
[87]#	University of Akron	50 kW	122 Nm	12,000 rpm	8,000 rpm (48 Nm)	N/A	60%	12/8	Liquid/Water
[88]	Illinois Inst of Tech	50 kW	300 Nm	6,000 rpm	1,600 rpm	1.18 kW/kg	85%	12/8	N/A
[89]	General Motors	56 kW	710 Nm	N/A	750 rpm	N/A	70%	24/16	Liquid/Coolant
[90, 91]	McMaster University	60 kW	210 Nm	13,500 rpm	2,750 rpm	2.64 kW/kg	92%	24/16	N/A
[20]†	Newcastle University	82 kW	285.8 Nm	10,500 rpm	2,750 rpm	2.52 kW/kg	N/A	12/8	N/A
[92]	Toyota Industries	100 kW	164.7 Nm	10,000 rpm	5,800 rpm	2.22 kW/kg	N/A	6/4	Liquid/Oil
[93]	HUST	101 kW	377.3 Nm	4,500 rpm	2,556 rpm	0.94 kW/kg	80%	8/6	Liquid/Coolant
[21–23, 42, 94]	Tokyo Inst of Tech	109 kW	209 Nm	13,900 rpm	5,400 rpm (185 Nm)	4.32 kW/kg	88%	18/12	Natural Air∗

Irregular torque-speed curve with no constant torque or constant power boundaries. † Segmental rotor SRM
∗ Only used for test purposes, in general, an oil cooling or a water jacket should be provided [23].

(a)

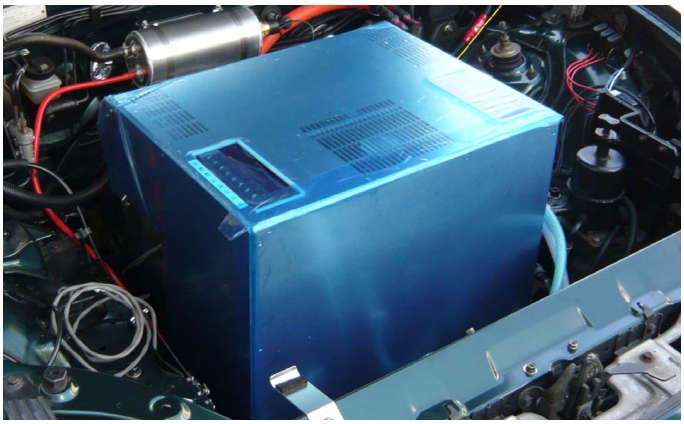

(b)

Figure 2.3: Prototype electric vehicle with the prototype SRM and (b) the drive circuit for the prototype SRM on the EV [96].

than that of well-designed PM machines [7], as the SRMs developed in early years have had either insufficient peak power output [77, 85, 86], power densities [88, 93] or efficiencies [87] to be considered in a practical HV/HEV application. However, these works are still worthwhile from today's perspective, as they have validated the feasibility of employing SRMs for use in vehicle propulsion.

SRMs have recently been the subject of research, as they are to be designed and manufactures to be compared with commercial EV/HEV IPM machines, such as the Nissan Leaf [20] and the Toyota Prius [21–23, 90, 91, 94, 96], etc. In particular, [90, 91] proposed an SRM with the same stator outer diameter of 264 mm, the same axial length of 108 mm and an almost identical torque-speed curve when compared to the Prius motor. In addition,

the efficiency contours are far better, thanks to the 0.1 mm thick 10JNEX900 lamination used to compensate for SRM's high iron losses at high speeds due to the large amplitude of the magnetic flux variations in stator and rotor poles, whereas the thickness of the Prius lamination is 0.35 mm [81].

The 18/12 SRM developed in [21–23, 94] also targets the Prius IPM machine with the same outer stator diameter and axial length, but with a reduced air gap length from 0.8 mm to 0.5 mm. The two torque-speed curves nearly overlapped with equivalent efficiency contours at the low-speed region below 2,768 rpm, but the SRM can be further boosted up to 109 kW at 5,400 rpm, and it can maintain this peak power up to the maximum speed of 13,900 rpm. This demonstrates a significant power advantage over the Prius motor in the high-speed range. The maximum power-to-weight ratio also increases from 3.37 kW/kg to 4.32 kW/kg excluding the rotor shaft weight, which is an apparent accomplishment when compared to other SRM propulsion designs, which all generally fall between the 1 kW/kg to 2.7 kW/kg range[88, 92, 93]. A performance comparison of this EV-scaled SRM with other motor technologies is carried out and the result is presented in Table 2.3, where it can be observed that SRMs developed at the Tokyo Institute of Technology have an equivalent level of performance in terms of peak power, efficiency and the maximum constant speed range when compared to most existing IPM machines found in the Toyota Prius, Nissan Leaf, GM Chevrolet Volt and the BMW i-3. In addition, the power-to-weight ratio of this specific SRM (4.32 kW/kg) far outperform even these IPM machines (1.1 to 2.5 kW/kg). However, despite the fact that this ratio is affected by the SRM's electromagnetic design, it is more associated with how well the cooling system is designed.

The Tesla Model S induction machine (IM) has a rugged rotor copper bar structure and excellent cooling loop design that is able to deliver 320 to 362 hp and only weights 70 lb [98] excluding all of the casing, gears and inverters, indicating a power-to-weight ratio of 7.50 to 8.50 kW/kg, which is far better when compared to IPM machines. The authors attribute the inferior power-to-weight ratio of most IPM machines to concerns over

Table 2.3: Comparison of different motor technologies designed for EV/HEV powertrains.

Motor type	Company & model	Year	Peak power	Peak torque	Maximum speed	Maximum speed at peak torque	Maximum power-to-weight ratio	Efficiency over 85% region	Total PM mass
[81]	Toyota Prius	2004	50 kW	300 Nm	6,000 rpm	1,650 rpm	1.11 kW/kg	82%	1.23 kg
[81]	Toyota Prius	2010	60 kW	190 Nm	13,000 rpm	3,150 rpm	1.63 kW/kg	91%	0.77 kg
[82]	Nissan Leaf	2011	80 kW	280 Nm	10,390 rpm	2,728 rpm	1.38 kW/kg	89%	1.89 kg
[97]	BMW i3	2012	125 kW	250 Nm	11,400 rpm	4,775 rpm	2.50 kW/kg	N/A	N/A
[83]	GM Volt	2013	110 kW	370 Nm	9,500 rpm	2,839 rpm	N/A	N/A	N/A
[98]	Tesla Model S/X	2014	240 kW	380 Nm	15,000 rpm	6,000 rpm	7.50 kW/kg	92%	0
[99]	GM Bolt	2015	150 kW	360 Nm	8,810 rpm	N/A	N/A	91%	N/A
[21–23, 42, 94]	Tokyo Inst of Tech	2013	109 kW	209 Nm	13,900 rpm	5,400 rpm (185 Nm)	4.32 kW/kg	88%	0

irreversible demagnetization, which may limit the amount of excessive current, and thus may limit the machine's overloading capability. Since SRMs have an even better thermal and mechanical robustness than induction machines and do not possess rare-earth magnets in the rotor, from a theoretical point of view, the power density of propulsion SRMs still has room to grow with improved electromagnetic and cooling designs.

The pulsed nature of the stator winding excitation of the SRM tends to result in a high-torque ripple compared to other machines. Thus, SRMs designed in [20, 23, 77, 85–88, 90–93] generally adopt a three-phase (6/4, 12/8, 18/12, 24/16) or a four-phase (8/6) topology to reduce the torque ripple by increasing the phase overlap through an increased number of phases. Although not all papers have disclosed the exact torque ripple at certain operating points, the torque ripple of SRMs is generally considered to be inferior to that of IPM machines or induction machines. Specifically, the peak-to-peak torque ripple of the SRM in [21, 22, 42, 94] is 34% of the average torque at the knee point, which is further intensified in the high rotational speed region, particularly at the continuous current region [23]. However, it is important to note that conventional automotive internal combustion engines (ICE) also have significant torque ripple [100], and since the EV/HEV propulsion motor is generally working at dynamic states, the problem of a large torque ripple may not be as important as in other applications which require a smooth torque working at a fixed number of operating points.

In addition, the torque ripple can be further compensated for advanced control techniques discussed in earlier sections or through a torsional shaft [23]. The high-frequency radial force on the stator poles can also result in objectionable acoustic noise and NVH [101] due to the excitation of the stator mechanical resonant modes. This problem is even more prominent when compared to IPM machines or induction machines and can be mitigated by noise reduction methods introduced earlier, i.e., the current waveform manipulation, or by installing effective noise-absorbing materials at the periphery of the SRM powertrain.

Aside from direct EV propulsion through a differential gear and shaft, another popular

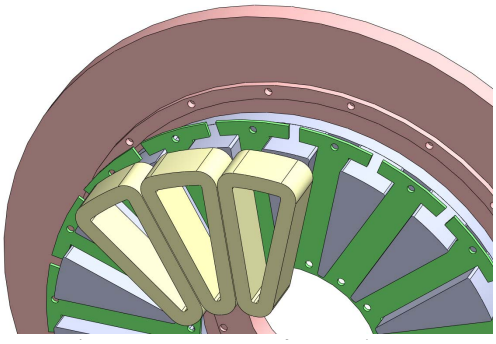

(a)

(b)

Figure 2.4: (a) (a) Prototype in-wheel SRM and (b) applying the SRM to an electric city commuter [102].

application of SRMs is the in-wheel electric machine on small-sized EVs for short daily commutes, which typically do not require machines with a large power rating due to their low weight, however this applications does demand that these machines be low-cost. A 3.2 kW axial-flux SRM is developed in [102] for electric city commuters with a larger torque-speed envelope and a reduced size compared to the targeted 2 kW PM machine, and figures illustrating this have been provided in Figure 2.4. In [64], a 5 kW SRM is carefully designed and optimized through multi-objective optimization, and the later experiment reveals the developed SRM meets all the requirements of their EVs. Other research proposes a 1.5 kW 12/26 segmented-rotor SRM (SSRM) with a compact size and high efficiency to replace the traditional BLDC motor in in-wheel EV applications, thus providing an alternative low-cost solution [103]. A similar 1.5 kW 12/16 SSRM is also reported in [104] for the same purpose.

Other important SRM applications in vehicles include the regenerative braking system

[105], air compressors [106] and the integrated starter/alternator (ISA) system [107–109], which all combine into a single electric machine that is traditionally separated into an internal-combustion-engine (ICE) crankshaft mounted starting motor, and a battery-charging generator.

2.6 Chapter Summary

This chapter presents a comprehensive review of the design of SRMs, including aspects of the mathematical modeling of electromagnetic fields and the multi-objective optimization. The mathematical modeling approaches can be classified into numerical and analytical methods, and the performance of the various multi-objective optimization methods applied to SRMs, including the deterministic method and the stochastic method, are systematically introduced and compared. Finally, the state-of-the-art technologies are presented for SRM designs for electric/hybrid electric vehicles and compared to existing commercial designs in the market.

CHAPTER 3

PREVIOUS WORK ON FAULT MODES AND DEMAGNETIZATION ASSESSMENT ON PERMANENT MAGNET SYNCHRONOUS MACHINES

Interior permanent magnet synchronous machines (IPMSMs) are widely employed by most automotive companies in their electric vehicles, including the Toyota Prius, the BMW i-3, the Nissan Leaf and the GM Chevrolet Bolt. Despite a successful history of employing induction motors, Tesla has also added permanent magnets into its new Model 3 motors [98]. The dominance of IPM machines can be mostly attributed to their high power density and their high efficiency for most conceivable operating conditions.

However, exposure to high temperatures or the strong demagnetizing MMF originating from the various fault conditions can demagnetize the neodymium-iron-boron(NdFeB)-type rare-earth permanent magnets up to the point of irreversible demagnetization [110, 111]. While this risk can be pretty much avoided in most applications by applying conservative motor designs with typical operating points driven away from the limit of irreversible demagnetization. Unfortunately, for automotive applications that involve a relentless demand for a high power density and the minimal magnet cost, the designs that are generally favored are those that operate very close to the limits of irreversible demagnetization (the knee point of its B–H curve) [112]. Therefore, the demagnetization issue is very difficult to eliminate in practice.

This chapter will present a comprehensive literature review on the demagnetization assessment induced by either the excessive rotor temperature or the different fault modes.

3.1 PM Machine Fault Characteristics

3.1.1 Drive Inverter Initiated Faults

Open-circuit faults for PM machines, in which one or multiple phases of the machine have become open-circuited, have been investigated by many researchers [113, 114]. This fault is more commonly caused by an electrical failure in the switching device inside the drive inverter. In addition, the short-circuit type faults in the drive inverter include the single phase-to-ground short-circuit fault and the three-phase symmetric short-circuit fault [115, 116]. The common methods used in analyzing the aforementioned faults include deriving new dq models for IPM machines with consideration of the fault conditions [113, 115], as well as the associated post-fault inverter control strategies [114].

3.1.2 Electric Machine Initiated Faults

The most common machine initiated fault is the turn-to-turn short-circuit fault in the stator windings. Theoretical results indicate that the fault current in the faulty turn will be at least n times (n being number of turns) greater than the three-phase symmetrical short-circuit current when the outer most single turn is shorted [117]. The internal short-circuit fault models for IPMSMs with both series and parallel winding connections have been developed in positive and negative sequence dq synchronous reference frames [118]. A number of inter-turn fault detection algorithms are developed based on the current/voltage harmonic spectrum [119] and the input impedance characteristics [120, 121].

3.2 Previous work on Demagnetization Analysis of IPMSMs

3.2.1 Demagnetization Characteristics

In spite of their rapid price increase, neodymium-iron-boron (NdFeB) magnets are still dominant in high-performance applications due to their highest remnant flux density and their coercive force. However, NdFeB magnets are inherently vulnerable to the risk of

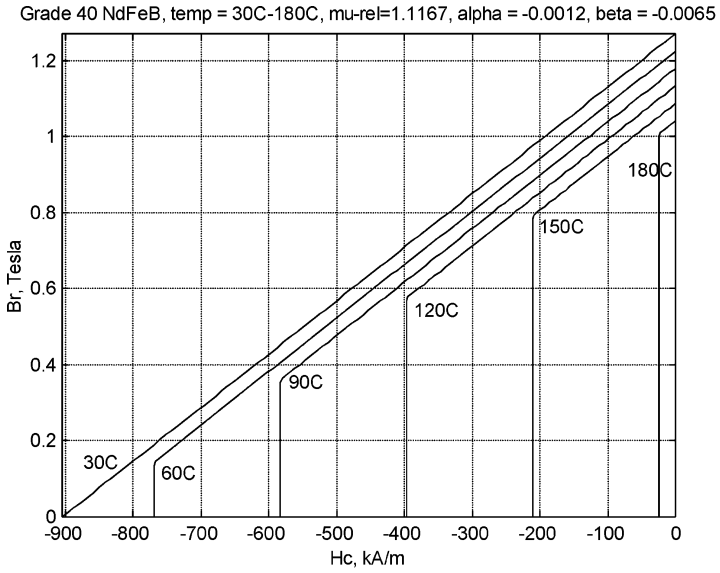

Figure 3.1: Demagnetization curves of Grade 40 NdFeB up to 180 °C (note the pronounced ”knee" in the B/H curve at temperatures above 90 °C) [111].

irreversible demagnetization, which is generally due to external demagnetizing fields or the rise in temperature [110]. Figure 3.1 demonstrates the demagnetization curves of the Grade 40 NdFeB magnet and it can be observed that the permanent magnet will become increasingly vulnerable to irreversible demagnetization as the remnant flux of the knee point significantly increases with temperature. The flux would reach around 0.8 T at around 150 °C, indicating that these permanent magnets can easily become irreversibly demagnetized after even just carrying a tiny amount of load or running at the flux-weakening region.

Figure 3.2 shows the normal nonlinear B-H curve of the NdFeB magnets at 150°C that can be used to assess the demagnetization properties of the Prius 2004 IPM machine. The permanent magnets could experience reversible demagnetization with a moderate rise in temperature and a stator current-induced demagnetization MMF, and the extent of the demagnetization intensifies while the PM machine operating point approaches the peak motor torque-speed curve envelop. Specifically, the reversible demagnetization region on the B-H curve, indicated by the green arrows, embodies the linear region above the knee point, such that the magnet B-H characteristics can migrate back and forth along this line while exposed to temperature fluctuations and stator current-induced MMF changes.

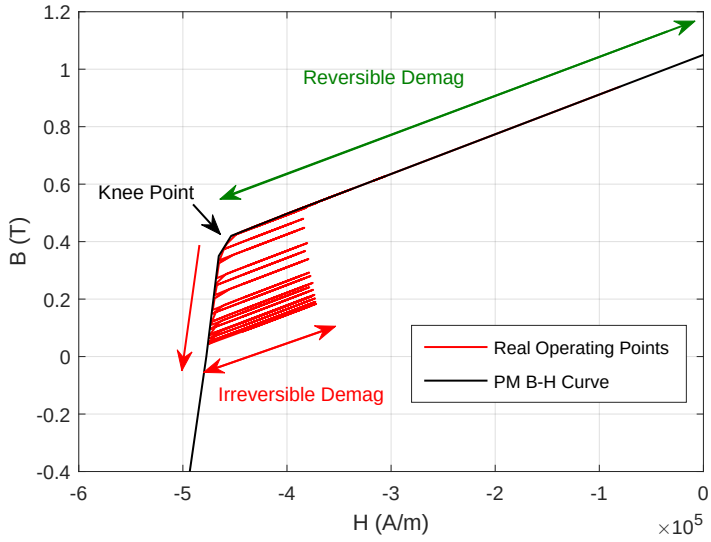

Figure 3.2: Illustration of real-time demagnetization process of permanent magnets.

The irreversible loss of magnetic strength can occur very quicily due to the presence of excessive demagnetizing MMFs at high temperatures, or it can be a naturally slow process with aging-related degradation, changes in the material structure or composition by corrosion or shock. In Figure3, the process for certain regions of the permanent magnets that move towards irreversible demagnetization is described as

1) First, the flux densities of certain affected magnet elements would pass through the knee point and move down along the original B-H curve under the influence of a continuously large demagnetization MMF.

2) At the next instant of time when the magnet is exposed to a re-magnetizing MMF, those magnet elements would not be able to go above the knee point again and back to the reversible demagnetization region, but it would rather move along a recovery line starting from its present location and it would be parallel with the original B-H curve linear region.

3) Once exposed to a new demagnetization MMF, the magnet elements would demagnetize along the new recovery lines until reaching the intersection of the recovery line

and the B-H curve. The magnetic properties can move down even further along the B-H curve if the demagnetization MMF still lasts.

4) Processes 1) to 3) would repeat and a large group of recovery lines are expected to form, as represented by the red lines in Figure 3.2. The operating point can continue moving down to the 3rd quadrant, indicating certain elements of the magnets are in fact reversely-magnetized.

In many practical cases, the demagnetization intensity depends on the combination of the effects of the real-time temperature and the demagnetizing MMF. The increased temperature, as long as it remains below the Curie point typically in the range of 400 to 500 °C, will only make the magnet B-H curve "softer" and more vulnerable to demagnetization, while the demagnetizing MMF is the external catalyst that drives the magnets to irreversible demagnetization.

3.2.2 Previous work on Demagnetization Analysis

Several techniques have been introduced in the literature to detect the demagnetization fault and to evaluate the demagnetization state of IPMSMs. Both semi-analytic [122] and FEA methods [112, 123–125] have been used to study the risk of demagnetization to check the minimum PM flux density [112, 123–125], as illustrated in Figure 3.3, a chart of the magnet demagnetization ratio values after a three-phase and a single-phase short-circuit fault. Other methods are also carried out including the use of hall effect sensors [126–128], torque ripple [129], electrical fundamental wave models [130], vibrations and acoustic noise. On the other hand, the PM magnetization state can be also revealed by monitoring its temperature, since the remnant flux and coercivity of the rare-earth PM materials will gradually deteriorate in response to the excessive heat. The PM temperature can be either measured or estimated, however, measuring its temperature once the machine is assembled is nontrivial, and existing solutions, including the infrared thermography techniques [131] with infrared light (IR) sensor/camera or the contact-type sensors through wireless transmissions,

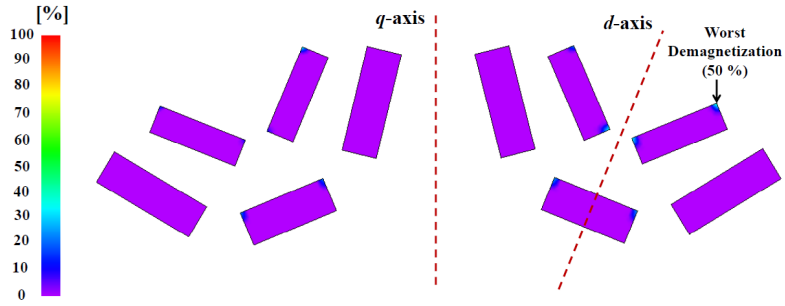

(a) Three-phase, symmetrical short-circuit fault

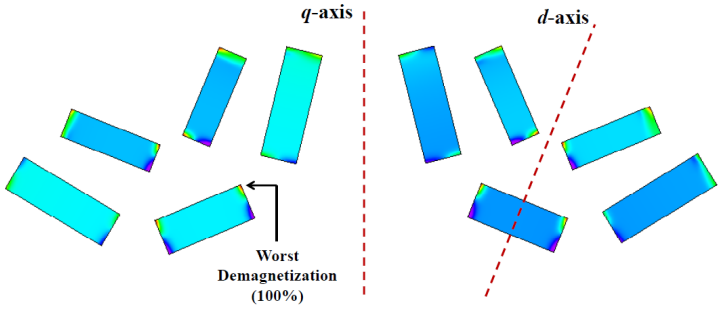

(b) Single-phase, asymmetrical short-circuit fault

Figure 3.3: Magnet demagnetization ratio values after two short-circuit faults [125]

are expensive and have restricted operating environments. In addition, the reduction in the back-EMF voltage amplitude after exposure to a demagnetizing current is also utilized to estimate the demagnetization state [132]. More recently, the permanent magnet resistance induced by the eddy current effect is also applied to estimate the temperature change inside the magnet [133] and then to infer the magnetizing state based on the demagnetization curves similar to Figure 3.2.

The demagnetization analysis of PM machines have been carried out at various faulty conditions, including static and dynamic eccentricities, magnet fractures [134], a sudden short-circuiting of the damper bars [135], a failure of the drive controllers or the position sensors [136], and single- [112, 125] and three-phase [123, 124] short-circuit faults. While the issue of PM demagnetization with a stator inter-turn fault has been investigated in [137, 138], the analyzed PM motor has a concentrated winding, which is different from the mainstream IPM machine with a more evenly distributed pattern and it is also more vulnerable to demagnetization. A test fixture design assessing permanent magnet demagnetization has

been also established in [139], and online detection methods based on and pulsating voltage injections are proposed in [140] and [141].

3.2.3 Previous work on Experimental Demagnetization Test

Up till now, only a very limited number of published papers are available that include significant amounts of experimental demagnetization data, such as [139, 142]. Part of the reason for this lack of coverage is that it is challenging to irreversibly demagnetize the magnets made from high grades of sintered rare-earth materials in the absence of high temperatures (>150 °C). In addition, none of the reported work to date has attempted to report experimental results on how quickly the magnet will get demagnetized in the presence of a fault, all of which have limited their generalization to many practical applications.

3.3 Chapter Summary

In this chapter, the principle and progress towards irreversible demagnetization of permanent magnets are systematically introduced, along with the different fault modes that may trigger the excessive temperature or demagnetization field. While previous attempts are made to investigate the demagnetization progress of IPM machines with an external three-phase-to-ground, and single-phase-to-ground short-circuit faults, less attention has been given to demagnetization cased by an inter-turn short-circuit fault, which is a very common fault.

CHAPTER 4
MULTI-OBJECTIVE DESIGN AND OPTIMIZATION OF SWITCHED RELUCTANCE MACHINES

4.1 Overview

Despite the promising prospect of SRM applications, the double-saliency of the SRM structure and its nonsinusoidal electromagnetic properties make the manual design of an SRM a difficult and challenging task. In a traditional SRM design, the initial selection of the important electromagnetic parameters, such as the flux density and MMF, are totally based on the designer's personal experience, and eventually the qualifying designs are found through many iterative and heuristic processes. Moreover, this experience-based method, aside from being tedious and inefficient, does not guarantee optimal machine performances.

This chapter thus establishes a fast and generalized multi-objective optimization design method for the switched reluctance machines with Particle Swarm Optimization. A generalized SRM analytical model compatible to any feasible stator and rotor slot combinations will be applied to determine the inductance and flux density profiles at arbitrary rotor positions, which is also verified by the finite element analysis. In addition, this chapter seeks to demonstrate that with appropriate design specifications and assumptions, the primary design variables in this model can be reduced to as low as five, which significantly simplifies the optimization process. PSO is then applied to intelligently search for the multi-objective optimized designs for the weighted-sum or vector based cost functions. Compared to the traditional machine design methods, the proposed scheme is able to find the optimized solutions with a competitive accuracy and a much faster computational speed.

4.2 Challenges with the Traditional Design Method of SRMs

In general, the conventional machine design method starts from the Essen's equation as the mechanical power is given as [143]

$$P_{mech} = \frac{\pi^2}{120}\omega_s k_1 (D_{is}^2 l_e) B_{g1} K_s \eta_{gap} \cos(\phi_{gap}) \tag{4.1}$$

where ω_s is the rotor speed in rad/s, k_1 is a constant of 4.44 for sinusoidal-excited AC machines, D_{is} and l_e are the stator bore diameter and active length, K_s and B_{g1} are the electric loading and the fundamental air-gap magnetic flux density, and η_{gap} and ϕ_{gap} are the air-gap efficiency and power factor, respectively. The machine designers generally start from the product of $D_{is}^2 l_e$ and follow a heuristic process to complete the machine design.

However, the output equation of the SRMs [28] is even more complicated

$$P_{mech} = \frac{\pi^2}{120}\omega_s \underbrace{(1 - \frac{1}{L_a^s/L_u})}_{saturation}(D_{is}^2 l_e) B_{g1} K_s \eta_{gap} k_{duty} \tag{4.2}$$

where L_a^s is the saturated inductance at the aligned position, L_u is the unaligned inductance, and k_{duty} is the duty cycle. Both L_a^s and L_u are functions of the SRM geometric parameters, L_a^s is also subject to change with different saturation levels. In order to use this equation in a similar way and obtain $D_{is}^2 l_e$, more assumptions have to be made on L_a^s and L_u, which further intensifies the heuristic process, and it is even more challenging to design an SRM than AC machines.

For example, if a machine designer wishes to come up with an initial design for a 0.75 kW, 10,000 rpm 6/4 SRM, based on rules of thumb, the following parameters are picked

$$(1 - \frac{1}{L_a^s/L_u}) = 0.7,\ l_e = 0.8 D_{is},\ B_{g1} = 1.5T,\ K_s = 25kA/m,\ \eta_{gap} = 0.8\ ,\ k_{duty} = 1$$

According to equation (4.2), this would lead to $D_{is} = 30.6$ mm and $l_e = 24.5$ mm. Then the rest of the SRM geometry will be calculated based on these assumptions. The SRM's aligned and unaligned inductance L_a^s and L_u would be calculated with the "flux tube" method illustrated in Figure 2.1. The results would be used to be compared with the initial assumptions, and if a large discrepancy is observed, a new set of assumptions have to be

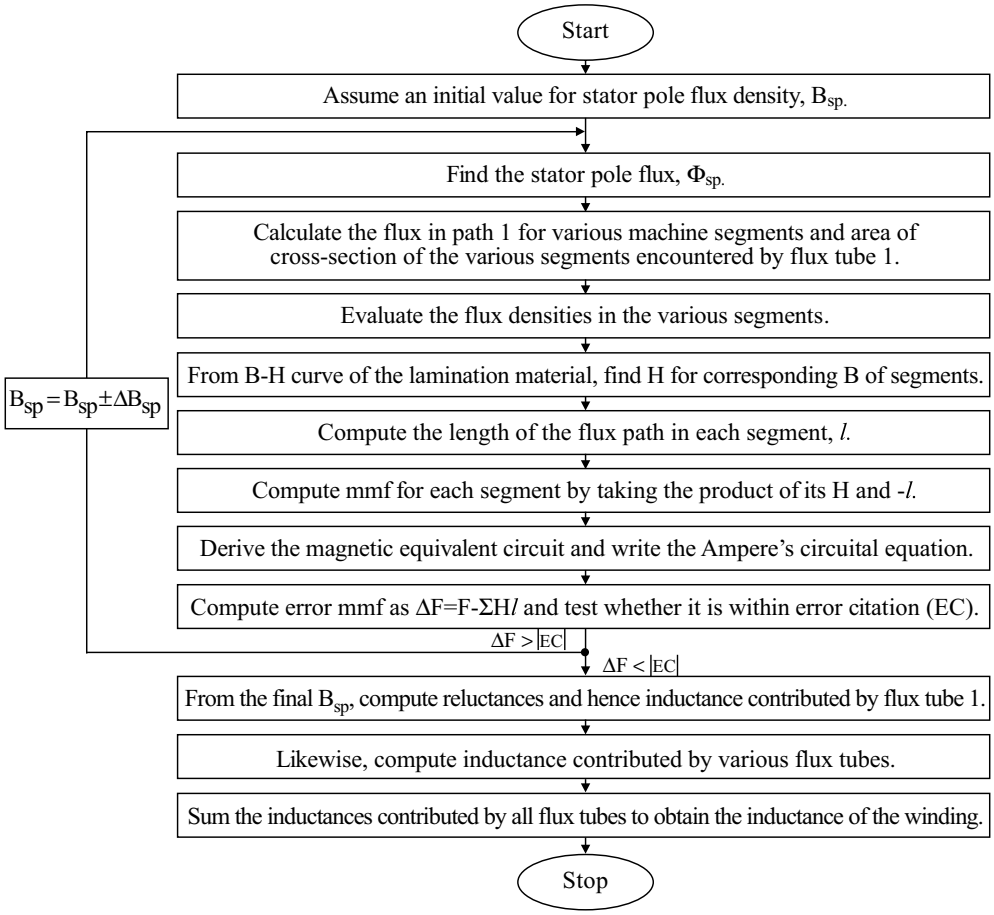

Figure 4.1: Flowchart of the "flux tube" method for calculating the SRM inductance.

made, and the process must be restarted from the initial equation (4.2). This heuristic design process will be repeated until there is a close level of agreement of the inductance, and until other machine performance indices are met. In addition, the calculation of inductance using the "flux tube" method is also performed in an iterative process for each rotor position, as demonstrated in the flow chart in Figure 4.1, indicating many more rounds of iterations are necessary to obtain the complete inductance profile at all rotor positions.

Moreover, this method of determining inductance falls short of generality, as the flux tube shapes need to be manually adjusted depending on each rotor position and the specific machine geometry in order to maintain a high level of accuracy, thus making it less feasible for use in finding the optimal machine design. Even if this traditional SRM design process is applied, many more iterations on the entire design process are still expected until perfor-

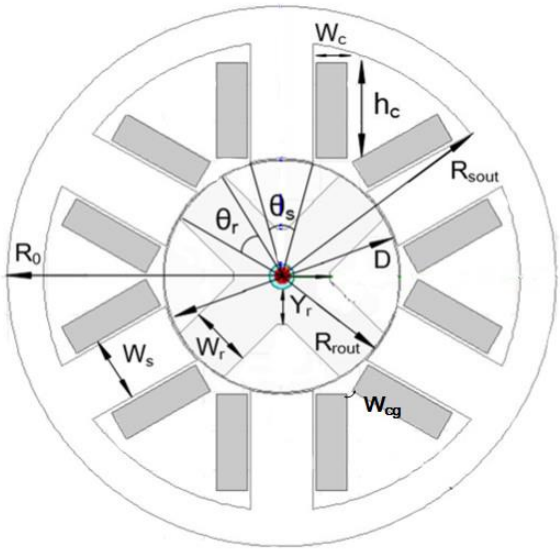

Figure 4.2: An SRM geometry demonstrating all the 13 geometric design variables.

mance specifications are met. Therefore, this traditional design is an iterative process, and it involves a number of designs evaluated by trial-and-error, which is inefficient and time consuming.

4.3 Proposed Analytical Design Method of SRMs

Advanced computational intelligence algorithms are suitable to find an optimal design of an SRM in a huge multi-dimensional search space. However, considering the feasibility and computational speed issues, it is necessary to derive a set of accurate and generalized analytical equations. In particular, these equations must be capable of determining the electromagnetic performance of an SRM in a few seconds at most, and they must be able to be executed many times faster than a single FEA run, which generally takes around 1-2 minutes on an ordinary computer.

4.3.1 Specifying Prime Design Variables and Designing the SRM Geometry

For the 17 variables that need to be determined, 5 variables are explicitly selected as the prime design variables in this chapter to be optimized by stochastic optimization algorithms.

These are the stator bore diameter D, the machine axial stack length of the stator lamination l_{stack}, the rotor pole arc angle θ_r, the stator pole arc angle θ_s, and the current density J, while the peak current I_p and number of turns per stator pole N are selected to be fixed values for this chapter.

However, because the wire gauges are discrete values, the winding current density is actually not exactly equal to the specified value but close to it. The type of standard gauge wire (AWG) could be selected with the closest diameter D_{wire} to the specified value.

Assuming the distance between two adjacent windings in the stator slot is minimal, then the maximum value of stator coil width w_c is

$$w_c = \frac{\pi D}{2N_s} - \frac{D}{4}\theta_s \tag{4.3}$$

A stator coil area A_{cu} could be given as

$$A_{\mathrm{ca}} = \frac{\pi D_{\mathrm{wine}}^2}{4} N \tag{4.4}$$

Combining the above two equations, the available coil height h_c can be determined as

$$h_{\mathrm{c}} = \frac{\pi D_{\mathrm{wise}}^2 N}{4} \left(\frac{2N_s}{2\pi D - N_s D \cdot \theta_s} \right) \tag{4.5}$$

The minimum stator pole height is approximately equal to the coil height, but the coil sitting at the root of the pole is usually not tight-fitting, thus the pole height is slighter greater than the coil height. Here the stator pole height h_s is assigned to be $h_s = 1.1h_{\mathrm{c}}$.

The stator yoke thickness Y_s is calculated based on the assumption that the maximum flux in the stator yokes are half of the flux from one stator pole, thus the back iron thickness has to be a minimum of half the width of stator pole. Due to considerations of mechanical robustness, Y_s is set as $Y_s = 0.6w_{\mathrm{st}}$, where w_{st} is the stator tooth width and is given as

$$w_{\mathrm{t}} = D \sin\left(\frac{\theta_s}{2}\right) \tag{4.6}$$

Since the switched reluctance machines used in special variable speed applications may not fall under the frame sizes categorized by NEMA, the design details could start from the bore diameter D and then could be determined all the way up to the outer diameter of the

stator lamination D_0 by adding the pole heights and back iron thickness as

$$D_0 = D + 2h_s + 2Y_s \tag{4.7}$$

A typical estimation of the air-gap length g is

$$g = 0.2 + 2\sqrt{\frac{D}{1000} \cdot \frac{L_{\text{stack}}}{1000}} \tag{4.8}$$

where D and l_{stack} are in millimeters. However, considering the manufacturing constrains, the air gap length should be typically greater than 0.3 mm, and the typical value of D and l_{stack} of small SRM machines are usually around 20-30 mm, making D_0 smaller than the mechanical constraint of 0.3 mm, and thus the air gap length is fixed at 0.3 mm in the rest of this chapter.

For the rotor section, the shaft diameter D_{shaft} is usually a fixed value, while the rotor back iron thickness is $Y_r = 0.6w_{\text{st}}$, then the rotor pole height is written as

$$h_r = \left(\frac{D - 2g - D_{\text{shaft}} - Y_r}{2}\right) \tag{4.9}$$

In this way, all of the main geometry parameters shown in Figure 4.2 can therefore be determined.

4.3.2 Determining SRM Inductance at Arbitrary Rotor Positions

The analytical equations applied are based on solving the partial differential equations of the magnetic potentials of the electromagnetic field in the air gap, stator slot and the rotor slot regions of the SRM. The flowchart in Figure 4.3 shows the complete calculation process. The total inductance is the sum of inductances contributed by the above three regions.

$$L = L_{a\dot{x}r} + L_{rotor} + L_{stator} \tag{4.10}$$

where L_{air}, L_{rotor} and L_{stator} are the inductance contributed by the air gap, the rotor slot and the stator slot regions, respectively.

As an example, the calculation of the inductance in the air gap region L_{air} is provided below, while the rotor slot and the stator slot inductance L_{rotor} and L_{stator} can be determined

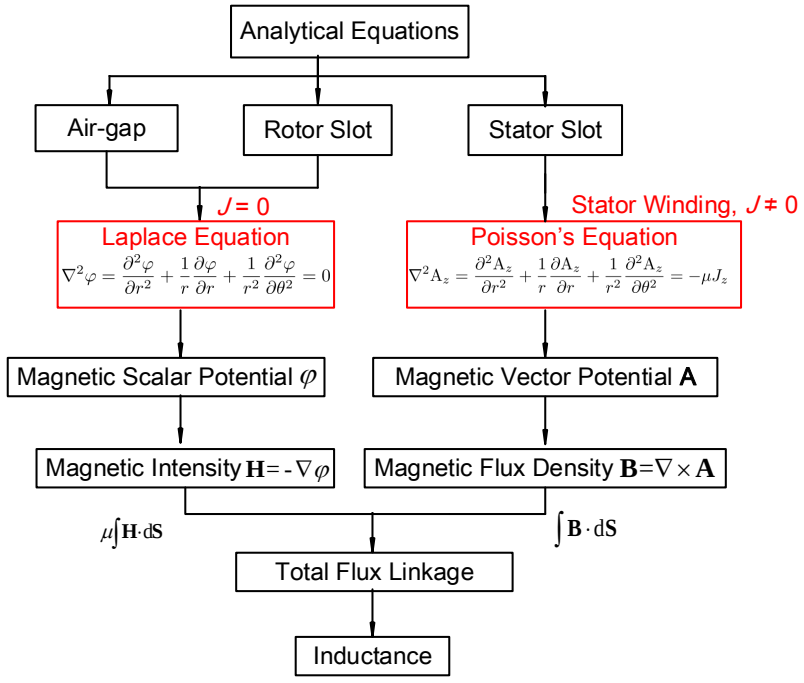

Figure 4.3: Flowchart of the analytical derivation of switched reluctance machines.

in a similar manner.

The homogeneous solution of Laplace equation in 2-D polar coordinate is

$$\varphi(r,\theta) = \sum_{n=1}^{\infty}(A_n r^{m_n} + B_n r^{-m_n}) \cdot (C_n \cos(m_n\theta)) \tag{4.11}$$

where A_n, B_n and C_n are determined by the boundary conditions as

$$\begin{cases} \varphi(R_{sin},\theta) = \sum_{odd} \dfrac{4F_{ag}}{n\pi}\sin(m_n\theta_s)\cos(m_n\theta) = \displaystyle\sum_{n=1}^{\infty} F_{ag\_an}\cos(m_n\theta) \\ \varphi(R_{rout},\theta) = constant \end{cases} \tag{4.12}$$

Based on the boundary conditions, the following equation set needs to be solved:

$$\begin{cases} A'_n R_{\sin}^{m_n} + B'_n R_{sin}^{-m_n} = F_{ag\_an} \\ A_n R_{rout}^{m_n} + B'_n R_{rout}^{-m_n} = 0 \end{cases} \tag{4.13}$$

The variables are defined as follows: R_{sin} and R_{sout} denote the inner and outer radius of the stator, while R_{rout} is the outer radius of the rotor, and an intermediate variable m_n can be expressed as $\pi n/2\theta_k$, where θ_k is half the angle of the rotor slot.

Then the magnetic scalar potential in the air gap region φ_{ag} after solving the above

equations become

$$\varphi_{ag}(r,\theta) = \sum_{nodd}\left[F_{ag\_an}\cdot\frac{\left(\frac{r}{R_{rout}}\right)^{m_n}-\left(\frac{r}{R_{rout}}\right)^{-m_n}}{\left(\frac{R_{sin}}{R_{rout}}\right)^{m_n}-\left(\frac{R_{sin}}{R_{rout}}\right)^{-m_n}}\right]\cos\left(m_n\theta\right) \tag{4.14}$$

Since there are no windings carrying a current in the air gap region, the magnetic field intensity $\mathbf{H}$ in the non-conductive air gap region where J=0 can be expressed in 2D polar coordinates by the magnetic scalar potential φ as

$$\mathbf{H} = -\nabla\varphi = -\left(\frac{\partial\varphi}{\partial r}\mathbf{a_r} + \frac{1}{r}\frac{\partial\varphi}{\partial\theta}\mathbf{a}_\theta\right) \tag{4.15}$$

where $\mathbf{a_r}$ is the unit radial vector, $\mathbf{a}_\theta$ is the unit tangential vector, and r and θ are the radial and tangential coordinates, respectively. The magnetic field intensity $\mathbf{H}$ on the rotor pole surface is obtained by substituting $\varphi_{ag}(r,\theta)$ into the above equation as

$$H(R_{rout},\theta) = -\sum_{odd}\left\{\frac{8F_{ag}m_n}{n\pi R_{rout}}\sin(m_n\theta_s)\left[\frac{\left(\frac{R_{rout}}{R_{sin}}\right)^{m_n}}{\left(1-\frac{R_{rout}}{R_{sin}}\right)^{2m_n}}\right]\cdot\cos(m_n\theta)\right\} \tag{4.16}$$

Then, the air gap flux linkage can be determined by taking the integral of the air gap flux density H along the path where the stator and rotor tooth overlap, and thus the air gap inductance is

$$L_{air} = \frac{N^2\mu_0 l_{stack}R_{rout}\int_{\theta_p-\theta_R}^{\theta_p+\theta_R}H_r\left(R_{\text{rout}},\theta\right)d\theta}{F_{ag}} \tag{4.17}$$

N is the number of turns per phase per pole, l_{stack} is the stack length, θ_r is half the angle of the rotor pole, while θ_p is the SRM rotational angle from the aligned position.

In addition, the equations above calculating the inductance profile are applicable to SRMs with arbitrary number of stator and rotor poles. This generality is reflected on the Fourier Series coefficients F_{air_an} associated with the boundary conditions of the magnetic potentials in the air gap regions, and this coefficient can be represented as piece-wise functions of the number of stator poles N_S, the number of rotor poles N_R, stator and rotor pole arc angles θ_S and θ_R, as well as other SRM geometric parameters.

4.3.3 SRM Performance Calculation

After designing the SRM geometry, the winding layout and after calculating the total inductance, the machine performance can be calculated. This includes the average torque, efficiency, torque ripple, weight, volume, and so on. The detailed calculation of the above performance indices are presented below.

Torque

The torque profile could be also obtained as

$$T_e = \frac{\partial L(\theta, i)}{\partial \theta} \cdot \frac{i^2}{2} \tag{4.18}$$

The average torque could be calculated as

$$T_{avg} = \frac{(W_a - W_u)\, N_s N_r}{4\pi} \tag{4.19}$$

where W_a and W_u are the stored electromagnetic energy at the aligned and unaligned positions, and N_s and N_r are the number of stator and rotor poles, respectively.

Here $W_a = \frac{1}{2} L_a i_a^2$ and $W_u = \frac{1}{2} L_u i_n^2$

The torque ripple could be given as

$$T_r = \frac{T_{\max} - T_{\min}}{T_{avg}} \tag{4.20}$$

However, if there are only two phases and no commutation, such as in the 4/2 switched reluctance machines, the minimum torque would always be zero, making the definition of the torque ripple less appealing as an optimization parameter. Thus the torque ripple would only be considered as a machine performance index to be optimized at 6/4, 12/8 or on other SRMs with larger stator/rotor pole combinations.

Efficiency

The efficiency of SRM is defined as

$$\eta_r = \frac{T_{as}\omega}{T_{as}\omega + P_{cas} + P_{cu} + B\omega^2 + etc\ldots} \tag{4.21}$$

The windage and frictional losses depend on the rotational speed and shaft characteristics, and those losses are generally determined through experiments conducted to calculate the power loss through means of applying an outside motor pulling the SRM without excitations. In the initial machine design process, what we should calculate in the electromagnetic aspects are the copper loss P_{Cu} and the iron loss P_{iron}.

In terms of calculating the multiple performance indices, the weight of an SRM is taken to be the active weight, which is the sum of the stator core, rotor core and the winding. The loss of the machine primarily consists of the copper loss and the iron loss. The copper loss can be simply given by

$$P_{cu} = I^2 R = \frac{1}{\sigma_{Cu}} I^2 \frac{2N_s N \left(w_t + l_{stack}\right)}{A_{cu}} \tag{4.22}$$

where w_t is the stator pole width, σ_{Cu} and A_{Cu} are the conductivity and the total cross-sectional area of copper windings.

The iron loss is obtained by applying the Steinmetz model [144–147], which separates the iron loss into the hysteresis loss P_{hys} and the eddy current loss P_{eddy}, based on the derivatives of the flux density. Traditionally, accurate estimations of flux densities are particularly challenging because of their non-sinusoidal nature. In this part, however, the flux density B at each part of the stator and rotor could be accurately and efficiently derived with the complete inductance profile obtained earlier for a given machine geometry and current profile. Moreover, for SRMs with stator/rotor pole numbers above 4/2, commutation effects should be considered and the situation involving simultaneous multi-phase excitation needs to be addressed. Thus a complete inductance matrix needs to be derived to calculate the flux density at different rotor positions [144].

Thus hysteresis loss density can be calculated with generalized Steinmetz equation as

$$P_{hss} = \frac{1}{T} \int_0^T k_{kss} \left| \frac{dB}{dt} \right|^a \left(\Delta B^{b-a} \right) dt \tag{4.23}$$

where ΔB is the flux density from peak to peak and k_{hys} is the hysteresis loss coefficient

defined by

$$k_{t\eta s} = \frac{k}{(2\pi)^{a-1} \int_0^{2\pi} |\cos\theta|^a \cdot 2^{b-a} d\theta} \tag{4.24}$$

where a, b and k are the same material parameters used in the earlier equations.

The eddy current loss density for lamination is

$$P_{eddy} = \frac{1}{12}\sigma\omega^2 d^2 B_{avg}^2 s = \frac{1}{T}\int_0^T \frac{k_{eddv}}{4\pi^2}\left(\frac{dB_{avg}(\mathrm{t})}{dt}\right)^2 dt \tag{4.25}$$

where σ is the conductivity, d is the thickness of a lamination, ω is the sinusoidal frequency, B_{avg} is the average flux density and s is the stacking factor. In this research, the hysteresis and eddy current loss coefficients are found by loss curve fitting through a least-square approach. Both the hysteresis and the eddy current losses will be calculated on every part of the stator/rotor tooth and yoke, and their sum will represent the total iron loss. After finding all of the power losses, the efficiency is obtained by the taking the output power over the sum of the output power plus various other losses.

Weight and Volume

The weight of the SRM is comprised of the weight of the stator core, stator teeth, stator winding, rotor core, rotor teeth and the frame. With a ρ_{Fe} = 7.8 $\mathrm{kg/m^3}$ estimated as the iron density, the weight of the stator core is

$$W_{sc} = \frac{\pi}{4}\left(D_0 - (D_0 - 2Y_s)^2\right) \cdot L_{stxk} \cdot \rho_{Fe} \tag{4.26}$$

The weight of the rotor core is

$$W_{rc} = \frac{\pi}{4}\left(D_{rin}^2 - D_{shdft}^2\right) \cdot l_{stack} \cdot \rho_{Fe} \tag{4.27}$$

The total weight of the stator teeth is

$$W_{st} = N_s \cdot \theta_s \cdot R_{\sin} \cdot h_s \cdot l_{stack} \cdot \rho_{Fe} \tag{4.28}$$

The weight of the rotor teeth is

$$W_{rt} = N_r \cdot \theta_r \cdot R_{rout} \cdot h_r \cdot l_{stack} \cdot \rho_{Fe} \tag{4.29}$$

The weight of the stator winding is (neglecting the weight of insulation components) is

$$W_{sw} = N_s \rho_{cu} A_{clwire} L_c \tag{4.30}$$

The weight of the machine frame is (assuming the machine frame has an additional length of 10% of the core length to allow for end winding clearances)

$$W_{fin} = \frac{\pi}{4} \rho_s \left((D_0 + 2Y_s)^2 - D_0^2 \right) L_{sack} (1 + 10\%) \tag{4.31}$$

The total weight of the SRM machine is the summation of all the previously calculated weights

$$W_t = W_{sc} + W_{rc} + W_{st} + W_{rt} + W_{sw} + W_{fin} \tag{4.32}$$

Allowing for the additional length of 10%, the volume of the machine is

$$V = \frac{\pi}{4} D_0^2 l_{stack} (1 + 10\%) \tag{4.33}$$

4.3.4 Validation of the Analytical Design Model with Finite Element Analysis

To evaluate the accuracy of the proposed analytical model for the SRM, a 2-D finite element analysis of 4/2, 6/4 and 12/8 SRMs are implemented as the benchmarks. The relative permeability of magnetic iron is $\mu_r = 4000$ and a trapezoidal current profile with an advanced turn-on for the excitation of each phase. The peak current is chosen as 2.5A.

4/2 SRM Verification

The analytical model of the SRM provides a comprehensive understanding of many physical quantities, such as the flux linkage, inductance, torque, etc. In contrast to the FEA-oriented machine design procedures, the analytical approach can significantly accelerate the design and optimization of an SRM. For one general design of an 4/2 SRM, it takes about 3 to 7 minutes for the AMD FX9370 CPU to finish the transient analysis with 3 cores running at the same time for a single task. But for this analytical method, it only takes a few seconds to compute the inductance profile using only one core. The simplification of equations and parallel computing can be implemented in the future to further accelerate the calculation.

Table 4.1: Geometric Parameters of the Benchmark 50,000 rpm 4/2 SRM.

Parameters	Value
Stator outer radius R_{sout}	26.57 mm
Stator inner radius R_{sin}	12.50 mm
Rotor outer radius R_{rout}	11.981 mm
Rotor inner radius R_{rin}	6.5 mm
Stator pole angle θ_s	60°
Rotor pole angle θ_r	80°
Stack length l_{stack}	20 mm
No. of turns/pole N	95

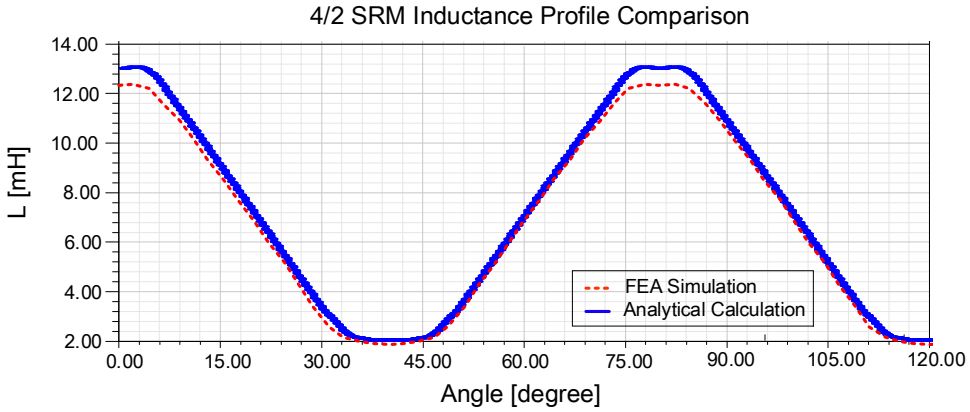

Figure 4.4: Comparison of benchmark 4/2 SRM inductance profiles obtained through analytical equations and FEA.

The geometric parameters of the 50,000 benchmark 4/2 SRM are summarized in Table 4.1. The comparison between the inductance profile obtained by the above analytical approach and the benchmark finite-element results are demonstrated in Fig. 4.4, where the red dotted curve is the inductance from FEA simulation and the blue curve is the inductance from analytical equations. Table 4.2 shows the percentage of errors. The errors of aligned and unaligned inductance are only 6.6% and -6.7%, respectively. The results of the computed torque profile is presented in Fig. 4.5, which also demonstrates a good level of agreement with FEA results.

Table 4.2: Percentage of Errors of the Inductance Obtained From Analytical Equations and FEA at Different Rotor Positions of the Benchmark 4/2 SRM.

Rotation Angle	Analytical	FEA	Error
0° (aligned)	13.03 mH	12.22 mH	6.6%
10°	12.90 mH	12.11 mH	6.5%
30°	9.61 mH	9.26 mH	3.8%
60°	4.38 mH	4.30 mH	1.8%
80°	1.88 mH	2.05 mH	-8.3%
90° (unaligned)	1.81 mH	1.94 mH	-6.7%

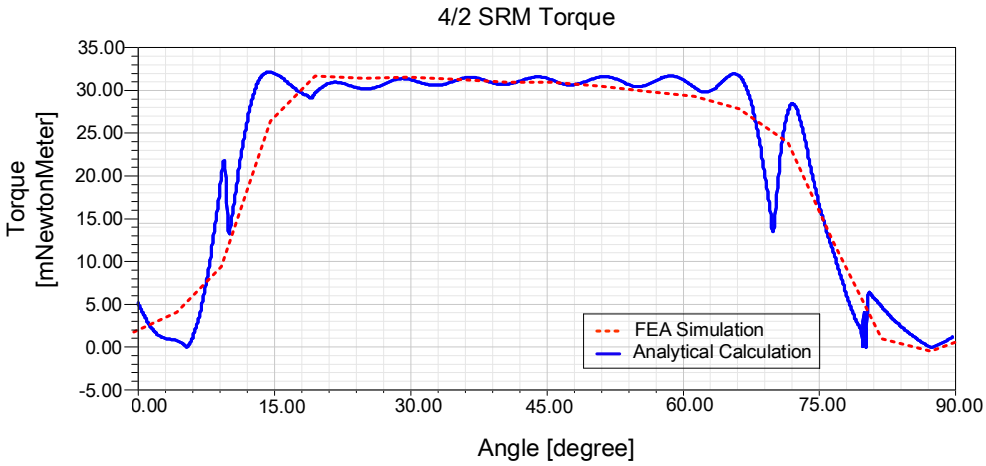

Figure 4.5: Comparison of benchmark 4/2 SRM torque profiles obtained through analytical equations and FEA.

12/8 SRM Verification

The typical SRM excitation current profile is the current of each phase that has been reduced to zero while the current of the proceeding phase is simultaneously turned on at the aligned position. In this way only positive torque is generated so that the SRM is being operated as efficiently as possible. For the two adjacent phases in the switching sequence, the aligned position of one phase corresponds to the unaligned position of the next phase, so there is no overlap in the current profile. The 4/2 SRM design method is based on this non-overlapped current profile, which is usually true for high-speed applications but is not valid for the high torque machine design.

To increase the output power and the torque density value, the conduction time of the

Table 4.3: Geometric Parameters of the Benchmark 2,000 rpm 12/8 SRM.

Parameters	Value
Stator outer radius R_{sout}	79 mm
Stator inner radius R_{sin}	39.5 mm
Rotor outer radius R_{rout}	39.2 mm
Rotor inner radius R_{rin}	21.525 mm
Stator pole angle θ_s	17.8°
Rotor pole angle θ_r	22°
Stack length l_{stack}	20.5 mm
No. of turns/pole N	111

Table 4.4: Percentage of Errors of the Inductance Obtained From Analytical Equations and FEA at Different Rotor Positions of the Benchmark 12/8 SRM.

Rotation Angle	Analytical	FEA	Error
0° (aligned)	50 mH	47.56 mH	5.1%
5°	44.63 mH	44.42 mH	0.5%
15°	24.06 mH	23.15 mH	5.2%
20°	9.96 mH	10.64 mH	3.9%
22.5° (unaligned)	8.94 mH	9.05 mH	-1.2%

current has to be increased, and the current profile needs to have some level of overlap between two adjacent phases. It is found that the “advanced turning-on current profile" has the highest average torque value, and thus it is chosen as the overlapped current profile for the later 6/4 and 12/8 SRM design, for the purposes of maximizing the torque density.

By applying the same set of analytical equations with the parameters in Table 4.3 as the input, the inductance profile obtained by the above analytical approach and the benchmark finite-element result in selecting M19 steel as the stator and rotor material. This is demonstrated in Figure 4.6, where the red dotted curve is the inductance from FEA simulation and the blue curve is the inductance from analytical equations. Table 4.4 shows the percentage of errors. The errors of the aligned and unaligned inductance are only 7.0% and -2.8% respectively. The results of the torque profile for the 12/8 SRM with standard M19 steel is presented in Fig. 4.7, which also demonstrates a high level of agreement with the FEA results. The result of the flux density of the benchmark 12/8 SRM at the aligned and unaligned positions after being calculated by FEA is plotted in Figure 4.8. For the stator teeth, the flux density is almost evenly distributed except for some small regions in the tooth

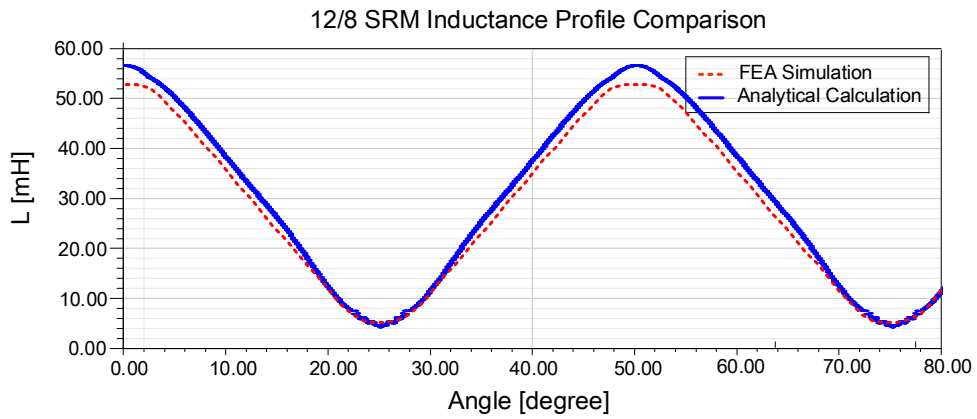

Figure 4.6: Comparison of benchmark 12/8 SRM inductance profiles obtained through analytical equations and FEA.

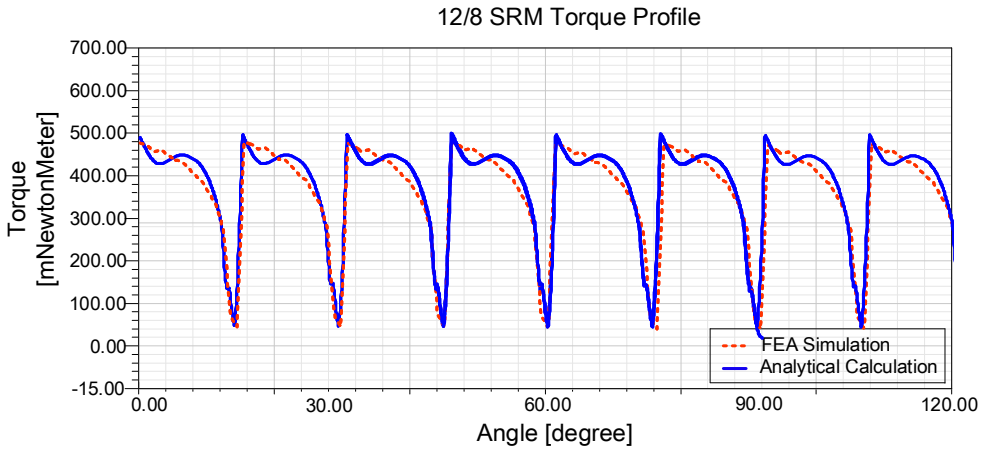

Figure 4.7: Comparison of benchmark 12/8 SRM torque profiles obtained through analytical equations and FEA.

root and tip. Hence, the flux density at the center of a stator tooth can be used to represent the average value of the stator teeth flux density. The comparison of these values obtained through analytical equations and FEA is shown in Fig. 4.9, and the high level of agreement between the two curves can further ensure the accuracy of the core loss calculation, which directly depends on the variation of flux density.

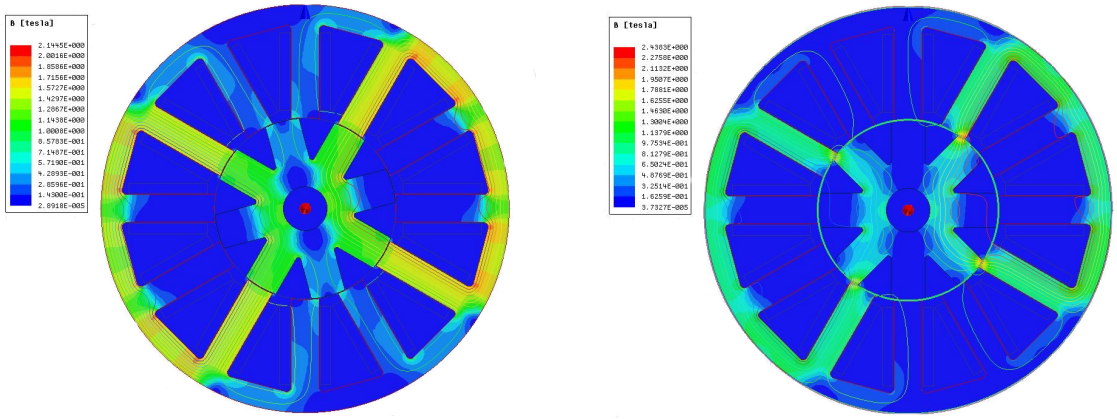

(a) (b)

Figure 4.8: Plot of flux densities calculated by FEA of 12/8 SRM at (a) aligned position and (b) unaligned position.

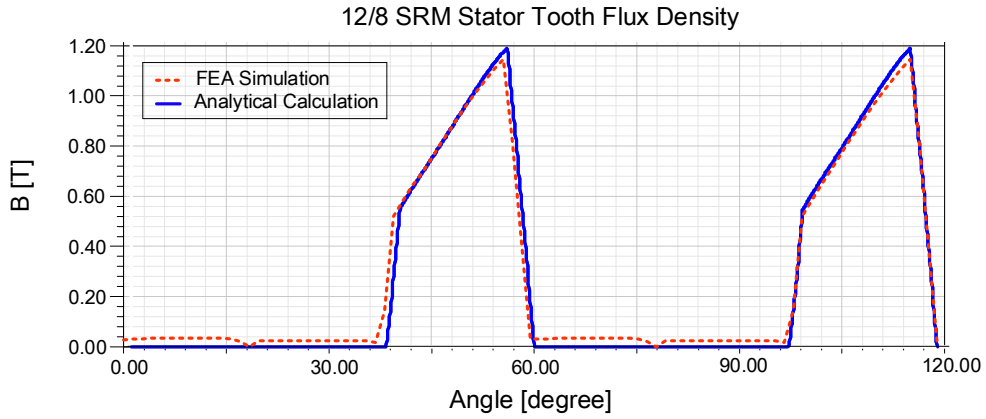

Figure 4.9: Comparison of benchmark 12/8 SRM stator tooth flux density profiles obtained through analytical equations and FEA.

4.3.5 Flowchart of the Proposed Switched Reluctance Machine Design Method

Figure 4.10 shows the flowchart of the proposed SRM analytical design method. These have two advantages over the classical design process. Firstly, there are only five prime design variables in the proposed method; D and l_{stack} are the stator bore diameter and the stack length, which are limited by the spatial limits; θ_S and θ_R are the angles of stator and rotor poles, which are constrained by the physical properties; and J is the current density in the windings, which is limited by the thermal and cooling constraints. Secondly, the

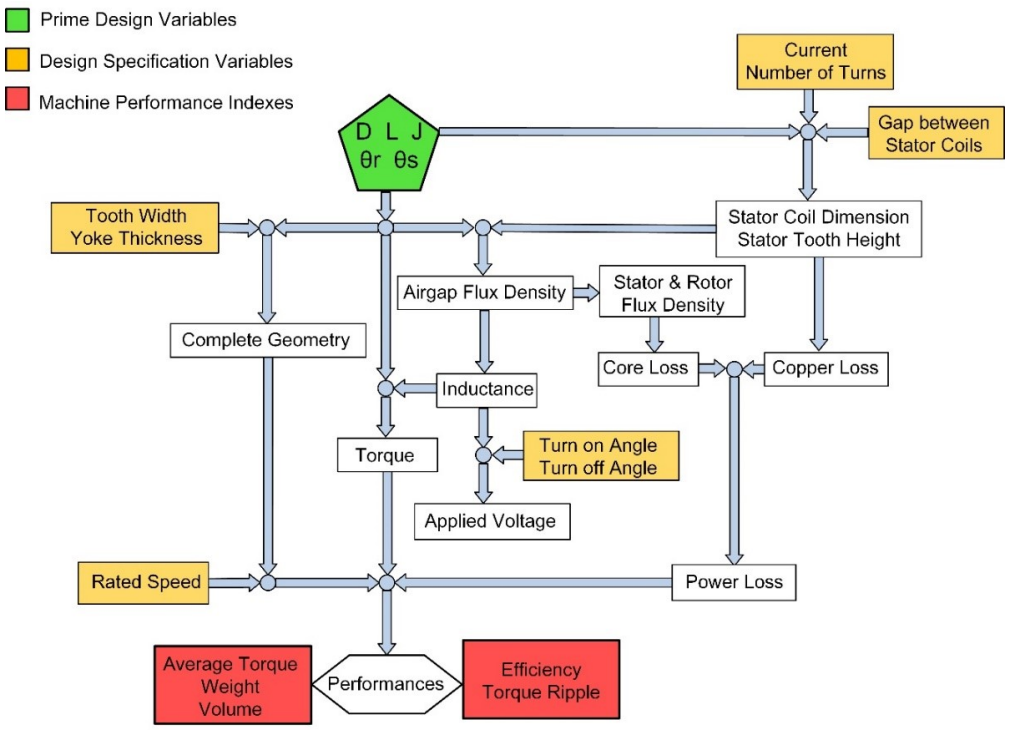

Figure 4.10: A flowchart of the proposed SRM multi-objective analytical design method.

proposed method starts from the five prime design variables and directly finds a machine design candidate with no iterations. This significantly saves time by eliminating the excessive calculations needed to perform the design iterations in the traditional design process. Thanks to the aforementioned two advantages, the proposed multi-objective design method is able to run more efficiently than the traditional machine design method, which significantly shortens the entire process.

After the machine geometry and winding layout have been designed through the flowchart shown in Figure 4.10, various machine performance indices can be calculated, including the average torque, efficiency, torque ripple, weight, volume, and so on. However, optimizing the torque ripple analytically is a rather complicated process since it largely depends on the current profile and its associated turn-on and turn-off angles, and the inductance profile, which is the fundamental to the torque profile calculation, will be further distorted with considerations of both the saturation and commutation effects. Therefore, the proposed research first performs a first-stage multi-objective SRM design with a fixed

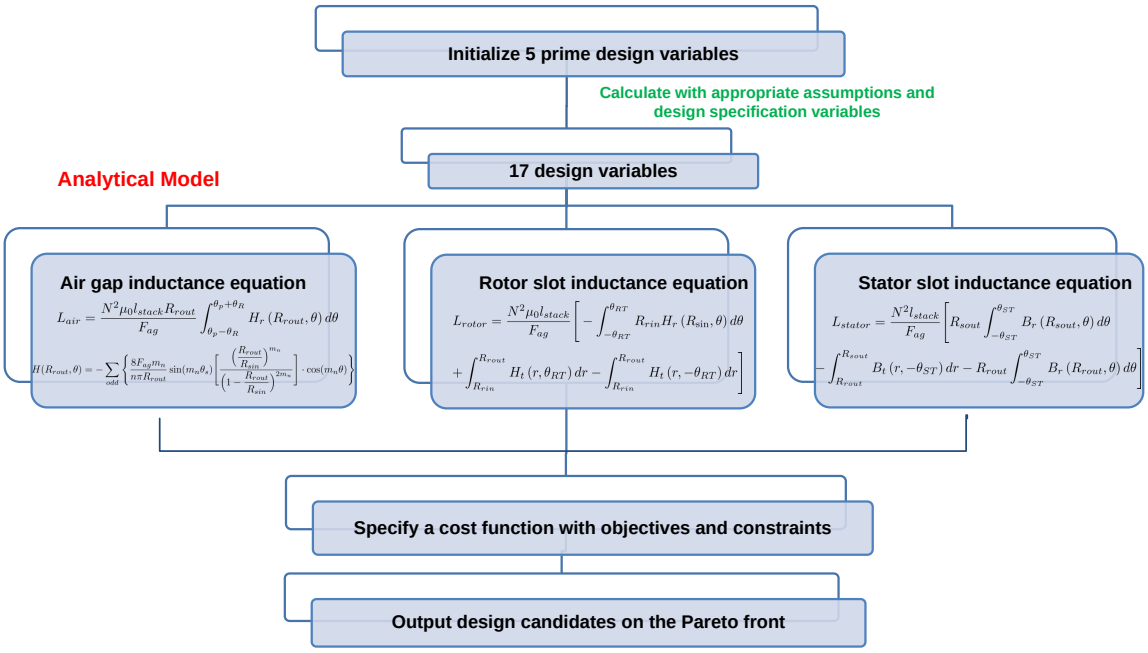

Figure 4.11: A flowchart of the proposed SRM multi-objective analytical design method displaying all of the analytical equations.

current profile with fixed turn-on and turn-off angles, and the optimization of torque ripple will be explored in the next chapter and integrated into this first-stage design process with the active current profile optimization.

An illustration of the flowchart incorporating all of the analytical equations in one place is presented in Figure 4.11, where the total inductance is contributed by the mutual inductance linked through the air gap, the stator and rotor slot leakage inductance, and the stator and rotor slot fringing inductance. All of the expressions for the flux intensity $\mathbf{H}$ in the air gap and the rotor slot are solved with Poisson's equation, and the flux density $\mathbf{B}$ in the stator slot region is solved with Laplace's equation. Details of the explicit forms for the above expressions can be found in [148].

4.4 Multi-Objective Optimization with a Weighted-Sum Scalar Cost Function

4.4.1 Weighed-Sum and Vector Objective Function based PSO

The design objective should be firstly defined before applying any optimization algorithms. In this section, the design objective is a cost function that is either a weighted-sum or a vector representation of the various machine performance indices (PIs), such as average torque (T_{avg}, in $mN \cdot m$), efficiency (Eff, in %), weight (W_t, in kilograms) and volume (Volume, in m3).

An example of such a weighted-sum-based design objective function is shown as

$$objective = W_t + 5000 \cdot Volume + 10 \cdot (1 - Eff) - 25 \cdot T_{avg} \tag{4.34}$$

The coefficients before each performance index, such as 25 before $-T_{avg}$, has two purposes. Firstly, they normalize each term in the objective function to have approximately the same order of magnitude. Secondly, designers can adjust those coefficients to represent how much importance each PI has in the overall performance evaluation. For example, if the optimization of the weight and volume are more important than the average torque and efficiency for high speed SRMs, the coefficients before $(1 - Eff)$ and $-T_{avg}$ should be increased to indicate such emphases on the weight and volume.

4.4.2 Design Constraints

Machine designs have to meet certain design constraints from various aspects, including spatial constraints, material constraints, manufacturing constraints and thermal constraints. The design constraints considered in this design of a generalized SRM are listed in Table 4.5. To include design constraints in the optimization process, the penalty function approach is used to convert constrained optimization problems into unconstrained optimization problems [149]. For weighted-sum based objective functions, the various design constraints are summed up as a penalty term, also known as a soft constraint, which is added to the

Table 4.5: List of constraints for switched reluctance machine design.

Parameters	Value
Shaft Radius	1.587 mm
Maximum Stator Current Density	7 A/mm^2
Airgap length	0.3 mm
Maximum Rotor Pole Angle	$2\pi/N_r$
Maximum Stator Pole Angle	$2\pi/N_s$
Minimum Stator and Rotor Pole Angle	0

objective function as

$$objective = W_t + 5000 \cdot Volume + 10 \cdot (1 - Eff) - 25 \cdot T_{avg} + penalty\_sum \quad (4.35)$$

For weighted-sum based objective functions, the design constraints can be integrated into the inequality and equality constraints.

Since the air-gap length has a dominant effect on the SRM performance and is usually limited by mechanical constrains, this thesis assumes an equal air-gap of 0.3 mm throughout the machine design and optimization process to make a fair comparison investigating the influence of the primes design variables on the multiple performance indices. The maximum current density is assumed to be 7 $\mathrm{A}/\mathrm{mm}2$ with natural air cooling, and this parameter can be accurately determined with consideration of the load profile and thermal modeling of SRMs.

4.4.3 Particle Swarm Optimization

Particle swarm optimization (PSO) is effective in solving problems with complicated local minima and discontinuities and is thus applied in this design optimization. PSO is an evolutionary computation technique developed in 1995 by Kennedy and Eberhart, and the procedures can be as summarized by the following steps

1) Define the solution space. Select the parameters that need to be optimized. In this case, the parameters are l_{stack}, D, J, θ_s and θ_r. Define a weighted-sum-based objective function or a vector-based objective function.

2) Initialize with random swarm locations and velocities.

3) Create a Pareto repository, which is a set of nondominated points found by PSO. At the initialization stage, the Pareto repository is the non-dominated solutions among the initial particles.

4) Systematically "fly" the particles through the solution space: The following steps are performed on each particle individually:

   a) For vector based MOOPs, evaluate each particle's vector multi-objective function and check its Pareto optimality with the Pareto repository. Update the Pareto repository with the non-dominated particles and discard the ones that are being dominated. Randomly select two Pareto solutions from the Pareto repository as the $pbest$ and $gbest$.

   b) Evaluate particle fitness: Compare to "global best" ($gbest$) and "personal best" ($pbest$);

   c) Update each particle's velocity according to the relative values of $pbest$ and $gbest$ by using the following equation

$$v_n = \omega \cdot v_n + c_1 rand0 \cdot (p_{best,n} - x_n) + \mathrm{c_2 rand}\,(\mathrm{g_{best,n}} - x_n) \tag{4.36}$$

6) Move each particle by applying the velocity for a given time step Δt, which is usually chosen to be one, and the position is updated to:

$$x_n = x_n + \Delta t \cdot v_n \tag{4.37}$$

Steps 5) and 6) are repeated until the termination criteria are met.

PSO emulates the behavior of a swarm of bees trying to locate places with the highest density of flowers [50]. The optimal search is attained by a combination of individual and collective knowledge. PSO is robust to the values of its running coefficients, and hence, simply by following a few guidelines [58], tuning the running coefficients can be usually neglected.

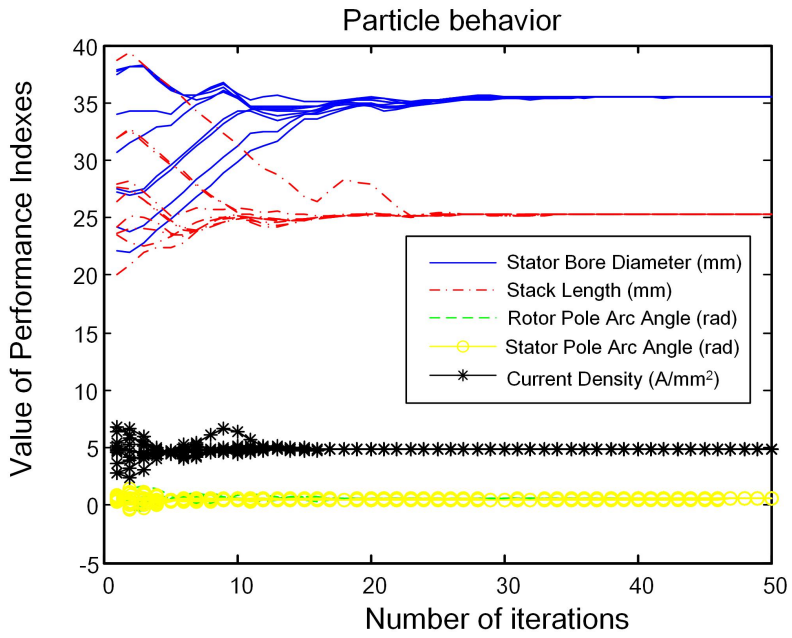

Figure 4.12: PSO particle behavior and process to convergence.

4.4.4 Optimization Results with Weighted-Sum Objective Functions

For the weighted-sum objective functions earlier, PSO is performed with a swarm of 10 particles and 50 iterations (giving 500 candidate designs) to find the optimal designs, and the coefficients in front of each performance index is slightly adjusted to emphasize different PIs for each machine design. Since the targeted machines to be optimized are small-scale and high-speed SRMs with a rated speed ranging from 10,000 rpm to 50,000 rpm, the efficiency of the optimized designs will likely not be ideal due to the excessive iron losses generated at high speeds. Figure 4.12 demonstrates the particle behavior of the PSO algorithms with five objectives, and it can be observed that all of the objectives converged after around 25 iterations, even though their initial values are given a wide latitude to vary. The entire optimization process of evaluating the 500 design candidates only takes around 10 minutes, as compared to several days on FEA.

The optimal design results of a 2.5 A-excited, 50,000 rpm 4/2 SRM are shown in Table 4.6. A 32% increase on the average torque is observed on optimal design A, which focuses

Table 4.6: Optimal 2.5A-excited, 50,000 rpm 4/2 SRM designs found by PSO.

	Original Design	Design A	Design B
$D_0\ (mm)$	77.21	55.52	57.11
$D\ (mm)$	25.00	29.20	25,41
$l_{stack}\ (mm)$	20.00	29.00	25.87
$\theta_s\ (rad)$	1.39	1.31	1.44
$\theta_r\ (rad)$	1.05	0.85	0.70
$J\ (A/mm^2)$	6.32	6.02	3.77
$T_{avg}\ (mN \cdot m)$	42.80	56.50	39.20
$Copperloss\ (W)$	2.31	4.70	2.60
$Weight\ (kg)$	0.57	0.52	0.46
$Volume\ (m^3)$	10.30×10^{-5}	7.72×10^{-5}	7.29×10^{-5}
$Output$	N/A	5.59	3.83
$Penalty$	N/A	0	0

on optimizing the average torque, and similar PSO optimizations are also executed in order to find another optimal design B with an emphasis on weight and volume. The results demonstrate significant improvements in terms of the desired PIs over the initial design.

Similar optimizations are also applied to the optimization of a 2.5A-excited, 10,000 rpm 6/4 SRM, and the results are displayed in Table 4.7. Optimal designs A and B focus on optimizing the average torque, while design C prioritizes minimizing the weight and volume. The results demonstrate design A is able to deliver a 25% increase in the average torque, while maintaining a slightly lower weight, volume and efficiency compared to the original benchmark design. In addition, design B is capable of producing 35% more torque with roughly the same weight, volume and efficiency.

Design C stresses more emphasis on weight and volume, as it can generate 92% of the average torque of the original design with only 60% of the original volume and 70% of the original weight.

The torque waveforms of the optimized designs and the original designs of 4/2 and 6/4 SRMs are compared in Figures 4.13 and 4.14. These results have verified that the optimized designs can be effectively obtained by the proposed multi-objective design method.

Table 4.7: Optimal 2.5A-excited, 10,000 rpm 6/4 SRM designs found by PSO.

	Original Design	Design A	Design B	Design C
$D_0\ (mm)$	70.00	52.68	56.44	53.43
$D\ (mm)$	30.60	28.81	31.53	28.21
$l_{stack}\ (mm)$	25.00	33.96	31.56	25.02
$\theta_s\ (deg)$	32.00	35.87	33.14	34.54
$\theta_r\ (deg)$	30.00	24.14	26.81	25.50
$J\ (A/mm^2)$	5.32	6.09	6.16	6.10
$T_{avg}\ (mN \cdot m)$	65.57	81.71	88.37	60.24
$Efficiency\ (\%)$	58.36	62.06	65.52	57.02
$Weight\ (kg)$	0.55	0.49	0.53	0.38
$Volume\ (m^3)$	10.58×10^{-5}	8.14×10^{-5}	8.69×10^{-5}	6.17×10^{-5}
$Output$	N/A	9.45	7.29	8.94
$Penalty$	N/A	0	0	0

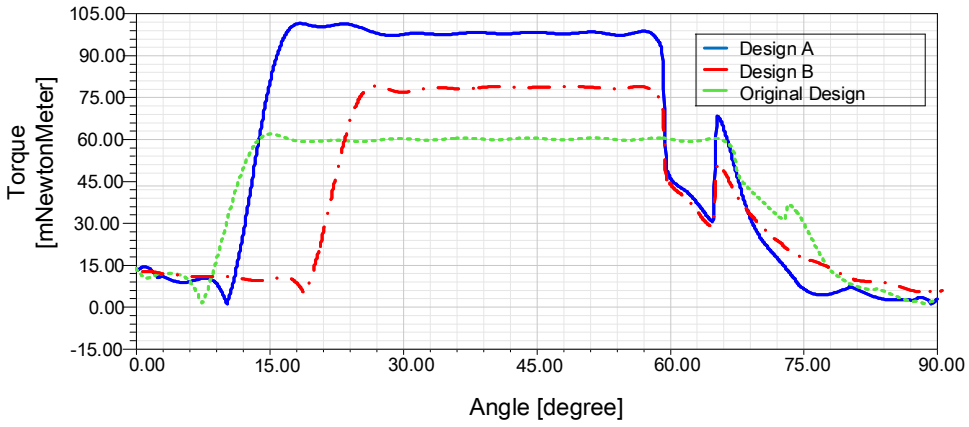

Figure 4.13: Comparison of torque profiles of the optimized designs and the benchmark 4/2 SRM.

4.4.5 Post Design Verification with FEA

In order to verify the accuracy of the optimized designs generated by the analytical model and particle swarm optimization, post design examinations on the optimized SRMs are conducted with FEA. It can be observed from Figure 4.15 that the output torque of the SRM designed by the proposed analytical design model closely aligns with the torque profile generated by the finite element analysis method.

Finally, all of the three optimized 6/4 SRM designs with weighted-sum objective functions are re-examined with FEA and the composition of the average torque and efficiency

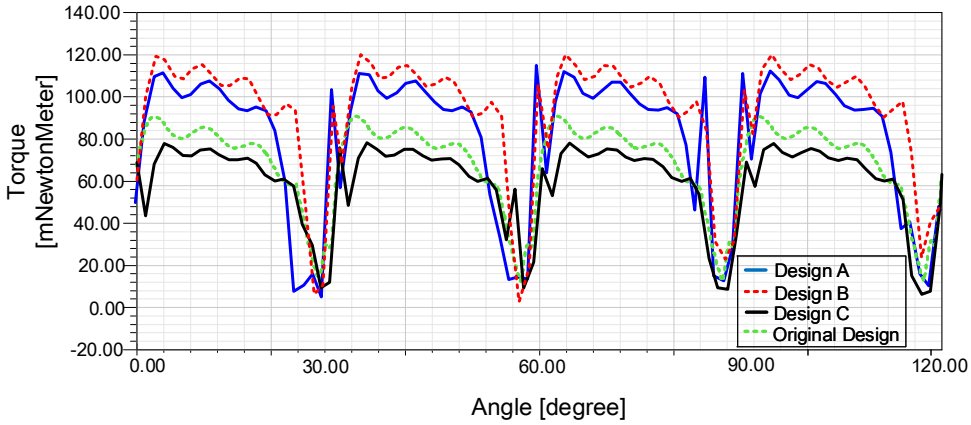

Figure 4.14: Comparison of torque profiles of the optimized designs and the benchmark 6/4 SRM.

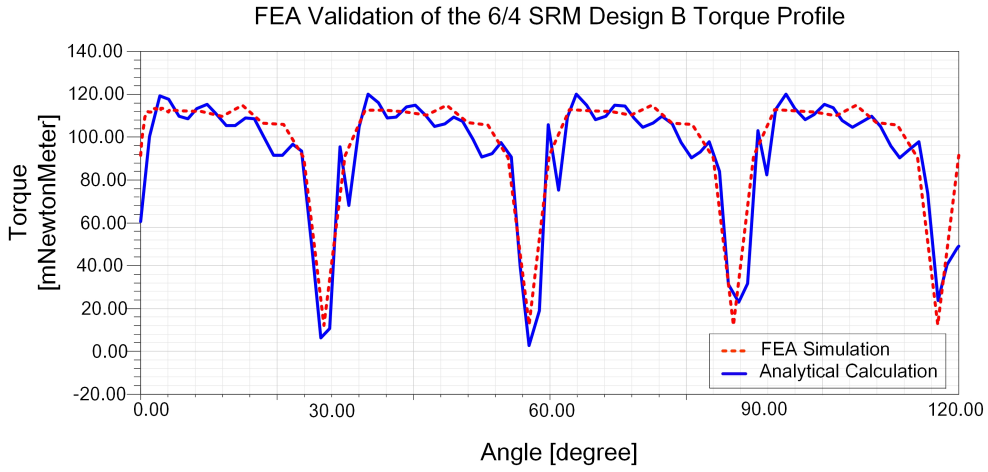

Figure 4.15: Validation of torque profile of the optimized Design B with FEA.

are summarized in Table 4.8, in which the highest discrepancy is 9.8%.

4.4.6 Improvement on Optimization Speed

A detailed analysis on the time-saving advantages of the proposed analytical design methods is presented below. Assume the automated FEA program will take one minute to auto-generate the 2D machine geometries, and the excitation and boundary conditions, as well as to assign the appropriate materials, and it will take another minute to complete executing the program, evaluating all of the performance indices, and validating if all of the

Table 4.8: Comparison of average torque and efficiency performance obtained from FEA and the proposed analytical design method.

	Average Torque ($mN \cdot m$)			Efficiency (%)		
6/4 SRM	Analytical	FEA	error	Analytical	FEA	error
Design A	81.7	83.7	2.4%	62.1	64.2	3.3%
Design B	88.4	93.1	5.0%	65.5	65.1	0.6%
Design C	60.2	63.9	5.8%	57.0	63.2	9.8%

constraints are met. It would normally take around a week to evaluate all the 4,000 designs. However, by employing these analytical models in the design process, it would only take up to one hour on an ordinary laptop. Therefore, for machine designs and optimizations that are computationally-intensive, it is both time-saving and economically sound to generate the optimized designs with the analytical methods in the first stage, and then these initial designs can be further verified and fine-tuned with FEA in the later design process.

4.5 Chapter Summary

In this chapter, a multi-objective design and optimization methods for the switched reluctance machines is presented based on rigorous analytical equations and particle swarm optimization algorithms. The proposed method is more efficient than traditional design methods as it can find an optimal design using no heuristic approaches or relying heavily on rules of thumb. An analytical benchmark model of a 6/4 SRM is presented and the results are verified by FEA simulation. PSO is performed on 4/2 and 6/4 SRMs and the optimized designs are found with respect to multiple machine performance indices, through either weighted-sum or vector objective functions. The optimal design of SRMs can be found and the approximation of the Pareto front can be completed in hours on an ordinary laptop computer, saving a significant amount of time and effort for machine designers, and the accuracy of the optimized designs are also validated by the post-design FEA examination. This method is also compatible with different machine design requirements that contribute to efficiently and accurately generating a multi-objective optimized switched reluctance

machine for targeted applications.

CHAPTER 5
INTEGRATED CURRENT PROFILE OPTIMIZATION OF SWITCHED RELUCTANCE MACHINES AND PERFORMANCE EVALUATION OF DIFFERENT OPTIMIZATION ALGORITHMS

5.1 Overview

The large torque ripple of a switched reluctance machine (SRM) caused by commutation and its nonlinear torque-producing nature is a major disadvantage for its widespread application. To mitigate this problem, current profiling for torque ripple minimization has been extensively pursued, however, most current profiling attempts are performed on existing SRM designs and thus will not guarantee a multi-objective optimized design in the entire design space for a specific application. This chapter thus proposes an active current profile optimization approach integrated into the initial multi-objective design and optimization stage of SRMs.

Due to the limitations of the enumerative and deterministic optimization algorithms, a variety of stochastic methods are widely applied in order to design and optimize an electric machine. The various stochastic optimization algorithms, in general, deal simultaneously with a set of possible solutions (populations), which allows them to find several members of the Pareto optimal set in a single “run" of the algorithm, instead of having to perform a series of separate runs as in the case of the traditional enumerate techniques. Solutions on the Pareto Optimal Front PF^* represent optimal solutions in the sense that improving the value in one dimension of the objective function vector leads to a degradation in at least one other dimension of the objective function vector. Therefore, the quality of the estimated Pareto Optimal Front PF^* will be vital to an efficient and effective design. Therefore, this chapter also compares the performance of different optimization algorithms by evaluating their

Pareto Fronts with a set of metrics, it then seeks to identify the most suitable optimization algorithm in the domain of electric machine design and optimization.

5.2 Integrated Current Profile Optimization

As presented in the earlier chapters, switched reluctance machines have a high level of reliability, are constructed in a robust manner. and are capable of good fault tolerance and efficient variable speed operation. However, one of the major drawbacks of the SRM drive system is the inherent large torque ripple caused by its double-salient structure. Specifically, the torque ripple is due to the nonlinear coupling between the phase current, rotor position, overlapping angle as well as the complete machine geometry determined in the initial design process. During the torque cycles, the torque dips are mostly caused by current commutation, while the rounded tops are due to saturation and the nonlinear torque-producing nature with single-phase excitation [38].

Therefore, it is reasonable to suggest that the most comprehensive approach for minimizing the torque ripple is to optimize the SRM stator/rotor pole arc angles as well as other geometric parameters, and at the same time perform active excitation current profile optimization. However, most of the existing approaches only seek to mitigate the torque ripple during the post-design stage, once all of the SRM geometric parameters are determined, either by performing the optimal current profiling [37–39, 74] or by applying advanced control techniques as the torque sharing functions (TSF) [40, 41]. In this way, however, the resultant phase current profiles and control algorithms are only optimal in terms of that particular, predetermined SRM design itself, while the combination of this predefined SRM geometry and its corresponding optimal current waveform or control algorithm is not necessarily the real optimal design for a specific application in the entire design space in terms of the various machine performance indices (PIs), such as the average torque, efficiency, torque ripple, weight and volume. In other words, the traditional post-design torque ripple minimization approaches in [37–41, 74] have not achieved their optimal possible levels from

a the machine design perspective, and thus there is still potential to enhance various SRM performance indices through user-defined multi-objective optimizations with an integrated active current profiling process. Therefore, the objective of this chapter is to further improve the torque dynamics of the switched reluctance machines right from the initial machine design stage.

If certain multi-objective optimization algorithms (MOOA) are selected to generate the Pareto fronts, then a large number of particles (population, or genes) are needed to adequately explore the design space and generate enough nondominated points, as shown in Figure 5.1. Although the finite element analysis based design of experiments (DOE) methods [74] are becoming increasing popular in recent years, it can be time consuming to generate the Pareto Front without setting up a high-throughput computing environment, or through employing some advanced computationally efficient FEA methods. Therefore, the proposed work on ultra-fast SRM analytical design models assisted with the integrated active current would take one minute to auto-generate the 2D machine geometries, excitations, boundary conditions and to assigning the appropriate materials, and it will take another minute to complete the execution of the program, to evaluate all the performance indices and to also validate if all the constraints are met. Under normal circumstances, it would take more than three weeks to execute. However, by employing the analytical model and the multi-objective design method proposed in this thesis, it would only take hours on an ordinary laptop computer. Therefore, for machine designs and optimizations that are computationally intensive, it is both time-saving and economically prudent to generate the optimized designs with the analytical methods in the first stage, and then these initial designs can be further verified or fine-tuned later with FEA in the later design refinement processes.

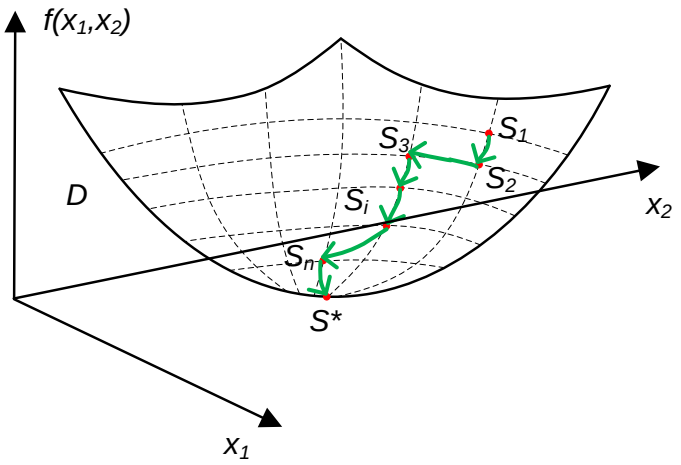

Figure 5.1: Optimization process in an entire search space.

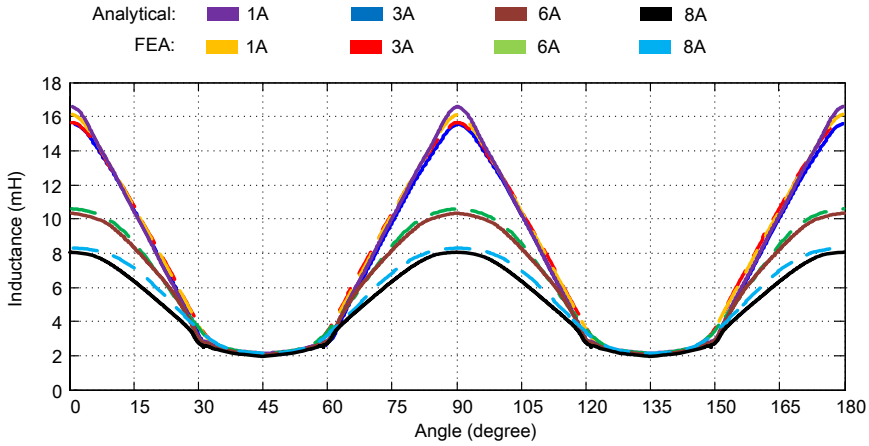

Figure 5.2: Single-phase inductance profile comparison of an 6/4 SRM obtained through the analytical model and FEA for various saturation conditions.

5.3 Analytical Model of SRMs Considering Both the Saturation and Commutation Effects

A key component in examining the effectiveness of the analytical saturation model is the function $\lambda(\theta, i)$, relating flux linkage to the different current profiles and the angular displacement. Since $\lambda(\theta, i)$ is equal to $L(\theta, i) \cdot i(t)$, the first step is to derive the analytical inductance profile $L(\theta, i)$ with a fixed single-phase current excitation, then this proposed analytical model will be verified under multi-phase excitations considering the different commutation effects as a result of the different current profiles. Moreover, different com-

mutation situations brought by different turn-on and turn-off angles will further distort the inductance profile and make it asymmetrical before and after commutation.

5.3.1 Single-Phase Inductance Profile Adjustment with Various Saturation Conditions

Based on some of the existing work on deriving the unsaturated analytical equations of SRMs based on the partial differential equations of the magnetic potentials in the polar coordinates, a magnetic circuit based on the SRM geometry is introduced to adjust the unsaturated inductance profiles with various saturation conditions and this adjustment process is briefly described as follows. Firstly, the total MMF produced by the stator windings is calculated as $2NI$, where N is the number of turns and I is the peak value of the stator current, and then the unsaturated flux linkage λ_u is calculated as $L(\theta) \cdot I$. With prior knowledge of the complete machine geometry, the flux density in the air-gap, stator/rotor pole and yoke can be easily determined, which is then interpolated into the realistic $B - H$ curve to determine the real magnetic intensity H and permeability μ in the aforementioned regions. After calculating the total reluctance R of the magnetic circuit, the saturated flux linkage λ_s can be calculated as $2NI/R$, which is compared with λ_u and the error term will be multiplied by an attenuation factor and added back to λ_u. This process of calculating λ_s and updating λ_u is repeated until the error term is smaller than a predefined threshold value.

With the aforementioned saturation adjustment method, it can be observed in Figure 5.2 that the inductance profiles obtained with the analytical models are very close to the FEA benchmark, even under highly saturated conditions.

However, it should be noted that this magnetic circuit based modification is intrinsically different from the pure magnetic circuit or the flux tube approach, which is unable to accurately determine the inductance profile of an SRM with different combination of stator and rotor poles, due to the limitations and difficulties of accurately defining the flux tubes at arbitrary rotor positions.

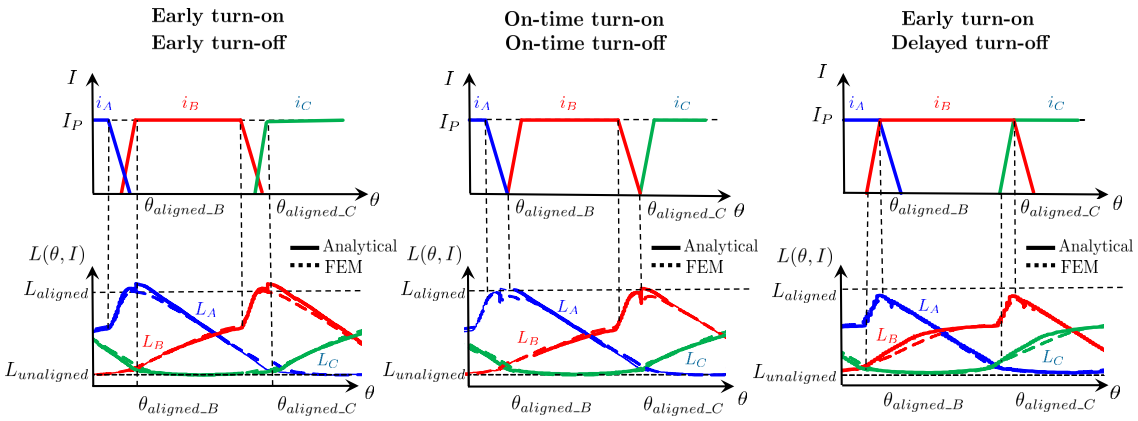

Figure 5.3: Simulation results for the network.

5.3.2 Multi-Phase Inductance Profile Adjustment with Various Commutation Conditions

Another major obstacle for optimizing the current profile during the SRM analytical design process is the complicated and distinct commutation scenarios that brings further distortions to the SRM saturated inductance profile, which later affects the torque dips. To fully illustrate this problem, the definitions of the phase current on-time turn-on and on-time turn-off are determined with respect to the aligned rotor angle of each phase $\theta_{aligned}$. Assume an SRM is rotating clockwise and is currently at the aligned position of phase B, and the term “on-time" stands for the situation as the phase B current will exactly drop to zero at the $\theta_{aligned}$ position, and the phase C current will exactly rise from zero.

For each of the multiple phases involved in the commutation process, only three possibilities exist: (i) early action (ii) on time and (iii) delayed action. By implementing the commutation matrix calculating the flux density in the stator/rotor tooth and in the yoke regions described in [144], the flux density at each part of the stator and rotor can be calculated before and after the commutation takes place. Figure 5.3 illustrates three different commutation scenarios with their corresponding current profiles, as well as the comparison of the saturated inductance profile obtained with the proposed analytical model (solid lines) and FEA (dotted lines), and the close agreement between the two verifies the accuracy of the analytical model with various commutation scenarios.

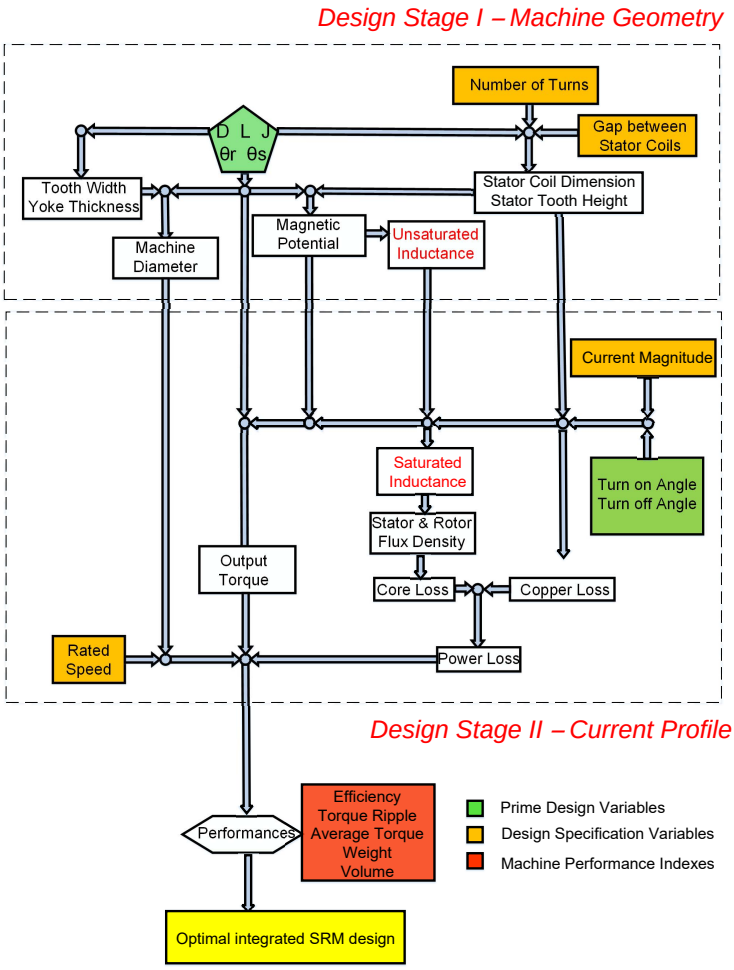

Figure 5.4: The proposed two-stage SRM multi-objective design flowchart with integrated current profile optimization.

5.4 Integrating Current Profile Optimization into the Multi-Objective Design Process

Figure 5.4 demonstrates the flowchart of the proposed two-stage SRM analytical design method with active current profile optimization. On the first stage, the initial machine geometry is designed with five prime design variables, in which D and l_{stack} are the stator bore diameter and the stack length, which are limited by the spatial limits; θ_s and θ_r are the angles of stator and rotor poles, which are constrained by the physical properties; and J is the current density in the windings, which is limited by the thermal and cooling constraints.

Then the unsaturated, single-phase inductance profile can be determined with the ultra-fast and accurate analytical models. On the second stage involving active current profiling, another two prime design variables, the turn-on angle θ_{on} and turn-off angle θ_{off} will be also determined by the multi-objective optimization algorithms to define the complete current profile. Then the three-phase saturated inductance profile can be adjusted per the specific current profiles, as some examples shown in Figure 5.3, based on the previous single phase unsaturated inductance. Only in this way can the torque profile and flux density be accurately determined with consideration of both the multi-phase commutations as well as the saturation effects. Finally, various performing indices can be calculated and evaluated by the MOOA algorithms to generate the future generations and the non-dominated points that form the Pareto front.

5.5 Multi-Objective Optimization with a Vector Cost Function

5.5.1 Vector Cost Function and Pareto Fronts

For the multi-objective optimization (MOO) formulation of the multiple performance indices, however, the weighted-sum approach only focuses the optimal search on one point rather than exploring the whole Pareto front, which is considered a more effective way of finding a host of different solutions than simply varying these weights.

A different formulation of the multi-objective optimization problem (MOOP) is to define the objective function to be a vector where each element represents a performance index. This MOOP can be formulated as:

Find the vector $\vec{x} = [l_{stack}, D, J, \theta_s, \theta_r]^T$ which satisfies the m inequality constraints

$$g_i(\vec{x}) \geq 0 \quad i = 1, 2, \ldots, m \tag{5.1}$$

and the p equality constraints

$$h(\vec{x}) = 0 \quad i = 1, 2, \ldots, p \tag{5.2}$$

to optimize the vector objective function

$$\vec{f}(\vec{x}) = [T_{ag}(\vec{x}), E(\vec{x}), Wt(\vec{x}), \text{Volume}(\vec{x})]^T \tag{5.3}$$

When sufficient points of the objective vector functions in the entire solution space have been computed, the non-dominated points can be regarded as Pareto optimal points, and it is then possible to approximate the Pareto front based on those non-dominated points. After the Pareto front is constructed, the designer can clearly identify the design trade-offs between the multiple performance indices and then select points from the Pareto front to meet specific design requirements. Those selected optimal designs are thus good candidates for further detailed designs and evaluations

5.5.2 Multi-Objective Differential Evolution (MODE) Algorithm

The vector-based multi-objective optimization algorithm (MOOA) can find an approximation of the whole Pareto-set based on several objectives. The so-called Pareto-optimal solution occurs if the improvement of one objective function simultaneously decreases at least one of the other objective functions. A parameter vector x^* is called Pareto optimal if there is no other vector x exists which simultaneously satisfy both conditions as follows

$$\begin{aligned} &f_i(x) \leq f_i(x^*) \text{ for all } \quad i \in \{1, \ldots, k\}, \\ &f_i(x) < f_i(x^*) \quad \text{for at least one } \quad i \in \{1, \ldots, k\} \end{aligned} \tag{1}$$

where k is the dimension of the multi-objective cost function $f(x)$.

Differential evolution is a very popular type of evolutionary algorithm proposed by Storn and Price [60] for optimization problems over a continuous domain, and the MODE algorithm is an extension of the Differential Evolution algorithm, to the multi-objective context. The DE algorithm has become increasingly popular and has been used in many practical cases, including the design and optimization of electric machines [50, 59, 61] mainly because it has demonstrated the ability to quickly converge and is easy to implement.

The fundamental idea of DE is to use vector differences for perturbing the vector

population. DE shares similarities with traditional evolutionary algorithms. However it does not use binary encoding as a simple genetic algorithm and it does not use a probability density function to self-adapt its parameters as an Evolution Strategy. Instead, DE performs mutations based on the distribution of the solutions in the current population. In this way, search directions and possible step sizes depend on the location of the individuals selected to calculate the mutation values.

The procedures of the MODE algorithm for the proposed SRM design and optimization problem can be as summarized by the following steps:

1. Define the solution space: define the prime design variables to be optimized as the vector $x \in \mathbb{R}$, where n is the number of prime design variables. In this case, x is defined as

$$x = [D,\ l_{stack},\ \theta_s,\ \theta_r,\ J,\ \theta_{on},\ \theta_{off}]^T$$

2. Identify the multi-objective cost function $f(x)$. For the two-dimensional multi-objective optimization problems of SRMs in the proposed research, $f(x)$ can be specified as $f(x) = [-T_d, -T_{ripple}]^T$ or $[-T_d, 1 - eff]^T$. For three-dimensional optimization problems, $f(x) = [-T_d, 1 - eff, -T_{ripple}]^T$, where T_d is the torque density, T_{ripple} is the torque ripple and eff denotes efficiency.

3. Specify the population size M and the lower and upper bounds of x as x_u and x_l, as well as the scaling factor and the crossover probability.

4. Initialization: calculate the initial values of the seven prime design variables for the first generation of population as

$$x_{j,1} = rand([1, N]) \cdot (x_u - x_l) + x_l$$

where $rand([1, N])$ is a $1 \times N$ vector with all elements following the standard uniform distribution on the open interval (0,1), j represents the j^{th} vector among the M prime design variable vectors. The subscript $g = 1$ denotes the first generation.

5. Mutation: starting from the first generation, three vectors of machine prime design variables $x_{1,g}$, $x_{2,g}$ and $x_{3,g}$ will be randomly chosen to generate a mutant vector $v_{i,g}$ by adding a scaled vector difference of $x_{1,g}$ and $x_{2,g}$ to $x_{3,g}$ as

$$v_{j,g} = F \cdot (x_{1,g} - x_{2,g}) + x_{3,g}$$

in which F is the user-defined scaling factor and its value is within the open interval of (0,1).

6. Crossover: the input vector of the machine's prime design variables to be accessed is a combination of elements from the mutant vector $v_{j,g}$ and the original vector $x_{j,g}$, with a user-defined crossover probability of $Cr \in (0, 1)$ as

$$v_{j,g} = F \cdot (x_{r1,g} - x_{r2,g}) + x_{r3,g}$$

$$u_{j,g} = [u_{j,1,g} \;\; u_{j,1,g} \;\; \ldots \;\; u_{j,i,g} \;\; \ldots \;\; u_{j,n,g}]^T$$

$$u_{j,i,g} = \begin{cases} v_{j,i,g} & if \; (rand\,(0,1) \leq C_r) \\ x_{j,i,g} & otherwise \end{cases}$$

where i demotes the i^{th} element in the vector of design variables.

7. Selection: with the predefined multi-objective cost function $f(x)$, the performance indices of each machine design candidate can be evaluated and compared to generate the set of nondominated points x^*. Then the next generation of design variable vectors are determined as

$$x_{j,g+1} = \begin{cases} u_{j,g} & if \; f(u_{j,g}) \leq f(x_{j,g}) \\ x_{j,g} & otherwise \end{cases}$$

Therefore, the design performance improves with each generation.

Steps 5) to 7) are repeated until the pre-specified termination criterion is satisfied, or the iterative optimization process ends.

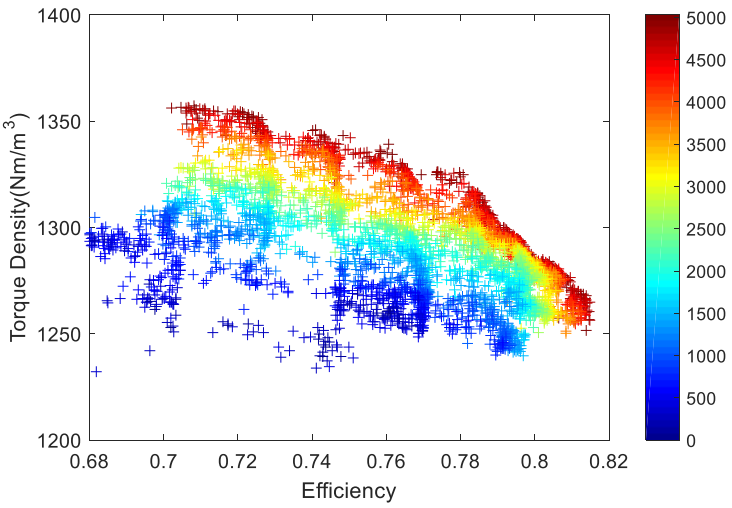

Figure 5.5: The evolution of the optimization process and the Pareto front of the SRM multi-objective design.

5.6 Integrated Optimization Results with Vector-Based Objective Functions

To initialize the multi-objective design and optimization process, seven parameters are selected as the independent design variables, as shown in Figure 5.4. For reference, the benchmark SRM is a small-scaled, high speed motor with a 6/4 typology, rated for 100 W at 10,000 r/min. The SRMs to be optimized are assumed to be current-fed with a peak value of 3A and a hysteresis tracking of the command current. For ultra-fast calculations, the machine performance indices will be estimated using the rigorous analytical models proposed, with considerations of both the saturation and the various commutation effects presented in Figure 5.2 and Figure 5.3. Other computational methods, such as FEA or simplified FEA, can also be employed, but would require more computational time. The combinations of 2-D objectives in this work involve maximizing the torque density while maximizing the motor efficiency, maximizing the torque density while minimizing the torque ripple, and maximizing efficiency while minimizing the torque ripple. During the design and optimization process, the air-gap length and the number of turns in the stator windings are fixed. Other machine design variables, such as the winding AWG size and geometry, were calculated on that basis. To better illustrate the progress of the Pareto front

over evolving generations, an optimization process consisting of 5,000 design candidates was carried out with the proposed SRM optimization algorithm, and the results are shown in Figure 5.5. The number of function evaluations, i.e., the sequence of the candidate designs, is color coded to provide an indication of the gradual convergence of the design space to the Pareto front vicinity. Figure 5.5 also determines the appropriate range of the torque density - efficiency profile and demonstrates its Pareto front baseline is a strongly nonlinear function.

All of the nondominated points form an approximation of the Pareto set of the vector optimization problem. A steady improvement of the Pareto front approximation is expected with the evolution of the generations in the multi-objective algorithms. It is anticipated that the multi-objective optimization algorithms will generate all of the nondominated solutions on the Pareto front, which provide a trade-off between the multiple performance indices that may mutually conflict. For example, the output torque density and weight represent vectors of two objectives, and maximizing one objective such as efficiency usually does not optimize another such as in the case with the torque ripple.

For the purpose of preforming comprehensive comparisons, the MODE algorithm has been applied in the following combinations: 1) 100 populations (generations), 50 iterations; 2) 40 populations, 25 iterations; and 3) 10 populations, 20 iterations, which lead to a number of 5000; 1000; and 200 design candidates, respectively. The Pareto fronts generated by torque density vs. efficiency; torque density vs. torque ripple and torque ripple vs. efficiency are demonstrated in Figure 6. It can be observed that with the increase of the evaluated design candidates, the Pareto fronts tend to be explored further, which leads to better designs each time.

Design variables with relative performance indices of selected optimized solutions found with the two objectives of maximal torque density and minimal torque ripple are listed in Table I. It can be observed that the optimized 6/4 SRM can reduce the torque ripple to 44% through active current profiling with the optimized machine geometry, while the torque ripple can be as large as 100% without introducing any commutation. It should be

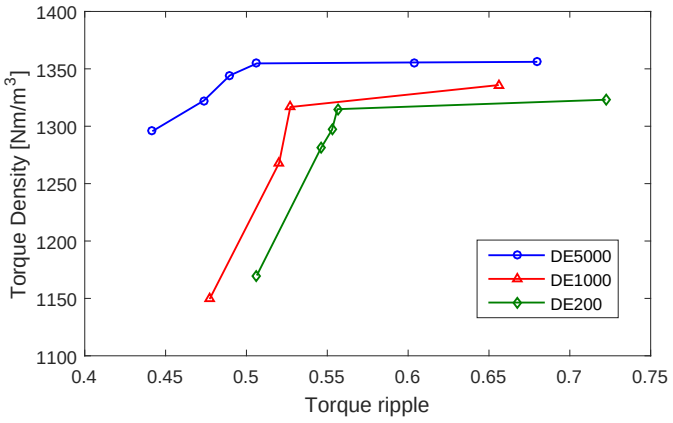

(a)

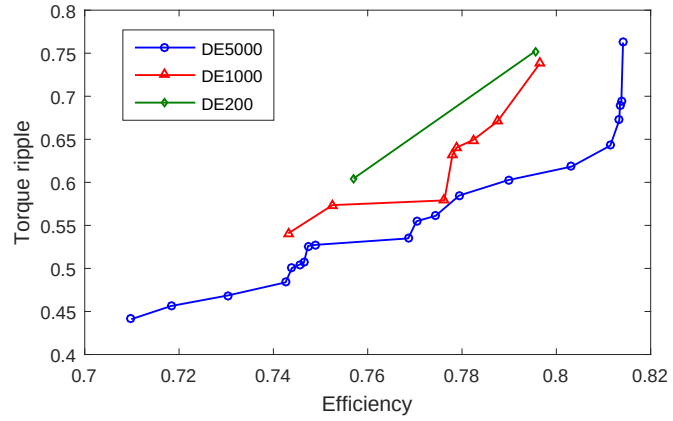

(b)

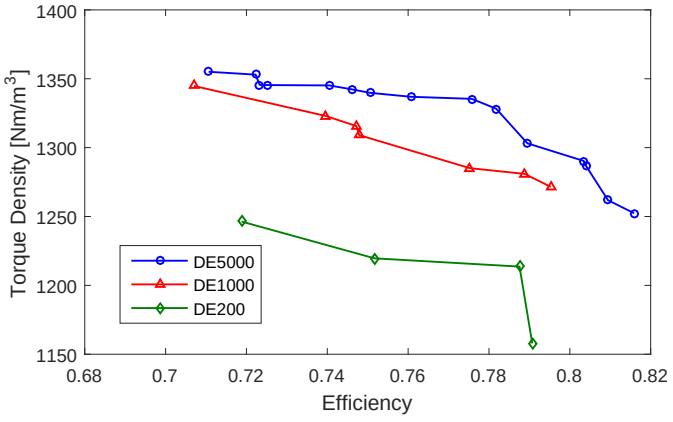

(c)

Figure 5.6: Comparison of the Pareto fronts with 200, 1,000 and 5,000 machine design candidates for (a) torque density vs. efficiency; (b) torque density vs. torque ripple and (c) torque ripple vs. efficiency

noted that these torque ripple values are based on the initial trapezoidal current waveform as demonstrated in Figure 5.3, and they can be further reduced with more advanced control strategies, such as the torque sharing function or by introducing additional harmonics on these trapezoidal curves. Moreover, the torque ripple minimization effect will also be more promising on SRMs with a large number of stator and rotor poles, such as the 12/10 topology.

5.7 Performance Evaluations and Comparisons of Multi-Objective Optimization Algorithms for the Analytical Design of Switched Reluctance Machines

The multi-objective optimization algorithms can be generally classified into three categories: enumerative, deterministic, and stochastic (random). Although the enumerative schemes are perhaps the simplest multi-objective search algorithm, as it only requires some finite, pre-defined search space, in which each possible solution is evaluated. However, it is easily seen that this technique is very inefficient or even infeasible over a huge search space. Deterministic algorithms attempt this by incorporating more problem domain knowledge, and many of them are considered graph/tree search algorithms. However, many electric machine multi-objective optimization problems are high-dimensional involving multi-physics modeling, and the derivative may not exist for many analytical models due to the discontinuity of certain design parameters, such as the stator winding gauge size and the number of turns in a stator slot.

Therefore, because of the aforementioned problems with the enumerative and deterministic optimization search algorithms, a variety of stochastic methods were developed as alternative approaches for electric machine design and optimization problems. The various stochastic optimization algorithms, in general, require a function assigning fitness values to possible solutions. In addition, they deal simultaneously with a set of possible solutions (populations), which allows them to find several members of the Pareto optimal set in a single “run" of the algorithm, instead of having to perform a series of separate runs as in the

case of the traditional enumerate techniques. A multi-objective optimization process' defining characteristic is the set of multiple objectives being simultaneously optimized. Solutions on the Pareto Optimal Front PF^* represent optimal solutions in the sense that improving the value in one dimension of the objective function vector leads to a degradation in at least one other dimension of the objective function vector. Once the Pareto front of an electric machine optimization problem has been found, the decision maker is presented the set of Pareto optimal solutions that have been generated, and they must choose certain points from this set based on some non-modelled human preferences. Thus, the final multi-objective optimization problem solution results from both the optimization and the decision-making process.

Because of the significance of the Pareto front, most machine design problems require efficient approaches that can at least approximate the Pareto Front within a reasonable amount of time. However, obtaining the exact Pareto front of an arbitrary electric machine optimization problem is usually difficult, and some algorithms cannot even guarantee optimal solutions. Nevertheless, reasonably accurate approximations of PF^* are generally acceptable within a limited computational time.

A good algorithm should be able to find the optimal solutions ocer a diverse domain and a feature a fast convergence speed, and the quality of the algorithms are determined by some systematic testing procedures. The quality of algorithms usually falls into two performance categories, efficiency and effectiveness. The efficiency is a measure of the computational effort required to obtain solutions. For example, this should include CPU time and the number of required evaluations/iterations. Effectiveness includes robustness (measuring how well the code recovers from improper input), convergence, accuracy, scalability and ease of use.

5.7.1 Metrics for Evaluation the Pareto Front

It is generally difficult to measure how well a set of prototype vectors compares to another, for example, comparing PF_{true} to PF_{known}. One could wish to determine how far apart the two sets are and how well they conform in shape. Thus evaluating the effectiveness of well-engineered multi-objective optimization algorithms require experimental assessment by executing numerous runs, and by applying a statistical analysis on the results. Measuring this nonlinear performance is quantified through the use of metrics. Five quality indicators listed below are employed in this work for evaluating multi-objective optimization algorithms' effectiveness in approximating the Pareto front sets.

1. Contribution Ratio (CR): The contribution ratio metric reports the number of vectors in PF_{known} that are in a close vicinity to the real Pareto front PF_{true}. If $CR = 1$, the PF_{known} is the same as PF_{true}, but when $CR = 0$, this indicates that none of the points in PF_{known} are in PF_{true}, and a higher CR is better.

2. Generational Distance (GD): this metric reports the average minimum Euclidean distance from all of the vectors in PF_{known} to any vector in PF_{true}. This is a type of convergence metric and any algorithm with a smaller GD has a better convergence to the real Pareto front PF_{true}.

3. Normalized Hyperarea/Hypervolume (HA, HR): The hyperarea (hypervolume) and hyperarea ratio metric relate to the area of the coverage of PF_{known} with respect to the objective space for a two-objective MOP. This equates to the summation of all of the rectangular area formed by the two objectives of any vector on the Pareto front PF_{known}.

4. Spacing (S): the spacing numerically describes the spread of the vectors in PF_{known} by measuring the distance variance of neighboring vectors. When $S = 0$, all of the vectors are evenly apart. The even spacing of the vectors during the searching

Table 5.1: List of Popular Quality Metrics Accessing the Performance of MOOA Algorithms.

Primary quality metrics	Mathematical definitions
Contribution Factor	$\frac{\lvert PF_{\text{known}}\rvert}{\lvert PF_{\text{true}}\rvert}$
Generational Distance	$\frac{\left(\sum_{i=1}^{n} d_i^p\right)^{1/p}}{\lvert PF_{\text{true}}\rvert}$
Hyperarea	$\frac{\{\bigcup \text{area}_i \mid vec \in PF_{known}\}}{\lvert PF_{known}\rvert}$
Spacing	$\sqrt{\frac{1}{\lvert PF_{known}-1\rvert}\sum_{i=1}^{\lvert PF_{\text{known}}\rvert}\left(\overline{d}-d_i\right)^2}$
Maximum Pareto Front Error	$\max_j\left\{\left\{\min_i\left(\sum_{k=1}^{m}\left\lvert f_k^i(x)-f_k^j(x)\right\rvert^p\right)^{1/p}\right\}\right\}$

process is important for ensuring the quality and diversity of the Pareto front vectors, since most experimental MOOAs perform certain types of fitness sharing (niching or crowding) in an attempt to spread all the population in the current round of iteration evenly along the known front.

5. Maximum Pareto Front Error (ME): this metric measures the largest minimum distance between each vector in PF_{known} and the corresponding closest vector in PF_{true}. A resultant of 0 indicates $PF_{known} \subseteq PF_{true}$, any other resultant value indicates at least one vector of PF_{known} is not in PF_{true}.

In summary, all of the quality indicators are listed in Table 5.1 with their respective mathematical definitions, where $|A|$ denotes the number of vectors x in space A, and $xi \in \mathbb{R}^m$ where m is the number of objectives $f(x)$ defined for any optimization problems.

5.7.2 Evaluation Results

The design and optimization process follows Figure 5.4. For the purpose of preforming comprehensive comparison, multi-objective NSGA-II, DE and PSO optimization were applied in the following combinations: 1) 100 populations (generations), 50 iterations; 2) 40 populations, 25 iterations; and 3) 10 populations, 20 iterations, which lead to a number of 5000; 1000; and 200 design candidates, respectively.

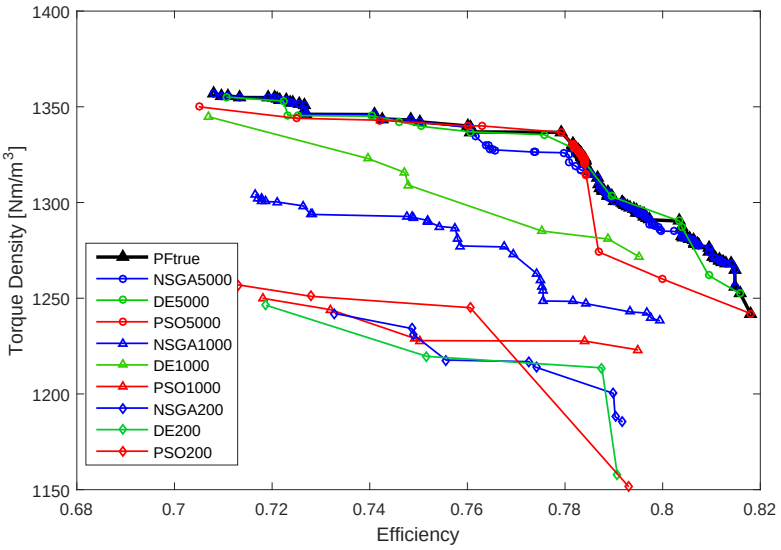

Figure 5.7: The evolution of the optimization process and the Pareto front of the SRM multi-objective design.

As shown in Figure 5.7, the union set of all the Pareto fronts generated by the 9 cases were assumed to be the real Pareto front PF_{true}, and it is compared with the Pareto front determined by the nine cases respectively. It can be observed that with the increase of evaluated design candidates, the Pareto fronts of the three algorithms tend to converge on the same trajectory, and DE has a distinct advantage over the other two algorithms when there are only 2000 design candidates evaluated. Significant discrepancies can be observed for the cases with 200 design candidates for all three methods.

Table 5.1 comprehensively demonstrates the five metrics applied in this work to produce a quantitative comparison of these Pareto fronts. It can be observed in Figure 5.8(a) that NSGA-II algorithm has the highest contribution factor to the real Pareto front, with DE coming next, while the PSO has the lowest contribution to the front. When there were only 1,000 or 200 design candidates evaluated, all three algorithms failed to contribute to constituting the real Pareto front, indicating that the algorithms are still evolving overtime and keep pushing and updating their Pareto fronts.

Both the generational distance and the maximum Pareto front error represents the

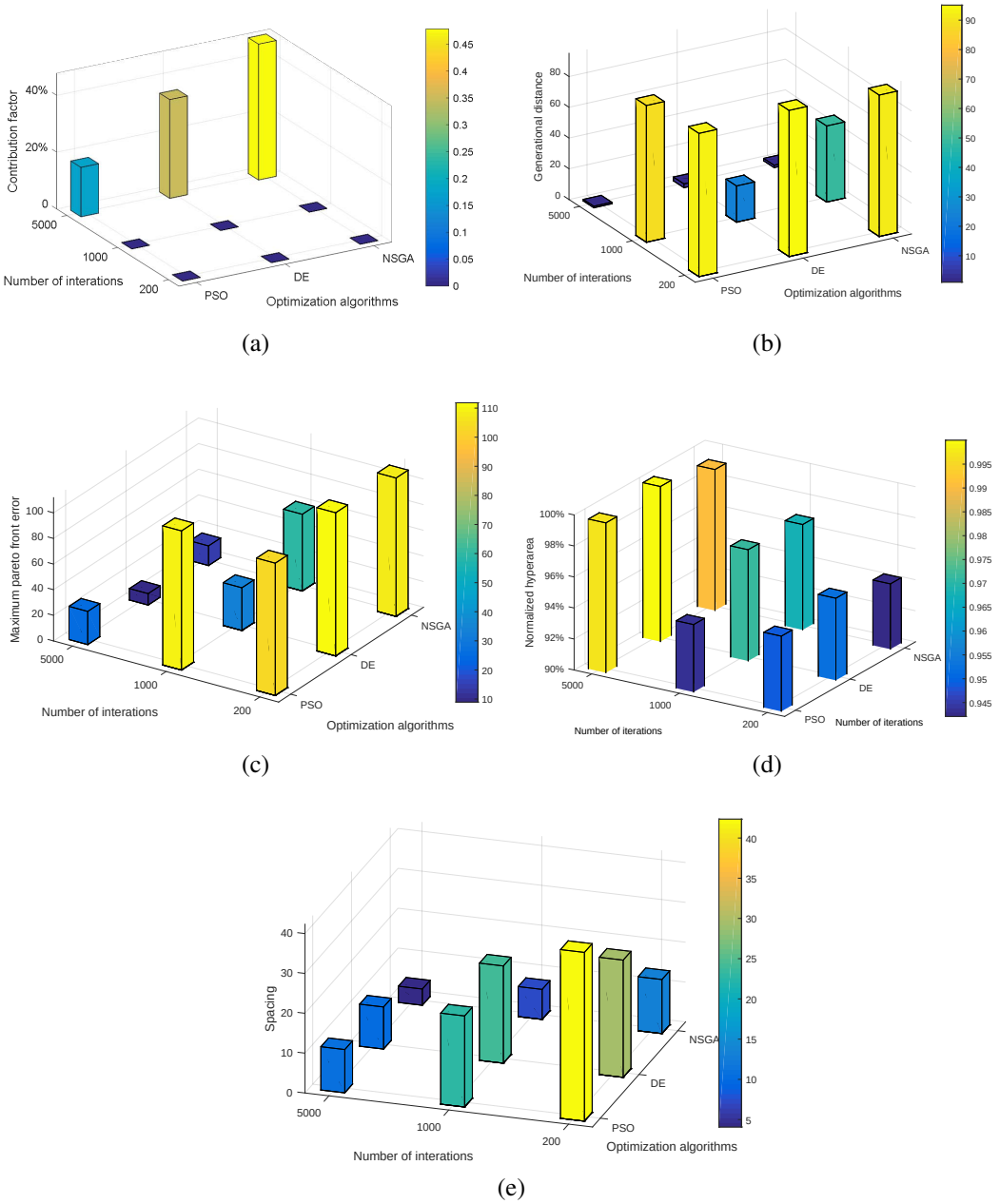

Figure 5.8: Comparison of the quality indicators for the NSGA-II, DE, and PSO optimal search with 5000, 1000 and 200 design candidates. (a) Contribution factor. (b) Generational distance. (c) Maximum Pareto front error. (d) Normalized hyperarea. (e) Spacing

"distance" from the current Pareto front PF_{known} to the real Pareto front PF_{true}, and a smaller distance indicates the algorithm is able to better conform to the real front. To indicate an equal attention being paid to the power density and efficiency, both of the two

objectives are normalized to the same order of magnitude. Both Figure 5.8(b) and (c) demonstrate DE has smaller errors or distances when compared to the other two algorithms, and this is particularly evident for the case employing the “medium" number of 1000 candidate designs. It should also be noted that, after 1000 designs, DE has converged to the close vicinity to the “correct" Pareto front but GA and PSO did not.

For a bi-objective problem, the hyperarea is equal to the area from the objective space that is dominated by a certain Pareto front, and a larger hyperarea indicates a better Pareto front. The hyperarea values reported in Figure 5.8(d) are normalized with respect to the Pareto front from the union set. The results from Figure 5.8(d) show that, for this benchmark problem, the performances of NSGA-II, PSO and DE are comparable if the optimization study is based on a very small number of only 200 candidate designs. However, at such a low number of samples, all the Pareto fronts are substantially different from the real Pareto front PF_{true}. When more candidate designs are included in the study, DE is superior.

Finally, Figure 5.8(e) represents spacing, which is how well the points on the Pareto front are evenly spaced apart. The results indicate NSGA-II has a better spacing metric when compared to the other two algorithms, as it has built-in niching comparison schemes. If both of the solutions belong to the same front, then the solution which is located in the less crowded region is preferred, thus making the points more evenly distributed along the Pareto front.

5.8 An Efficient Multi-Objective Bayesian Algorithm for SRM Optimization

As presented in the earlier section, a number of stochastic multi-objective optimization algorithms have been applied in order to better explore the solution space and to find a set of non-dominated designs that approximate the Pareto front of design objectives, such as the Non-Dominated Sorting Genetic Algorithm (NSGA-II), the multi-objective differential evolutionary algorithm (MODE), and the multi-objective particle swarm optimization (MOPSO) algorithm. Compared to the deterministic methods that require gradient calculation, the

stochastic nature of these algorithms makes themselves “gradient free“ but will sometimes stick at the local optimum. In addition, they also suffer from relatively low convergence rates if the hyper-parameters are not properly tuned, as well as slow computational speeds if there are hundreds or thousands of genes/particles involved in for each round of iteration.

Compared to the population-based stochastic optimization algorithms used in electric machine optimization, the Bayesian optimization framework is a powerful optimization tool that is able to take advantage of the information from the prior optimization history and will ultimately make an optimal search more efficient. Specifically, Bayesian optimization algorithms have been widely applied in optimization problems, especially in the field of machine learning and computer vision where evaluations of the objective functions are costly or the derivatives are often not accessible. Because of their similarities to electrical machine design and optimization problems, this section seeks to apply an expected-improvement-based Bayesian optimization approach for the automated analytical design of switched reluctance machines, and the expected improvement is selected as the acquisition function to balance exploration and exploitation throughout the optimization process. This section also seeks to find out if the Bayesian optimization method would be more effective and efficient in terms of finding nondominated design candidates in a small number of iterations, when compared to the popular stochastic algorithms.

As a brief literature survey, Bayesian optimization based on probabilistic learning [150–154] has emerged as a very powerful solution for multi-objective design problems in some domains. In the power industry, it has been successfully applied in optimizing the electrical equipment configuration problems in a power plant [155], Maximum Power Point Tracking (MPPT) of photovoltaic power plants [156], fault diagnostics and classification of nuclear power plant thermocouples [157], power electronics components in shipboard systems [158], probabilistic classification and identification of plugged-in electric loads [159], altitude optimization of airborne wind energy systems [160], as well as the design of analog circuits [161]. Other applications employing Bayesian optimization includes the optimal design of

Archimedes screw turbines [162] and deep neural network hardware accelerators [163].

However, the most prominent application of Bayesian optimization lies in the field of machine learning and computer vision when training the hyper-parameters of deep neural networks [164–168], which determines a stochastic observable classification or object detection accuracy [165] on a particular data set such as the ImageNet. Because the Bayesian optimization framework is very data efficient, it is particularly useful in situations where evaluations of the objective functions are costly or the derivatives are not accessible. In these situations, Bayesian optimization is able to take advantage of the full information provided by the history of the optimization to make an optimal search highly efficient [168].

5.8.1 Expected-Improvement based Multi-Objective Bayesian Optimization Algorithm

This subsection will a new perspective on applying the multi-objective Bayesian optimization algorithm (MOBOA) on electric machine design and optimization problems for the first time. Specifically, in a classical BOA, Gaussian Processes (GP) are trained to model the employed objective function [169, 170], which is refined incrementally via Bayesian posterior updating when new machine design candidates are generated. In turn, the developed GP model of the objective function is used to determine the next round of input vectors to evaluate. The proposed approach will be tested on a switched reluctance machine benchmark study, and compared with the widely-employed NSGA-II algorithm.

Formulation of Bayesian Optimization

Mathematically, the optimization problem involved in finding a global maximizer (or minimizer) of an objective function f is

$$\mathbf{x}^{\star} = \arg\max_{\mathbf{x}\in\mathcal{X}} f(\mathbf{x}) \tag{1}$$

where $\mathcal{X}$ is the design space of interest. Fundamentally, Bayesian optimization algorithm (BOA) is a sequential model-based approach to solving problem (1). In general, the Gaussian process is used to model possible objective functions, and this model is sequentially refined

Algorithm 1 Bayesian Optimization Algorithm (BOA)

1: **Require**: the design parameter initialization $\mathbf{x}_1$, the concurrent training cycle *n*, the total number of training cycles *N*.
2: Construct a BP probabilistic surrogate model.
3: **for** $n = 1, 2, ..., N$ **do**
4: Select a new $\mathbf{x}_{n+1}$ that optimizes the acquisition function $\mathbf{x}_{n+1} = \arg\max_{\mathbf{x}} \alpha(\mathbf{x}; \mathcal{D}_n)$.
5: Query the objective function to obtain $y_{n+1} = f(\mathbf{x}_n)$.
6: Augment the data set $D_{n+1} = D_n, (\mathbf{x_{n+1}}, \mathbf{y_{n+1}})$.
7: Update the statistical model.
8: **end for**
9: **return** best $f(x)$ recorded during iterations

as new data (the locations $\mathbf{x_n}$ where f has been evaluated, and the corresponding outputs $f(\mathbf{x_n})$) becomes available via Bayesian posterior updating. Equipped with this probabilistic model, we can sequentially induce an acquisition function $\alpha_n :\mapsto \mathbb{R}$ that leverages the uncertainty in the posterior to guide future exploration. Intuitively, the acquisition function evaluates the utility of candidate points for the next evaluation of f; therefore, $\mathbf{x_{n+1}}$ is selected by maximizing α_n, where the index n indicates the current sequence of iteration. After N queries, the algorithm makes a final recommendation $\mathbf{x}_N$, which represents the BOA's best estimate of the optimizer.

The overall Bayesian optimization approach can be summarized in Algorithm 1 and the details of the Gaussian process model and the acquisition function will be discussed in the following sections.

The Gaussian Process Model

The motivation of using the Gaussian Process to model objective functions is that its model prediction and model uncertainty in the posterior have closed forms. A Gaussian process model $Y(\mathbf{x})$ is characterized by its prior mean function $\mu_0 : \mathcal{X} \mapsto \mathbb{R}$ and its

positive-definite kernel, or covariance function $\mathbf{k} : \mathcal{X} \times \mathcal{X} \mapsto \mathbb{R}$ as [170]:

$$\begin{aligned} \mu_0 &:= \mathbb{E}(Y(\mathbf{x})), \mathbf{x} \in \mathcal{X} \\ k(\mathbf{x}, \mathbf{x}') &:= \textit{Cov}(Y(\mathbf{x}), Y(\mathbf{x}')), (\mathbf{x}, \mathbf{x}') \in \mathcal{X}^2 \end{aligned} \tag{2}$$

In particular, $Y(\mathbf{x}_{1:n}) \sim N(\mu(\mathbf{x}_{1:n}), k(\mathbf{x}_{1:n}, \mathbf{x}_{1:n}))$, where $k(\mathbf{x}_{1:n}, \mathbf{x}_{1:n})$ is the matrix of $k(\mathbf{x}_i, \mathbf{x}_j), 1 \leq i, j \leq n$, that we write in short as $Y \sim GP(\mu_0, k)$.

The key advantage of GPs is that for any new point $\mathbf{x} \in \mathcal{X}$, the joint distribution of $Y(\mathbf{x}_{1:n})$ and $Y(\mathbf{x})$ can be simply given by:

$$\begin{pmatrix} Y(\mathbf{x}_{1:n}) \\ Y(\mathbf{x}) \end{pmatrix} \sim \mathcal{N}\left(\begin{pmatrix} m(\mathbf{x}_{1:n}) \\ m(\mathbf{x}) \end{pmatrix}, \begin{pmatrix} k(\mathbf{x}_{1:n}, \mathbf{x}_{1:n}) & k(\mathbf{x}_{1:n}, \mathbf{x}) \\ k(\mathbf{x}, \mathbf{x}_{1:n}) & k(\mathbf{x}, \mathbf{x}) \end{pmatrix} \right) \tag{3}$$

which provides tractable analytical expressions for marginal and conditional distributions. In particular, conditioning the GP on this new point $\mathbf{x}$ results in another Gaussian process with

$$\begin{aligned} \mu_n(\mathbf{x}) &= \mu_0(\mathbf{x}) + \mathbf{k}(\mathbf{x})^T (\mathbf{K} + \sigma^2 \mathbf{I})^{-1} (\mathbf{y}_{1:n} - m(\mathbf{x}_{1:n})) \\ k_n(\mathbf{x}, \mathbf{x}') &= k(\mathbf{x}, \mathbf{x}) - \mathbf{k}(\mathbf{x})^T (\mathbf{K} + \sigma^2 \mathbf{I})^{-1} \mathbf{k}(\mathbf{x}') \end{aligned} \tag{4}$$

where $k(\mathbf{x}) := (k(\mathbf{x}, \mathbf{x}_1), ..., k(\mathbf{x}, \mathbf{x}_n))^T$ and $\mathbf{K} := (k(\mathbf{x}_i, \mathbf{x}_j))_{1 \leq i,j \leq n}$ are the vector of covariances of $Y(\mathbf{x})$ and the covariance matrix of $Y(\mathbf{x}_{1:n})$, respectively. This gives the probabilistic prediction of this new point $\mathbf{x}$.

The mean $\mu_n(\mathbf{x})$ can be viewed as the predicted value of the objective function at this point, while the variance $k_n(\mathbf{x}, \mathbf{x}')$ can be viewed as the confidence of the prediction. In this way, this GP model is refined incrementally every time when new data sets become available, and this model is then used to predict the objective functions of other unexplored locations to compute the values of the acquisition functions, and ultimately determine the next round of input vectors to evaluate.

The choice between the covariance and mean function is inevitably of utmost importance as they dictate the properties of the corresponding GP. To illustrate the sample paths of GPs with different combinations of mean and covariance functions, Figure. 5.9(a) presents three waveforms. The red dashed line shows the quadratic trend with a Matérn $5/2$ kernel

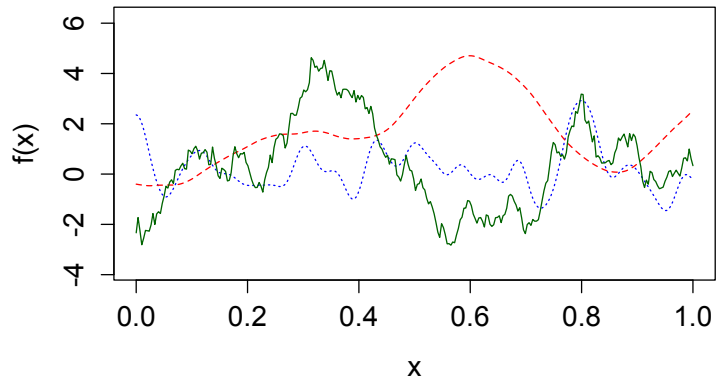

(a)

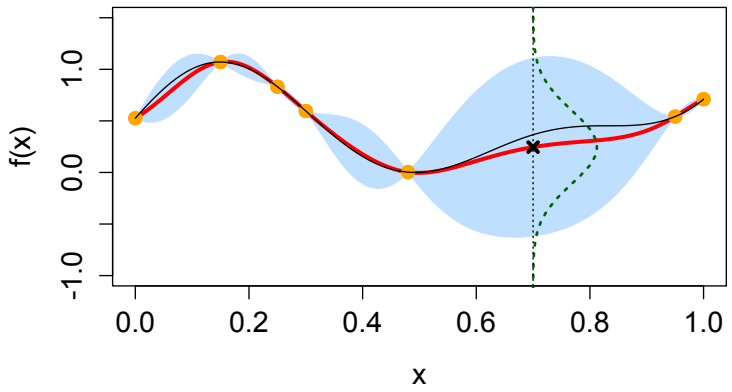

(b)

Figure 5.9: (a) Three simulated sample paths of GPs with different mean and covariance functions (red dotted–quadratic trend with a Matérn $5/2$ kernel, green solid–constant trend with an exponential kernel, blue dotted–constant trend with a periodic Gaussian kernel) and (b) illustration of the principle of GP models predicting the objective function values and the prediction intervals (in blue) showing probable improvement partitioned by the data points.

originated from the Matérn covariance function, the green solid line shows the constant trend with an exponential kernel while the blue dotted line demonstrates the constant trend with a periodic Gaussian kernel.

Figure 5.9(b) demonstrates a simple example of the objective function prediction process of a GP model using a constant trend with a Matérn $5/2$ kernel in the 2-D plane, the true underlying objective function is in black, while the predicted values are plotted in red. The blue regions are the prediction intervals showing probable improvement partitioned by seven data points (observations) represented as orange dots. The maximum observation is at $\mathbf{x}^{\star} = 0.7$, and the Gaussian distribution of which is added as a dashed line. The shaded area in the superimposed Gaussian above the dashed line can be used as a measure of improvement, $I(x)$. Figure 1 (b) also suggests the model predicts almost no possibility of improvement at the observation points of either $\mathbf{x} < 0.4$ or $\mathbf{x} > 0.8$, while selecting the orange dot around $\mathbf{x} = 0.5$ as more likely to obtain the largest improvement. In addition, it can be easily observed that the accuracy of the GP model highly depends on the number of observation points, and the incremental refinement can be achieved as each new data point becomes available.

For simplicity, this section employs the constant mean function and the squared exponential covariance function.

Acquisition Functions with Expected-Improvement-Based Policies

In Bayesian optimization, a popular choice of acquisition function is based on the improvement function, denoted by $I(x)$, which can be used to measure the expected improvement (EI). A formal definition of an improvement function I can be written as [170]:

$$I(\mathbf{x}, v, \theta) := (v - \tau)\mathbb{I}(v > \tau). \tag{5}$$

Note that $I > 0$ only if there is an improvement. Since the random variable v is normally distributed, the acquisition function based on expected-improvement can be computed

analytically as:

$$\alpha_{\mathrm{EI}}(\mathbf{x};\mathcal{D}_n) := \mathbb{E}\left[I(\mathbf{x},v,\theta)\right] = \left(\mu_n(\mathbf{x}) - \tau\right)\Phi\left(\frac{\mu_n(\mathbf{x}) - \tau}{\sigma_n(\mathbf{x})}\right) + \sigma_n(\mathbf{x})\phi\left(\frac{\mu_n(\mathbf{x}) - \tau}{\sigma_n(\mathbf{x})}\right) \tag{6}$$

when $\alpha_n > 0$ and vanishes otherwise. Φ is the standard normal probability cumulative function and ϕ is the standard normal probability density function. Although the target objective value (i.e., the best reachable objective value) is often unknown during the optimization process, in practice τ is adaptively set to the best observed value $y^+ = max_{i=1:n}y_i.$, and the next data point will be generated by maximizing the improvement enabled by this acquisition function. Another emerging type of acquisition function is based on predictive entropy search [171] that offers an even better level of performance when compared to the expected-improvement based functions at many occasions, while this predictive entropy search is still a research frontier for scientists and engineers in the field of computer science or optimization.

Unfortunately, at this moment it is also often unclear how to handle the trade-offs between the exploration and exploitation for BOAs in the acquisition function, as a significant amound of exploration, and many iterations can go by without improvement. Too much exploitation can lead to local maximization.

5.8.2 Multi-Objective Extension of Bayesian Optimization Algorithm

In this section, the basic Bayesian optimization algorithm is extended in order to deal with the multi-objective problems by manipulating the weighted sum aggregation as the optimization kernel, as shown in Algorithm 2. Starting with the initial samples, at each iteration, a normalized random weight vector ω with a dimension of the number of objectives m will be generated. By maximizing the expected improvement, a new data point can be determined, which is then added to the training set to further maximize the objective function via Bayesian posterior updating. Note that in general we would not have an

Algorithm 2 Multi-Objective Bayesian Optimization Algorithm (MOBOA)

1: **Require**: the design parameter initialization $\mathbf{x}_1$, the concurrent training cycle *n*, the total number of training cycles *N*, the dimension of objectives to be optimized m
2: **for** $n = 1, 2, ..., N$ **do**
3: Randomly generate a normalized weight vector $\omega \subseteq \mathbb{R}^m$, where $\sum_{i=1}^{m} \omega_i = 1$.
4: Find $\mathbf{x}$ that optimizes the acquisition function $\mathbf{x}_{n+1} = \arg\max_{\mathbf{x}} \alpha(\mathbf{x}; \mathcal{D}_n)$ using the GP models, where $\mathcal{D}_n$ is the weighted-sum of each objective to be optimized after normalization.
5: Evaluate the objective function to obtain the values of the objectives and constraints at $\mathbf{x}$.
6: Augment the data set $D_{n+1} = D_n, (\mathbf{x_{n+1}}, \mathbf{y_{n+1}})$.
7: Train the GP models using the new data set and recalculate the GP hyper-parameters.
8: **end for**
9: **return** the Pareto front and the Pareto set extracted from the data set $(\mathbf{x_N}, \mathbf{y_N})$

adequate exploration with a fixed weight vector ω, so they are randomly generated here for simplicity, but there are better solutions available than simply generating random weights. This new data point is possibly located in the vicinity of the true Pareto front. With the new data points, the accuracy of the GP models of $\mathbf{y}$ can be improved as the iteration continues.

The new data points found by maximizing the EIs would be gradually converging to the true Pareto-optimal front. As a result, a very high-quality approximation of the Pareto front can be expected from the data set generated by the MOBOA algorithm.

5.9 Optimization Results and Comparison

For the purpose of performing a comprehensive comparison, multi-objective NSGA-II and MOBOA optimizations are applied to evaluate 200, 1,000, and 2,000 design candidates, respectively. Figures 4(a) through (c) demonstrate the Pareto fronts generated by the two methods when the objective is set to maximize the torque density and efficiency simultaneously. It can be observed that with the increase of evaluated design candidates, the Pareto fronts generated by both approaches tend to converge on the same trajectory, and the MOBOA has a distinct advantage. The MOBOA solutions nearly dominated all of the solutions generated by NSGA-II. A similar dominance of MOBOA can be also found

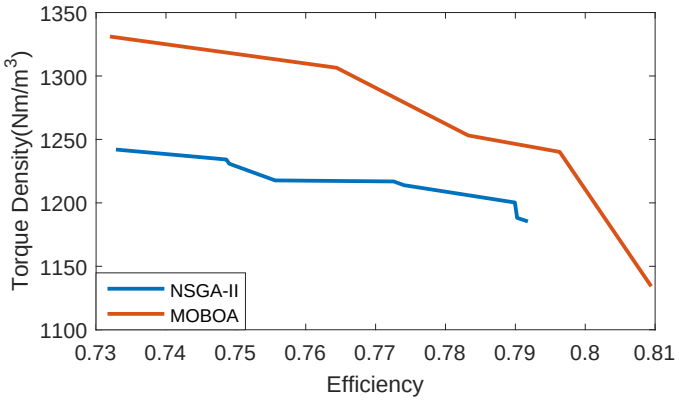

(a)

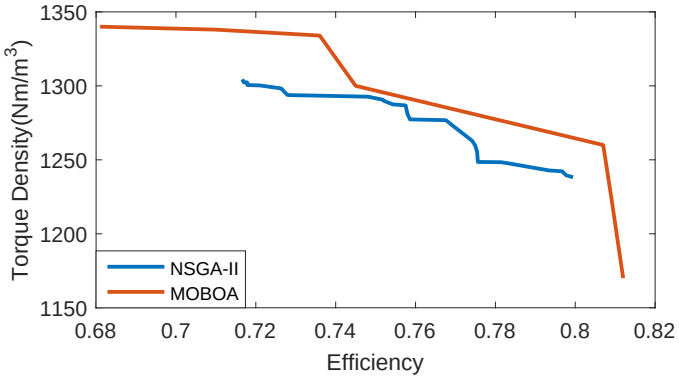

(b)

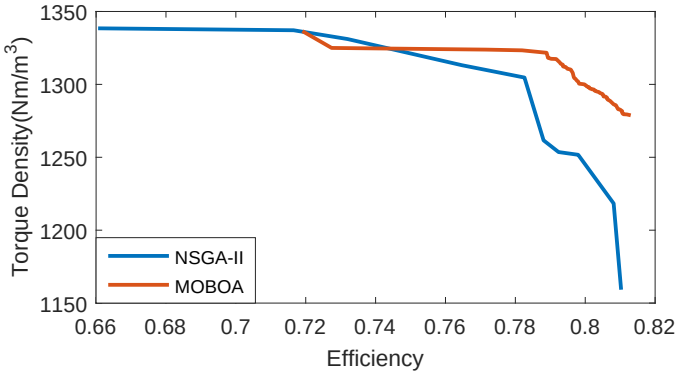

(c)

Figure 5.10: Comparison of Pareto fronts: torque density vs. efficiency after (a) 200 evaluations; (b) 1,000 evaluations; (c) 2,500 evaluations; torque ripple.

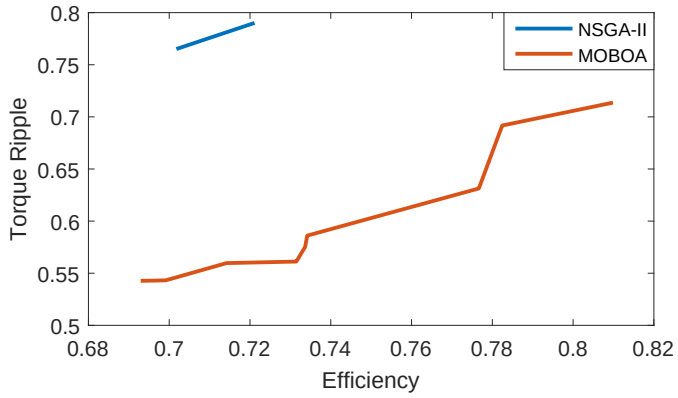

(a)

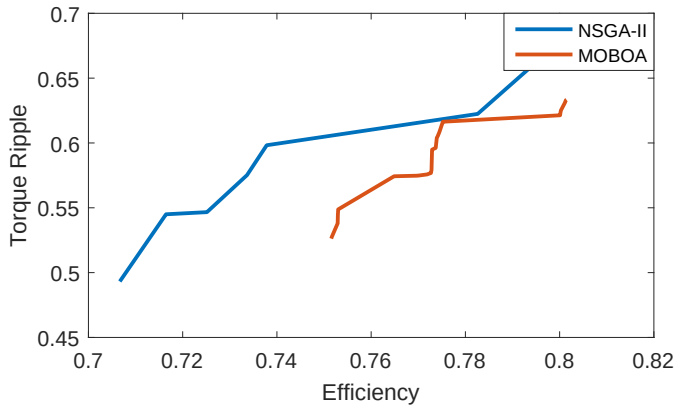

(b)

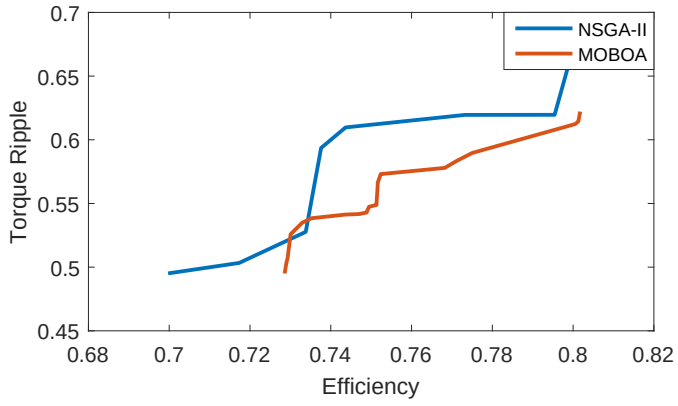

(c)

Figure 5.11: Comparison of Pareto fronts: torque ripple vs. efficiency after (a) 200 evaluations; (b) 1,000 evaluations and (c) 2,500 evaluations.

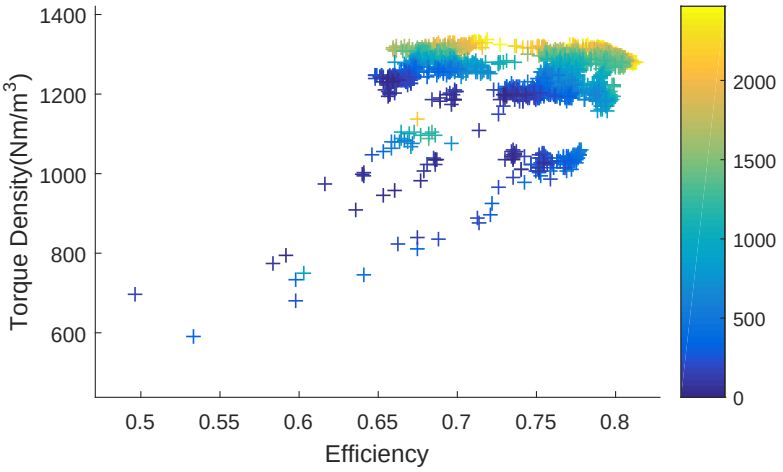

Figure 5.12: Cumulative set of SRM design candidates.

in Figures 4(d) to (f) when the objective is changed to minimize the torque ripple and to maximize efficiency. Moreover, after a careful evaluation of Figure 4(a) and (b), the Pareto front of MOBOA after 200 evaluations even dominate that of NSGA-II after 1000 evaluations, indication that MOBOA requires much fewer evaluations and less computational time to generate solutions of similar qualities, thereby validating the efficiency of the Bayesian optimization algorithm.

5.10 Chapter Summary

This chapter first presents an ultra-fast analytical design approach for the multi-objective design and optimization of SRMs coupled with an active current profile optimization. In addition, the proposed method is very time-saving and offers machine designers accurate, handy, and convenient initial designs, which can be further verified or fine-tuned by FEA.

This chapter also compares the nonlinear Pareto front generated by three popular multi-objective optimization algorithms. The statistical results, correlated with all data obtained with different quality indicators, point to the superiority of the DE algorithms over NSGA-II and PSO algorithms in terms of the convergence speed and the quality of the final Pareto front. In addition, a new perspective on applying the multi-objective Bayesian optimization

algorithm (MOBOA) is presented. Specifically, the Gaussian processes are trained to model the employed objective function, which is refined incrementally via Bayesian posterior updating each time that new machine design candidates are generated. In turn, the developed GP model of the objective function is used to determine the next round of input vectors to evaluate. The results show that MOBOA can achieve more accurate approximations of the Pareto front with a small number of evaluations when compared to the NSGA-II algorithm.

Many researchers, especially in the fields of machine learning and data science, are still in a relentless pursuit of improving the Bayesian optimization algorithm. It is our hope that the Bayesian optimization will prove itself as an effective and efficient algorithm in the electric machine design domain, and that the community will embrace the fascinating new problems and applications it opens up.

CHAPTER 6
VISUALIZATION AND DATA MINING OF MULTI-OPERATING POINT OPTIMIZATION OF SWITCHED RELUCTANCE MACHINES

6.1 Overview

The traditional methods used for presenting and visualizing the non-dominating solutions in multi-objective electric machine optimization problems mainly include parallel coordinate plots, histogram plots, and scatter plots displaying the approximation of the Pareto fronts. However, their usefulness in visualization performances decreases with the increase of non-dominating design candidates, or with the increase in the number of objectives to be optimized. In particular, since the aforementioned methods cannot perform clustering or classification operations on the input data set, it is very difficult to locate or identify the values of all of the objectives for a specific candidate, even after identifying one or two objectives of such candidates that favorably meet certain design requirements. This is common in a series of 2-D plots with Pareto fronts. Moreover, the objectives of different design candidates become nearly indistinguishable in a parallel coordinate plot. As an attempt to tackle this problem in the machine design domain, this chapter presents a case study that utilizes the self-organizing map (SOM) to visualize the design objectives of a high-speed switched reluctance machine. The results demonstrate that the SOM provides useful information with its intrinsic functionalities including data clustering, component-plane displays and data projections that are not offered by some conventional visualization techniques. Therefore, the SOM visualization can allow for the more effective integration of the knowledge and expertise of machine designers into specific electric machine design and optimization problems, and it may also assist them in the final decision-making process to choose the most appropriate designs.

6.2 Visualization Challenges in Electric Machine Optimization

As presented in the earlier sections, the design and optimization of electric machines are often formulated as multi-physics and multi-objective optimization problems, in which the most commonly used objectives are the volume or active weight of the machine, the material cost, the maximum or average torque, the torque ripple, and the efficiency or losses (core and copper) [50]. In general, some of these objectives are in conflict with each other, and thus requires solving a multi-objective optimization problem (MOOP).

The most commonly used methods for MOOPs are evolutionary algorithms with a Pareto-based fitness assignment, as presented in details in Chapter 5. Despite their success, the difficulty of solving MOOPs increases with the number of objectives. In addition, presenting and visualizing the solution set of a many-objective problem (with four or more objectives) could end up becoming problematic [172–175], as the Pareto-ranking will no longer work as a good discriminator for the candidate solutions, as most of them would become non-dominated in a high-dimensional space [176–178]. Specifically, the number of solutions that is required to approximate the Pareto front grows exponentially with the number of objectives, indicating the population size or the maximum bound for generations needs to further increase to ensure convergence. Besides, even if a reasonable number of solutions can be found, it is difficult to present and visualize them in such a hyper-dimensional objective space, and it is even harder for machine designers who are attempting to select the most appropriate candidates from the solution set for a targeted application.

A pertinent literature survey reveals that the data visualization in many-objective electric machine design is still an under-explored domain. While the scatter plots and parallel coordinates can be logically straightforward, distinguishing between the the data points on these plots may become difficult, when dealing with a large number of elements in a solution set. The only traceable work employing a non-classic visualization tool in the field of electric machine designs uses an Aggregate Tree (AT) [179], in conjunction with the

parallel coordinates to assist in the progressive preference articulation, aiding the decision making process of an interior permanent magnet synchronous motor design. The results show that the “AT is able to provide insight into the electrical machine design problem (in accordance with the common knowledge of physics) as well as guidance in the reduction of objectives".

In this context, this section seeks to propose a methodology employing self-organizing maps (SOM) to assist the visualization and data mining of the electric machine design solution set, which can be used by machine designers and engineers to better understand the relationships between the different objectives, and to help facilitate the most appropriate selection. In this section, the visualization of the objectives with SOM is demonstrated using a case study on a high-speed switched reluctance machine (SRM).

6.3 Visualization and Data Mining of Switched Reluctance Machine Optimization with Self-Organizing Maps

6.3.1 Establishing the Self-Organizing Map Framework

As a brief literature survey, the basic SOM framework has already been extensively applied as an analytical and visualization tool in exploratory data analysis [180–182]. It has already found use in plenty of practical applications ranging from industrial process control and finance analyses to the management of very large document collections. Successful applications of SOM in the power industry include the detection of electric machine faults or defects [183, 184], as well as the identification and probabilistic classification of miscellaneous electric loads [159]. In addition, there are also attempts to adapt or transform the SOM framework into some SOM-type optimization algorithms [185, 186]. An extensive research has also been performed in the area of visualization and data mining to assist or replace the classical visualization methods [187–194], especially in regards to the Pareto fronts [194].

The majority of SOM applications deals with variables with concrete, measurable

attributes, on the basis of which we intend to sort and cluster the SRM design candidates based on their quantifiable features or performance indices that provide more information than human intuition. In addition, the basic SOM algorithm can compute extensive mappings in a reasonable amount of time, using only personal computers.

The Structure of the SOM Framework

Usually the SOM framework is formed onto a low-dimensional (usually two-dimensional) array, where the nodes (or neurons) are organized as a hexagonal or rectangular grid, as shown in Figure 6.1(a). Then the SOM uses such a low-dimensional grid of neurons to capture and represent the high-dimensional input data, in this case the SRM design candidates in this chapter. The nature of an SOM is a nonlinear projection of the input density function onto the SOM array, whereupon the similarity relationships between all of the data items in the input data base become explicit, which is not typical to some usual clustering methods.

Since the SOM representation shrinks the dimension of the input data, the scales of the horizontal and vertical directions of the SOM array should approximately comply with the extensions of the input-data distribution in the two principal dimensions, namely, those two orthogonal directions in which the variances of the data set are the largest.

A very coarse rule-of-thumb may be that about 50 input-data items per node on average should be sufficient, otherwise the resolution is limited by the sparsity of the data [182]. Therefore, a compromise must be made between resolution and statistical accuracy when visualizing clusters. Typical SOM typically utilize between a few dozen to a few hundred nodes in the classification of text and speech.

The Basic SOM Batch Training Algorithm

The nature of the SOM algorithm is a combination of the K-means clustering and the smoothing methods, where the weights of all of the nodes $\boldsymbol{m}$ would be randomly initialized at first, and then all of the nodes would then compete for the right to respond to the input

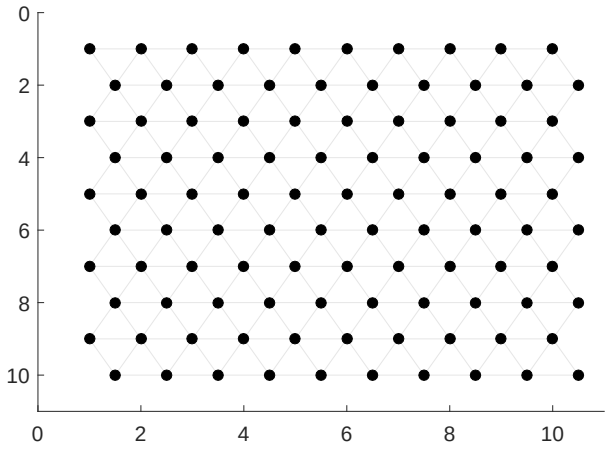

(a)

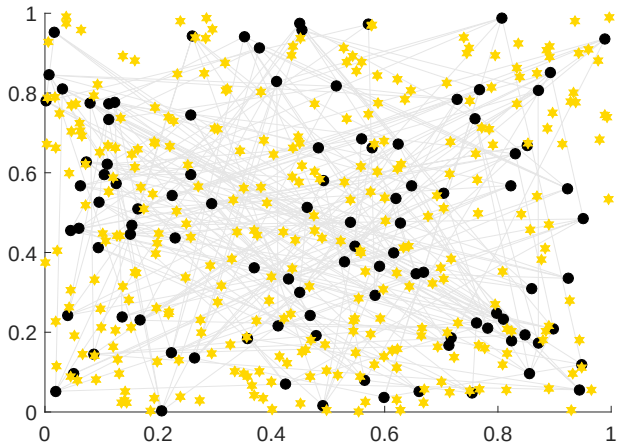

(b)

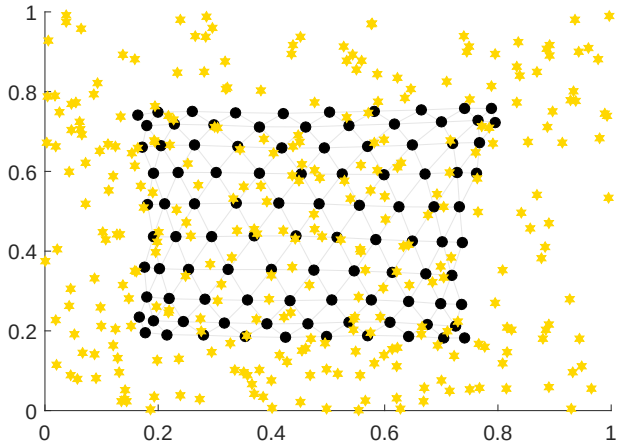

(c)

Figure 6.1: SOM representations in (a) output space, (b) input space and (c) after training.

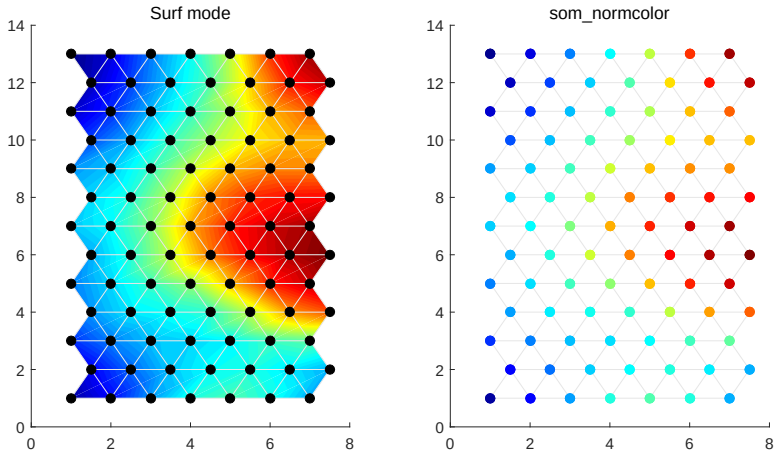

Figure 6.2: The “surf" and “normcolor" functions to visualize input data features with an SOM.

data. However, only one node wins at a time, and the weight of the node will be updated based on its current neighborhood function. In Figure 6.1(b) and (c), the black dots show the positions of the SOM nodes or neurons, while the yellow dots are the training data, and the gray lines show the connections between the neighboring SOM nodes. Since the SOM is generally initialized at random, the positions of the nodes in the input space are completely disorganized. During the training process, the map organizes itself and folds to the input training data, as shown in Figure 6.1(c).

The nature of the SOM algorithm is a combination of the K-means clustering and the smoothing methods, where the weights of all of the nodes $\boldsymbol{m}$ would be randomly initialized at first, and then all of the nodes would compete for the right to respond to the input data. However, only one node wins at a time, and the weight of the node will be updated based on its current neighborhood function. In Figure 6.1(b) and (c), the black dots show positions of the SOM nodes or neurons, the yellow dots are the training data, and the gray lines show connections between the neighboring SOM nodes. Since the SOM is generally initialized at random, the positions of the nodes in the input space are completely disorganized. During the training process, the map organizes itself and folds to the input training data, as shown in Figure 6.1(c).

Compared to the sequential training algorithm, which takes only one single input vector of data at each training step and then updates, the batch training algorithm presents all of the input data to the neuron grid at first before any updates are made, and the training speed is significantly faster without the need to tune the time-variable learning rate parameter $\alpha(t)$.

The SOM batch training algorithm is defined as follows by its inventor Kohohen as shown in Algorithm 3 [180, 181].

Algorithm 3 The Batch Training Algorithm of an SOM

1: **Require**: the input data set $\boldsymbol{X} \subseteq \mathbb{R}^{num \times n}$, the number of input data vectors *num*, the number of optimization objectives *n*, an SOM with *K* nodes, each node assigned a corresponding weight vector $\boldsymbol{m_i} \subseteq \mathbb{R}^n$, the concurrent training cycle *t*, the total number of training cycles *T*.
2: **for** $t = 1, 2...T$ **do**
3: **for** $q = 1, 2...num$ **do**
4: Find the best matching unit (BMU) node c_q for input data vector x_q such that
5: $c_q = \arg\min\{\|x_q - m_i\|\}$, where $\|\cdot\|$ is the distance function, typically the
6: Euclidean for a 2-D SOM.
7: **end for**
8: **for** $i = 1, 2...K$ **do**
9: Define the the neighborhood set N_i of nodes for the "bubble" neighborhood
10: function $h_{ci}(t)$, where $h_{ci}(t)$ has a value 1 in a neighborhood set N_i of or
11: otherwise 0.
12: Update the weight according to $\boldsymbol{m_i}(t+1) = \dfrac{\sum_{q=1}^{N_i} h_{ci}(t)\boldsymbol{x_q}}{\sum_{q=1}^{K} h_{ci}(t)}$
13: **end for**
14: **end for**

With this algorithm, the correct final values of the *weight vectors* will develop gradually iterative learning. After training, those input data vectors with similar values are mapped to nodes positioned close to one another and form a cluster, whereas less similar input vectors will be situated gradually farther away in the SOM. Every input data item shall select its BMU or node, as well as a subset of its spatial neighbors in the SOM. Then the weights m_i of each node will be replaced by the computed means in one concurrent computing operation over all of the nodes of the array, as shown in step 13 of the batch training algorithm. In this case of SRM design visualization, different SRM designs with similar performance

indices or features will be partitioned into the same cluster, and different clusters of design candidates are expected to have quite different features.

In addition, the values of the multiple features or performance indices of the input data are usually color-coded to offer the most compelling visual effect. Examples of two effective built-in functions in the MATLAB SOM toolbox [12] used to simulate indexed colors to form a specific colormap include the “surf" function for the map and the “normcolor" function for the grid, both of which are illustrated in Figure 6.2.

U-matrix and Clustering

The Unified Distance Matrix, or the U-matrix as it is often referred to in the literature, is introduced in [180, 181] as a common way to represent the information given by a SOM. Rather than displaying the values of the input data features, the U-matrix illustrates the weight vectors in a SOM by showing the distances between the adjacent pairs of nodes. Specifically for each node, the distances between itself and its adjacent nodes are calculated and presented with different bars of color, or possibly bars in gray scale. Small values are represented by light colors to illustrate the closely-spaced neurons, and large values are represented by dark colors to showcase the regions sandwiched by some pairs of neurons and to indicate that these neurons are in fact very far apart. Thus, a group of light-colored regions in the U-matrix plot can be roughly considered as a cluster, while the dark parts indicate more of the boundary regions. This facilitates the clustering and classification of the input data set in an unsupervised manner that does not require any human intervention.

It is also worthwhile to note that the map dimension of most SOMs is two-dimensional. However, the input space dimension is generally much higher than two. As indicated in the earlier text, the map in this case cannot perfectly reflect all of the information contained in the dataset. Rather, it follows the two orthogonal directions in which the variances in the data set are the largest, also known as the two principal dimensions. Despite the imperfection of this method, it does offer the convenience of visualizing an input data set with many

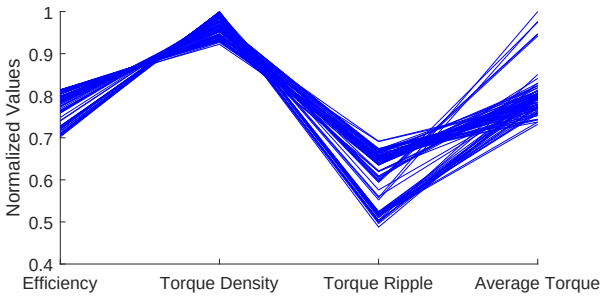

Figure 6.3: Parallel coordinate of the SRM design candidates.

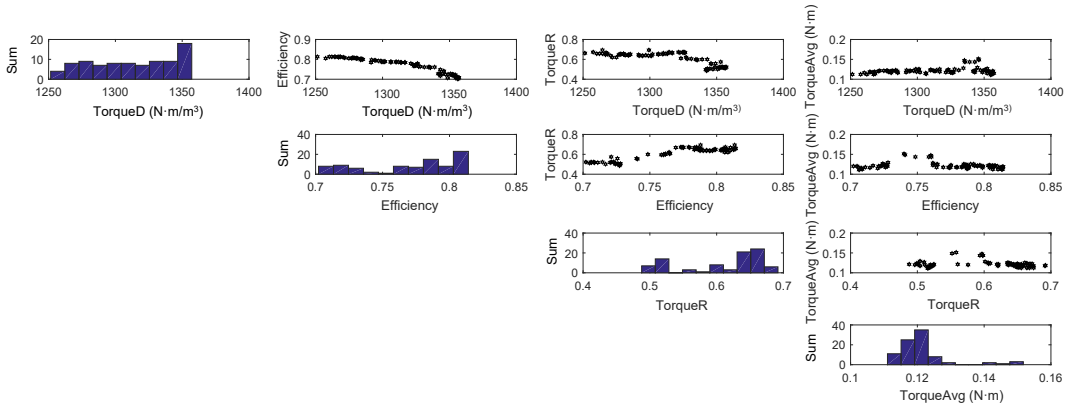

Figure 6.4: Scatter plots and histograms of the four features of the SRM design candidates.

objectives and delivering the best possible approximation within a 2-D space.

6.3.2 Visualizing Multi-Objective SRM Design Candidates with SOMs

Benchmark Many-Objective Design and Optimization of SRMs

The SRM many-objective (4 or more dimensions) optimization problem in this section is approached by combining the optimal evolutionary search algorithms with a proposed analytical modeling and a multi-physics and multi-objective design model, as presented in detail in the earlier chapters and in Figure 5.4.

Specifically, there are four objectives to be visualized, namely the average torque, torque density, efficiency and torque ripple. A many-objective optimization applying NSGA-II algorithm is performed with 100 populations and 50 iterations, indicating a total of 5,000 design candidates to evaluate. A parallel coordinate plot, which is perhaps one of the most

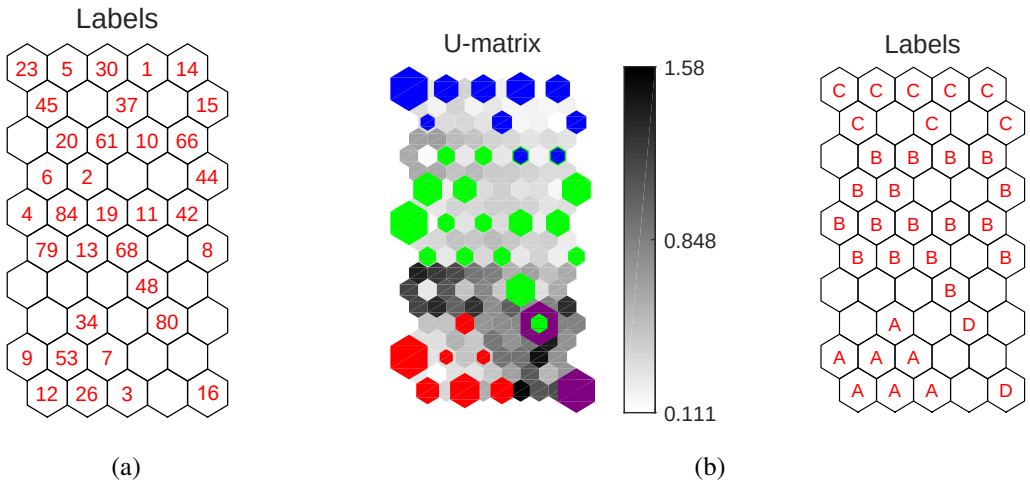

(a) (b)

Figure 6.5: Visualization of SRM design candidate data clustering and distribution: (a) labeling on an SOM and (b) U-matrix and clustering.

straightforward and widely-applied visualization techniques in electric machine optimization, is shown with the four specific objectives with normalized values from 0 to 1 in Figure 6.3, demonstrating the performance indices or features of the 87 SRM design candidates on the Pareto front of the torque density and efficiency. Other traditional visualization plots, the histograms and scatter plots, are presented in Figure 6.4 that explicitly shows the 2-D Pareto fronts and the inner relationships between either two out of the four features. Although the conflicting nature among the features themselves can be observed in these plots, i.e., a higher efficiency is generally associated with a lower torque density, it's already counter-intuitive to pick a specific candidate right from this plot, as it is challenging to identify and locate the position of each design candidate in each scatter subplot, not to mention in the absence of other advanced visualization functionalities such as data clustering.

With the help of SOM, however, the data visualization techniques of which can be taken advantage of and are of use are presented in three categories: visualization of (1) data clusters and shape; (2) components and variables and (3) data projections. In addition, the number of objectives can be further increased to include the material cost and copper or iron losses, among other objectives. This is all while preserving most of the clarity and integrity of all the features of the input set, as the SOM itself is a nonlinear mapping tool operating

from an arbitrary hyper-dimensional space onto the 2-D space.

Visualization of Data Clusters and Shape

To better differentiate the 87 SRM design candidates selected in the earlier section, they are labeled sequentially, from 1 to 87. After training with the SOM batch algorithm and taking these 87 design candidates as input vectors, their specific locations on the SOM are presented in Figure 6.5(a). Not all 87 labels are labeled, since the SOM could interpret the features of several design candidates as close enough, and thus allocate them to the same unit. Thus, only one label is shown to represent the rest.

The "U-matrix" that is demonstrated in Figure 6.5(b) shows the distances between neighboring units, and thus visualizes the structure of the clusters in the map. Note that the U-matrix visualization has many more hexagons than the component planes of Figure 6.5(a), since all of the distances *between* adjacent map units are shown, not only the distance values *at* the map units. Large values, or the dark regions on the U-matrix plot denote a large distance between neighboring map units, which form the cluster borders. In Figure 6.5(b), the SRM map has four clusters, and these are labeled "A" to "D". Note some intertwined regions are shown between clusters B and C.

Visualization of Components and Variables

The visualization of the component plane in Figure 6.6 demonstrate what kind of values the prototype vectors among the map units possess for different input vector components, or the features/performance indices of the SOM design candidates. The value is indicated through color, and the colorbar on the right indicates the range. Assisted by the SOM clustering plot, it can be easily observed that on the borders of the clusters, the values of the important variables can change very rapidly. Moreover, when compared to the parallel coordinate or the scatter plot methods, valuable information can be extracted from the SOM visualizations in a more intuitive and straightforward manner. For example, one can

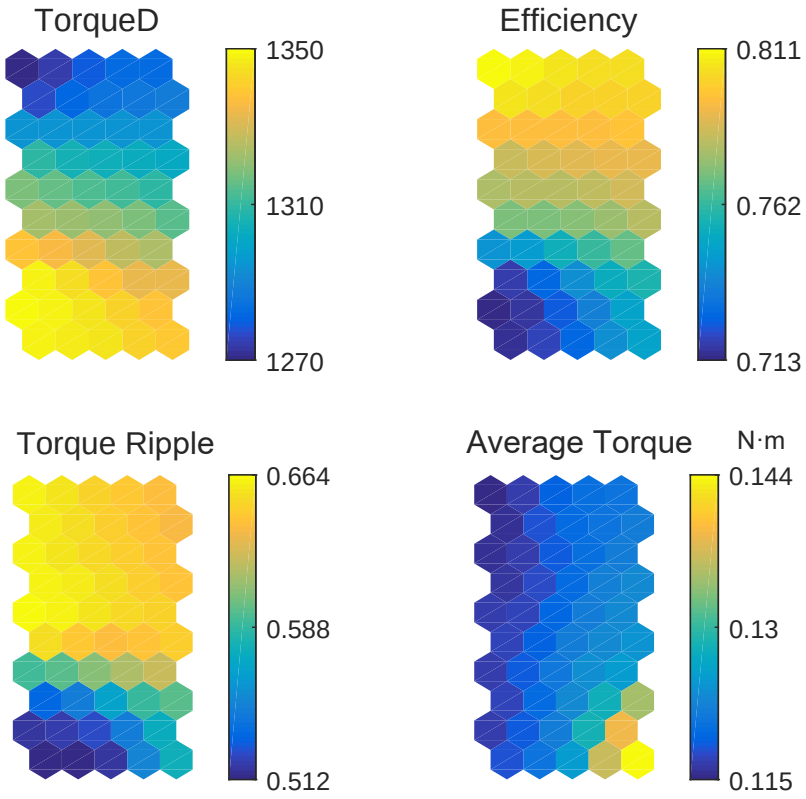

Figure 6.6: Visualization of SRM design candidate components and variables.

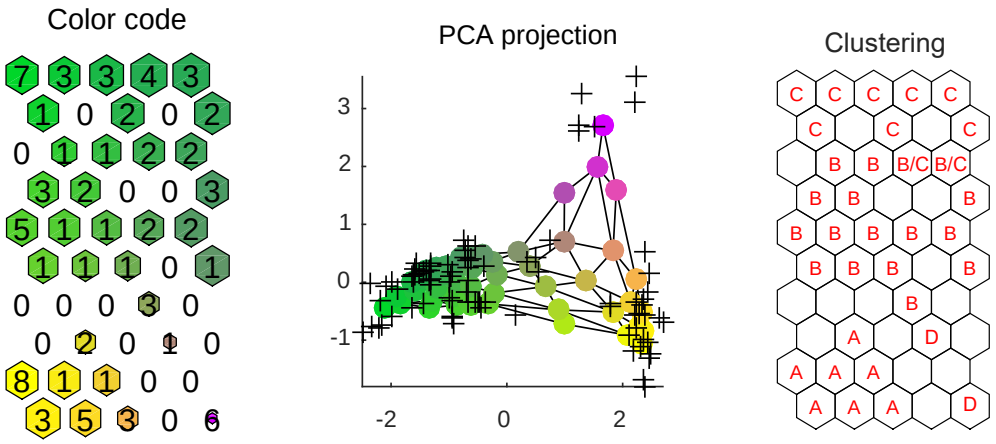

(a) (b) (c)

Figure 6.7: Visualization of SRM design candidate (a) hit histogram, (b) PCA projection and (c) data clustering.

easily tell that cluster D components, which is represented by the SRM design candidate number “16”, have overall higher torque densities, lower efficiencies, lower torque ripple,

and higher average torques compared to the rest of the components at different clusters. Since most of the four objectives appear to be conflicting from Figure 6.6, machine designers often have to make some compromises and meet the design requirements. For example, they can decide to look more specifically at the upper corner of cluster A that offers the top performance in maximizing the torque density, and above-average performances in increasing the efficiency and reducing the torque ripple, while the average torque drops to somewhere slightly below average. By aligning the visualization of the component values in Figure 6.6 to the visualization of the clusters in Figure 6.7, it can be concluded that designs "*34*" and "*7*" are of interest and can be selected for the next stage of design.

However, the above examples showcasing the design candidate selection process would be far less intuitive in a parallel coordinate plot or in a series of 2-D scatter plots displaying the Pareto fronts, as it requires some extra effort to distinguish one design candidate from the rest, especially in the decision making stage which involves numerous comparisons among different candidates. This counter-intuitive location identification process has to be exercised in a back-and-forth manner.

Visualization of Data Projections

A principle component projection can be also made for the input data and applied to the SOM, which has the data projected onto the space spanned by its two greatest eigenvectors. Figure 6.7(a) demonstrates the hit histogram with clustering information and the number of hits in each unit, and the PCA projection is shown in Figure 6.7(b). It can be observed that the PCA projection plot validates the data clustering plot of SOM, demonstrating the four clusters are well-separated, although 'B' and 'C' are slightly mixed up along their borders.

6.4 Electric Machine Optimization with Multiple Operating Points

6.4.1 Challenges with Visualizing Electric Machine Optimizations

The optimization of electric machines at multiple operating points is crucial for applications that require frequent changes on speeds and loads, such as the electric vehicles, to strive for the machine optimal performance across the entire driving cycle. However, the number of objectives that would need to be optimized would significantly increase with the number of operating points considered in the optimization, thus posting a potential problem in regards to the the visualization techniques currently in use, such as in the scatter plots of the Pareto fronts, the parallel coordinates, and in the principal component analysis (PCA), inhibiting their ability to provide machine designers with intuitive and informative visualizations of all of the design candidates and their ability to pick a few for further fine-tuning with performance verification. Therefore, the following sections will propose the utilization of t-distributed stochastic neighbor embedding (t-SNE) to visualize the optimization objectives of various electric machine design candidates with various operating conditions, which constitute a high-dimensional set of data that would lie on several different, but related, low-dimensional manifolds. Finally, two case studies of switched reluctance machines are presented to illustrate the superiority of the t-SNE when compared to traditional visualization techniques used in electric machine optimizations.

The process of electric machine design is a complex mixture of multi-physics field interactions and multi-objective optimizations [50]. In the recent years, there has also been an increasing demand to optimize these machines at multiple operating points [195, 196] for applications that require frequent changes of speeds and loads, such as an electric vehicle with driving cycles, in which the objectives at different operating points may be in conflict with each other and the overall dimension of objectives will increase substantially.

As demonstrated in the earlier sections of this chapter, data visualization in many-objective electric machine design is still an under-explored domain. While the scatter plots

and parallel coordinates can be logically straightforward and easy to follow, the data points on these plots may become difficult, or even impossible to distinguish when dealing with elements of large dimensions in a solution set. In addition, both of the above algorithms do not offer the ability to cluster or to reduce the dimensions of the dataset, making it even harder to be implemented in electric machines optimized at multiple operating points. The few traceable work employing a non-classic visualization tool in the field of electric machine designs uses an Aggregate Tree (AT) [179] and SOM, however, the dimension of objectives for machine design candidates that can be properly addressed by these techniques are still limited, and their visualization performance will still be compromised.

In this context, the following sections will propose a methodology employing t-distributed stochastic neighbor embedding (t-SNE) to assist the visualization and data mining of the electric machine design solution set, which can be used by machine designers and engineers to better understand the relationships between the different objectives, and to then facilitate them to make the most appropriate pick in a more effective way. In this section, the strength of t-SNE when compared to traditional visualization techniques, such as PCA and Isomap, is demonstrated using two case studies on a high-speed switched reluctance machine (SRM).

6.4.2 Formulation of Electric Machine Optimization with Multiple Operating Points

After performing an optimization process on electric machines for targeted applications, the design candidates form a collection of N high-dimensional objects $(\mathbf{x}_1, \mathbf{x}_2, \ldots, \mathbf{x}_N) \in \mathbb{R}^D$, where D is the number of objectives to be optimized. For commonly applied stochastic optimization algorithms, N is determined by the initial population size and the number of iterations, which can vary from a few hundred to hundreds of thousands.

When an electric machine is only optimized for a single operating point, the number of dimensions, D, is usually not large (usually around 3 to 8 based on the references in [50]), as the objectives associated with electric machines are typically the average torque, torque ripple, efficiency, torque density, machine weight, volume, quantified measures

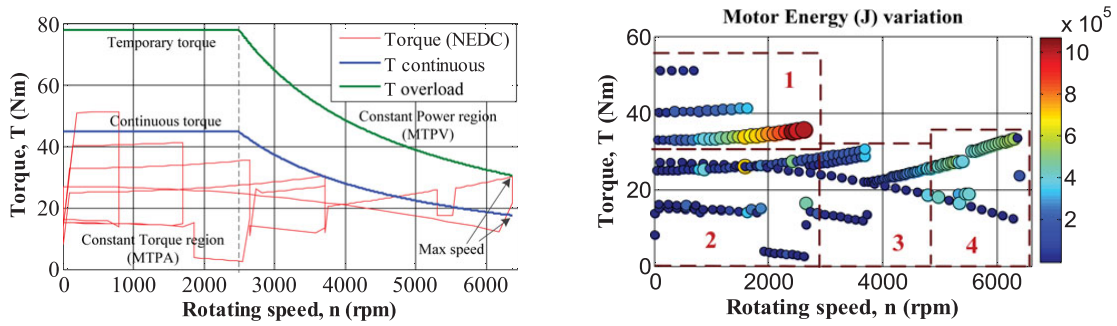

(a) (b)

Figure 6.8: (a) Illustration of the New European Drive Cycle (NEDC) for an electric vehicle (red line) and its torque-speed curve; and (b) motor energy distribution and clustering over the NEDC with torque and rotating speed [196].

of the manufacturing complexity such as the stator tooth-slot shape [197], as well as permanent magnet (PM) relevant metrics for PM machines such as the PM cost, volume, and its demagnetization vulnerability with various faults. With a relatively small D, the size of design candidates N can be also well regulated, since it is still easy to construct effective Pareto fronts when the number of objectives D is small. In this scenario, classical visualization approaches such as the scatter plots of Pareto fronts, parallel coordinates and PCA should still be able to provide useful insights and intuitions to guide the next-stage fine-tuning and decision making process. However, for certain applications where the electric machine is experiencing frequent changes in speed and load, such as in electric vehicles that follow some volatile and unpredictable driving cycles, such as thoses illustrated in Figure 6.8(a), then this driving cycle will be visualized in different clusters, the centroids of which will serve as the representative operating points to optimize an electric machine, as can be seen in Figure 6.8(b), which has 4 clusters. This multi-operating point based optimization ensures an overall optimal performance across the entire driving cycle [195, 196]. If the number of operating point is M (typically greater than 2), D is redefined as the number of objectives for a single operating point, then the design candidates will form a new collection of N high-dimensional objects $(\mathbf{x}_1, \mathbf{x}_2, \ldots, \mathbf{x}_N) \in \mathbb{R}^{MD}$. In this case, the PCA is less likely to generate satisfactory visualization results, not to mention the scatter plots or

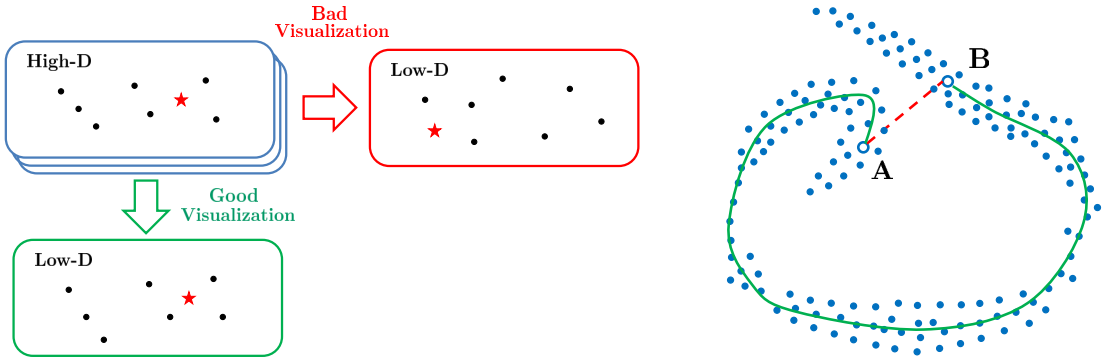

Figure 6.9: (a) Illustration of projecting the data points from the high-dimensional space to the low-dimensional map; and (b) example of a nonlinear manifold in which the Euclidean distance fails to reflect the actual pairwise similarities between points.

the parallel coordinates, due to the inherent limitations of the algorithms themselves, as will be explained in the next subsection. In addition, t-SNE will be introduced to visualize these machine design candidates optimized for multiple operating points.

6.5 Visualization of Multi-Objective Switched Reluctance Machine Optimization for Various Operating Conditions with t-SNE

6.5.1 Establishing the t-SNE Framework Visualizing Electric Machine Candidates

Preserving Local Similarities in Visualizations

For visualizing the N high-dimensional electric machine design candidates $(\mathbf{x}_1, \mathbf{x}_2, \ldots, \mathbf{x}_N) \in \mathbb{R}^{MD}$, it is desirable to obtain a good level of intuition for how these design candidates are arranged in the data space to facilitate the later decision making process, for example, how many clusters they form, the structure of the local data manifold, etc. While the traditional visualization methods such as parallel coordinates and scatter plots can indeed provide some simple and nice plots, they can only effectively visualize a few dimensions at once.

Another popular method of visualizing data is to form a projection from the high-dimensional space to a low-dimensional map, where the distances between points reflect

the similarities in the data. A good projection needs to properly preserve the point-wise distances in such a way that the low-dimensional map can accurately reflect the original high-dimensional space, as shown in Figure 6.9(a). To do this, it is generally necessary to minimize some objective functions that measure the discrepancy between the similarities (distances) in the original high-dimensional data and in the low-dimensional map.

One technique of this distance-based visualization uses the principal component analysis (PCA), which attempts to find the first principal component by minimizing the *linear* projection errors and while simultaneously maximizing the variance of the projected data. However, since PCA only examines the linear Euclidean distances between points, for some high-dimensional data that are more likely to form nonlinear manifolds, the Euclidean distances between points would not adequately reflect their similarity, as depicted in Figure 6.9(b). The Euclidean distance (red dotted line) suggests that points A and B are similar, whereas they are actually very far apart when considering the entire manifold (green solid line). In addition, PCA tends to preserve the large pairwise distances over the small ones, since the low-dimensional subspace is found with maximal variance, indicating this subspace will tend to be aligned such as to go close to the points lying far away from the center.

Despite its simplicity and popularity, PCA in fact does not work well for visualization, since it only preserves large pairwise distances that are not reliable. Rather, the very small pairwise distances between points and their nearest neighbors can accurately preserve the local similarities, even with very curved data manifolds, as can be seen in Figure 6.9(b). There has thus been an evolution of visualization techniques during the last 20 years, as evidenced by improved algorithms such as the Isomap [198], locally linear embedding [199], stochastic neighbor embedding (SNE) [200], and t-SNE [201].

The Formulation of t-SNE

The t-SNE algorithm was proposed in 2008 [201] and has become one of the most popular high-dimensional data visualization techniques over the past decade. The algorithm

assigns each datapoint a location in a two or three-dimensional map. This technique is a variation of Stochastic Neighbor Embedding (SNE), and is much easier to optimize, and produces significantly better visualizations, by reducing the tendency to crowd points together in the center of the map. t-distributed stochastic neighbor embedding is better than existing techniques at creating a single map that reveals structure at many different scales. This is particularly important for high-dimensional data that lie on several different, but related, low-dimensional manifolds, such as images of objects from multiple classes seen from multiple viewpoints. For visualizing the structure of very large data sets, t-SNE can use random walks on neighborhood graphs to allow the implicit structure of all of the data to influence the way in which a subset of the data is displayed. The performance of t-SNE can be seen on a wide variety of data sets and compared with many other non-parametric visualization techniques, including Sammon mapping, Isomap, and Locally Linear Embedding. The visualizations produced by t-SNE are significantly better than those produced by the other techniques on nearly all of the data sets, including MNIST dataset, CIFAR-10 image dataset, and TIMIT speech dataset, and street view house numbers on Google map.

The t-SNE algorithm utilizes a joint probability distribution to model the similarity in high-dimensional space,

$$p_{ij} = \frac{\exp\left(-\left\|\mathbf{x}_i - \mathbf{x}_j\right\|^2 / 2\sigma^2\right)}{\sum_k \sum_{l \neq k} \exp\left(-\left\|\mathbf{x}_k - \mathbf{x}_l\right\|^2 / 2\sigma^2\right)}. \tag{6.1}$$

where σ is the variance parameter of Gaussian, which is obtained via a binary search that produces a probability distribution P_i with a fixed perplexity $Perp$ specified by the user.

Moreover, to eliminate the “crowding problem", t-SNE employs the “student t-distribution" with one degree of freedom to model the similarity between data y_i and y_j in low-dimensional space as

$$q_{ij} = \frac{\left(1 + \left\|\mathbf{y}_i - \mathbf{y}_j\right\|^2\right)^{-1}}{\sum_k \sum_{l \neq k} \left(1 + \left\|\mathbf{y}_k - \mathbf{y}_l\right\|^2\right)^{-1}}. \tag{6.2}$$

t-SNE finds the optimal low-dimensional representations for matching p_{ij} and q_{ij} to the

greatest extent. This is achieved by minimizing the following Kullback-Leibler divergence measuring the difference between two probability distributions,

$$C(Y) = KL(P||Q) = \sum_{i} \sum_{j \neq i} p_{ij} \log \frac{p_{ij}}{q_{ij}}. \tag{6.3}$$

t-SNE calculates the optimal low-dimensional representation Y by minimizing $C(Y)$ over all data points with a gradient descent method, and the gradient of which is derived as

$$\frac{\delta C}{\delta y_i} = 4 \sum_{j} \left(p_{ij} - q_{ij}\right) \left(y_i - y_j\right) \left(1 + \|y_i - y_j\|^2\right)^{-1}. \tag{6.4}$$

which can be interpreted as a simulation of an *N-body system*.

6.5.2 The t-SNE Algorithm

The t-SNE algorithm is defined as follows by its inventor van der Maaten as shown in Algorithm 3 [201], which is much easier to optimize and ultimately yields significantly more useful visualizations than those produced by the other techniques. Besides its ability to preserve small pairwise distances while also not collapsing all points onto a single point by introducing the t-distribution that has a long tail than those in a standard Gaussian process, t-SNE can use random walks on neighborhood graphs of very large data sets, and allow the implicit structure of all of the data to influence the way in which a subset of the data is displayed.

6.5.3 Visualizing Multi-Objective SRM Design Candidates with t-SNE

Specifically, the benchmark SRM is a small-scaled, high speed machine with a $6/4$ typology, rated at 100 W and 10,000 rpm, and thus the efficiency suffers when compared to conventional SRMs because of the drastic increase in iron loss at a high speed, and the intrinsic torque ripple is still large because of its $6/4$ topology. Three operating points of interest are selected to optimize the SRM performance:

1. Operating point A: 0.18 N·m and 2,000 rpm, with 3 A current excitation;

2. Operating point B: 0.08 N·m and 5,000 rpm, with 2 A current excitation;

Algorithm 4 t-Distributed Stochastic Neighbor Embedding (t-SNE)

Require: the input data set $\chi = \{x_1, x_2, \ldots, x_n\}$, perplexity $Perp$, number of iterations T,
learning rate η, momentum $\alpha(t)$.
begin
  compute high-dimensional pairwise distances p_{ij} with equation (1)
  sample initial solution $\mathcal{Y}^{(0)} = \{y_1, y_2, \ldots, y_n\}$ from $\mathcal{N}(0, 10^{-4}I)$
  for $t = 1, 2...T$ **do**
    compute low-dimensional pairwise distances q_{ij} with equation (2)
    compute gradient $\frac{\delta C}{\delta y}$ with equation (4)
    set $\mathcal{Y}^{(t)} = \mathcal{Y}^{(t-1)} + \eta\frac{\delta C}{\delta y} + \alpha(t)\left(\mathcal{Y}^{(t-1)} - \mathcal{Y}^{(t-2)}\right)$
  end
end
Results: low-dimensional data representation $\mathcal{Y}^{(T)} = \{y_1, y_2, \ldots, y_n\}$.

3. Operating point C: 0.02 N·m and 10,000 rpm, with 1 A current excitation.

The excitation current is regulated by the hysteresis controller. During the design and optimization process, the air-gap length and the number of turns in the stator windings are fixed. Other machine design variables, such as the winding AWG size and other geometric parameters that depend on the prime design variables specified earlier, can be calculated on that basis. For ultra-fast calculations, the machine performance indices or features are estimated using an analytical model with automated scripts, which includes the steel saturation and various commutation effects. Other computational methods, such as the FEA or the simplified FEA, could be also employed, but there require a significantly longer computational time, as it must evaluate hundreds or thousands of design candidates. A many-objective optimization is performed with 20 populations and 50 iterations, which generated 460 design candidates by excluding those that failed to meet the design constraints.

6.5.4 Case Study 1: Visualization SRM Designs Candidates Optimized for a Single Operating Point

For this case study, the SRM is only optimized under operating point A, and five objectives are selected, namely the average torque, torque density, efficiency, torque ripple,

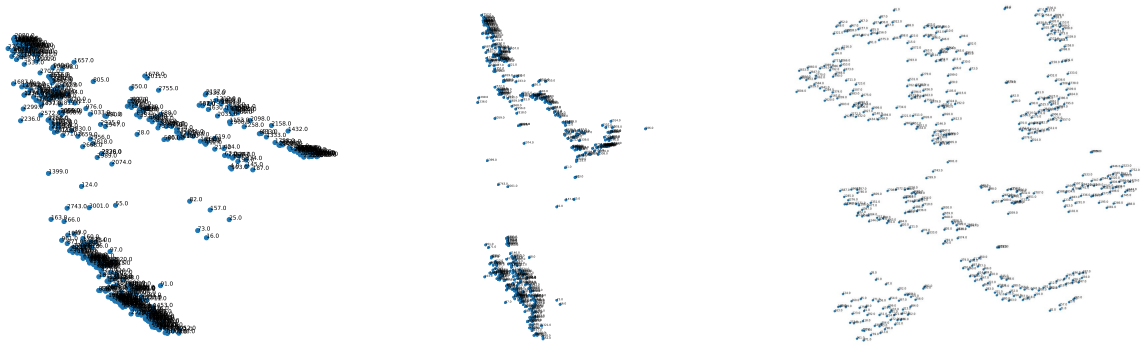

(a) (b) (c)

Figure 6.10: Visualization of the 460 SRM design candidates optimized for a single operating point with 5 objectives: (a) visualization by PCA; (b) visualization by Isomap; and (c) visualization by t-SNE.

and machine volume. In this scenario, it is already challenging to visualize these five dimensions with either a parallel coordinate plot or a scatter plot of Pareto fronts because of the complexity and going back-and-forth to identify and locate the position of each design candidate in these plots. However, standard data clustering methods such as PCA and Isomap may still bring valuable insights, since the dimension size (five) is not super large. As can be observed in Figure 6.10(a) and (b), PCA seems to be able to successfully identify six clusters while still left out some outliers, and Isomap also seems to suggest five or six clusters, although some clusters are placed very close together. The visualization results of t-SNE is also presented in Figure 6.10(c), where 7 clusters are explicitly presented without much overlap, and it also cross validated the approximate visualization performance of PCA and Isomap with a modest objective dimension size.

6.5.5 Case Study 2: Visualization SRM Designs Candidates Optimized for Multiple Operating Points

In this case study, all of the three operating points are taken into account in the optimization process, and the torque density, average torque, efficiency, and torque ripple for all three points are set as objectives, giving a total of 13 objectives including the machine volume. By observing the visualization results in Figure 6.11, it is obvious that t-SNE has a lot more

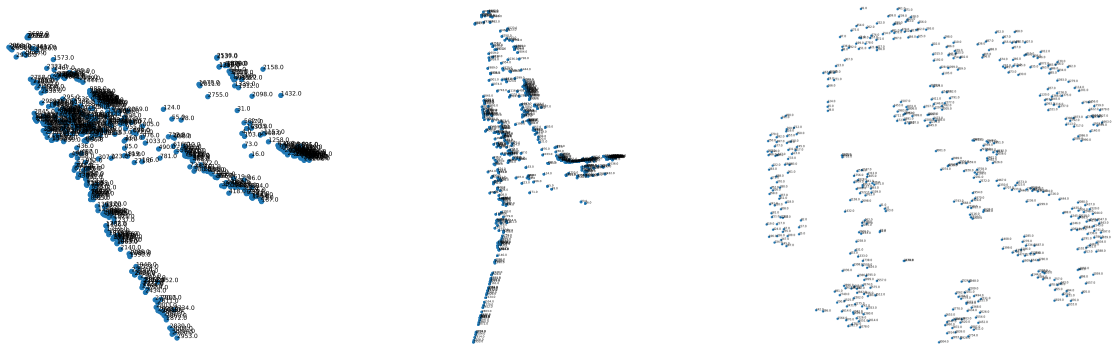

(a) (b) (c)

Figure 6.11: Visualization of the 460 SRM design candidates optimized for 3 operating points with 13 objectives: (a) visualization by PCA; (b) visualization by Isomap; and (c) visualization by t-SNE.

structure than that offered in PCA and Isomap plots. The 8 clusters are well-separated in this low-dimensional map, and there are fairly larger distances between the clusters when compared to PCA and Isomap, which failed to generate distinguishable clusters.

Starting from the visualization provided by t-SNE, machine designers can obtain soem insight on how these design candidates are arranged in the data space, and the centroid of each cluster can be picked to represent other design candidates in the same cluster. Therefore, and therefore these picks combined can also well represent all the design candidates in the data space. Starting from here, it is possible to proceed with the next-stage of the design fine-tuning and prototype validation.

6.5.6 Chapter Summary

In this chapter, a case study on an SRM design optimization case study with four objectives is visualized with the help of self-organizing maps (SOM) visualizing the data clusters, component planes and data projections. It is demonstrated that compared with the conventional visualization methods of parallel coordinates or a series of scatter plots with 2-D Pareto fronts, the SOM offers intuitive, simple and straightforward information that could assist the machine designers in their decision making process in order to choose the

most appropriate designs candidate for any targeted applications.

To further provide a solution to this multi-objective optimization of electric machines considering multiple operating points, the t-SNE algorithm has been successfully applied to visualize SRM design candidates optimized at multiple operating points, and these visualizations are significantly better than those produced by other techniques such as PCA and Isomap. By projecting the high-dimensional data onto a low-dimensional map, t-SNE is able to provide more informative and intuitive insights to machine designers on picking either the initial designs to perform a second round of optimization and fine-tuning, or the final prototype validation.

CHAPTER 7
ROTOR THERMAL MONITORING OF INTERIOR PERMANENT MAGNET MACHINES VIA HIGH FREQUENCY SIGNAL INJECTION

7.1 Overview

Permanent magnet (PM) magnetization state estimation in interior permanent magnet synchronous machines (IPMSMs) can be important for precise torque control and health prognostics [110, 202]. However, prolonged exposure to high temperatures while operating, especially with various types of drive-inverter initiated or machine winding short circuit faults [124, 125, 140, 203], can demagnetize the PM to the point of irreversible demagnetization, which results in the degradation of the torque production and efficiency, and such damage is time consuming and costly to repair.

Instead of PM temperature measurement, the PM temperature can be also estimated with thermal models or by measuring the high-frequency (HF) PM secondary resistance that changes with temperature, which is a byproduct of the induced magnet eddy-current loss incurred when an alternating high-frequency magnetic field is applied to the PM [133, 204, 205]. Due to the relatively high electrical conductivity of rare-earth magnets, the resultant eddy-current loss in a magnet can be significant. To generate the HF magnetic field required to induce the PM resistance, the high-frequency signal injection based methods have been widely employed [133, 204]. In particular, extensive research has been performed on field-oriented-controlled (FOC) PM machine rotor temperature estimation with direct HF current or voltage injection [133]. For DTC-controlled PM machines, however, alternative injection methods need to be developed since the current/voltage signals cannot be directly controlled in closed-loop forms [206–209].

This section thus proposes a novel high-frequency torque injection-based rotor thermal

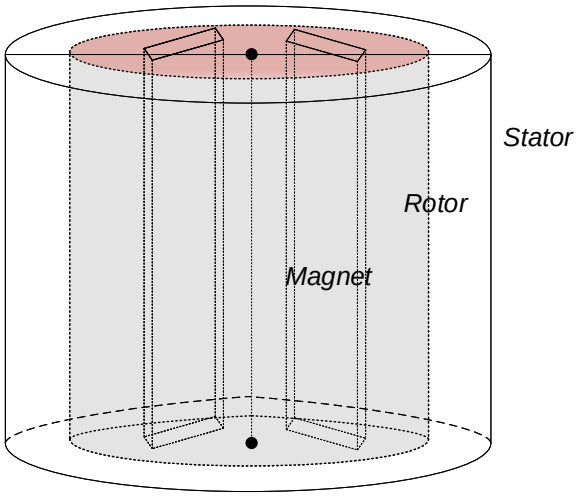

Figure 7.1: Simple illustration of an IPMSM with “V-shaped" magnets.

monitoring scheme. It first validates the principle of superimposing the appropriate torque signal for determining the HF resistances with the extracted HF voltage and the current signals in the stationary reference frame. In addition, the principle of PM resistance extraction and real-time signal processing techniques are also briefly discussed. Finally, the accuracy of the proposed thermal monitoring scheme is verified with the experimental results being collected while at a constant-load condition.

7.2 Principle of Rotor Magnet Temperature Estimation via High-Frequency Resistance Induced by the Eddy Currents

Figure 7.1 demonstrates a sketch diagram of an IPMSM, and only one pair of magnets in a single pole is plotted for simplicity. With high frequency signal injection, the induced eddy current loss per unit volume can be expressed as

$$P_{eddy} = \frac{1}{12}\sigma\omega^2 d^2 B_\alpha^2 \tag{7.1}$$

where σ is the conductivity, d is the thickness of a lamination, ω is the sinusoidal frequency, and B_α is the average flux density. With a higher frequency, the eddy current loss P_{eddy}

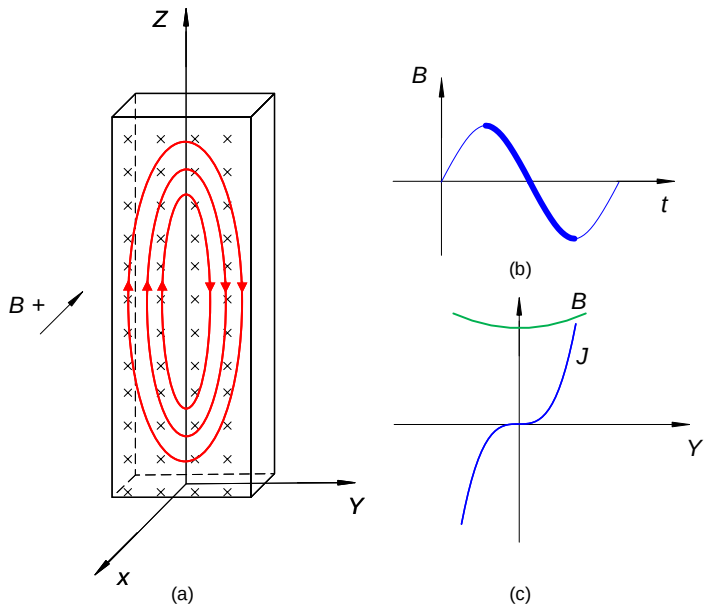

Figure 7.2: (a) The distribution of eddy current on a permanent magnet; (b) stator flux density waveform (possible position associated with the eddy current direction) and (c) stator flux density and current density profile of a permanent magnet due to a non-predominant skin effect.

increases in a quadratic manner. In addition, the skin depth can be written as

$$\Delta = \sqrt{\frac{2\rho}{\omega\mu}} \tag{7.2}$$

For the Prius IPMSM, the width of each magnet is 51.2 mm, the resistivity ρ is $1.4 \times 10^{-6}\,\Omega\mathrm{m}$, the permeability is $\mu = 1.05\mu_0$. Based on the above equation, the skin depth of the 5^{th} order, 7^{th} order and 9^{th} order harmonics are 33.6 mm, 28.4 mm and 25.0 mm, respectively, indicating that the skin effect would be intensified by injecting higher order harmonic signals, and thus the equivalent magnet resistance reflected to the stator side would be more prominent. Figure 7.2 illustrates a possible direction of the eddy current with its immediate stator flux density profile.

As discussed above, the injection of a periodic high frequency signal is a viable option for high frequency resistance estimation a magnet. Choosing the magnitude of the high frequency signal involves a trade-off between the signal-to-noise ratio and the induced magnet losses, as larger magnitudes are advantageous for the practical implementation of the

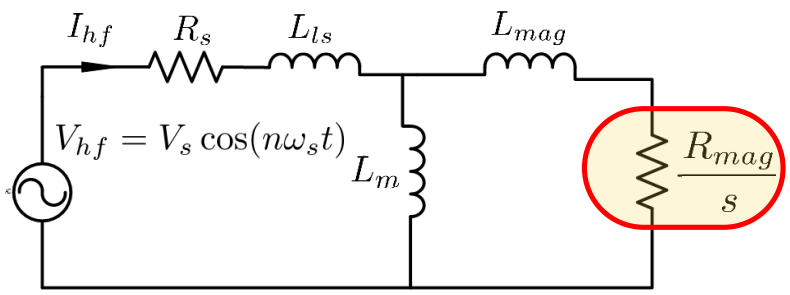

$$s = \frac{n\omega_s - \omega_s}{n\omega_s} = \frac{n-1}{n}$$

Figure 7.3: High frequency equivalent circuit of an IPMSM at steady state with an “equivalent slip".

method, because of its large signal-to-noise ratio, however, it will also result in larger losses due to the eddy current and it will also distort the normal operation of the IPMSM. Therefore, the magnitude is generally ranges from 2% to 5% of the rated value. More importantly, choosing the frequency of the high frequency signal involves a trade-off between the induced power loss and the skin effect consideration.

The magnet’s resistance can be also represented in the high-frequency IPMSM equivalent circuit, which is very similar to that of an induction machine, as demonstrated in Figure 7.3, where R_s and L_{ls} are the stator resistance and leakage inductance, L_m is the mutual inductance, L_{lmag} and R_{mag} are the eddy-current induced permanent magnet resistance and inductance. The slip for the high-frequency IPMSM circuit at a steady state is also defined as $n - 1/n$, where n is the harmonic order of the injected high-frequency signal.

It can be easily observed that when no high-frequency signal injection exists, $n = 1$, and then $s = 0$. The effective resistance of the magnet seen from Figure 7.3 would become ∞, which means the magnet branch of Figure 7.3 does not exist. This is in accordance with the fact that there is no rotor resistance or rotor loss when an IPMSM is operating at a synchronous speed. When n becomes larger, the equivalent slip becomes close to 1, and then the high-frequency resistance can be obtained by extracting the high-frequency

line-to-ground voltage V_{hf} and current I_{hf}, and perform the following calculation

$$R_{hf} = \frac{|V_{hf}|}{|I_{hf}|} \cos \angle(\theta_i - \theta_v) \tag{7.3}$$

where $|V_{hf}|$ and $|I_{hf}|$ are the magnitude of the high-frequency component of the injected harmonic order, θ_v and θ_i are their respective phase angles. Both the current sensors and the DC bus voltage sensors are commonly available in typical motor drives. Therefore, the proposed thermal monitoring method requires no additional hardware change.

Since the calculated high-frequency resistance is a combination of the stator winding resistance R_s and the PM resistance R_{mag} due to the eddy current loss, the stator resistance R_{s0} at room temperature T_0 and the real-time stator temperature T_s are both required in order to decouple the PM resistance from the stator resistance. The rotor temperature can then be estimated as

$$T_r = T_0 + \frac{R_{hf} - R_{mag} - R_{s0}[1 + \alpha_{Cu}(T_s - T_0)]}{\alpha_{mag} \cdot R_{mag}} \tag{7.4}$$

where α_{Cu} and α_{mag} are the copper and the stator-reflected PM temperature coefficient of resistance, while T_s and T_r are the stator and rotor temperature.

7.3 High-Frequency Resistance Extraction in DTC-Controlled IPMSMs

As discussed above, the rotor temperature can be estimated from the resistive change induced by the eddy currents, which can be calculated with the injected high-frequency voltage (current) and the response high-frequency current (voltage), For the direct-torque-controlled (DTC) IPM machines, alternative signal injections schemes need to be investigated, since there are no active current or voltage control loops in the DTC algorithm.

7.3.1 Generating the Appropriate High-Frequency Rotating Flux for Signal Injection

In order to minimize the negative effects brought about by the normal operation of IPM machines due to high-frequency signal injection, it is desirable to inject balanced three-phase high-frequency current offsets into the IPM motor three-phase windings, which

can be expressed as

$$\begin{bmatrix} \Delta i_a \\ \Delta i_b \\ \Delta i_c \end{bmatrix} = \begin{bmatrix} M\cos(n\theta) \\ M\cos(n\theta - 2\pi/3) \\ M\cos(n\theta + 2\pi/3) \end{bmatrix} \tag{7.5}$$

where M is the magnitude of the injected high-frequency current, and n is the harmonic order with respect to the fundamental frequency. Then the equivalent high-frequency current to be injected into the stationary reference frame is

$$\begin{bmatrix} \Delta i_{ds}^s \\ \Delta i_{qs}^s \end{bmatrix} = \frac{2}{3}\begin{bmatrix} 1 & -\frac{1}{2} & -\frac{1}{2} \\ 0 & \frac{\sqrt{3}}{2} & -\frac{\sqrt{3}}{2} \end{bmatrix} \begin{bmatrix} \Delta i_a \\ \Delta i_b \\ \Delta i_c \end{bmatrix} = \begin{bmatrix} M\cos(n\theta) \\ M\sin(n\theta) \end{bmatrix} \tag{7.6}$$

where the superscript s denotes the stationary reference frame, Δi_{ds}^s and Δi_{qs}^s are the desired high-frequency current in the stationary reference frame.

The IPMSM equations in the rotor reference frame can be represented as

$$\begin{bmatrix} v_{ds}^r \\ v_{qs}^r \end{bmatrix} = R_s \begin{bmatrix} i_{ds}^r \\ i_{qs}^r \end{bmatrix} + \begin{bmatrix} p & -\omega_r \\ \omega_r & p \end{bmatrix} \begin{bmatrix} \lambda_{ds}^r \\ \lambda_{qs}^r \end{bmatrix} \tag{7.7}$$

where v_{ds}^r, v_{qs}^r, λ_{ds}^r and λ_{qs}^r are the stator voltages and flux linkages in the rotor reference frame, R_s is the stator resistance, ω_r is the rotor speed and p is the differential operator. The flux linkages can be further defined as

$$\begin{bmatrix} \lambda_{ds}^r \\ \lambda_{qs}^r \end{bmatrix} = \begin{bmatrix} L_d & 0 \\ 0 & L_q \end{bmatrix} \begin{bmatrix} i_{ds}^r \\ i_{qs}^r \end{bmatrix} + \begin{bmatrix} \lambda_{pm} \\ 0 \end{bmatrix} \tag{7.8}$$

in which L_d and L_q are the inductances for d^r and q^r-axis, and λ_{pm} is the flux linkage of the permanent magnet. Similarly, the IPMSM equations in the stationary reference frame is

$$\begin{bmatrix} v_{ds}^s \\ v_{qs}^s \end{bmatrix} = R_s \begin{bmatrix} i_{ds}^s \\ i_{qs}^s \end{bmatrix} + \begin{bmatrix} p & 0 \\ 0 & p \end{bmatrix} \begin{bmatrix} \lambda_{ds}^s \\ \lambda_{qs}^s \end{bmatrix} \tag{7.9}$$

We then define the transformation matrix converting the stationary reference frame to the

synchronous reference frame, T, as

$$\mathrm{T} = \begin{bmatrix} \cos\theta & \sin\theta \\ -\sin\theta & \cos\theta \end{bmatrix} \tag{7.10}$$

then the flux linkage in the stationary reference frame is

$$\begin{aligned} \begin{bmatrix} \lambda_{ds}^{s} \\ \lambda_{qs}^{s} \end{bmatrix} =& \mathrm{T}^{-1} \begin{bmatrix} \lambda_{ds}^{r} \\ \lambda_{qs}^{r} \end{bmatrix} = \mathrm{T}^{-1} \begin{bmatrix} L_d & 0 \\ 0 & L_q \end{bmatrix} \mathrm{T} \begin{bmatrix} i_{ds}^{s} \\ i_{qs}^{s} \end{bmatrix} + \mathrm{T}^{-1} \begin{bmatrix} \lambda_{pm} \\ 0 \end{bmatrix} \\ =& \begin{bmatrix} \Sigma L + \Delta L\cos(2\theta) & \Delta L\sin(2\theta) \\ \Delta L\sin(2\theta) & \Sigma L - \Delta L\cos(2\theta) \end{bmatrix} \begin{bmatrix} i_{ds}^{s} \\ i_{qs}^{s} \end{bmatrix} + \lambda_{pm} \begin{bmatrix} \cos\theta \\ \sin\theta \end{bmatrix} \end{aligned} \tag{7.11}$$

in which $\Sigma L = (L_d + L_q)/2$ and $\Delta L = (L_d - L_q)/2$. Then the small signal change of flux linkage $\Delta\lambda_{ds}^{s}$ and $\Delta\lambda_{qs}^{s}$ can be expressed as

$$\begin{bmatrix} \Delta\lambda_{ds}^{s} \\ \Delta\lambda_{qs}^{s} \end{bmatrix} = \begin{bmatrix} \Sigma L + \Delta L\cos(2\theta) & \Delta L\sin(2\theta) \\ \Delta L\sin(2\theta) & \Sigma L - \Delta L\cos(2\theta) \end{bmatrix} \begin{bmatrix} \Delta i_{ds}^{s} \\ \Delta i_{qs}^{s} \end{bmatrix} \tag{7.12}$$

After substituting (7.6) into (7.12) and after performing some trigonometric transformations, the small signal model for the flux linkages can be written as

$$\begin{bmatrix} \Delta\lambda_{ds}^{s} \\ \Delta\lambda_{qs}^{s} \end{bmatrix} = \begin{bmatrix} \Sigma L \cdot M\cos(n\theta) + \Delta L \cdot M\cos[(n-2)\theta] \\ \Sigma L \cdot M\sin(n\theta) - \Delta L \cdot M\sin[(n-2)\theta] \end{bmatrix} \tag{7.13}$$

which yields the desired high-frequency flux linkage to be injected into the direct torque control scheme. In addition, the trajectory of this high-frequency flux linkage is a set of eclipses centering around the origin, and thus this mechanism is referred to as the “rotating flux linkage" injection.

After injecting the flux linkage offset in (7.13), the high-frequency voltage and current components will appear as the system response, which can be used to calculate the high-frequency rotor resistance for estimating the PM temperature. This mechanism can be also validated in the following steps. If a small signal approximation of the high frequency voltage is used with the IPM machine framework depicted in equation (7.7) in the stationary

reference frame can be expressed as

$$\begin{aligned}\begin{bmatrix} v_{ds}^s + \Delta v_{ds}^s \\ v_{qs}^s + \Delta v_{qs}^s \end{bmatrix} =& R_s \begin{bmatrix} i_{ds}^s + \Delta i_{ds}^s \\ i_{qs}^s + \Delta i_{qs}^s \end{bmatrix} + \begin{bmatrix} p & 0 \\ 0 & p \end{bmatrix} \begin{bmatrix} \lambda_{ds}^s + \Delta \lambda_{ds}^s \\ \lambda_{qs}^s + \Delta \lambda_{qs}^s \end{bmatrix} \\ &+ \begin{bmatrix} R_{rhf\_\alpha} & 0 \\ 0 & R_{rhf\_\beta} \end{bmatrix} \begin{bmatrix} \Delta i_{ds}^s \\ \Delta i_{qs}^s \end{bmatrix}\end{aligned} \tag{7.14}$$

Subtracting (7.7) from (7.14), the complete small signal model after rotating flux injection is

$$\begin{bmatrix} \Delta v_{\alpha s} \\ \Delta v_{\beta s} \end{bmatrix} = \begin{bmatrix} R_\alpha & 0 \\ 0 & R_\beta \end{bmatrix} \begin{bmatrix} \Delta i_{\alpha s} \\ \Delta i_{\beta s} \end{bmatrix} + \begin{bmatrix} p & 0 \\ 0 & p \end{bmatrix} \begin{bmatrix} \Delta \lambda_{\alpha s} \\ \Delta \lambda_{\beta s} \end{bmatrix} \tag{7.15}$$

where $R_\alpha = R_s + R_{rhf\_\alpha}$ and $R_\beta = R_s + R_{rhf\_\beta}$.

Substituting (7.13) into (7.15), the model becomes a form shown below

$$\begin{aligned}\begin{bmatrix} \Delta v_{ds}^s \\ \Delta v_{qs}^s \end{bmatrix} &= \begin{bmatrix} R_{dhf} & 0 \\ 0 & R_{qhf} \end{bmatrix} \begin{bmatrix} \Delta i_{ds}^s \\ \Delta i_{qs}^s \end{bmatrix} + \begin{bmatrix} p & 0 \\ 0 & p \end{bmatrix} \begin{bmatrix} \Sigma L \cdot M\cos(n\theta) + \Delta L \cdot M\cos[(n-2)\theta] \\ \Sigma L \cdot M\sin(n\theta) - \Delta L \cdot M\sin[(n-2)\theta] \end{bmatrix} \\ &= \underbrace{\begin{bmatrix} R_{dhf} & 0 \\ 0 & R_{qhf} \end{bmatrix} \begin{bmatrix} \Delta i_{ds}^s \\ \Delta i_{qs}^s \end{bmatrix} + \begin{bmatrix} -n\Sigma L \cdot M\sin(n\theta) p\theta \\ n\Sigma L \cdot M\cos(n\theta) p\theta \end{bmatrix}}_{n^{th}\ order\ harmonic\ component} \\ &+ \underbrace{\begin{bmatrix} -(n-2)\Delta L \cdot M\sin[(n-2)\theta] p\theta \\ -(n-2)\Delta L \cdot M\cos[(n-2)\theta] p\theta \end{bmatrix}}_{(n-2)^{th}\ order\ harmonic\ component}\end{aligned}$$

The above expression contains the frequency component of both the n^{th} and the $(n-2)^{th}$ order. With appropriate signal processing techniques, both of the frequency components should be accurately extracted from the real-time current and voltage measurements. However, since the amplitude of the n^{th} harmonic order is larger and more distinguishable compared to the $(n-2)^{th}$ order, the n^{th} order components should be utilized for estimating the high-frequency rotor resistance R_r and thus the PM temperature.

Since $p\theta = \omega_r$ and define $\omega_n = n\omega_r$, the above expression can be updated by only taking

its n^{th} order component as

$$\begin{bmatrix} \Delta v^s_{dsn} \\ \Delta v^s_{qsn} \end{bmatrix} = \begin{bmatrix} R_d & 0 \\ 0 & R_q \end{bmatrix} \begin{bmatrix} \Delta i^s_{ds} \\ \Delta i^s_{qs} \end{bmatrix} + \begin{bmatrix} -\omega_n \Sigma L \cdot M \sin(n\theta) \\ \omega_n \Sigma L \cdot M \cos(n\theta) \end{bmatrix} + \begin{bmatrix} R_{rhf\_\alpha} & 0 \\ 0 & R_{rhf\_\beta} \end{bmatrix} \begin{bmatrix} \Delta i^s_{ds} \\ \Delta i^s_{qs} \end{bmatrix} \tag{7.16}$$

where the n^{th} order high-frequency voltages are v^s_{dsn} and v^s_{qsn}. Substituting (2) into (13) yields

$$\begin{bmatrix} \Delta v^s_{dsn} \\ \Delta v^s_{qsn} \end{bmatrix} = \begin{bmatrix} R_d & 0 \\ 0 & R_q \end{bmatrix} \begin{bmatrix} \Delta i^s_{ds} \\ \Delta i^s_{qs} \end{bmatrix} + \omega_n \Sigma L \begin{bmatrix} -\Delta i^s_{qs} \\ \Delta i^s_{ds} \end{bmatrix} \tag{7.17}$$

Since the complex notation j is equivalent to the transformation matrix in (3) with $\theta = \pi/2$ as

$$j = \begin{bmatrix} 0 & 1 \\ -1 & 0 \end{bmatrix}$$

Therefore, equation (7.17) can be updated to

$$\begin{bmatrix} \Delta v^s_{dsn} \\ \Delta v^s_{qsn} \end{bmatrix} = \begin{bmatrix} R_d + j\omega_n \Sigma L & 0 \\ 0 & R_q + j\omega_n \Sigma L \end{bmatrix} \begin{bmatrix} \Delta i^s_{ds} \\ \Delta i^s_{qs} \end{bmatrix} \tag{7.18}$$

which is the very familiar $R - L$ circuit equation. Therefore, injecting the small signal change of the high frequency flux linkage in equation (7.13) into the DTC control scheme can produce the desired high frequency voltage and current signals for calculating the high-frequency resistance, and consequentially the PM temperature.

7.3.2 Generating the Appropriate High-Frequency Torque for Signal Injection

Since DTC has direct control on both the flux linkage and the electromagnetic torque, which enables the mechanism of injecting high-frequency torque signals along with the aforementioned flux linkage signals. Assume a small change ΔT_{em} at a high frequency (e.g.,

the 5^{th} order) is superimposed on the original torque signal as

$$T_{em} + \Delta T_{em} = \frac{3}{2}\frac{poles}{2}[(\lambda_{ds}^s + \Delta\lambda_{ds}^s)(i_{qs}^s + \Delta i_{qs}^s) - (\lambda_{qs}^s + \Delta\lambda_{qs}^s)(i_{ds}^s + \Delta i_{ds}^s)] \quad (7.19)$$

Subtracting it from the original T_{em} signal while neglecting the second-order small signal approximations. Then the small change of torque can be written as

$$\Delta T_{em} = \frac{3}{2}\frac{poles}{2}(\Delta\lambda_{ds}^s i_{ds}^s + \lambda_{ds}^s \Delta i_{qs}^s - \Delta\lambda_{qs}^s i_{ds}^s - \lambda_{qs}^s \Delta i_{ds}^s) \quad (7.20)$$

Finding a simplified equation for the torque offset to be superimposed is a nontrivial task, since substituting (7.13) into the above equation yields

$$\begin{aligned}\Delta T_{em} = \frac{3}{2}\frac{poles}{2}\big\{&[\Sigma L \cdot M\cos(n\theta) + \Delta L \cdot M\cos((n-2)\theta)] \cdot i_{qs}^s \\ &-[\Sigma L \cdot M\sin(n\theta) + \Delta L \cdot M\sin((n-2)\theta)] \cdot i_{ds}^s \\ &+ \left[\Sigma L \cdot i_{ds}^s + \Delta L \cdot \cos(2\theta) \cdot i_{ds}^s + \Delta L \cdot \sin(2\theta) \cdot i_{qs}^s + \lambda_{pm}\cos\theta\right] \cdot M\sin(n\theta) \\ &- \left[\Delta L \cdot \sin(2\theta) \cdot i_{ds}^s + \Sigma L \cdot i_{qs}^s - \Delta L \cdot \cos(2\theta) \cdot i_{qs}^s + \lambda_{pm}\sin\theta\right] \cdot M\cos(n\theta)\big\}\end{aligned}$$

After performing some rigorous trigonometric derivation processes, the above equation can be greatly simplified into

$$\Delta T_{em} = \frac{3}{2}\frac{poles}{2}P\{2\Delta L i_{qs}^s \cos[(n-2)\theta] + 2\Delta L i_{ds}^s \sin[(n-2)\theta] + \lambda_{pm}\sin[(n-1)\theta]\} \quad (7.21)$$

7.3.3 Illustration of the Proposed High-Frequency Torque Injection Technique

There are several important implications of the proposed torque injection signal (7.21) that can be summarized as follows, for the first term, since i_{ds}^s and i_{qs}^s are sine-wave current signals at the fundamental frequency, while being multiplied by another $(n-2)^{th}$ order signal will yield a combination of a $(n-1)^{th}$ and a $(n-3)^{th}$ order signal. Since the last term in (7.21) is also of $(n-1)^{th}$ order, the expression in (7.21) indicates that a combination of the $(n-1)^{th}$ and $(n-3)^{th}$ order varying torque command needs to be superimposed on the original torque reference to practically inject the high-frequency current component, while no modification for the flux control loop is required. Although the inner DTC loop

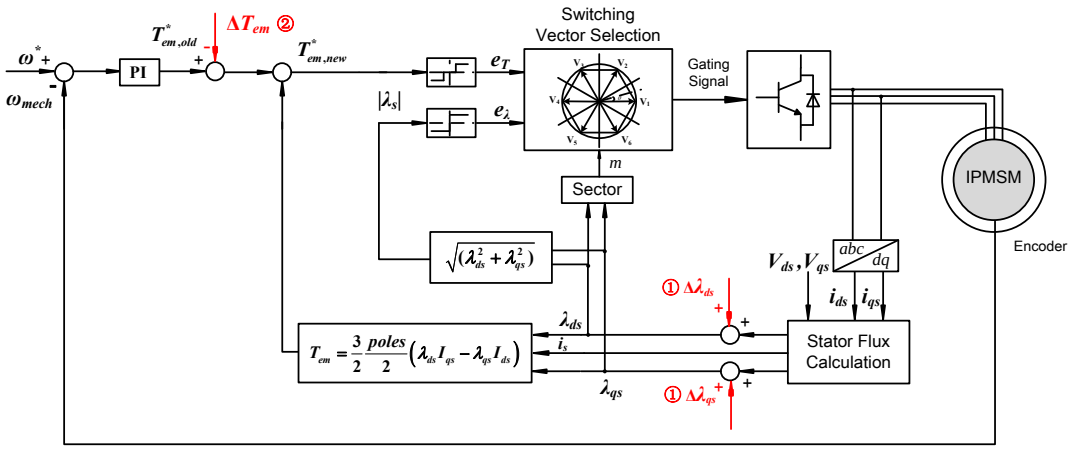

Figure 7.4: Block diagram of the proposed high-frequency torque injection method on a conventional DTC scheme.

for a typical IPM motor generally does not have a bandwidth that is capable of reinforcing the high-frequency torque bias to be exactly the same as this reference torque deviation, the actual system response can still be kept stable at a constant magnitude at the desired high frequency, which is sufficient to trigger the high-frequency current and voltage signals.

In particular, it is interesting to observe from the equation (7.21), that for a surface-mounted PM machine with $L_D = L_q$ and hence $\Delta L = 0$, only a $(n-1)^{th}$ order torque offset signal is needed to trigger the desired high-frequency voltage and current signals for high-frequency resistance extraction.

The block diagram of this injection method based on the conventional DTC scheme is demonstrated in Figure 7.4. Similar to the earlier discussion, although the bandwidth of the speed loop is typically too low to completely cancel out ΔT_{em}, the output of the speed regulator $T_{em,old}$ will still be varying sinusoidally and will be partially compensating for the external injection ΔT_{em}, due to the small speed ripple. As a result, the magnitude of the actual torque ripple in $T_{em,new}$ is reduced, and the phase is shifted. However, this torque bias is still a combination of sine waves varying at the $(n-1)^{th}$ and $(n-3)^{th}$ order, but with a different magnitude and phase angle, when compared with the external injection signal. In addition, this sine-wave torque injection does result in a small amount of extra torque ripple. However, considering the inertia of the rotor and load, the speed ripple is almost

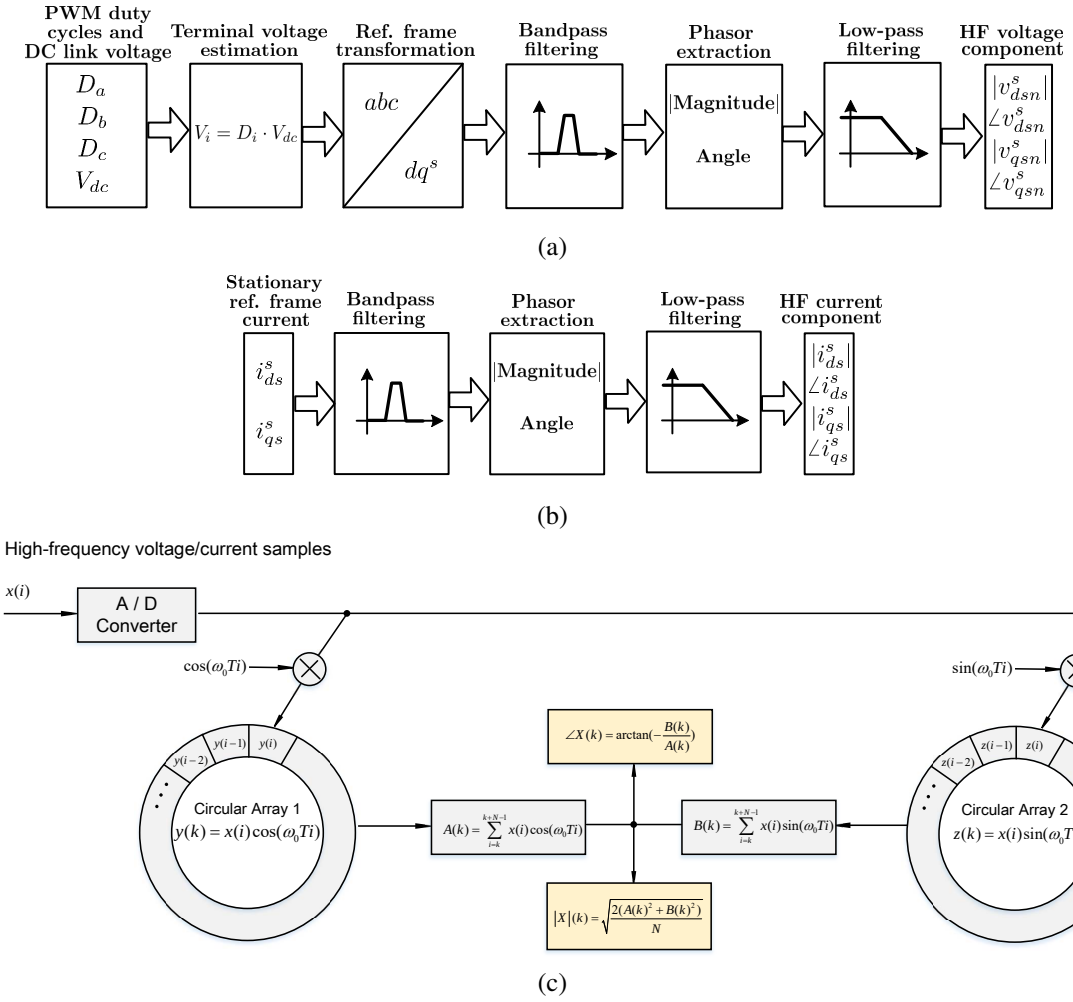

Figure 7.5: Signal process techniques for extracting high-frequency current and voltage.

unnoticeable. Moreover, the injection technique must only be implemented for a short period of time, such as for 20 seconds every 10 minutes; and the speed ripple can be further limited by choosing a small enough $\Delta i_{ds}(P)$. To summarize, the impact of this high-frequency signal injection on the normal operation of the IPM motors is almost negligible.

7.4 Real-Time Signal Processing Techniques

As demonstrated in Figure 7.5(a) and (b), two second-order Butterworth bandpass filters are designed to extract the high-frequency voltage and current signals. Assume that the measured high-frequency voltage and current signals are uniformly sampled at a rate of

N samples per period, the phasor extraction computations can be implemented with high efficiency using a circular array based algorithm [210]. Computations, such as moving averages and discrete Fourier transformations, can be implemented in this way.

As demonstrated in Figure 7.5(c), this phasor extraction algorithm starts from setting up two circular arrays with N entries each, all with zero initial values. Then two accumulators defined as $A(k)$ and $B(k)$ are also set to zero. As each data sample $x(i)$ arrives, the following steps are performed

1. Compute the two temporary values updating the following sums recursively at each new available data sample

$$y(k) = x(i)\cos(\omega_0 T i)$$
$$z(k) = x(i)\sin(\omega_0 T i)$$

   where ω_0 is the base frequency, and T is the sampling period.

2. Update the two accumulators as

$$A(k) = A(k-1) + y(i) - y(i-N)$$
$$B(k) = B(k-1) + z(i) - z(i-N)$$

   where N is the sampling rate and is equal to $2\pi/\omega_0 T$.

3. Overwrite the N-step-previous values $y(iN)$ and $z(iN)$ with the present values of $y(i)$ and $z(i)$ in the arrays. The above expressions have more compact forms as

$$A(k) = \sum_{i=k}^{k+N-1} x(t)\cos(\omega_0 T i)$$
$$B(k) = \sum_{i=k}^{k+N-1} x(i)\cos(\omega_0 T i)$$

4. Compute the magnitude and angle at the present step

$$|X(k)| = \sqrt{\frac{2(A(k)^2 + B(k)^2)}{N}}$$
$$\angle X(k) = \arctan(-\frac{B(k)}{A(k)})$$

Table 7.1: Parameters of the IPM Machine.

Parameters	Value
Rated power (P_{rated})	1 hp
Number of poles	4
Rated voltage (V_{rated})	230 V
Rated current (I_{rated})	2.86 A
Stator resistance R_s	2.85 Ω
d-axis inductance (L_d)	14.41 mH
q-axis inductance (L_q)	27.92 mH
Rated speed (ω_{rated})	1,800 rpm
Inertia (J)	0.0050 kg · m^2

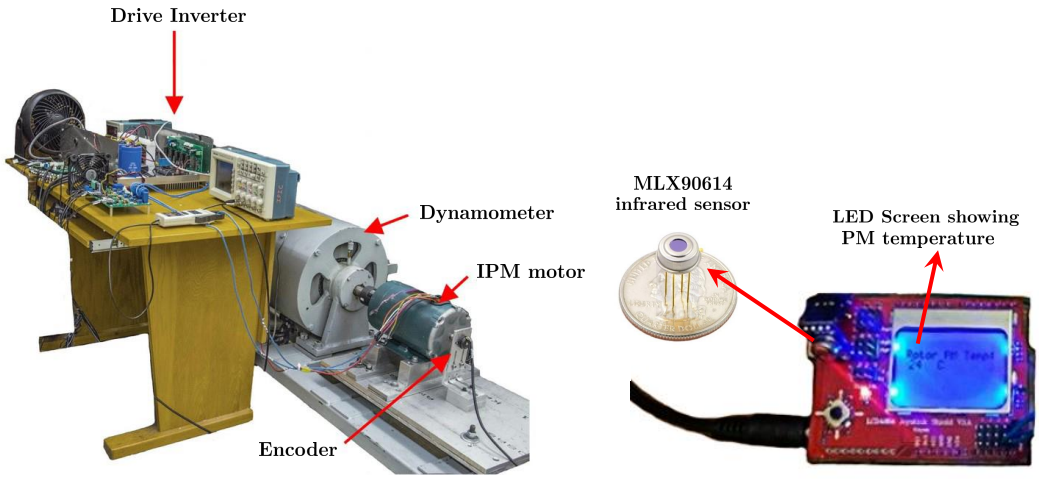

(a) (b)

Figure 7.6: (a) Experimental setup for the proposed rotor thermal monitoring method and (b) displaying the measured rotor temperature with an Arduino board .

Finally, the computed voltage/current magnitude and phase angle values will then pass through second-order low pass filters to eliminate any remaining high-frequency harmonics, and thus thus the high-frequency resistance can be calculated.

7.5 Experimental Results

7.5.1 Experiment Setup

A programmable inverter drive is used to validate the proposed thermal monitoring method, and the entire hardware system is illustrated in Figure 7.6(a). An Analog Device

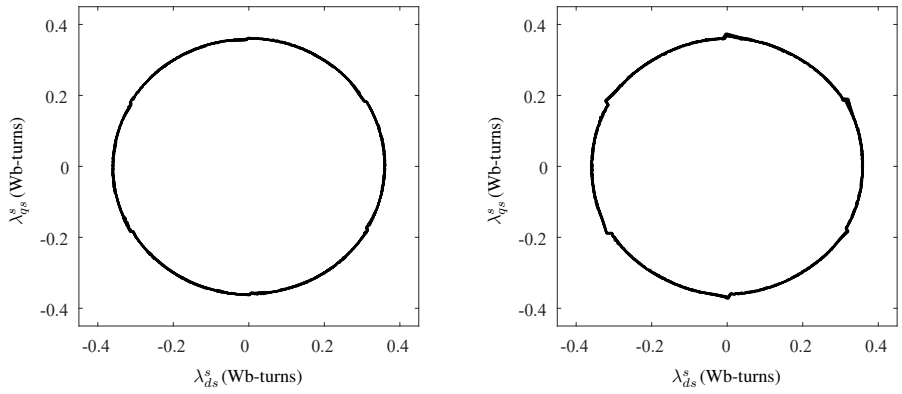

Figure 7.7: 2-D flux linkage diagram (a) before high-frequency rotating flux injection and (b) after high-frequency rotating flux injection.

21369 DSP is employed in conjunction with a Xilinx Spartan-3 field-programmable gate array (FPGA) as the motor controller. The inverter runs at 20-kHz PWM frequency. A direct torque control scheme is implemented in the inverter drive and the proposed thermal monitoring method is integrated in the control algorithm. The parameters of the IPM motor is displayed in Table 7.1.

The stator temperature T_s is measured with four K-type thermocouples attached to the stator winding, while the reference rotor temperature is measured with the Melexis MLX90614 infrared sensor through two measuring holes drilled on the motor end cap. The sensor is controlled with an Arduino UNO board installed with a LCD screen demonstrating the real-time value of the measured PM temperature, as shown in Figure 7.6(b).

7.5.2 High Frequency Voltage, Current and Flux Linkage Waveforms

The 2-D flux linkage waveform of λ^s_{ds} against λ^s_{qs} is demonstrated in Figure 7.7. Before the injection of the high-frequency signal, it can be observed in Figure 7.7(a) that the trajectory is almost a perfect circle with its center in the origin, which indicates that the flux linkage of the IPM machine is well-regulated and there is very little intrinsic DC offset or high-frequency harmonics. After manually injecting the rotating high-frequency flux

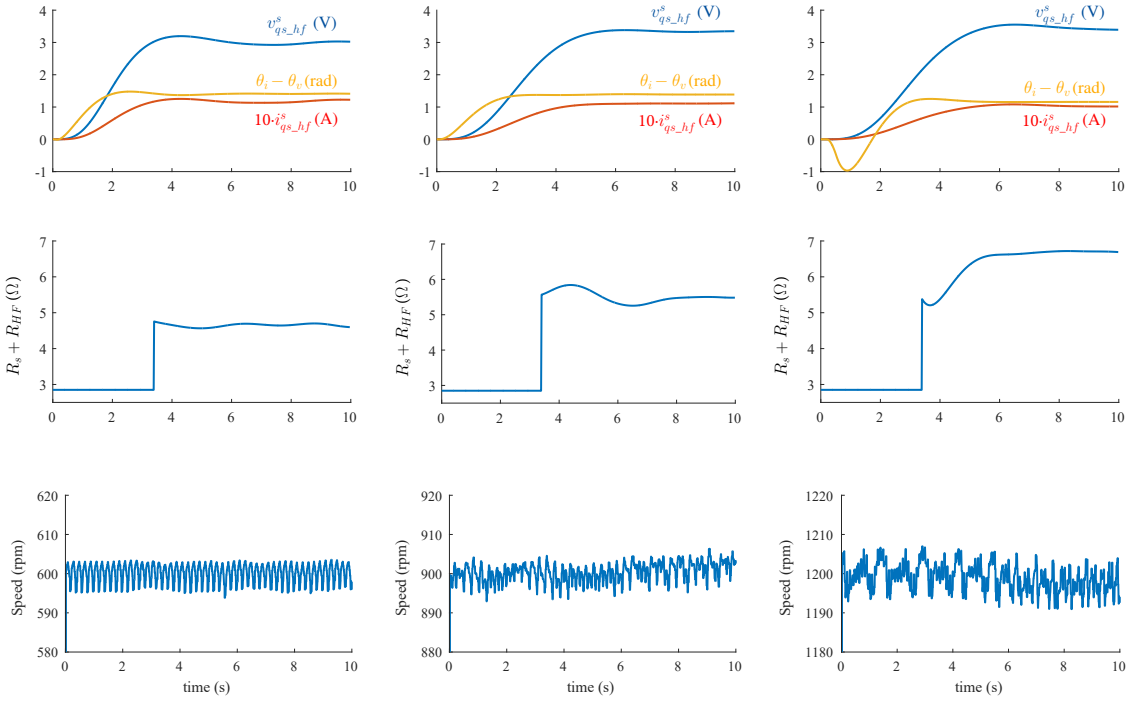

Figure 7.8: High-frequency voltage, current, phasor angle, resistance, and speed signals with high-frequency rotating flux injection at (a) 600 rpm; (b) 900 rpm and (c) 1,200 rpm.

linkage, a noticeable distortion on the circle can be observed that clearly demonstrates the high-frequency contents have been added onto the original circular trajectory.

The high-frequency voltage, current, phasor angle, resistance, and speed signals are presented in with high-frequency rotating flux injection Figure 7.8 at (a) 600 rpm; (b) 900 rpm and (c) 1,200 rpm. Because of their small magnitudes, the high-frequency current signals are magnified by 10 times to comfortably place the voltage, current and phasor offset values in one plot. It can be observed that for a typical 15 second injection period, the estimated resistance needs around 4 to 6 second to stabilize due to delays in the phasor extraction algorithm and the proposed real-time signal processing method demonstrated in Figure 7.5. In addition, the estimated resistance values are larger at higher speeds, clearly indicating this reflected magnet resistance is largely induced by the eddy current effect on the permanent magnets, which would become more significant at higher frequencies.

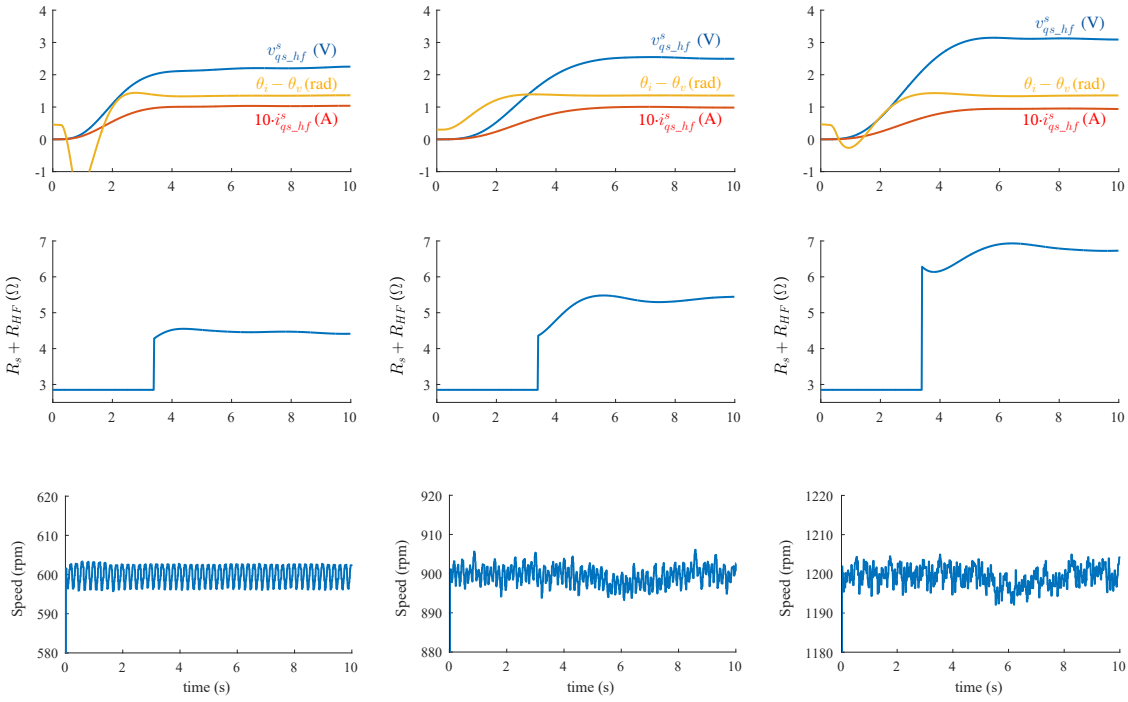

(g) (h) (i)

Figure 7.9: High-frequency voltage, current, phasor angle, resistance, and speed signals with high-frequency torque injection at (a) 600 rpm; (b) 900 rpm and (c) 1,200 rpm.

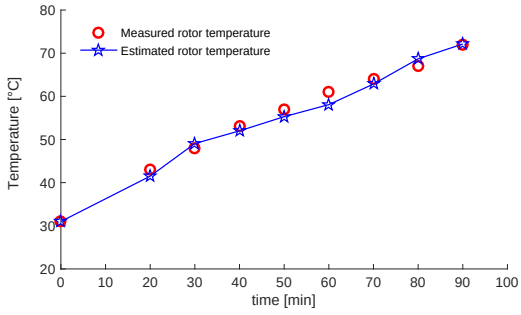

(a)

Figure 7.10: Rotor temperature estimation performance with high-frequency rotating flux injection.

Very similar results and resistance values are estimated with the proposed high-frequency torque injection scheme, and are shown in Figure 7.9.

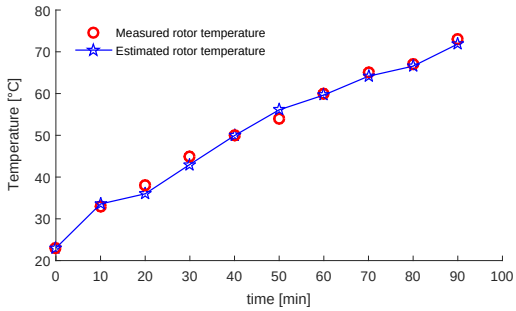

(a)

Figure 7.11: Rotor temperature estimation performance with high-frequency torque injection.

7.5.3 Temperature Estimation at Steady State with HF Signal Injection

To validate the proposed method, the IPM machine is running continuously at 150% of its rated current at 600 rpm, and the torque reference is injected into the DTC algorithm for 15 seconds every 10 minutes. The reference stator resistance R_{s0} is first measured when the machine is at the room temperature T_0. Then the PM temperature is tracked over time using equation (7.4). The experimental result with both the measured PM temperature and the estimated PM temperature of the flux injection and torque injection are shown in Figure 7.10 and Figure 7.11, respectively. As can be observed, the estimated magnet temperature tracks the temperature measurement from the infrared sensors very closely. The maximum temperature deviation is less than 3 °C for both plots.

7.6 Conclusion

This chapter proposes a nonintrusive thermal monitoring scheme for the permanent magnets inside the direct-torque-controlled IPM machines using high-frequency torque injection. The proposed method requires no additional sensors or hardware except for those already available in the IPMSM drives. Compared to the temperature measurement taken by the infrared sensors, the maximum error of the proposed method is less than 3 °C at the steady state condition.

CHAPTER 8
DEMAGNETIZATION ASSESSMENT OF PERMANENT MAGNET SYNCHRONOUS MACHINES WITH STATOR INTER-TURN FAULTS

8.1 Overview

This chapter investigates the process of irreversible demagnetization for the 2004 Prius interior permanent magnet (IPM) synchronous machine due to a large demagnetizing MMF caused by an inter-turn short circuit fault. An equivalent circuit, coupled with finite element analysis, is used to determine the inter-turn short-circuit fault current, as well as the concomitant magnetic flux plot. In particular, the distribution of the demagnetizing MMF throughout the conductive lamination as well as the conductive permanent magnet material is shown, together with the transient degradation of the permanent magnet flux density below the knee point. This transient analysis indicates that even an early-stage inter-turn fault can ultimately trigger irreversible demagnetization on significant portions of the rotor magnets, when operating near the limit of the capability curve. In addition, demagnetization caused by an excessive demagnetization MMF can occur within a few electrical cycles, and the corner of the magnet adjacent to the faulty stator winding is the most vulnerable part to becoming irreversibly demagnetized. Furthermore, the impact of the inter-turn fault sevin turn reveals irreversible demagnetization can happen even during a one-turn short-circuit fault, and the irreversible demagnetization ratio is proportional to the number of faulty turns.

8.1.1 Analytical Calculation of Electromagnetic Quantities

A stator winding inter-turn fault is considered to be one of the most common machine-initiated faults that can also cause demagnetization, since such a short circuit can also give rise to a large fault current and generate an excessive demagnetizing MMF at a certain rotor

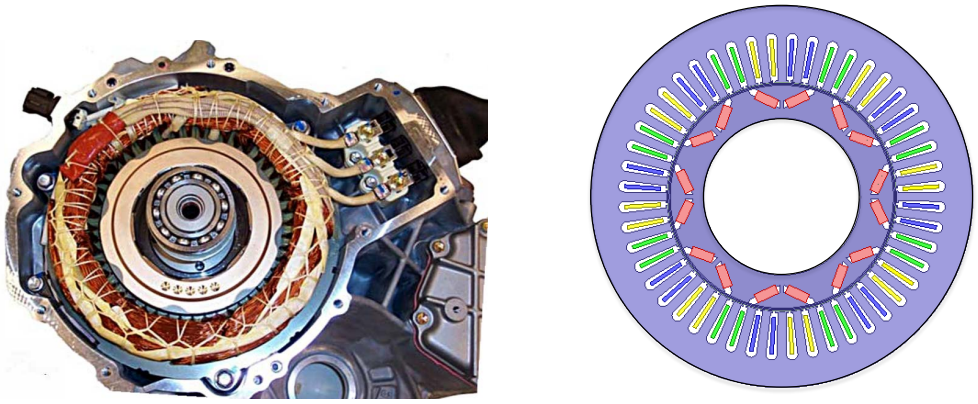

(a) (b)

Figure 8.1: (a) Prius 2004 IPM motor stator and rotor and (b) motor cross section view [28].

position. In addition, despite not being within the scope of this chapter, another side effect is the generation of excessive heat in the faulty turns, as the contact impedance among the shorted turns is much lower compared to that of healthy turns. The winding inter-turn faults generally start at an incipient stage, with an insulation breakdown of one or a few turns in one phase, which in turn leads to a large fault current that would circulate inside the inter-turn short-circuited area, in addition to an overshoot of the phase current. This generates severe heating that could further damage the insulation layer of adjacent healthy turns. Under this mechanism, an inter-turn fault is able to penetrate other neighboring turns that could end up causing more catastrophic failures, such as the line-to-line short-circuit faults and the single-phase line-to-ground short-circuit faults.

For the various PM machine typologies employed in automotive applications, it has been suggested in [112] that burying the magnets inside the rotor, or inside the interior PM (IPM) rotor configuration, generally improves the demagnetization performance compared to the surface-mounted PM rotor type. In addition, the machine configurations with distributed windings are generally more resistant to demagnetization than the configurations with fractional-slot concentrated windings.

The purpose of this section is to investigate the transient demagnetization characteristics of a specific IPM machine designed for automotive applications under the excessive demag-

netizing MMF introduced by the stator turn faults, highlighting the most demagnetization-prone locations on the permanent magnets, as well as identifying the impact of the turn fault severity factor, μ, and the contact resistance, R_f, on the results. The benchmark machine is thus selected as the 50 kW Toyota Prius 2004 IPM motor [81], which is the most demagnetization-resilient PM motor type as suggested in [112], as it features buried magnets and distributed windings. The Prius 2004 IPM motor with its shaft and housing present are illustrated in Figure 8.1(a) and its cross-sectional view is displayed in Figure 8.1(b).

8.2 Stator Inter-Turn Fault Modeling and Demagnetization Characteristics of Rare-Earth Permanent Magnets

The transient demagnetization characteristics of the benchmark IPM machine will be carefully investigated with finite element analysis. The baseline machine has 8 poles, 2 slots per pole per phase, 9 conductors per slot arranged in a single-layered distributed winding pattern, which indicates a total of 72 turns per phase. Each rotor pole contains a single magnet layer that consists of two sintered NdFeB magnets arranged in a V-shape form. For each permanent magnet under observation, the six points M to S, are given special attention during the investigation by recording the flux density and the flux intensity values at these points during the fault events, as identified in Figure 8.2(a).

8.2.1 IPM Stator Inter-Turn Fault Modeling

The modeling of the inter-turn fault begins from the earliest stage with only 1-turn shorted-circuited, with the smallest severity factor μ of 1.4%, as shown in Figure 8.2(b), where the yellow, green and blue sections represent the healthy windings of Phase A, B and C, respectively. The small red sections on top of the yellow region represent the short-circuited single turn that will carry a large circulating current, and its equivalent resistance and inductance will be excluded from phase A while performing the FE analysis. Similarly, models with more faulty turns are represented, as demonstrated in Figure 8.2(c), (d) and (e),

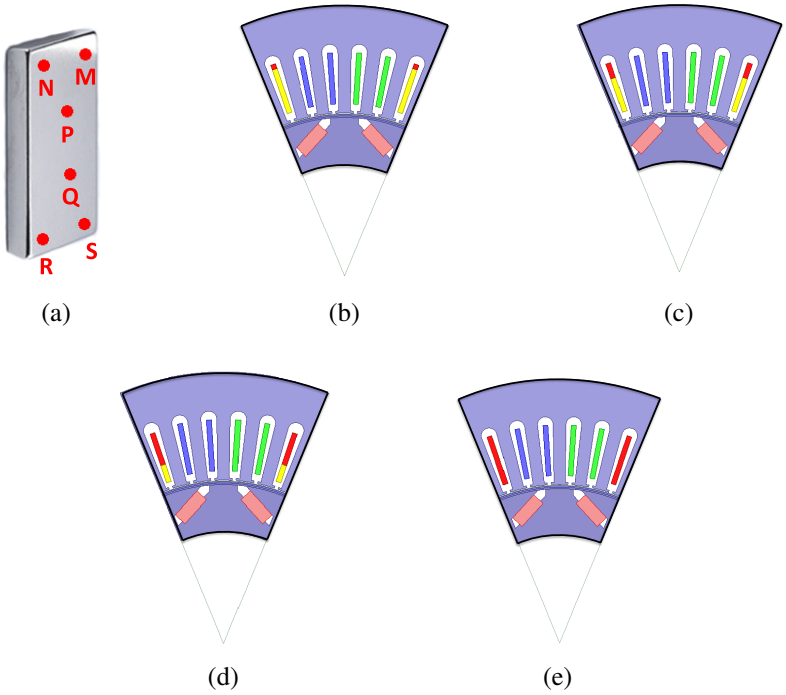

Figure 8.2: (a) Six typical points M to S selected on a permanent magnet for demagnetization analysis; (b) cross-section of 1-turn short-circuited; (c) cross-section of 3-turn short-circuited; (d) cross-section of 6-turn short-circuited and (e) cross-section of 9-turn short-circuited

where 3, 6, and 9 turns are short-circuited, representing a severity factor μ of 4.2%, 8.3% and 12.5%, respectively.

8.2.2 Demagnetization Characteristics of Permanent Magnets

Figure 8.3 shows the normal nonlinear B-H curve of the NdFeB magnets at 150 °C that are used to assess the demagnetization properties of the benchmark Prius 2004 IPM machine. The permanent magnets could experience reversible demagnetization under a moderate temperature rise and a stator current-induced demagnetization MMF, and the extent of the demagnetization intensifies while the PM machine operating point approaches the peak of the motor torque-speed curve envelope. Specifically, the reversible demagnetization region on the B-H curve, indicated by green arrows, embodies the linear region above the knee point, such that the magnet B-H characteristics can migrate back and forth along this line

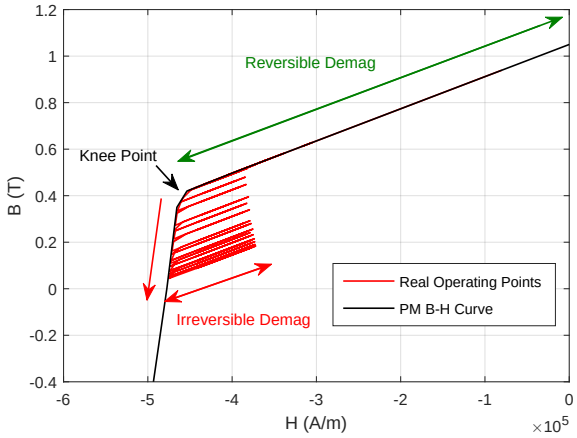

Figure 8.3: Illustration of real-time demagnetization process of permanent magnets.

while exposed to temperature fluctuations and stator current-induced MMF changes. The irreversible loss of magnetic strength can occur very quickly due to the presence of excessive demagnetizing MMFs at high temperatures. It can also be a naturally slow process with aging-related degradation, with changes in the material structure or composition caused by corrosion or shock. In Figure 3, the process for certain regions of the permanent magnets that move towards irreversible demagnetization is described as

1. Firstly, the flux densities of certain affected magnet elements would pass through the knee point and move down along the original B-H curve under the influence of a continuously large demagnetization MMF.

2. At the next instant of time when the magnet is exposed to a re-magnetizing MMF, those sections of the magnet would not be able to go above the knee point again and back to the reversible demagnetization region, but it would rather move along a recovery line starting from its present location and parallel to the original B-H curve linear region.

3. Once exposed to a new demagnetization MMF, the magnet section would demagnetize along the new recovery line until reaching the intersection of the recovery line and the B-H curve. The magnet properties can move down even further along the B-H curve

if the demagnetization MMF still lasts.

4. The processes 1) to 3) would repeat and a large group of recovery lines are expected to form, as represented by the red lines in Figure 3. The operating point may continue moving down into the 3rd quadrant, indicating certain elements of the magnets are in fact reversely-magnetized.

In many practical cases, the demagnetization intensity depends on the combination of the real-time temperature and the demagnetizing MMF. The increased temperature, as long as belong it lies below the curie point typically in the range of 400 to 500°C, will only make the magnet B-H curve "softer" and more vulnerable to demagnetization, while the demagnetizing MMF is the external catalyst that drives the magnets to irreversible demagnetization. The scope of this chapter will be limited to irreversible demagnetization caused by the demagnetizing MMF applied under an assumption of a constant operating temperature. This is a reasonable assumption, apart from the turbulent acceleration stage, as the temperatures at relatively stable conditions tend to change rather slowly compared to electrical terms. The nonlinear B-H characteristics of the magnets in the second and third quadrants, especially in the knee area, is provided as a data set to the finite element simulation in order to facilitate the demagnetization analysis.

8.3 Transient Analysis Results of Demagnetization with A Stator Inter-Turn Fault

In many practical cases, the intensity of the demagnetization depends on the combination of the effects of the real-time temperature changes and the demagnetizing MMF. The increased temperature, as long as it is below the Curie point, which is typically in the range of 400 to 500 °C, will only make the magnet B-H curve "softer" and more vulnerable to demagnetization, while the demagnetizing MMF is the external catalyst that drives the magnets to irreversible demagnetization. The scope of this section will be limited to the irreversible demagnetization caused by the demagnetizing MMF applied under an

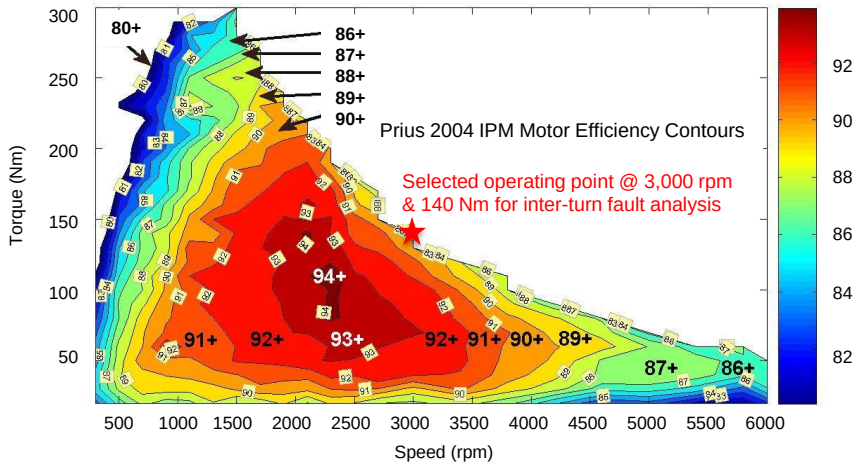

Figure 8.4: Prius 2004 IPM motor efficiency map [81]

assumption of a constant operating temperature, which is an rational assumption apart from the unstable acceleration stage, as the temperatures at relatively stable conditions tend to change rather slowly, when compared to electrical terms. The nonlinear B-H characteristics of the magnets in the second and third quadrant, especially in the knee area, is provided as a data set to the finite element simulation in order to facilitate the demagnetization analysis.

In the proposed finite element analysis, the benchmark IPM motor is running at 3,000 rpm with an input RMS phase current of 106 A and an average torque of 140 N·m, as its operating point is pushed to the vicinity of the maximum torque-speed envelope of its intrinsic capability curve, as shown in Figure 8.4. At this point, the magnetic characteristics of the weakest spots on the magnets are close to the knee point, but have not passed it nor fallen down to the level of irreversible demagnetization.

8.3.1 Input and Circulating Current Response

Figure 8.5 shows the input current and the calculating current response calculated by the FE analysis by introducing an 9-turn (12.5% severity factor) inter-turn short-circuit fault on Phase A at 20 ms, and the contact resistance R_f is estimated to be 10% of the total resistance of those faulty turns at the healthy condition. A moderate increase of the phase A current by 16% is observed as the initiated inter-turn fault is still at an early stage. Figure 8.5(b)

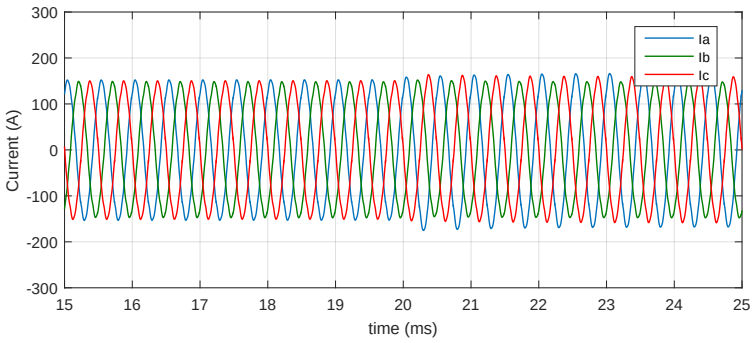

(a)

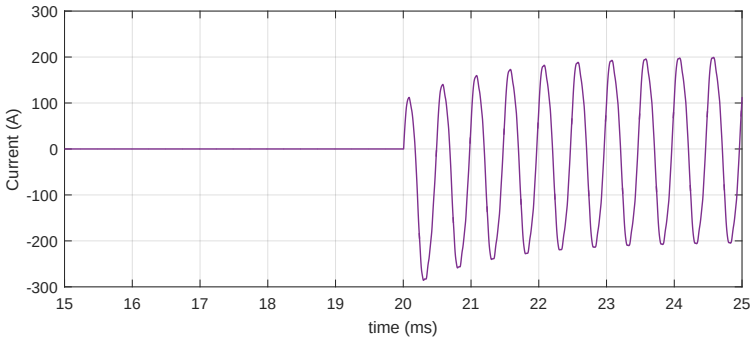

(b)

Figure 8.5: Current Response to the 9-turn (12.5% severity factor) inter-turn short-circuit fault (a) three-phase current and (b) circulating current.

shows the magnitude of the circulating current is approximately 1.4 times of the healthy phase current with a slight phase lag.

8.3.2 Progression of Irreversible Demagnetization

Figure 8.6(a) demonstrates the flux intensity vector distribution diagram of an 9-turn (12.5% severity factor) inter-turn short-circuit fault on Phase A. It can be observed that all of the six points selected on the magnet are exposed to an external magnetic field contributed by the stator windings, and for some magnets the external magnetic field has the same direction as that of the PM magnetization, which serves as the magnetizing MMF that could maintain or recover the strength of these magnets. When the direction is experienced in the opposite direction relative to the PM magnetization, the external magnetic field serves as the demagnetizing MMF. In addition, the magnetic flux density of the six positions on the

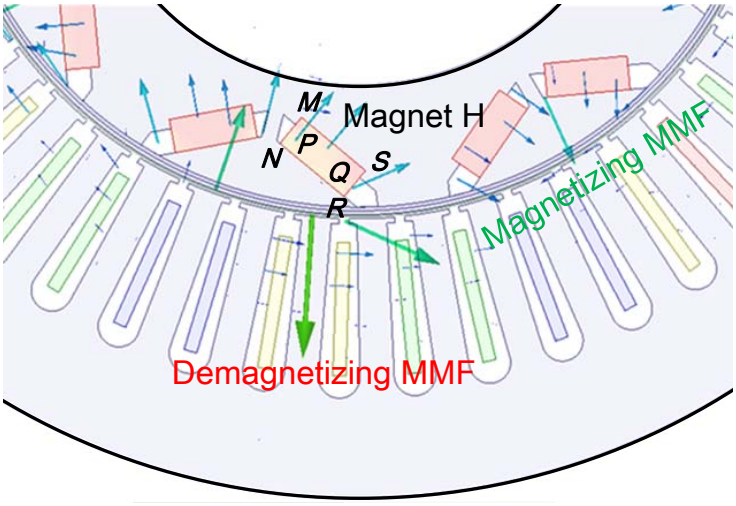

(a)

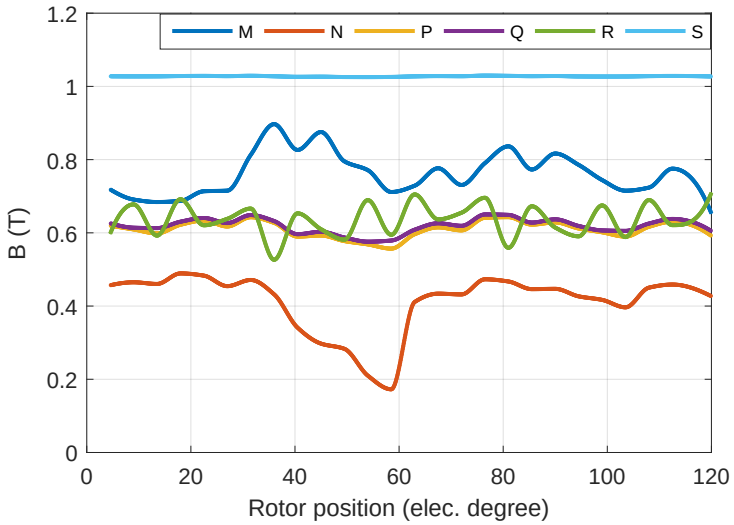

(b)

Figure 8.6: (a) Flux intensity (H) vector distribution diagram and (b) magnetic flux density waveforms for the six points identified inside the magnet following the introduction of an 9-turn (12.5% severity factor) inter-turn fault shown in Figure 2(e).

magnet are plotted against the rotor position in Figure 8.6(b), and it can be identified that point N, the corner of the magnet at the faulty stator winding side, has already entered a state of irreversible demagnetization, as its minimum flux density drops below 0.2 T.

It is important to keep in mind that the all of the magnets experience either some form of magnetizing or demagnetizing MMF during the normal operation of IPM machines, indicating that the magnets are being repeatedly magnetized and demagnetized in a reversible

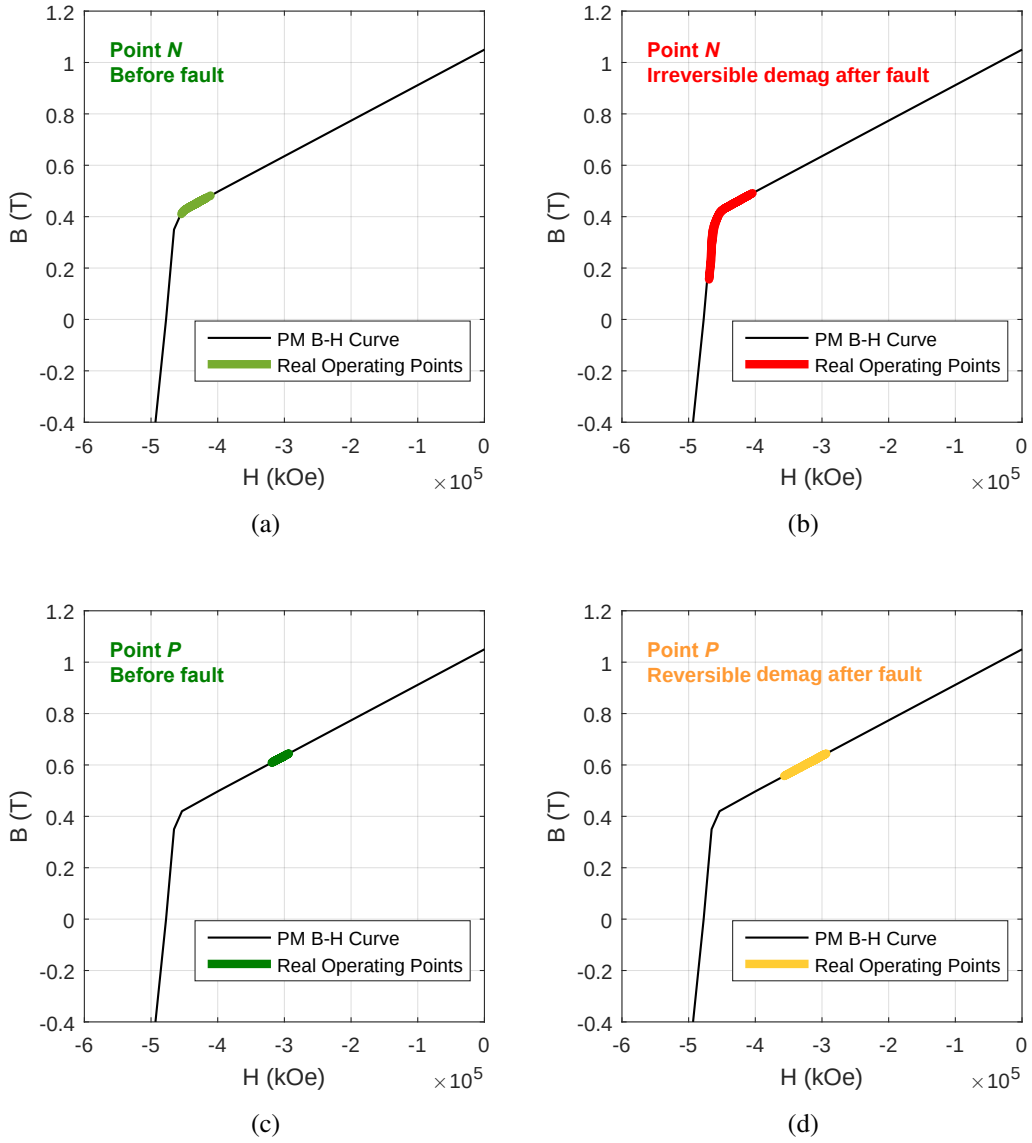

Figure 8.7: B-H curve with an 9-turn (12.5% severity factor) inter-turn fault of (a) point N before the application of inter-turn fault; (b) point N after the application of inter-turn fault; (c) point P before the application of inter-turn fault and (d) point P after the application of inter-turn fault.

manner above the knee point, while the duration and intensity of both of the types of MMF are determined by the motor operating point and its control algorithms. However, the transient current overshoot during faulty conditions, among which the inter-turn fault is still considered a very moderate one when compared to three-phase or single-phase short circuit faults, can intensify both the magnetizing and demagnetizing MMF. This current overshoot

can become detrimental to those locations on the magnet whose magnetic properties are only slightly above the knee point, an example given as point N in Figure 8.7(a), as only a moderate increase of the demagnetizing MMF would lead to the irreversible demagnetization shown in Figure 8.7(b). However, for the center of the magnets or on those positions close to the shaft, this mild increase of the demagnetizing MMF will only bring down the flux density by less than 0.1 T and will ultimately result in a deeper reversible demagnetization that can be ultimately recovered, as depicted in Figure 8.7(c) and (d).

The irreversible demagnetization progress of one PM pair is also presented to show that when the inter-turn fault occurs, the corners of the magnet at the faulty stator winding side are the section that is the most vulnerable to demagnetization. Figures 8.8(a) to (d) demonstrate the contour plots of the two PMs with the maximum value set to the remnant flux level, and it can be observed that all of the positions, except for the two top corners on the motor shaft side, are at least reversibly demagnetized because of the large stator current at this instantaneous operating point, and the 0.5 T to 0.75 T range is also the normal operating range of the PMs working under this condition. To better illustrate the irreversible demagnetization process, another set of contour plots are presented in Figures 6 (e) to (h) where the maximum flux density of the color map is set to 0.6 T, and any regions shaded green should be considered irreversibly demagnetized, as the knee point of this X196 NdFeB magnet is just slightly above 0.4 T.

It can be initially observed that at 200 ms when the inter-turn fault is applied, only a tiny portion of the PM corners at the stator winding side seem to be at the edge of irreversible demagnetization, while the rest of the parts remain healthy. As the condition intensifies under the continued influence of the demagnetizing MMF, the first demagnetization regions appear at 202.75 ms, and additional neighboring regions are affected, until the machine reaches the worst-case condition at 203.25 ms, while the minimum flux density drops below 0.2 T. The time that elapses from the triggering of the fault to the worst-case scenario highly depends on the rotor position and speed, but it generally falls within one or a few electric

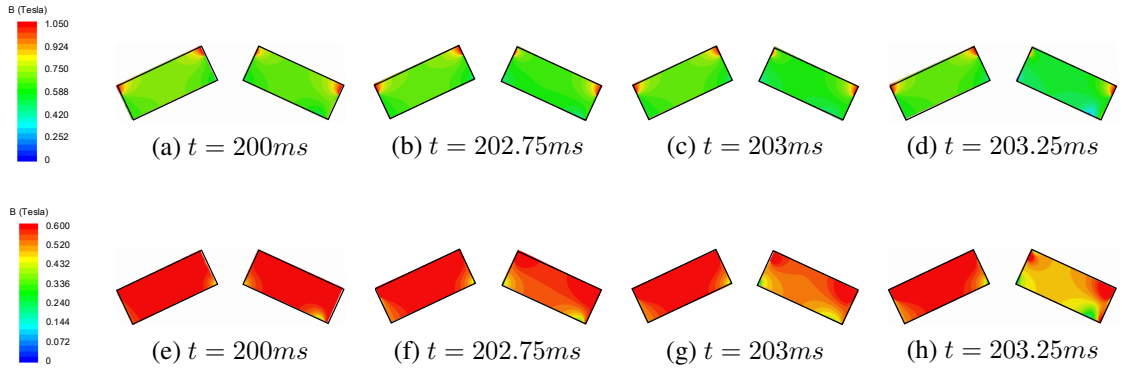

Figure 8.8: Contour plots of the irreversible demagnetization progress with an 9-turn (12.5% severity factor) inter-turn fault.

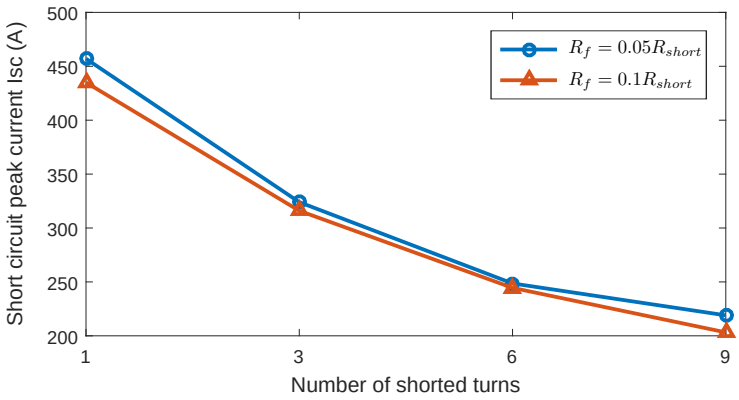

Figure 8.9: Illustration of the inter-turn fault short-circuit current with respect to the fault severity μ and contact resistance R_f.

cycles and will generally lie within the millisecond range.

8.3.3 Impact of the Inter-turn Fault Severity Factor and Equivalent Fault Resistance

The above figures and analyses focused primarily on the inter-turn short-circuit fault at an operating point of 3,000 rpm and 140 Nm, with a fault severity factor $\mu = 12.5\%$, and by an equivalent fault resistance R_f that is equal to $1/20$ of the total resistance of the shorted 9 turns. By observing Fig. 8.8, it is evident that an irreversible demagnetization has already occurred even though the turn fault is still at an incipient stage. Therefore, from a research point of view, it is of practical interest to investigate the impact of the inter-turn fault severity factor μ and the equivalent resistance of the fault, R_f, on the emergence of

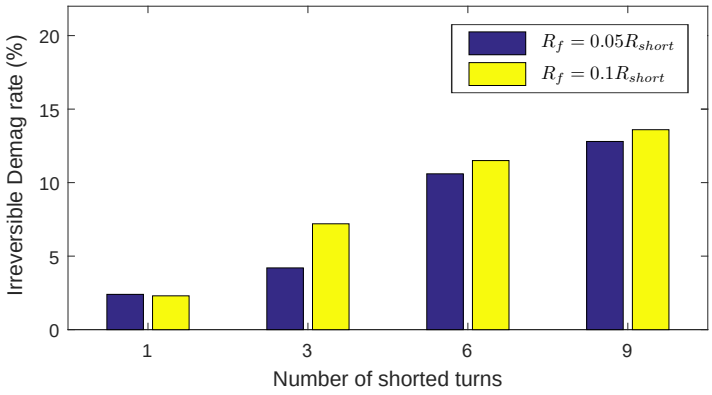

Figure 8.10: Percentage of the irreversible demagnetization area over the entire magnet surface area for different fault severity μ and contact resistance R_f.

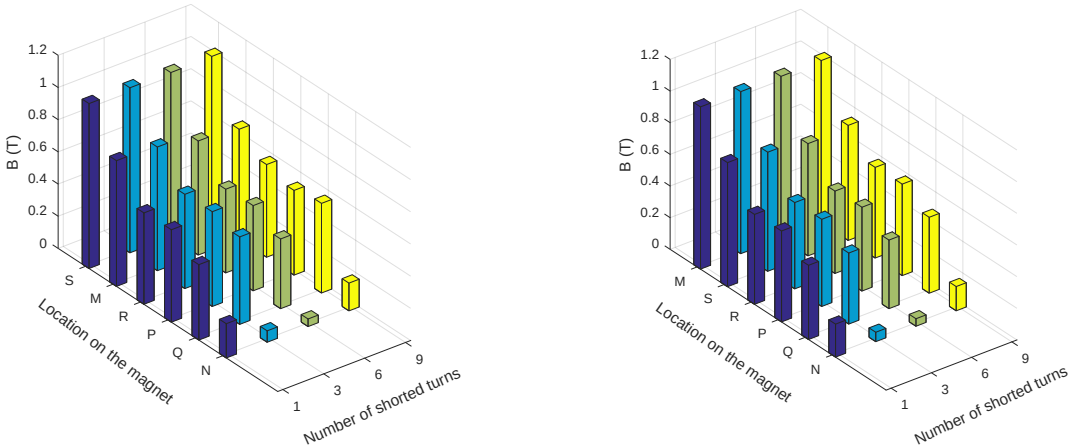

(a) (b)

Figure 8.11: The minimum flux density of the six points M–S specified on the magnet with respect to the number of shorted turns (fault severity μ) and contact resistance R_f: (a) $R_f = 0.05R_{short}$ and (b) $R_f = 0.1R_{short}$.

this irreversible demagnetization. In other words, it is of interest to determine whether there exists some threshold values of these parameters to indicate the occurrence of a fault, or if there is potentially no impact at all.

Keeping this in mind, therefore, the same techniques and procedures described in this chapter are applied in order to analyze the phenomenon of irreversible demagnetization by varying the fault severity factor μ and the equivalent fault resistance R_f. As demonstrated in Figure 8.2, four stages of fault severity of 1-turn, 3-turn, 6-turn and 9-turn faults are taken

into consideration, while the fault resistance R_f is set to either $1/10$ or $1/20$ of the total resistance for the total number of turns being shorted, generating a sum of 8 cases.

Figure 8.9 illustrates the peak short-circuit current during an inter-turn fault with respect to the fault severity μ and the contact resistance R_f, demonstrating an inversely-proportional relationship between the fault current and the total number of turns that are being shorted. Since there are a total of 72 turns per phase for this IPM motor, shorting 1 or 9 turns would not make a huge difference to its self-impedance per phase. However, since the shorted turns are from the same phase and also are of the same slot, the shorted-path would be exposed to the same magnetic flux linkage and would have some current induced inside this loop, and then the impedance of the shorted-path would be deterministic to this portion of current. It is also revealed that the fault current can increase even further with a decrease of the contact resistance R_f.

The percentage of the area suffering from irreversible demagnetization over the entire surface area of the magnet is shown in Figure 8.10, and it can be observed that the demagnetization intensifies along with the increase of the fault severity μ and the contact resistance R_f, with a peak demagnetization rate of around 15%. Figure 8.11 demonstrates the minimum flux density of the six points M to S, as specified in Figure 2, against the number of shorted turns, while the results featuring the different contact resistances are shown in Figures 10(a) and (b), respectively. It is interesting to see the minimum values of point N, the point that is the most vulnerable to irreversible demagnetization, is obtained with 6 turns shorted, rather than 9 turns.

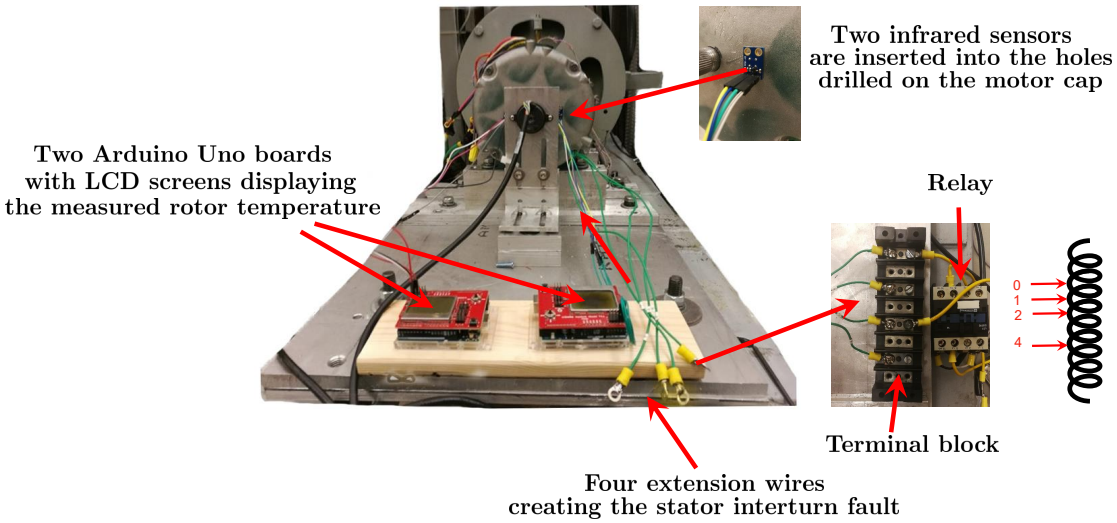

Figure 8.12: Experimental setup for introducing the inter-turn fault to the IPM machine.

8.4 Experimental Results Assessing Demagnetization Conditions under Inter-Turn Short-Circuit Faults

8.5 Chapter Summary

This chapter investigates the dynamic demagnetization characteristics of the Prius 2004 IPM motor with an inter-turn short-circuit fault at an incipient stage. Through the fault analysis, the current response and the progress towards irreversible demagnetization are all thoroughly presented, and demagnetization time falls within one or a few electric cycles and are typically within the millisecond range. In addition, it is identified that the corner of the magnet at the faulty stator winding side is the most vulnerable to irreversible demagnetization. Furthermore, the impacts of the fault severity factor μ and the equivalent contact resistance R_f are thoroughly analyzed, and they ultimately indicate the fact that an irreversible demagnetization can occur during a single-turn short-circuit fault, and the irreversible demagnetization ratio is proportional to the number of faulty turns.

The proposed analysis establishes an analysis framework as well as a case study on a real EV-scaled motor, which is beneficial to the design and optimization of IPM machines. This is especially true in regards to determining the optimal shape and placement of the

permanent magnets for the purpose of avoiding irreversible demagnetization at the incipient stage of the inter-turn short-circuit faults.

CHAPTER 9

CONCLUSIONS, CONTRIBUTIONS, AND RECOMMENDED FUTURE WORK

9.1 Conclusions

This dissertation has proposed a method carrying out the analytical design and optimization of switched reluctance machines (SRM), as influenced by the saturation and commutation effects, and visualized with advanced machine learning algorithms, specifically under multiple operating points. It has also proposed a method for the thermal monitoring of interior permanent magnet (IPM) machines, and it has concluded as demagnetization assessment under the stator inter-turn short-circuit fault.

Chapter One has introduced the background information regarding the design and optimization of electrical machines and stated the objective of this research.

Chapter Two presents a comprehensive review of the design of SRMs, including aspects of the mathematical modeling of the electromagnetic field and multi-objective optimization. The mathematical modeling approaches can be classified into numerical and analytical methods. Performance indices of the various multi-objective optimization methods typically applied to SRMs, including evolutionary algorithms, are systematically introduced and compared. Finally, state-of-the-art technologies are presented for SRM designs and for electric/hybrid electric vehicles, and then compared to existing commercial designs in the market.

In Chapter Three, the principle and progress towards irreversible demagnetization of permanent magnets are systematically introduced, along with different fault modes that may trigger the excessive temperature or demagnetization field. While previous attempts are made to investigate the demagnetization progress of IPM machines under the drive inverter-initiated three-phase-to-ground and single-phase-to-ground short-circuit faults, less

attention has been paid to demagnetization under the most common fault type – the inter-turn short-circuit fault.

Chapter Four has presented multi-objective design and optimization methods for the switched reluctance machines based on rigorous analytical equations and particle swarm optimization algorithms. The proposed method is more efficient than the traditional design methods as it can find an optimal design without the use of heuristic approaches. An analytical benchmark model of a 6/4 SRM is presented and results are verified by an FEA simulation. A PSO is performed on 4/2 and 6/4 SRMs, and the optimized design is found with respect to multiple machine performance indices, through either weighted-sum or vector objective functions. The optimal design of SRMs can be found and the approximation of the Pareto front can be completed in hours on an ordinary laptop computer, saving a significant amount of time and effort for machine designers. The accuracy of the optimized design is then validated by the post-design FEA examination. This method is also compatible with different machine design requirements in order to efficiently and accurately generate a multi-objective optimized switched reluctance machine for targeted applications.

Chapter Five has proposed an ultra-fast analytical design approach for the multi-objective design and optimization of an SRM, coupled with active current profile optimization. In addition, the proposed method is very time-saving, and offers machine designers accurate, handy and convenient initial designs, which can be further verified or fine-tuned by FEA. This chapter has also compared the nonlinear Pareto front generated by three popular multi-objective optimization algorithms. Statistical results, which correlate with all data obtained with different quality indicators, point to the superiority of DE algorithms over NSGA-II and PSO, in terms of the convergence speed and the quality of the final Pareto front. In addition, a new perspective on applying the multi-objective Bayesian optimization algorithm (MOBOA) is presented. Specifically, Gaussian processes are trained to model the employed objective function, which is refined incrementally via Bayesian posterior updating each time when new machine design candidates are generated. In turn, the developed GP model of

the objective function is used to determine the next round of input vectors to evaluate. The results show that MOBOA can achieve better approximations of the Pareto front with a small number of evaluations compared to the NSGA-II algorithm.

In Chapter Six, a case study on an SRM design optimization case study with four objectives is visualized with the help of self-organizing maps (SOM) visualizing data clusters, component planes and data projections. It is demonstrated that compared with the conventional visualization method of parallel coordinates or scatter plots with 2-D Pareto fronts, the SOM offers intuitive, simple and straightforward information that could assist machine designers in their decision-making process in choosing the most appropriate designs candidate for any targeted applications. To further simplify the many-objective optimization of electric machines considering multiple operating points, the t-SNE algorithm has been successfully applied to visualize SRM design candidates optimized under multiple operating points, and these visualizations are significantly better than those produced by other techniques such as PCA and Isomap. By projecting the high-dimensional data onto a low-dimensional map, t-SNE is able to provide more informative and intuitive insights to machine designers attempting to select the initial designs, to those attempting to perform a second round of optimization and fine-tuning, or for use in the final prototype validation.

Chapter seven has proposed a novel nonintrusive thermal monitoring scheme for the permanent magnet inside IPM machines using high-frequency flux and torque injection. The proposed method requires no additional sensors or hardware except for those already available in IPMSM drives. Compared to the temperature measurement taken by infrared sensors, the maximum error of the proposed method is less than 3 °C at the steady state condition.

Chapter Eight has investigated dynamic demagnetization characteristics of the Prius 2004 IPM motor, with an inter-turn short-circuit fault at an incipient stage. Through the fault analysis, the current response and the progress towards irreversible demagnetization are thoroughly presented, and demagnetization time falls within one or a few electric cycles,

and it typically in the millisecond range. In addition, it is identified that the corner of the magnet that is at the faulty stator winding side is the part that is the most vulnerable part to irreversible demagnetization. Furthermore, impacts of the fault severity factor μ and the equivalent contact resistance R_f are thoroughly analyzed, indicating an irreversible demagnetization can occur during a single-turn short-circuit fault, and the irreversible demagnetization ratio is proportional to the number of faulty turns.

9.2 Contributions

The main contributions of this research are summarized as follows:

1. A comprehensive literature survey of recent progresses in the multi-objective design and optimization of switched reluctance machines has been presented. In addition, SRMs designed for EV applications have been summarized and compared with other machine types found in commercial EVs. Various SRMs are compared in terms of the power density, the maximum power, and the overall efficiency retrieved from the efficiency map.

2. A comprehensive literature survey of existing methods evaluating the demagnetization severity of IPM machines has been presented. Various driver inverter and machine faults that can trigger the irreversible demagnetization have been summarized, with an emphasis on impacts of the stator inter-turn fault.

3. A novel electromagnetic analytical multi-objective design method of switched reluctance machines has been developed, which needs only five prime design variables but is able to design SRMs in fine details. The advantage over the traditional and other existing SRM design methods is that this proposed method does not have the heuristic selection of the design variables such as the saturation coefficient of inductance. The computing time is almost negligible and the design cycle is significantly reduced

compared to the traditional heuristic machine design method or the numerical method such as FEA.

4. A new method for multi-objective designs of switched reluctance machines with active current profile integration has been developed. The effect of turn-on and turn-off angles on the performance of SRMs can thus be comprehensively investigated from the quantitative comparison of results. The proposed method is fast and accurate as it has taken both the commutation and saturation effects into account.

5. A systematic comparison of the efficiency and effectiveness of three mainstream multi-objective optimization algorithms (MOOAs) has been performed on the SRM design and optimization, and it has been identified that the Differential Evolution offers an overall superior performance compared to the Particle Swarm Optimization and the Nondominated Sorting Genetic Algorithm in terms of exploration and exploitation.

6. A novel implementation of the Self-Organizing Map has been proposed to visualize the design and optimization of SRMs with four or more objectives considering a single operating point. The clustering and visualization of each objective have provided intuitive results when compared to the traditional visualization approaches, such as the parallel coordinate and the scatter plot of the Pareto Front, thereby facilitating machine designers with the decision-making process. In addition, a new implementation of the t-Stochastic Neighboring Embedding has been proposed to visualize the design and optimization of SRMs with more than ten objectives at multiple operating points. Hundreds of design candidates can be distinctively clustered in the high-dimensional space, when compared to the traditional Principal Component Analysis (PCA) and Isomap. The centroid of each cluster can be selected for the later fine-tuning process.

7. An innovative application of the Bayesian optimization on the multi-objective optimization of electric machines has been proposed. The Bayesian optimization is able to gather the function evaluations as data and form the posterior distribution

over the objective function, which in turn can be used to determine the next round of query points with the highest probability of improvement. Compared to the popular stochastic multi-objective optimization algorithms, the result obtained by the Bayesian optimization has proven to be more efficient and able to better approximate the Pareto front with fewer number of iterations.

8. A sensorless rotor thermal-monitoring method has been proposed for IPM machines with direct torque controls. The major difficulty encountered by the existing methods, the intrusive process of installing additional sensors with wireless communication capability, has been mitigated with the proposed method by injecting either high-frequency flux or torque signals with drive inverters. Even with only 3% of injected high-frequency signal, the method achieves a temperature estimation error less than 3 °C for the steady-state condition.

9. A flexible and detailed finite-element model has been built for the IPM machines with the stator inter-turn short-circuit fault. The model can be easily modified to simulate the turn fault with any number of shorted turns so that better understanding of the demagnetization behaviors during the fault transient can be obtained with regard to the time duration and severity of the fault. Results have shown that the irreversible demagnetization are likely to occur along the motor's maximum capability curve, and the corner of magnets closest to the stator windings and aligned to the d-axis is the most vulnerable location for irreversible demagnetization.

The research work presented in this dissertation has resulted in the following publications [148, 211–232]:

Journal Papers:

[J1] S. Zhang, S. Li, R. G. Harley, and T. G. Habetler, "Performance evaluation and comparison of multi-objective optimization algorithms for the analytical design of

switched reluctance machines," *CES Trans. Electri. Mach. Syst.*, vol. 1, no. 1, pp. 58-65, Mar. 2017.

[J2] S. Li, S. Zhang, J. Dang, T. Habetler and R. G. Harley, “Analytical calculation of the phase inductance profile of switched reluctance machines," *IEEE Trans. Energy Convers.*, vol. PP, no. PP, pp. PP-PP, 2019.

[J3] S. Li, S. Zhang, C. Gong, T. G. Habetler and R. G. Harley, “An enhanced analytical calculation of the phase inductance of switched reluctance machines," *IEEE Trans. Ind. Appl.*, vol. 55, no. 2, pp. 1392–1407, Mar./Apr. 2019.

[J4] S. Li, S. Zhang, T. G. Habetler and R. G. Harley, “Modeling, design optimization and applications of switched reluctance machines – A review," *IEEE Trans. Ind. Appl.*, vol. 55, no. 3, pp. 2660–2681, May/June 2019.

Preprint Papers:

[P1] S. Zhang, S. Zhang, B. Wang, and T. G. Habetler, "Machine learning and deep learning algorithms for bearing fault diagnostics – A comprehensive review," *arXiv preprint arXiv:1901.08247*, 2019.

Conference Papers:

[C1] S. Li, S. Zhang, J. Dang, T. G. Habetler, and R. G. Harley, "Calculating the unsaturated inductance of 4/2 switched reluctance motors at arbitrary rotor positions based on partial differential equations of magnetic potentials," in *Proc. North Amer. Power Symp. (NAPS)*, Charlotte, NC, Oct. 2015, pp. 1-8.

[C2] S. Zhang, S. Li, J. Dang, T. G. Habetler, and R. G. Harley, "Multi-objective design and optimization of generalized switched reluctance machines with particle swarm intelligence," in *Proc. IEEE Energy Conv. Congr. Expo. (ECCE)*, Milwaukee, WI, Sept. 2016, pp. 1-7.

[C3] S. Li, S. Zhang, T. G. Habetler, and R. G. Harley, "Fast and accurate analytical calculation of the unsaturated phase inductance profile of 6/4 switched reluctance machines," in *Proc. IEEE Energy Conv. Congr. Expo. (ECCE)*, Milwaukee, WI, Sept. 2016, pp. 1-8.

[C4] S. Zhang, S. Li, R. G. Harley, and T. G. Habetler, "A multi-objective analytical design approach of switched reluctance machines with integrated active current profile optimization," in *Proc. IEEE Int. Electr. Mach. Drives Conf. (IEMDC)*, Miami, FL, 2017, pp. 1-6.

[C5] S. Li, S. Zhang, T. G. Habetler, and R. G. Harley, "A survey of multiphysics modeling and design optimization of switched reluctance machines," in *Proc. IEEE Int. Electr. Mach. Drives Conf. (IEMDC)*, Miami, FL, 2017, pp. 1-7.

[C6] S. Li, S. Zhang, C. Jiang, T. G. Habetler, and R. G. Harley, "A fast control-integrated and multiphysics-based multi-objective design optimization of switched reluctance machines," in *Proc. IEEE Energy Conv. Congr. Expo. (ECCE)*, Cincinnati, OH, Oct. 2017, pp. 730-737.

[C7] S. Zhang, S. Li, L. He, J. A. Restrepo, and T. G. Habetler, "A high-frequency rotating flux injection based rotor thermal monitoring scheme for direct-torque-controlled interior permanent magnet synchronous machines," in *Proc. IEEE Int. Electr. Mach. Drives Conf. (IEMDC)*, Miami, FL, May. 2017, pp. 1-6.

[C8] S. Zhang, S. Li, L. He, J. A. Restrepo, and T. G. Habetler, "A high-frequency torque injection-based rotor thermal monitoring scheme for direct-torque-controlled interior permanent magnet synchronous machines," in *Proc. IEEE Energy Conv. Congr. Expo. (ECCE)*, Cincinnati, OH, Oct. 2017, pp. 3552-3558.

[C9] S. Zhang, and T. G. Habetler, "A transient model of interior permanent magnet machines under stator winding inter-turn short circuit faults," in *Proc. 43rd Annu.*

Conf. IEEE Ind. Electron. Soc. (IECON'17), Bejing, China, Oct./Nov. 2017, pp. 1-6.

[C10] S. Zhang, and T. G. Habetler, "Transient demagnetization characteristics of permanent magnet synchronous machines with stator inter-turn short circuit faults for automotive applications," in *Proc. IEEE Energy Conv. Congr. Expo. (ECCE)*, Portland, OR, Sep. 2018, pp. 1661-1667.

[C11] S. Zhang, R. G. Harley, and T. G. Habetler, "An efficient multi-objective Bayesian optimization approach for automated analytical design of switched reluctance machines," in *Proc. IEEE Energy Conv. Congr. Expo. (ECCE)*, Portland, OR, Sep. 2018, pp. 4290-4295.

[C12] S. Zhang, S. Li, R. G. Harley, and T. G. Habetler, "Visualization and data mining of multi-objective electric machine optimizations with self-organizing maps: a case study on switched reluctance machines," in *Proc. IEEE Energy Conv. Congr. Expo. (ECCE)*, Portland, OR, Sep. 2018, pp. 4296-4302.

[C13] S. Zhang, S. Zhang, S. Li, and T. G. Habetler, "Visualization of multi-objective switched reluctance machine optimization under multiple operating conditions with t-SNE," in *Proc. IEEE Energy Conv. Congr. Expo. (ECCE)*, Baltimore, MD, Sep. 2019.

Research activities outside the scope of this dissertation has resulted in the following publications:

Conference Papers:

[C14] S. Zhang, A. M. Qwbaiban, J.-M. Huh, and T. G. Habetler, "Dimension and mechanical structure design of low-cost heliostats in concentrated solar power plants," in *Proc. IEEE Energy Conv. Congr. Expo. (ECCE)*, Baltimore, MD, Sep. 2019.

[C15] S. Zhang, B. Wang, C. Lin, D. Lin, K. H. Teo, and T. G. Habetler, "Quantification of rolling-element bearing fault severity of induction machines," in *Proc. IEEE Int.*

Electr. Mach. Drives Conf. (IEMDC), San Diego, CA, May. 2019, pp. 1-6.

[C16] S. Zhang, S. Zhang, B. Wang, and T. G. Habetler, "Deep learning algorithms for bearing fault diagnostics – A review," in *Proc. IEEE Int. Symp. Diagno. Power Electron. Drives (SDEMPED)*, Toulouse, France, Aug. 2019.

[C17] S. Li, S. Zhang, C. Jiang, L. He, and R. G. Harley, “An enhanced active DC-flux injection based approach for thermal monitoring of induction machines with direct torque control schemes," in *Proc. IEEE Energy Conv. Congr. Expo. (ECCE)*, Cincinnati, OH, Oct. 2017, pp. 3537–3544.

[C18] T. P. Tshimanga, S. Zhang, E. Bezabih, L. He, V. Iyer, amd R. G. Harley, “Stator temperature estimation of open-loop controlled induction machines via active DC voltage injection," in *Proc. North Amer. Power Symp. (NAPS)*, Charlotte, NC, Oct. 2015, pp. 1–5.

In addition, several more journal and conference papers, based on the research presented in this thesis, are being prepared.

9.3 Recommended Future Work

While this PhD dissertation has presented contributions to various aspects of design optimization of switched reluctance machines and condition monitoring of demagnetization of interior permanent magnet machines, there are several directions in which further research could build upon the results presented in this work.

1. A cost model can be developed for switched reluctance machines and added into the design objective. The cost of the product is always one of the major concerns for manufacturers. Hence, the proposed method will find more applications if machine cost is included.

2. The majority of works on electric machine optimization employs some gradient-free, population-based stochastic methods. Besides their simplicity, this popularity is also attributed to the difficulty while taking derivatives of the motor's analytical model, since certain variables can only be discrete values or integers, such as the number of turns in a stator slot. However, the recent progress on nonsmooth optimization, such as the stochastic gradient descent, as well as the mixed integer nonlinear programming, may have the potential to approximate the derivatives and perform machine optimizations with deterministic methods.

3. For different applications, there might be special design considerations and requirements. For example, a good flux-weakening capability and a high torque burst capability are desired for traction motors in electric vehicle applications. Such special application-based challenges are presently solved by designer's experience and by trial-and-error. Since the proposed design method already designs SRMs in fine details, these special considerations can be possibly added into the proposed design method. Some multi-objective optimization algorithms may possibly find designs that not only meet those additional challenges, but also have better performances (higher efficiency, cooler, less weight, etc.) than existing designs.

4. Theoretically investigate the relationship between the induced eddy current and the magnetic resistance, which can provide general guidelines and a solid theoretical ground for applying this high-frequency signal injection scheme to monitor the magnet temperature on any permanent magnet machine.

5. Research can be carried out to apply machine learning and deep learning algorithms on the thermal monitoring and demagnetization assessment of IPM machines. The time-series data collected may be those already measured, such as the electric current, speed, and stator winding temperatures. These algorithms can typically learn and identify convoluted fault features not commonly observable or interpretable by humans.

REFERENCES

[1] H. Lee and G. Lovellette, "Will electric cars transform the US market?" *HKS Faculty Research Working Paper Series RWP11-032, John F. Kennedy School of Government, Harvard University.*, 2011.

[2] E. Musk, *The secret Tesla Motors master plan (just between you and me)*, [Online]. Available: https://www.tesla.com/blog/secret-tesla-motors-master-plan-just-between-you-and-me.

[3] *How it works - Google self-driving car project*, [Online]. Available: https://www.google.com/selfdrivingcar/how/.

[4] "The Rare-Earth Crisis", *MIT Technology Review, April 2011*, [Online]. Available: https://www.technologyreview.com/s/423730/the-rare-earth-crisis.

[5] "Final Report on Assessment of Motor Technologies for Traction Drives of Hybrid and. Electric Vehicles, *U.s. Department of Energy Report, March 2011*, [Online]. Available: https://info.ornl.gov/sites/publications/files/pub28840.pdf.

[6] A. Emadi, *Advanced electric drive vehicles*. CRC Press, 2014.

[7] T. Jahns, "Getting rare-earth magnets out of ev traction machines: A review of the many approaches being pursued to minimize or eliminate rare-earth magnets from future ev drivetrains," *IEEE Electrific. Mag.*, vol. 5, no. 1, pp. 6–18, Mar. 2017.

[8] C. Zwyssig, J. W. Kolar, and S. D. Round, "Megaspeed drive systems: Pushing beyond 1 million r/min," *IEEE/ASME Trans. Mechatronics*, vol. 14, no. 5, pp. 564–574, Oct. 2009.

[9] A. Tenconi, S. Vaschetto, and A. Vigliani, "Electrical machines for high-speed applications: Design considerations and tradeoffs," *IEEE Trans. Ind. Electron.*, vol. 61, no. 6, pp. 3022–3029, Jun. 2014.

[10] D. Gerada, A. Mebarki, N. L. Brown, C. Gerada, A. Cavagnino, and A. Boglietti, "High-speed electrical machines: Technologies, trends, and developments," *IEEE Trans. Ind. Electron.*, vol. 61, no. 6, pp. 2946–2959, Jun. 2014.

[11] E. Bostanci, M. Moallem, A. Parsapour, and B. Fahimi, "Opportunities and challenges of switched reluctance motor drives for electric propulsion: A comparative study," *IEEE Trans. Transp. Electri.*, vol. 3, no. 1, pp. 58–75, Mar. 2017.

[12] K. M. Rahman, B. Fahimi, G. Suresh, A. V. Rajarathnam, and M. Ehsani, "Advantages of switched reluctance motor applications to EV and HEV: Design and control issues," *IEEE Trans. Ind. Appl.*, vol. 36, no. 1, pp. 111–121, Jan. 2000.

[13] C. Kamalakannan, V. Kamaraj, S. Paramasivam, and S. R. Paranjothi, "Switched reluctance machine in automotive applications – a technology status review," in *Proc. Int. Conf. Electri. Energy Syst.*, Jan. 2011, pp. 187–197.

[14] A. Mitra and A. Emadi, "On the suitability of large switched reluctance machines for propulsion applications," in *Proc. IEEE Transp. Electri. Conf.Expo. (ITEC)*, Jun. 2012, pp. 1–5.

[15] Y. Gao and M. D. McCulloch, "A review of high power density switched reluctance machines suitable for automotive applications," in *Proc. Int. Conf. Electri. Mach.*, Sep. 2012, pp. 2610–2614.

[16] A. M. Omekanda, "Switched reluctance machines for EV and HEV propulsion: State-of-the-art," in *Proc. IEEE Workshop Electri. Mach. Design, Control Diagno. (WEMDCD)*, Mar. 2013, pp. 70–74.

[17] A. Chiba and K. Kiyota, "Review of research and development of switched reluctance motor for hybrid electrical vehicle," in *Proc. IEEE Workshop Electri. Mach. Design, Control Diagno. (WEMDCD)*, Mar. 2015, pp. 127–131.

[18] N. Zabihi and R. Gouws, "A review on switched reluctance machines for electric vehicles," in *Proc. IEEE Int. Symp. Ind. Electron. (ISIE)*, Jun. 2016, pp. 799–804.

[19] B. Burkhart, A. Klein-Hessling, I. Ralev, C. P. Weiss, and R. W. De Doncker, "Technology, research and applications of switched reluctance drives," *CPSS Trans.Power Electron. Appl.*, vol. 2, no. 1, pp. 12–27, 2017.

[20] J. D. Widmer, R. Martin, and B. C. Mecrow, "Optimization of an 80-kW segmental rotor switched reluctance machine for automotive traction," *IEEE Trans. Ind. Appl.*, vol. 51, no. 4, pp. 2990–2999, Jul. 2015.

[21] K. Kiyota and A. Chiba, "Design of switched reluctance motor competitive to 60-kW IPMSM in third-generation hybrid electric vehicle," *IEEE Trans. Ind. Appl.*, vol. 48, no. 6, pp. 2303–2309, Nov. 2012.

[22] M. Takeno, A. Chiba, N. Hoshi, S. Ogasawara, M. Takemoto, and M. A. Rahman, "Test results and torque improvement of the 50-kW switched reluctance motor de-

signed for hybrid electric vehicles," *IEEE Trans. Ind. Appl.*, vol. 48, no. 4, pp. 1327–1334, Jul. 2012.

[23] K. Kiyota, T. Kakishima, and A. Chiba, "Comparison of test result and design stage prediction of switched reluctance motor competitive with 60-kW rare-earth pm motor," *IEEE Trans. Ind. Electron.*, vol. 61, no. 10, pp. 5712–5721, Oct. 2014.

[24] D. Lin, P Zhou, S Stanton, and Z. Cendes, "An analytical circuit model of switched reluctance motors," *IEEE Trans. Magn.*, vol. 45, no. 12, pp. 5368–5375, Nov. 2009.

[25] N. K. Sheth and K. Rajagopal, "Calculation of the flux-linkage characteristics of a switched reluctance motor by flux tube method," *IEEE Trans. Magn.*, vol. 41, no. 10, pp. 4069–4071, Oct. 2005.

[26] F. E. Fleming and C. S. Edrington, "Real-time emulation of switched reluctance machines via magnetic equivalent circuits," *IEEE Trans. Ind. Electron.*, vol. 63, no. 6, pp. 3366–3376, Jan. 2016.

[27] J. M. Kokernak and D. A. Torrey, "Magnetic circuit model for the mutually coupled switched-reluctance machine," *IEEE Trans. Magn.*, vol. 36, no. 2, pp. 500–507, Mar. 2000.

[28] R. Krishnan, *Switched reluctance motor drives: modeling, simulation, analysis, design, and applications*. New York: CRC Press, 2001.

[29] R. Krishnan, M Abouzeid, and X Mang, "A design procedure for axial field switched reluctance motors," in *Proc. IEEE Ind. Appl. Soc. Annu. Meet.*, 1990, pp. 241–246.

[30] A. Radun, "Analytically computing the flux linked by a switched reluctance motor phase when the stator and rotor poles overlap," *IEEE Trans. Magn.*, vol. 36, no. 4, pp. 1996–2003, Jul. 2000.

[31] ——, "Analytical calculation of the switched reluctance motor's unaligned inductance," *IEEE Trans. Magn.*, vol. 35, no. 6, pp. 4473–4481, Nov. 1999.

[32] A. V. Radun, "Design considerations for the switched reluctance motor," *IEEE Trans. Ind. Appl.*, vol. 31, no. 5, pp. 1079–1087, Sep. 1995.

[33] Y. Tang and J. A. Kline, "Modeling and design optimization of switched reluctance machine by boundary element analysis and simulation," *IEEE Trans. Energy Convers.*, vol. 11, no. 4, pp. 673–680, Dec. 1996.

[34] Y. Tang, "Characterization, numerical analysis, and design of switched reluctance motors," *IEEE Trans. Ind. Appl.*, vol. 33, no. 6, pp. 1544–1552, Nov. 1997.

[35] T. Miller, "Nonlinear theory of the switched reluctance motor for rapid computer-aided design," *IEE Proc. B (Electri. Power Appl.)*, vol. 137, 337–347(10), 6 Nov. 1990.

[36] Y. Duan, "Method for design and optimization of surface mount permanent magnet machines and induction machines," PhD thesis, Georgia Institute of Technology, Dec. 2010.

[37] R. Mikail, I. Husain, Y. Sozer, M. S. Islam, and T. Sebastian, "Torque-ripple minimization of switched reluctance machines through current profiling," *IEEE Trans. Ind. Appl.*, vol. 49, no. 3, pp. 1258–1267, May 2013.

[38] D. S. Schramm, B. W. Williams, and T. C. Green, "Torque ripple reduction of switched reluctance motors by phase current optimal profiling," in *Proc. Annu. IEEE Power Electron. Spec. Conf. (PESC)*, Toledo, Spain, 1992, 857–860 vol.2.

[39] A. M. Stankovic, G. Tadmor, Z. J. Coric, and I. Agirman, "On torque ripple reduction in current-fed switched reluctance motors," *IEEE Trans. Ind. Electron.*, vol. 46, no. 1, pp. 177–183, Feb. 1999.

[40] X. D. Xue, K. W. E. Cheng, and S. L. Ho, "Optimization and evaluation of torque-sharing functions for torque ripple minimization in switched reluctance motor drives," *IEEE Trans. Power Electron.*, vol. 24, no. 9, pp. 2076–2090, Sep. 2009.

[41] I. Husain and M. Ehsani, "Torque ripple minimization in switched reluctance motor drives by PWM current control," *IEEE Trans. Power Electron.*, vol. 11, no. 1, pp. 83–88, Jan. 1996.

[42] A. Chiba, K. Kiyota, N. Hoshi, M. Takemoto, and S. Ogasawara, "Development of a rare-earth-free sr motor with high torque density for hybrid vehicles," *IEEE Trans. Energy Convers.*, vol. 30, no. 1, pp. 175–182, Mar. 2015.

[43] Q. Yu, B. Bilgin, and A. Emadi, "Design considerations of switched reluctance machines with high power density," in *Proc. IEEE Transp. Electri. Conf.Expo. (ITEC)*, Jun. 2016, pp. 1–5.

[44] H. Goto, S. Murakami, and O. Ichinokura, "Design to maximize torque-volume density of axial-flux srm for in-wheel EV," in *Proc. Annu. Conf. IEEE Ind. Electron. Soc. (IECON)*, Nov. 2015, pp. 5191–5196.

[45] J. A. Reyer and P. Y. Papalambros, "Combined optimal design and control with application to an electric dc motor," *J. Mech. Design*, vol. 124, no. 2, pp. 183–191, 2002.

[46] T. de Paula Machado Bazzo, J. F. KÃűlzer, R. Carlson, F. Wurtz, and L. Gerbaud, "Multiphysics design optimization of a permanent magnet synchronous generator," *IEEE Trans. Ind. Electron.*, vol. 64, no. 12, pp. 9815–9823, Dec. 2017.

[47] Y. Chen, W. Fu, and X. Weng, "A concept of general flux-modulated electric machines based on a unified theory and its application to developing a novel doubly-fed dual-stator motor," *IEEE Trans. Ind. Electron.*, vol. 64, no. 12, pp. 9914–9923, Dec. 2017.

[48] Q. Wang, S. Niu, and L. Yang, "Design optimization and comparative study of novel dual-pm excited machines," *IEEE Trans. Ind. Electron.*, vol. 64, no. 12, pp. 9924–9933, Dec. 2017.

[49] N. Boules, "Design optimization of permanent magnet dc motors," *IEEE Trans. Ind. Appl.*, vol. 26, no. 4, pp. 786–792, Jul. 1990.

[50] Y. Duan and D. M. Ionel, "A review of recent developments in electrical machine design optimization methods with a PM synchronous motor benchmark study," *IEEE Trans. Ind. Appl.*, vol. 49, no. 3, pp. 1268–1275, May 2013.

[51] K. Idir, L. Chang, and H. Dai, "Error-based global optimization approach for electric motor design," *IEEE Trans. Magn.*, vol. 34, no. 5, pp. 2861–2864, Sep. 1998.

[52] V. Gradinaru, L. Tutelea, and I. Boldea, "25 kW, 15 krpm, 6/4 PMSM: Optimal design and torque pulsation reduction via FEM," in *Proc. Int. Conf. Optimization Electri. Electro. Equipment*, May 2008, pp. 249–256.

[53] F. Messine, B. Nogarede, and J. Lagouanelle, "Optimal design of electromechanical actuators: A new method based on global optimization," *IEEE Trans. Magn.*, vol. 34, no. 1, pp. 299–308, Jan. 1998.

[54] K. R. Davey and B. B. Gamble, "Numerical design of synchronous generators," *IEEE Trans. Magn.*, vol. 41, no. 8, pp. 2391–2397, Aug. 2005.

[55] M. Mitchell, *An Introduction to Genetic Algorithms*. Cambridge, MA, USA: MIT Press, 1996, ISBN: 0-262-13316-4.

[56] G. F. Uler and O. A. M. and, "Utilizing genetic algorithms for the optimal design of electromagnetic devices," *IEEE Transactions on Magnetics*, vol. 30, no. 6, pp. 4296–4298, Nov. 1994.

[57] N. Bianchi and S. Bolognani, "Design optimisation of electric motors by genetic algorithms," *IEE Proc. - Electri. Power Appl.*, vol. 145, no. 5, pp. 475–483, Sep. 1998.

[58] Y. del Valle, G. K. Venayagamoorthy, S. Mohagheghi, J. Hernandez, and R. G. Harley, "Particle swarm optimization: Basic concepts, variants and applications in power systems," *IEEE Trans. Evol. Comput.*, vol. 12, no. 2, pp. 171–195, Apr. 2008.

[59] G. Y. Sizov, P. Zhang, D. M. Ionel, N. A. O. Demerdash, and M. Rosu, "Automated multi-objective design optimization of pm ac machines using computationally efficient fea and differential evolution," *IEEE Trans. Ind. Appl.*, vol. 49, no. 5, pp. 2086–2096, Sep. 2013.

[60] R. Storn and K. Price, "Differential evolution–a simple and efficient heuristic for global optimization over continuous spaces," *J. Global Optimiz.*, vol. 11, no. 4, pp. 341–359, 1997.

[61] J. Brest, S. Greiner, B. Boskovic, M. Mernik, and V. Zumer, "Self-adapting control parameters in differential evolution: A comparative study on numerical benchmark problems," *IEEE Trans. Evol. Comput.*, vol. 10, no. 6, pp. 646–657, Dec. 2006.

[62] J.-H. Choi, S. Kim, J.-M. Shin, J. Lee, and S.-T. Kim, "The multi-object optimization of switched reluctance motor," in *Proc. Int. Conf. Electri. Mach. Syst. (ICEMS)*, Nov. 2003, 195–198 vol.1.

[63] B. Mirzaeian, M. Moallem, V. Tahani, and C. Lucas, "Multiobjective optimization method based on a genetic algorithm for switched reluctance motor design," *IEEE Trans. Magn.*, vol. 38, no. 3, pp. 1524–1527, May 2002.

[64] X. D. Xue, K. W. E. Cheng, T. W. Ng, and N. C. Cheung, "Multi-objective optimization design of in-wheel switched reluctance motors in electric vehicles," *IEEE Trans. Ind. Electron.*, vol. 57, no. 9, pp. 2980–2987, Sep. 2010.

[65] A. M. Omekanda, "A new technique for multidimensional performance optimization of switched reluctance motors for vehicle propulsion," *IEEE Trans. Ind. Appl.*, vol. 39, no. 3, pp. 672–676, May 2003.

[66] H. Cheng, H. Chen, and Z. Yang, "Design indicators and structure optimisation of switched reluctance machine for electric vehicles," *IET Electri. Power Appl.*, vol. 9, no. 4, pp. 319–331, 2015.

[67] J. W. Jiang, B. Bilgin, B. Howey, and A. Emadi, "Design optimization of switched reluctance machine using genetic algorithm," in *Proc. IEEE Int. Electri. Mach., Drives Conf. (IEMDC)*, May 2015, pp. 1671–1677.

[68] S. Smaka, S. Konjicija, S. Masic, and M. Cosovic, "Multi-objective design optimization of 8/14 switched reluctance motor," in *Proc. IEEE Int. Electri. Mach., Drives Conf. (IEMDC)*, May 2013, pp. 468–475.

[69] C. Ma and L. Qu, "Multiobjective optimization of switched reluctance motors based on design of experiments and particle swarm optimization," *IEEE Trans. Energy Convers.*, vol. 30, no. 3, pp. 1144–1153, Sep. 2015.

[70] E. Öksüztepe, "In-wheel switched reluctance motor design for electric vehicles by using a pareto-based multiobjective differential evolution algorithm," *IEEE Trans. Veh. Technol.*, vol. 66, no. 6, pp. 4706–4715, Jun. 2017.

[71] Z. Ren, D. Zhang, and C.-S. Koh, "Multi-objective worst-case scenario robust optimal design of switched reluctance motor incorporated with FEM and Kriging," in *Proc. Int. Conf. Electri. Mach. Syst. (ICEMS)*, Oct. 2013, pp. 716–719.

[72] D. Ilea, M. M. Radulescu, F. Gillon, and P. Brochet, "Multi-objective optimization of a switched reluctance motor for light electric traction applications," in *Proc. IEEE Veh. Power Propul. Conf.*, Sep. 2010, pp. 1–6.

[73] J. H. Fisch, P. C. Kjaer, J. J. Gribble, and T. J. E. Miller, "Pareto-optimal firing angles for switched reluctance motor control," in *Int. Conf. Genetic Algorithms Eng. Syst.*, Sep. 1997, pp. 90–96.

[74] C. Ma, L. Qu, R. Mitra, P. Pramod, and R. Islam, "Vibration and torque ripple reduction of switched reluctance motors through current profile optimization," in *Proc. IEEE Annu. Appl. Power Electron. Conf. Expo. (APEC)*, Long Beach, CA, Mar. 2016, pp. 3279–3285.

[75] M. M. Borujeni, A. Rashidi, and S. M. Saghaeian Nejad, "Optimal four quadrant speed control of switched reluctance motor with torque ripple reduction based on EM-MOPSO," in *Power Electron. Drive Syst. Technol. Conf. (PEDSTC)*, Feb. 2015, pp. 310–315.

[76] M. M. Namazi, M. M. Borujeni, A. Rashidi, S. M. S. Nejad, and J. Ahn, "Torque ripple reduction of switched reluctance motor drive with adaptive sliding mode control and particle swarm optimization," in *IEEE Int. Conf. Adv. Intell. Mechatronics (AIM)*, Jul. 2015, pp. 371–376.

[77] N. Schofield, S. A. Long, D. Howe, and M. McClelland, "Design of a switched reluctance machine for extended speed operation," *IEEE Trans. Ind. Appl.*, vol. 45, no. 1, pp. 116–122, Jan. 2009.

[78] Z. Q. Zhu and D. Howe, "Electrical machines and drives for electric, hybrid, and fuel cell vehicles," *Proc. IEEE*, vol. 95, no. 4, pp. 746–765, Apr. 2007.

[79] Z. Q. Zhu, W. Q. Chu, and Y. Guan, "Quantitative comparison of electromagnetic performance of electrical machines for hevs/evs," *CES Trans. Electri. Mach. Syst.*, vol. 1, no. 1, pp. 37–47, Mar. 2017.

[80] K. Kiyota, H. Sugimoto, and A. Chiba, "Comparing electric motors: An analysis using four standard driving schedules," *IEEE Ind. Appl. Mag.*, vol. 20, no. 4, pp. 12–20, Jul. 2014.

[81] T. A. Burress, S. L. Campbell, C. Coomer, C. W. Ayers, A. A. Wereszczak, J. P. Cunningham, L. D. Marlino, L. E. Seiber, and H.-T. Lin, "Evaluation of the 2010 toyota prius hybrid synergy drive system," Mar. 2011.

[82] Y. Sato, S. Ishikawa, T. Okubo, M. Abe, and K. Tamai, "Development of high response motor and inverter system for the Nissan LEAF electric vehicle," in *SAE 2011 World Congr. & Exhibit.*, SAE International, Apr. 2011.

[83] K. M. Rahman, S. Jurkovic, C. Stancu, J. Morgante, and P. J. Savagian, "Design and performance of electrical propulsion system of extended range electric vehicle (EREV) Chevrolet Volt," *IEEE Trans. Ind. Appl.*, vol. 51, no. 3, pp. 2479–2488, May 2015.

[84] F. Lambert, *Tesla motor designer explains Model 3's transition to permanent magnet motor*, `https://electrek.co/2018/02/27/tesla-model-3-motor-designer-permanent-magnet-motor/`, Accessed: Apr. 2018.

[85] K. Ohyama, M. N. F. Nashed, K. Aso, H. Fujii, and H. Uehara, "Design using finite element analysis of switched reluctance motor for electric vehicle," in *Int. Conf. Inf. Commun. Technol.*, vol. 1, Apr. 2006, pp. 727–732.

[86] K. Watanabe, S. Aida, A. Komatsuzaki, and I. Miki, "Driving force characteristics of 40kW switched reluctance motor for electric vehicle," in *Proc. Int. Conf. Electri. Mach. Syst. (ICEMS)*, Oct. 2007, pp. 1894–1898.

[87] W. Uddin, T. Husain, Y. Sozer, and I. Husain, "Design methodology of a switched reluctance machine for off-road vehicle applications," *IEEE Trans. Ind. Appl.*, vol. 52, no. 3, pp. 2138–2147, May 2016.

[88] Z. Yang, F. Shang, I. P. Brown, and M. Krishnamurthy, "Comparative study of interior permanent magnet, induction, and switched reluctance motor drives for ev and hev applications," *IEEE Trans. Transport. Electrific.*, vol. 1, no. 3, pp. 245–254, Oct. 2015.

[89] K. M. Rahman and S. E. Schulz, "Design of high-efficiency and high-torque-density switched reluctance motor for vehicle propulsion," *IEEE Trans. Ind. Appl.*, vol. 38, no. 6, Nov. 2002.

[90] M. Kasprzak, J. W. Jiang, B. Bilgin, and A. Emadi, "Thermal analysis of a three-phase 24/16 switched reluctance machine used in hevs," in *Proc. IEEE Energy Conv. Congr. Expo. (ECCE)*, Sep. 2016, pp. 1–7.

[91] J. W. Jiang, B. Bilgin, and A. Emadi, "Three-phase 24/16 switched reluctance machine for a hybrid electric powertrain," *IEEE Trans. Transport. Electrific.*, vol. 3, no. 1, pp. 76–85, Mar. 2017.

[92] T. Uematsu and R. S. Wallace, "Design of a 100 kW switched reluctance motor for electric vehicle propulsion," in *Proc. IEEE Annu. Appl. Power Electron. Conf. Expo. (APEC)*, vol. 1, Mar. 1995, pp. 411–415.

[93] S. Wang, Q. Zhan, Z. Ma, and L. Zhou, "Implementation of a 50-kW four-phase switched reluctance motor drive system for hybrid electric vehicle," *IEEE Trans. Magn.*, vol. 41, no. 1, pp. 501–504, Jan. 2005.

[94] A. Chiba, Y. Takano, M. Takeno, T. Imakawa, N. Hoshi, M. Takemoto, and S. Ogasawara, "Torque density and efficiency improvements of a switched reluctance motor without rare-earth material for hybrid vehicles," *IEEE Trans. Ind. Appl.*, vol. 47, no. 3, pp. 1240–1246, May 2011.

[95] I. Boldea, L. N. Tutelea, L. Parsa, and D. Dorrell, "Automotive electric propulsion systems with reduced or no permanent magnets: An overview," *IEEE Trans. Ind. Electron.*, vol. 61, no. 10, pp. 5696–5711, Oct. 2014.

[96] T. Imakawa, K. Chimata, N. Hoshi, A. Chiba, M. Takemoto, and S. Ogasawara, "Characteristic measurements of switched reluctance motor on prototype electric vehicle," in *IEEE Int. Electri. Veh. Conf.*, Mar. 2012, pp. 1–8.

[97] H. Boeriu, *BMW i3 - official specs*, `https://www.bmwblog.com/2013/07/10/bmw-i3-official-specs/`, Accessed: Apr. 2018.

[98] C. Morris, *Elon Musk: Cooling, not power-to-weight ratio, is the challenge with ac induction motors*, `https://chargedevs.com/newswire/elon-musk-cooling-not-power-to-weight-ratio-is-the-challenge-with-ac-induction-motors/`, Accessed: Apr. 2018.

[99] F. Momen, K. Rahman, and Y. Son, "Electrical propulsion system design of Chevrolet Bolt battery electric vehicle," *IEEE Trans. Ind. Appl.*, vol. 55, no. 1, pp. 376–384, Jan. 2019.

[100] R. I. Davis and R. D. Lorenz, "Engine torque ripple cancellation with an integrated starter alternator in a hybrid electric vehicle: Implementation and control," *IEEE Trans. Ind. Appl.*, vol. 39, no. 6, pp. 1765–1774, Nov. 2003.

[101] F. L. M. dos Santos, J. Anthonis, F. Naclerio, J. J. C. Gyselinck, H. Van der Auweraer, and L. C. S. Góes, "Multiphysics NVH modeling: Simulation of a switched reluctance motor for an electric vehicle," *IEEE Trans. Ind. Appl.*, vol. 61, no. 1, pp. 469–476, Jan. 2014.

[102] K. Takase, H. Goto, and O. Ichinokura, "Design and experiment of double stator structure axial-flux sr motor for electric city commuters," in *Proc. Int. Conf. Electri. Mach. Syst. (ICEMS)*, Nov. 2016, pp. 1–6.

[103] S. P. Nikam, V. Rallabandi, and B. G. Fernandes, "A high-torque-density permanent-magnet free motor for in-wheel electric vehicle application," *IEEE Trans. Ind. Appl.*, vol. 48, no. 6, pp. 2287–2295, Nov. 2012.

[104] R. Madhavan and B. G. Fernandes, "Axial flux segmented srm with a higher number of rotor segments for electric vehicles," *IEEE Trans. Energy Convers.*, vol. 28, no. 1, pp. 203–213, Mar. 2013.

[105] M. Hsieh, P. Li, H. Ting, C. Hsu, C. Chang, W. Lin, and L. Chang-Chien, "A regenerative braking system for switched reluctance machine applied to electric vehicles," in *Proc. Int. Conf. Electri. Mach. Syst. (ICEMS)*, Nov. 2016, pp. 1–6.

[106] T. Raminosoa, B. Blunier, D. Fodorean, and A. Miraoui, "Design and optimization of a switched reluctance motor driving a compressor for a PEM fuel-cell system for automotive applications," *IEEE Trans. Ind. Electron.*, vol. 57, no. 9, pp. 2988–2997, Sep. 2010.

[107] B. Fahimi, A. Emadi, and R. B. Sepe, "A switched reluctance machine-based starter/alternator for more electric cars," *IEEE Trans. Energy Convers.*, vol. 19, no. 1, pp. 116–124, Mar. 2004.

[108] N. Schofield and S. Long, "Generator operation of a switched reluctance starter/generator at extended speeds," *IEEE Trans. Veh. Technol.*, vol. 58, no. 1, pp. 48–56, Jan. 2009.

[109] M. V. Zaharia, F. Gillon, and M. M. Radulescu, "Design optimization of a switched reluctance machine-based integrated starter/alternator for automotive applications," in *Proc. Int. Conf. Electri. Mach. (ICEM)*, Sep. 2016, pp. 1577–1583.

[110] S. Ruoho, J. Kolehmainen, J. Ikaheimo, and A. Arkkio, "Interdependence of demagnetization, loading, and temperature rise in a permanent-magnet synchronous motor," *IEEE Trans. Magn.*, vol. 46, no. 3, pp. 949–953, Mar. 2010.

[111] M. T. Thompson, "Practical issues in the use of ndfeb permanent magnets in maglev, motors, bearings, and eddy current brakes," *Proc. IEEE*, vol. 97, no. 11, pp. 1758–1767, Nov. 2009.

[112] G. Choi, Y. Zhang, and T. M. Jahns, "Experimental verification of rotor demagnetization in a fractional-slot concentrated-winding pm synchronous machine under drive fault conditions," *IEEE Trans. Ind. Appl.*, vol. 53, no. 4, pp. 3467–3475, Jul. 2017.

[113] B. A. Welchko, T. M. Jahns, and S. Hiti, "IPM synchronous machine drive response to a single-phase open circuit fault," *IEEE Trans. Power Electron.*, vol. 17, no. 5, pp. 764–771, Sep. 2002.

[114] N. Bianchi, S. Bolognani, and M. Dai Pre, "Strategies for the fault-tolerant current control of a five-phase permanent-magnet motor," *IEEE Trans. Ind. Appl.*, vol. 43, no. 4, pp. 960–970, Jul. 2007.

[115] B. A. Welchko, T. M. Jahns, W. L. Soong, and J. M. Nagashima, "IPM synchronous machine drive response to symmetrical and asymmetrical short circuit faults," *IEEE Trans. Energy Convers.*, vol. 18, no. 2, pp. 291–298, Jun. 2003.

[116] K. W. Klontz, T. J. E. Miller, M. I. McGilp, H. Karmaker, and P. Zhong, "Short-circuit analysis of permanent-magnet generators," *IEEE Trans. Ind. Appl.*, vol. 47, no. 4, pp. 1670–1680, Jul. 2011.

[117] A. J. Mitcham, G. Antonopoulos, and J. J. A. Cullen, "Implications of shorted turn faults in bar wound pm machines," *IEE Proc. - Electri. Power Appl.*, vol. 151, no. 6, pp. 651–657, Nov. 2004.

[118] B. Gu, J. Choi, and I. Jung, "Development and analysis of interturn short fault model of pmsms with series and parallel winding connections," *IEEE Trans. Power Electron.*, vol. 29, no. 4, pp. 2016–2026, Apr. 2014.

[119] J. Park and J. Hur, "Detection of inter-turn and dynamic eccentricity faults using stator current frequency pattern in ipm-type bldc motors," *IEEE Trans. Ind. Electron.*, vol. 63, no. 3, pp. 1771–1780, Mar. 2016.

[120] J. Park, C. Jeong, S. Lee, and J. Hur, "Early detection technique for stator winding inter-turn fault in bldc motor using input impedance," *IEEE Trans. Ind. Appl.*, vol. 51, no. 1, pp. 240–247, Jan. 2015.

[121] S. Cheng, P. Zhang, and T. G. Habetler, "An impedance identification approach to sensitive detection and location of stator turn-to-turn faults in a closed-loop multiple-motor drive," *IEEE Trans. Ind. Electron.*, vol. 58, no. 5, pp. 1545–1554, May 2011.

[122] J. Farooq, S. Srairi, A. Djerdir, and A. Miraoui, "Use of permeance network method in the demagnetization phenomenon modeling in a permanent magnet motor," *IEEE Trans. Magn.*, vol. 42, no. 4, Apr. 2006.

[123] J. D. McFarland and T. M. Jahns, "Influence of d- and q-axis currents on demagnetization in pm synchronous machines," in *Proc. IEEE Energy Conv. Congr. Expo. (ECCE)*, Sep. 2013, pp. 4380–4387.

[124] J. D. McFarland and T. M. Jahns, "Investigation of the rotor demagnetization characteristics of interior PM synchronous machines during fault conditions," *IEEE Trans. Ind. Appl.*, vol. 50, no. 4, pp. 2768–2775, Jul. 2014.

[125] G. Choi and T. M. Jahns, "Interior permanent magnet synchronous machine rotor demagnetization characteristics under fault conditions," in *Proc. IEEE Energy Conv. Congr. Expo. (ECCE)*, Sep. 2013, pp. 2500–2507.

[126] D. Fernandez, D. Hyun, Y. Park, D. D. Reigosa, S. B. Lee, D. Lee, and F. Briz, "Permanent magnet temperature estimation in pm synchronous motors using low-cost hall effect sensors," *IEEE Trans. Ind. Appl.*, vol. 53, no. 5, pp. 4515–4525, Sep. 2017.

[127] D. Reigosa, D. Fernandez, C. Gonzalez, S. B. Lee, and F. Briz, "Permanent magnet synchronous machine drive control using analog hall-effect sensors," *IEEE Trans. Ind. Appl.*, vol. 54, no. 3, pp. 2358–2369, May 2018.

[128] D. Reigosa, D. Fernández, Y. Park, A. B. Diez, S. B. Lee, and F. Briz, "Detection of demagnetization in permanent magnet synchronous machines using hall-effect sensors," *IEEE Trans. Ind. Appl.*, vol. 54, no. 4, pp. 3338–3349, Jul. 2018.

[129] M. Zhu, W. Hu, and N. C. Kar, "Torque-ripple-based interior permanent-magnet synchronous machine rotor demagnetization fault detection and current regulation," *IEEE Trans. Ind. Appl.*, vol. 53, no. 3, pp. 2795–2804, May 2017.

[130] O. Wallscheid, A. Specht, and J. Böcker, "Observing the permanent-magnet temperature of synchronous motors based on electrical fundamental wave model quantities," *IEEE Trans. Ind. Electron.*, vol. 64, no. 5, pp. 3921–3929, May 2017.

[131] S. Stipetic, M. Kovacic, Z. Hanic, and M. Vrazic, "Measurement of excitation winding temperature on synchronous generator in rotation using infrared thermography," *IEEE Trans. Ind. Electron.*, vol. 59, no. 5, pp. 2288–2298, May 2012.

[132] D. D. Reigosa, D. Fernandez, T. Tanimoto, T. Kato, and F. Briz, "Permanent-magnet temperature distribution estimation in permanent-magnet synchronous machines using back electromotive force harmonics," *IEEE Trans. Ind. Appl.*, vol. 52, no. 4, pp. 3093–3103, Jul. 2016.

[133] D. D. Reigosa, D. Fernandez, Z. Zhu, and F. Briz, "PMSM magnetization state estimation based on stator-reflected PM resistance using high-frequency signal injection," *IEEE Trans. Ind. Appl.*, vol. 51, no. 5, pp. 3800–3810, Sep. 2015.

[134] W. le Roux, R. G. Harley, and T. G. Habetler, "Detecting rotor faults in low power permanent magnet synchronous machines," *IEEE Trans. Power Electron.*, vol. 22, no. 1, pp. 322–328, Jan. 2007.

[135] T. Hosoi, H. Watanabe, K. Shima, T. Fukami, R. Hanaoka, and S. Takata, "Demagnetization analysis of additional permanent magnets in salient-pole synchronous machines with damper bars under sudden short circuits," *IEEE Trans. Ind. Electron.*, vol. 59, no. 6, pp. 2448–2456, Jun. 2012.

[136] S. S. Nair, V. I. Patel, and J. Wang, "Post-demagnetization performance assessment for interior permanent magnet ac machines," *IEEE Trans. Magn.*, vol. 52, no. 4, pp. 1–10, Apr. 2016.

[137] K. Kim, Y. Lee, and J. Hur, "Transient analysis of irreversible demagnetization of permanent-magnet brushless dc motor with interturn fault under the operating state," *IEEE Trans. Ind. Appl.*, vol. 50, no. 5, pp. 3357–3364, Sep. 2014.

[138] H. Kim and J. Hur, "Dynamic characteristic analysis of irreversible demagnetization in SPM- and IPM-type BLDC motors," *IEEE Trans. Ind. Appl.*, vol. 53, no. 2, pp. 982–990, Mar. 2017.

[139] H. Xiong, J. Zhang, M. W. Degner, C. Rong, F. Liang, and W. Li, "Permanent-magnet demagnetization design and validation," *IEEE Trans. Ind. Appl.*, vol. 52, no. 4, pp. 2961–2970, Jul. 2016.

[140] Y. Lee and T. G. Habetler, "An on-line stator turn fault detection method for interior PM synchronous motor drives," in *Proc. IEEE Annu. Appl. Power Electron. Conf. Expo. (APEC)*, Feb. 2007, pp. 825–831.

[141] S.-C. Yang, "Online turn fault detection of interior permanent-magnet machines using the pulsating-type voltage injection," *IEEE Trans. Ind. Appl.*, vol. 52, no. 3, pp. 2340–2349, May 2016.

[142] G. Choi and T. M. Jahns, "Demagnetization characteristics of permanent magnet synchronous machines," in *Proc. Annu. Conf. IEEE Ind. Electron. Soc. (IECON)*, Oct. 2014, pp. 469–475.

[143] T. A. Lipo, *Introduction to AC Machine Design*. Hoboken, New Jersey: John Wiley & Sons, Inc., 2017.

[144] V. Raulin, A. Radun, and I. Husain, "Modeling of losses in switched reluctance machines," *IEEE Trans. Ind. Appl.*, vol. 40, no. 6, pp. 1560–1569, Nov. 2004.

[145] P. N. Materu and R. Krishnan, "Estimation of switched reluctance motor losses," *IEEE Trans. Ind. Appl.*, vol. 28, no. 3, pp. 668–679, May 1992.

[146] Y. Hayashi and T. J. E. Miller, "A new approach to calculating core losses in the srm," *IEEE Trans. Ind. Appl.*, vol. 31, no. 5, pp. 1039–1046, Sep. 1995.

[147] Q. Yu, B. Bilgin, and A. Emadi, "Loss and efficiency analysis of switched reluctance machines using a new calculation method," *IEEE Trans. Ind. Electron.*, vol. 62, no. 5, pp. 3072–3080, May 2015.

[148] S. Li, S. Zhang, J. Dang, T. G. Habetler, and R. G. Harley, "Analytical calculation of the phase inductance profile of switched reluctance machines," *IEEE Trans. Energy Convers.*, vol. PP, no. PP, PP–PP, 2019.

[149] T. Back, D. B. Fogel, and Z. Michalewicz, Eds., *Handbook of Evolutionary Computation*, 1st. Bristol, UK, UK: IOP Publishing Ltd., 1997, ISBN: 0750303921.

[150] J. Snoek, H. Larochelle, and R. P. Adams, "Practical bayesian optimization of machine learning algorithms," in *Proc. Advances Neural Infor. Process. Syst. (NIPS)*, ser. NIPS'12, Lake Tahoe, Nevada: Curran Associates Inc., 2012, pp. 2951–2959.

[151] Z. Ghahramani, "Probabilistic machine learning and artificial intelligence," *Nature*, vol. 521, no. 7553, p. 452, 2015.

[152] M. Pelikan, D. E. Goldberg, and E. Cantú-Paz, "Boa: The bayesian optimization algorithm," in *Proc. 7th Int. Conf. Parallel Problem Solving Nature*, ser. GECCO'99, Orlando, Florida, 1999, pp. 525–532, ISBN: 1-55860-611-4.

[153] M. Laumanns and J. Ocenasek, "Bayesian optimization algorithms for multi-objective optimization," in *Proc. 7th Int. Conf. Parallel Problem Solving Nature*, J. J. M. Guervós, P. Adamidis, H.-G. Beyer, H.-P. Schwefel, and J.-L. Fernández-Villacañas, Eds., Berlin, Heidelberg, 2002, pp. 298–307.

[154] P. Feliot, J. Bect, and E. Vazquez, "A bayesian approach to constrained single- and multi-objective optimization," *J. of Global Optimization*, vol. 67, no. 1, pp. 97–133, Jan. 2017.

[155] Y. Katsumata and T. Terano, "Bayesian optimization algorithm for multi-objective solutions: Application to electric equipment configuration problems in a power plant," in *Proc. IEEE Congr. Evol. Comput.*, vol. 2, Dec. 2003, 1101–1107 Vol.2.

[156] H. Abdelrahman, F. Berkenkamp, J. Poland, and A. Krause, "Bayesian optimization for maximum power point tracking in photovoltaic power plants," in *Proc. European Control Conf. (ECC)*, Jun. 2016, pp. 2078–2083.

[157] S. Mandal, B. Santhi, S. Sridhar, K. Vinolia, and P. Swaminathan, "Nuclear power plant thermocouple sensor-fault detection and classification using deep learning and generalized likelihood ratio test," *IEEE Transactions on Nuclear Science*, vol. 64, no. 6, pp. 1526–1534, Jun. 2017.

[158] A. J. Mair, E. M. Davidson, S. D. J. McArthur, S. K. Srivastava, K. Schoder, and D. A. Cartes, "Machine learning techniques for diagnosing and locating faults through the automated monitoring of power electronic components in shipboard power systems," in *Proc. IEEE Electric Ship Technologies Symp.*, Apr. 2009, pp. 469–476.

[159] L. Du, J. A. Restrepo, Y. Yang, R. G. Harley, and T. G. Habetler, "Nonintrusive, self-organizing, and probabilistic classification and identification of plugged-in electric loads," *IEEE Trans. Smart Grid*, vol. 4, no. 3, pp. 1371–1380, Sep. 2013.

[160] A. Baheri and C. Vermillion, "Altitude optimization of airborne wind energy systems: A bayesian optimization approach," in *Proc. IEEE Amer. Control Conf. (ACC)*, May 2017, pp. 1365–1370.

[161] W. Lyu, P. Xue, F. Yang, C. Yan, Z. Hong, X. Zeng, and D. Zhou, "An efficient bayesian optimization approach for automated optimization of analog circuits," *IEEE Trans. Circuits Syst. I*, vol. 65, no. 6, pp. 1954–1967, Jun. 2018.

[162] M. Lisicki, W. Lubitz, and G. W. Taylor, "Optimal design and operation of archimedes screw turbines using bayesian optimization," *Appl. Energy*, vol. 183, pp. 1404 –1417, 2016.

[163] B. Reagen, J. M. HernÃąndez-Lobato, R. Adolf, M. Gelbart, P. Whatmough, G. Wei, and D. Brooks, "A case for efficient accelerator design space exploration via bayesian optimization," in *roc. IEEE/ACM Int. Symp. Low Power Electron. & Design (ISLPED)*, Jul. 2017, pp. 1–6.

[164] J. Snoek, O. Rippel, K. Swersky, R. Kiros, N. Satish, N. Sundaram, M. M. A. Patwary, P. Prabhat, and R. P. Adams, "Scalable bayesian optimization using deep neural networks," in *Proc. Int. Conf. Mach. Learn.*, ser. ICML'15, Lille, France, 2015, pp. 2171–2180.

[165] Y. Zhang, K. Sohn, R. Villegas, G. Pan, and H. Lee, "Improving object detection with deep convolutional networks via bayesian optimization and structured prediction," in *Proc. IEEE Conf. Computer Vision & Pattern Recognition (CVPR)*, Jun. 2015, pp. 249–258.

[166] Y. Chen, M. W. Hoffman, S. G. Colmenarejo, M. Denil, T. P. Lillicrap, M. Botvinick, and N. de Freitas, "Learning to learn without gradient descent by gradient descent," in *Proc. Int. Conf. Machine Learning (ICML)*, vol. 70, Aug. 2017, pp. 748–756.

[167] B. Shahriari, K. Swersky, Z. Wang, R. P. Adams, and N. de Freitas, "Taking the human out of the loop: A review of bayesian optimization," *Proc. IEEE*, vol. 104, no. 1, pp. 148–175, Jan. 2016.

[168] E. Brochu, V. M. Cora, and N. De Freitas, "A tutorial on bayesian optimization of expensive cost functions, with application to active user modeling and hierarchical reinforcement learning," *arXiv preprint arXiv:1012.2599*, 2010.

[169] C. M. Bishop, *Pattern recognition and machine learning*. springer, 2006.

[170] C. E. Rasmussen, "Gaussian processes in machine learning," in *Summer School on Machine Learning*, Springer, 2003, pp. 63–71.

[171] J. M. Henrández-Lobato, M. W. Hoffman, and Z. Ghahramani, "Predictive entropy search for efficient global optimization of black-box functions," in *Proc. Adv. Neural Inf. Process. Syst.*, ser. NIPS'14, Montreal, Canada, 2014, pp. 918–926.

[172] J. Vesanto and E. Alhoniemi, "Clustering of the self-organizing map," *IEEE Trans. Neural Netw.*, vol. 11, no. 3, pp. 586–600, May 2000.

[173] K. Tasdemir and E. Merenyi, "Exploiting data topology in visualization and clustering of self-organizing maps," *IEEE Trans. Neural Netw.*, vol. 20, no. 4, pp. 549–562, Apr. 2009.

[174] M. C. Ferreira de Oliveira and H. Levkowitz, "From visual data exploration to visual data mining: A survey," *IEEE Trans. Vis. Comput. Graphics*, vol. 9, no. 3, pp. 378–394, Jul. 2003.

[175] D. J. Walker, R. Everson, and J. E. Fieldsend, "Visualizing mutually nondominating solution sets in many-objective optimization," *IEEE Trans. Energy Convers.*, vol. 17, no. 2, pp. 165–184, Apr. 2013.

[176] T. Tusar and B. Filipic, "Visualization of pareto front approximations in evolutionary multiobjective optimization: A critical review and the prosection method," *IEEE Trans. Energy Convers.*, vol. 19, no. 2, pp. 225–245, Apr. 2015.

[177] Z. He and G. G. Yen, "Visualization and performance metric in many-objective optimization," *IEEE Trans. Energy Convers.*, vol. 20, no. 3, pp. 386–402, Jun. 2016.

[178] C. Dudas, A. H. C. Ng, and H. Boström, "Post-analysis of multi-objective optimization solutions using decision trees," *Intell. Data Anal.*, vol. 19, no. 2, pp. 259–278, Mar. 2015.

[179] R. Silva, A. Salimi, M. Li, A. R. R. Freitas, F. G. Guimaraes, and D. A. Lowther, "Visualization and analysis of tradeoffs in many-objective optimization: A case study on the interior PM motor design," *IEEE Trans. Instrum. Meas.*, vol. 52, no. 3, pp. 1–4, Mar. 2016.

[180] T. Kohonen, *Self-Organising Maps*. New York: Springer, 2001.

[181] ——, *MATLAB Implementations and Applications of the Self-Organizing Map*. Helsinki: Unigrafia Bookstore Helsinki, 2014.

[182] J. Vesanto, E. Alhoniemi, J. Himberg, K. Kiviluoto, and J. Parviainen, "Self-organizing map for data mining in matlab: The som toolbox," *Simul. News Eur.*, vol. 25, no. 54, 1999.

[183] W. Li, S. Zhang, and G. He, "Semisupervised distance-preserving self-organizing map for machine-defect detection and classification," *IEEE Trans. Instrum. Meas.*, vol. 62, no. 5, pp. 869–879, May 2013.

[184] A. Widodo, D. Satrijo, M. Huda, G. Lim, and B. Yang, "Application of self organizing map for intelligent machine fault diagnostics based on infrared thermography images," in *Proc. Int. Conf. Bio-Inspired Comput.: Theories Appli. (BIC-TA),*, Sep. 2011, pp. 123–128.

[185] H. Zhang, X. Zhang, X.-Z. Gao, and S. Song, "Self-organizing multiobjective optimization based on decomposition with neighborhood ensemble," *Neurocomput.*, vol. 173, no. P3, pp. 1868–1884, Jan. 2016.

[186] H. Zhang, A. Zhou, S. Song, Q. Zhang, X. Gao, and J. Zhang, "A self-organizing multiobjective evolutionary algorithm," *IEEE Transactions on Evolutionary Computation*, vol. 20, no. 5, pp. 792–806, Oct. 2016.

[187] E. Filatovas, D. Podkopaev, and O. Kurasova, "A visualization technique for accessing solution pool in interactive methods of multiobjective optimization," *Int. J. Comput. Commu. & Control*, vol. 10, no. 4, pp. 508–519, 2015.

[188] J. Vesanto, "Som-based data visualization methods," *Intel. Data Anal.*, vol. 3, pp. 111–126, 1999.

[189] K. Witowski, M. Liebscher, and T. Goel, "Decision making in multi-objective optimization for industrial applications–data mining and visualization of pareto data," in *Proc. 8th World Congr. SMO*, 2009.

[190] M. Yoshimi, T. Kuhara, K. Nishimoto, M. Miki, and T. Hiroyasu, "Visualization of pareto solutions by spherical self-organizing map and itâăźs acceleration on a gpu," *J. Software Eng. Appl.*, vol. 5, no. 03, p. 129, 2012.

[191] T. Richardson, B. Nekolny, J. Holub, and E. H. Winer, "Visualizing design spaces using two-dimensional contextual self-organizing maps," *AIAA J.*, vol. 52, no. 4, pp. 725–738, 2014.

[192] S. Obayashi and D. Sasaki, "Visualization and data mining of pareto solutions using self-organizing map," in *Proc. 2nd Int. Evolutionary Multi-Criterion Optimization Conf. (EMO),*, ser. EMO'03, Faro, Portugal, 2003, pp. 796–809.

[193] N. Suzuki, T. Okamoto, and S. Koakutsu, "Visualization of pareto optimal solution sets using the growing hierarchical self-organizing maps," *IEEJ Trans. Electron. Inf. Syst.*, vol. 135, pp. 908–919, 2015.

[194] S. Chen, D. Amid, O. M. Shir, L. Limonad, D. Boaz, A. Anaby-Tavor, and T. Schreck, "Self-organizing maps for multi-objective pareto frontiers," in *Proc. IEEE Pacific Vis. Symp. (PacificVis),*, Feb. 2013, pp. 153–160.

[195] A. G. Sarigiannidis, M. E. Beniakar, and A. G. Kladas, "Fast adaptive evolutionary PM traction motor optimization based on electric vehicle drive cycle," *IEEE Trans. Veh. Technol.*, vol. 66, no. 7, pp. 5762–5774, Jul. 2017.

[196] R. C. P. Silva, T. Rahman, M. H. Mohammadi, and D. A. Lowther, "Multiple operating points based optimization: Application to FSCW electric motors," *IEEE Trans. Ind. Electron.*, vol. 65, no. 2, pp. 1719–1727, Feb. 2018.

[197] M. E. Beniakar, A. G. Sarigiannidis, P. E. Kakosimos, and A. G. Kladas, "Multiobjective optimization of a surface mounted PM actuator with fractional slot winding for aerospace applications," *IEEE Trans. Magn.*, vol. 50, no. 2, pp. 665–668, Feb. 2014.

[198] J. B. Tenenbaum, V. d. Silva, and J. C. Langford, "A global geometric framework for nonlinear dimensionality reduction," *Science*, vol. 290, no. 5500, pp. 2319–2323, 2000.

[199] S. T. Roweis and L. K. Saul, "Nonlinear dimensionality reduction by locally linear embedding," *Science*, vol. 290, pp. 2323–2326, 2000.

[200] G. E. Hinton and S. T. Roweis, "Stochastic neighbor embedding," in *Adv. Neural Inf. Proc. Syst. 15*, 2003, pp. 857–864.

[201] L. van der Maaten and G. Hinton, "Visualizing data using t-SNE," *J. Machi. Learning Res.*, vol. 9, pp. 2579–2605, 2008.

[202] T. Sebastian, "Temperature effects on torque production and efficiency of PM motors using NdFeB magnets," *IEEE Trans. Ind. Appl.*, vol. 31, no. 2, pp. 353–357, Mar. 1995.

[203] Y. Lee, "A stator turn fault detection method and a fault-tolerant operating strategy for interior PM synchronous motor drives in safety-critical applications," PhD thesis, Georgia Institute of Technology, 2007.

[204] D. Ishak, Z. Q. Zhu, and D. Howe, "Eddy-current loss in the rotor magnets of permanent-magnet brushless machines having a fractional number of slots per pole," *IEEE Trans. Magn.*, vol. 41, no. 9, pp. 2462–2469, Sep. 2005.

[205] N. Limsuwan, T. Kato, C. Yu, J. Tamura, D. D. Reigosa, K. Akatsu, and R. D. Lorenz, "Secondary resistive losses with high-frequency injection-based self-sensing in IPM machines," *IEEE Trans. Ind. Appl.*, vol. 49, no. 4, pp. 1499–1507, Jul. 2013.

[206] L. He, S. Cheng, Y. Du, R. G. Harley, and T. G. Habetler, "Stator temperature estimation of direct-torque-controlled induction machines via active flux or torque injection," *IEEE Trans. Power Electron.*, vol. 30, no. 2, pp. 888–899, Feb. 2015.

[207] L. He, S. Cheng, R. G. Harley, and T. G. Habetler, "A torque-injection-based approach for thermal monitoring of induction machines with direct torque control," in *Proc. IEEE Int. Electri. Mach., Drives Conf. (IEMDC)*, May 2013, pp. 93–99.

[208] L. He, S. Cheng, Y. Du, R. G. Harley, and T. G. Habetler, "A DC-flux-injection approach for thermal monitoring of induction machines with direct torque control," in *Proc. IEEE Energy Conv. Congr. Expo. (ECCE)*, Sep. 2013, pp. 2115–2122.

[209] L. He, J. Restrepo, S. Cheng, R. G. Harley, and T. G. Habetler, "An improved DC-signal-injection method with active torque-ripple mitigation for thermal monitoring of field-oriented-controlled induction motors," in *Proc. IEEE Energy Conv. Congr. Expo. (ECCE)*, Sep. 2015, pp. 4447–4454.

[210] S. Meliopoulos and G. J. Cokkinides, *Power system relaying, theory and applications*, ECE6323 Lecture Notes, Georgia Institute of Technology, 2016.

[211] S. Zhang, S. Li, R. G. Harley, and T. G. Habetler, "Performance evaluation and comparison of multi-objective optimization algorithms for the analytical design of switched reluctance machines," *CES Trans. Electri. Mach. Syst.*, vol. 1, no. 1, pp. 58–65, Mar. 2017.

[212] S. Li, S. Zhang, C. Gong, T. G. Habetler, and R. G. Harley, "An enhanced analytical calculation of the phase inductance of switched reluctance machines," *IEEE Trans. Ind. Appl.*, vol. 55, no. 2, pp. 1392–1407, Mar. 2019.

[213] S. Li, S. Zhang, T. G. Habetler, and R. G. Harley, "Modeling, design optimization and applications of switched reluctance machines – A review," *IEEE Trans. Ind. Appl.*, vol. 55, no. 3, pp. 2660–2681, May 2019.

[214] S. Zhang, S. Zhang, B. Wang, and T. G. Habetler, "Machine learning and deep learning algorithms for bearing fault diagnostics – A comprehensive review," *arXiv preprint arXiv:1901.08247*, 2019.

[215] S. Li, S. Zhang, J. Dang, T. G. Habetler, and R. G. Harley, "Calculating the unsaturated inductance of 4/2 switched reluctance motors at arbitrary rotor positions based on partial differential equations of magnetic potentials," in *Proc. North Amer. Power Symp. (NAPS)*, Charlotte, NC, Oct. 2015, pp. 1–8.

[216] T. P. Tshimanga, Shen Zhang, E. Bezabih, L. He, V. Iyer, and R. G. Harley, "Stator temperature estimation of open-loop controlled induction machines via active dc voltage injection," in *Proc. North Amer. Power Symp. (NAPS)*, Charlotte, NC, Oct. 2015, pp. 1–5.

[217] S. Zhang, S. Li, J. Dang, R. G. Harley, and T. G. Habetler, "Multi-objective design and optimization of generalized switched reluctance machines with particle swarm intelligence," in *Proc. IEEE Energy Conv. Congr. Expo. (ECCE)*, Milwaukee, WI, Sep. 2016, pp. 1–7.

[218] S. Li, S. Zhang, T. G. Habetler, and R. G. Harley, "Fast and accurate analytical calculation of the unsaturated phase inductance profile of 6/4 switched reluctance machines," in *Proc. IEEE Energy Conv. Congr. Expo. (ECCE)*, Milwaukee, WI, Sep. 2016, pp. 1–8.

[219] S. Zhang, S. Li, R. G. Harley, and T. G. Habetler, "A multi-objective analytical design approach of switched reluctance machines with integrated active current profile optimization," in *Proc. IEEE Int. Electri. Mach., Drives Conf. (IEMDC)*, Miami, FL, May 2017, pp. 1–6.

[220] S. Zhang, S. Li, L. He, J. A. Restrepo, and T. G. Habetler, "A high-frequency rotating flux injection based rotor thermal monitoring scheme for direct-torque-controlled interior permanent magnet synchronous machines," in *Proc. IEEE Int. Electri. Mach., Drives Conf. (IEMDC)*, Miami, FL, May 2017, pp. 1–6.

[221] S. Li, S. Zhang, T. G. Habetler, and R. G. Harley, "A survey of electromagnetic - thermal modeling and design optimization of switched reluctance machines," in *Proc. IEEE Int. Electri. Mach., Drives Conf. (IEMDC)*, Miami, FL, May 2017, pp. 1–7.

[222] S. Zhang, S. Li, L. He, J. A. Restrepo, and T. G. Habetler, "A high-frequency torque injection-based rotor thermal monitoring scheme for direct-torque-controlled interior permanent magnet synchronous machines," in *Proc. IEEE Energy Conv. Congr. Expo. (ECCE)*, Cincinnati, OH, Oct. 2017, pp. 3552–3558.

[223] S. Li, S. Zhang, C. Jiang, L. He, and R. G. Harley, "An enhanced active dc-flux injection based approach for thermal monitoring of induction machines with direct torque control schemes," in *Proc. IEEE Energy Conv. Congr. Expo. (ECCE)*, Cincinnati, OH, Oct. 2017, pp. 3537–3544.

[224] S. Li, S. Zhang, C. Jiang, J. R. Mayor, T. G. Habetler, and R. G. Harley, "A fast control-integrated and multiphysics-based multi-objective design optimization of switched reluctance machines," in *Proc. IEEE Energy Conv. Congr. Expo. (ECCE)*, Cincinnati, OH, Oct. 2017, pp. 730–737.

[225] S. Zhang and T. G. Habetler, "A transient model of interior permanent magnet machines under stator winding inter-turn short circuit faults," in *Proc. Annu. Conf. IEEE Ind. Electron. Soc. (IECON)*, Beijing, China, Oct. 2017, pp. 1765–1770.

[226] ——, "Transient demagnetization characteristics of interior permanent magnet synchronous machines with stator inter-turn short circuit faults for automotive applications," in *Proc. IEEE Energy Conv. Congr. Expo. (ECCE)*, Portland, OR, Sep. 2018, pp. 1661–1667.

[227] S. Zhang, S. Li, R. G. Harley, and T. G. Habetler, "Visualization and data mining of multi-objective electric machine optimizations with self-organizing maps: A case study on switched reluctance machines," in *Proc. IEEE Energy Conv. Congr. Expo. (ECCE)*, Sep. 2018, pp. 4296–4302.

[228] ——, "An efficient multi-objective bayesian optimization approach for the automated analytical design of switched reluctance machines," in *Proc. IEEE Energy Conv. Congr. Expo. (ECCE)*, Portland, OR, Sep. 2018, pp. 4290–4295.

[229] S. Zhang, B. Wang, C. Lin, D. Lin, K. H. Teo, and T. G. Habetler, "Quantification of rolling-element bearing fault severity of induction machines," in *Proc. IEEE Int. Electri. Mach., Drives Conf. (IEMDC)*, Portland, OR, May 2019, pp. 1–7.

[230] S. Zhang, S. Zhang, B. Wang, and T. G. Habetler, "Deep learning algorithms for bearing fault diagnostics – A review," in *Proc. IEEE Int. Symp. Diagno. Power Electron. Drives (SDEMPED)*, Toulouse, France, Aug. 2019, pp. 1–7.

[231] S. Zhang, S. Zhang, S. Li, and T. G. Habetler, "Visualization of multi-objective switched reluctance machine optimization under multiple operating conditions with t-sne," in *Proc. IEEE Energy Conv. Congr. Expo. (ECCE)*, Baltimore, MD, Sep. 2019, pp. 1–7.

[232] S. Zhang, A. M. Qwbaiban, J.-M. Huh, and T. G. Habetler, "Dimension and mechanical structure design of low-cost heliostats in concentrated solar power plants," in *Proc. IEEE Energy Conv. Congr. Expo. (ECCE)*, Baltimore, MD, Sep. 2019, pp. 1–7.

VITA

Shen Zhang received the B.S. degree with the highest distinction in electrical engineering from the Honors School, Harbin Institute of Technology, Harbin, China, in 2014. He is currently working toward the Ph.D. degree at the School of Electrical and Computer Engineering, Georgia Institute of Technology, Atlanta, GA.

Since August 2014, he has been working on the design, optimization and condition monitoring of electric machines in the electric power group of the Georgia Institute of Technology. He was a research intern at Eaton China Innovation Center, Shanghai, China, in 2014, where he received the Best Intern Award. In 2016 summer, he was a research intern at Tesla, Inc., Fremont, CA. In 2018 summer, he was a research intern at Mitsubishi Electric Research Laboratory, Cambridge, MA.

His research interests include design, control, condition monitoring and diagnostics of electric machines, control of power electronics, powertrain engineering in electric vehicles, machine learning and data mining.